Mechanical properties of micro-architectured lattices: Edge effects, fatigue and fracture

Ioannis Christodoulou

Department of Mechanical Engineering
University College London

A thesis submitted for the degree of

Doctor of Philosophy

December 18, 2016

Declaration

I, Ioannis Christodoulou, confirm that the work presented in this thesis is my own. Where information has been derived from other sources, I confirm that this has been indicated in the thesis.

Abstract

Micro-architectured lattices offer unique combinations of stiffness, strength and toughness at low density that makes them ideal for lightweighting applications. This thesis quantifies, compare and contrast various aspects of the mechanical performance of micro-architectured lattices with special emphasis on the role of microstructure upon their effective macroscopic properties. The differences in mechanical performance between lattices with a stochastic and various regular-periodic micro-architectures (Square, Hexagonal, Triangular and Kagome micro-structure), with each exhibiting either a stretch or bending-dominated deformation at the cell-scale, are systematically quantified.

First, the elastic and yield properties of infinite-sized lattices are obtained by finite-element modelling of representative unit-cells, applying the appropriate boundary conditions, where there is an excellent agreement with analytical predictions from existing literature. By relaxing the 'infinite-size' assumption, the effects of finite specimen size on the effective macroscopic stiffness and strength are quantified for uniaxial and shear loadings. The predicted size effects were found to be a direct consequence of the strong and weak boundary layers that emanate from the specimen boundaries. The influence of these edge effects on the macroscopic stiffness and strength are quantified for the Square, Triangular and Kagome lattices, and the results compared to existing ones for the Diamond, Hexagonal and stochastic Voronoi lattices in the literature.

Second, in addition to the monotonic loading studied above, the cyclic stress-life response is also investigated for the regular lattices. A non-linear continuous fatigue damage model for high cycle fatigue is implemented which allows the simulation of strain accumulation in lattices until failure. The proposed model is able to predict with reasonable accuracy the S-N curves for Diamond lattices to shear fatigue where experimental data is available in the literature. The numerical model is then used to elucidate the shear and uniaxial fatigue response of other periodic lattice micro-architectures. Fatigue damage is found to originate in locations that are also affected by the boundary

layers. A major difference in the response between bending- and stretching-dominated lattices is revealed; the bending-dominated micro-architectures accumulate damage within a larger lattice area (volume) and in a more progressive manner compared to their stretch-dominated counterparts.

Last, the fracture toughness of stochastic Voronoi lattices is studied using an idealised LEFM (Linear Elastic Fracture Mechanics) approach and the results compared to those of periodic lattices. The role of relative density, micro-structure regularity and loading mode are also explored. It will be shown that the toughness predicted by numerical simulations of the CT (compact tension) and SENB-3PB (single-edge notched in three-point bending) test specimens reveal a specimen-size dependency and a disparity with the corresponding predictions by the idealised LEFM approach: the origins of these are also clarified.

Acknowledgements

First of all, I would like to sincerely and gratefully acknowledge my PhD supervisor, Dr PJ Tan. This research project would not be possible without his advice, help and support. The regular, and often lengthy, discussions we had about my project provided me with a lot of ideas on how to proceed with my research, helped me to clarify my own thoughts and explain the results of my work; most importantly, on how to fill in gaps and to address potentially questionable areas. His high expectations, without a doubt, pushed my limits to an even higher level and has helped to improve the quality and impact of this work. Lastly, he gave me the confidence and encouragement to keep going with my research in times of doubt and difficulties.

A huge thank you goes to my parents and brother for their love, support, trust and encouragement. Moreover, I cannot forget the support of my close friends: Constantinos, Panagiotis, Menelaos and above all Maria who encouraged me during some difficult times. Finally, I want to thank my colleagues and friends at the High Strain Rate Laboratory of UCL; in particular Yuan Ye (Usher), Anna Chiara-Faralli and Liu Liu for a wonderful, and conducive, working environment.

Last, but not least, I am grateful to Dr Tan for supporting me financially during my PhD, through an EPSRC-DTA studentship and other funds.

Contents

List of Figures

List of Tables

Nomenclature

A	lattice area
E_s,E^*	elastic modulus of cell wall material and lattice
G^*	shear modulus of lattice
H	lattice height, measured along x_2
$\overline{H}$	number of complete cells along x_2
$\overline{R}$	dimensionless aspect ratio
$\overline{R}_c$	central dimensionless aspect ratio for Triangular lattices
W	lattice width, measured along x_1
$\overline{W}$	number of complete cells along x_1
Z	Nodal connectivity
d_0	average cell size
l,$\hat{l}$	uniform and average cell wall length
t	uniform cell wall thickness
u_1, u_2	displacement in the x_1 and x_2 directions
x_1, x_2	cartesian coordinates with origin centred at crack tip
I	isotropy parameter
Λ	cell-regularity parameter
U	strain energy
γ_{12}	shear strain
ε_{11}, ε_{22}	uniaxial strain in the x_1 and x_2 directions
ε_{ij}	strain tensor
η, ψ	energy absorption efficiency of a lattice
κ_v	Vertex perturbation parameter
ν_s, ν^*	Poisson's ratio of cell wall material and lattice
$\overline{\rho}$	relative density
$\rho_{\mathrm{s}}, \rho^*$	density of cell wall and lattice material
σ_{ij}	stress tensor
$(\sigma_y)_s$,σ_y^*	uniaxial yield strength of cell wall material and lattice

τ_y^*	shear yield strength of lattice
ω_{12}	in-plane rotation

Edge effects

M_{ab}	moments experienced by the strut ab at node a
RF_1,RF_2	reaction force in x_1 and x_2
T, B, L and R	top, bottom, left and right divisions of ∂V
λ	normalised overhanging cell size in Square lattice
∂V	boundary of *finite-sized* lattice
l_{BBL}	length of bending-dominated boundary layer
h	characteristic size of the unit-cell
θ_{ab}	rotation of strut ab at node a
$\overline{\rho}_{A-M}$	transition $\overline{\rho}$ for which lattice in not axial dominated
$\overline{\rho}_{B-M}$	transition $\overline{\rho}$ for which lattice in not bending dominated

Fatigue

D	cell wall fatigue damage parameter
M_0, c, β, b	NLCD model parameters
N	cycle number
N_f, N_f^*	cell wall and lattice cycles to failure
R, R^*	cell wall and macroscopic load ratio
l_{nl}	nonlocal continuum characteristic length
δD	NLCD 'jump-in-cycle' control parameter
ε_{max}	strain at maximum stress
κ_b	buckling imperfection severity parameter
$\bar{\sigma}, \bar{\sigma}^*$	mean cell wall and macroscopic uniaxial stress
$\sigma_{\text{amp}}, \sigma_{\text{amp}}^*$	cell wall and macroscopic stress amplitude
σ_e	cell wall endurance strength of
σ_{e_0}	cell wall endurance strength of cell wall for $R = -1$
σ_e^*	lattice uniaxial endurance strength
$\sigma_{\text{max}}^*, \sigma_{\text{min}}^*$	maximum and minimum macroscopic uniaxial stress
$\sigma_{\text{max}}, \sigma_{\text{min}}$	maximum and minimum cell wall stress
σ_p^*	lattice peak stress
σ_{u}	cell wall ultimate tensile strength

τ_e^*	lattice shear endurance strength
τ_{max}^*, τ_{min}^*	maximum and minimum macroscopic shear stress
ω, ω^*	cell wall and lattice modulus damage parameter

Fracture

B	stress biaxiality ratio
$\mathcal{G}$	energy release rate
K_{I}, K_{II}	mode I and II stress intensity factor (SIF)
K_{IC}, K_{IIC}	mode I and II fracture toughness
K_{eff},$K_{\text{eff,C}}$	effective and critical effective stress intensity factor
M	mode-mixity parameter
N	number of terms in DFA
T	T-stress
U_b,U_a,U_s	strain energy due to bending, axial stretch and shear
W	fracture testing specimen principal dimension
r, θ	polar coordinates centred at the crack-tip
r_{DFA}	annulus radius for DFA known points
α	crack length
$\bar{\varepsilon}_{eq}$	equivalent strain
η	ratio of bending to total strain energy
σ_f	tensile fracture strength of cell wall
σ_{max}	maximum tensile stress in an element

Abbreviations

BBL	bending boundary layer
BLA	boundary layer analysis
CT	compact tension
DFA	displacement field analysis
FE	finite element
NLCD	non-linear continues damage model for fatigue
NLCD-FE	coupled NLCD with FE model
SEN(B)	single-edge notched in bending
SIF	stress intensity factor
UC	unit-cell

Sub/superscripts

s	cell wall properties
$*$	macroscopic properties and loading parameters
∞	loading parameters applied at infinity
ps	plane strain properties
UC	infinite-sized macroscopic properties estimated by unit-cell method

Chapter 1

Background

The development of cost-effective, high-strength lightweight components that reduces the weight of a product without compromising cost, performance and/or safety is essential to compete in today's global market. Important considerations for light-weighting are, typically, the strength-to-weight ratio (σ/ρ) and/or the stiffness-to-weight ratio (E/ρ) of the material from which a component is made. Invariably, it is almost always a combination of properties that matter when comparing materials performance. To get an overview of the different strategies, it is instructive to examine *material property charts*. Figure 1.1 gives an example of how the elastic modulus and strength of different material classes vary with their density; it also delineates accessible parts of the material property space from the ones that are not. There are a number of strategies that might be employed to achieve light-weighting. One method is to manipulate the chemistry of materials to create new alloys although the potential for any substantive gain is small. Another is to employ heat treatment or mechanical working but this, too, is limited. Man-made hybrids – natural materials (cork, bamboo or wood) also belong to the same family – are a recent development with the biggest potential. They can be broadly categorised into two sub-classes: the first is the ubiquitous composites that utilise combinations of materials to exploit favourable properties of each, often by imbedding strengthening particles (fibres, fabrics, etc.) within a softer or brittle matrix; and, the second involves manipulating material distribution in space, to control its microstructure, to create *lattices*. It is the latter which the present thesis is concerned with.

Man-made foams – a class of *cellular solids* – is a typical example of a hybrid that offers significant weight-saving potential. It has a microstructure comprising of an interconnected network of beams and plates with a large void volume ratio. Consequently, foams have density that are significantly lower than other classes of material and they

tend to occupy the lower left region of material property charts when plotted against density, see Fig. 1.1 (Ashby et al., 2000; Gibson and Ashby, 1997). Nearly all materials can be foamed: metals, polymers, even ceramics. However, the nature of the foaming process invariably gives rise to a microstructure that is, intrinsically, stochastic. In principle, it is possible to improve on the mechanical performance of these stochastic foams, at the same density, by simply controlling its microstructure – see recent review by Fleck et al. (2010). Therefore, it is convenient to divide man-made foams into two further sub-classes: (1) foams with a stochastic microstructure (stochastic foams); and, (2) lattices, or *micro-architectured materials*, with a periodic microstructure obtained by tessellating two-dimensional (2D) or three-dimensional (3D) space using one, or more, geometric shapes (or cells) without overlap and/or gaps.

To increase the rate of uptake by the industry – its use in lightweighting applications saves energy and fuel, while contributing positively to the low carbon emissions agenda – their mechanical response to external loadings will need to be better understood. The present thesis aims to fill in a few key gaps in our current state of knowledge concerning their mechanical performances and how they compare to the more widely-adopted stochastic foams. Topics to be addressed will include: (1) the modelling of how their intensive (bulk) mechanical properties are affected by edge-effects under remote shear and uniaxial loadings; (2) modelling of their shear and compression fatigue response; and, (3) modelling of their fracture response and the consequences of adopting standard test specimen geometries for toughness measurements.

1.1 Topology

A lattice material is characterised by three distinct length scales at the

- microscale,
- mesoscale, also known as the cell-scale, and
- macroscale.

Their bulk response to remote macroscopic loading is dictated not only by the solid material from which the *cell walls* are made but, crucially, on how its individual cells are arranged on the cell-scale. The properties that characterise the different features of the

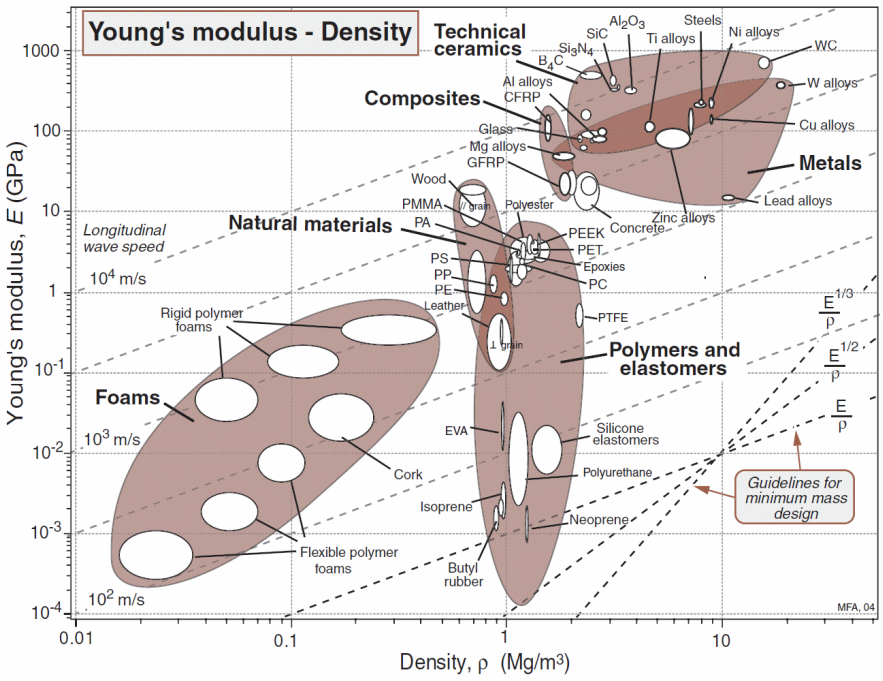

(a)

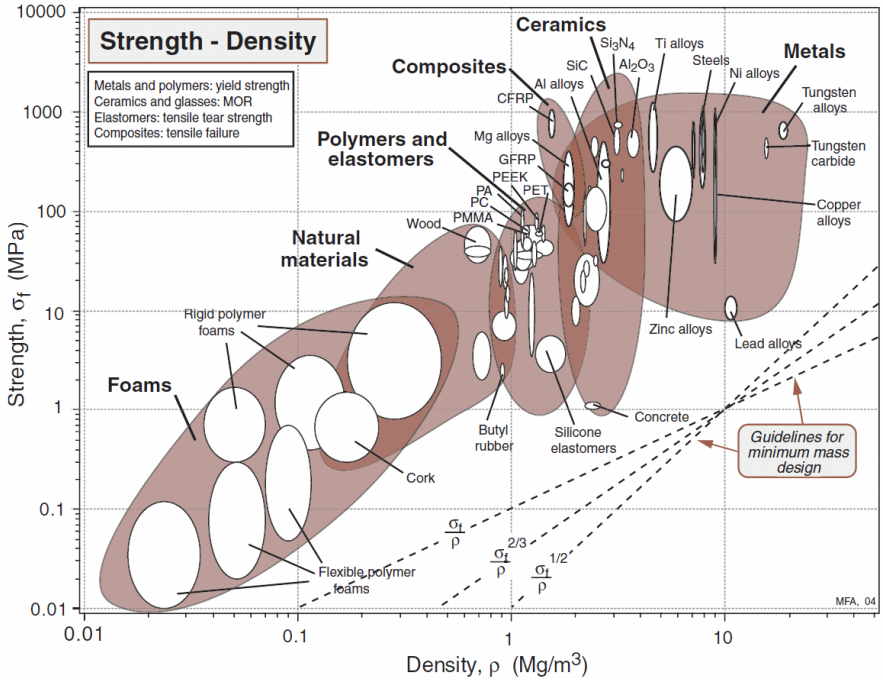

(b)

Figure 1.1: Material property charts: (a) Elastic modulus and (b) Strength versus density. (Source: Ashby, 2005)

cell-scale are known, collectively, as *topology*. One of the most important topological feature of a lattice is, arguably, its *nodal connectivity* (Z): defined as the number of cell walls that meet at a common node. This is because the dominant mode of deformation – this can either be stretch or bending, or their combination thereof – experienced by individual cell walls is dictated, to a large extent, by its nodal connectivity Z (Deshpande et al., 2001b).

Lattices exist either in two- (2D) or three- (3D) dimensional form. 2D lattices comprised of a framework of struts, or cell walls, arranged to form cells in a plane – see Fig. 1.2a. In a similar vein, 3D lattices fill space: this is achieved either with prismatic cells as in Fig. 1.2b (Cote et al., 2006; Fleck and Deshpande, 2004; Wadley et al., 2003); or, through a 3D arrangement of struts (Wadley et al., 2003; Wallach and Gibson, 2001). If the faces of the cells are covered by a membrane, the resulting lattice has *closed-cells* as shown in Fig. 1.2c. On the other hand, if no such membrane exists, the lattice has a 'wireframe-like' network referred to as *open-cell* as shown in Fig. 1.2d. This distinction – closed or open – applies only to 3D lattices and foams. Analysing 3D foams/lattices is much more challenging compared to their 2D counterparts which are easier. Therefore, stochastic 2D foams and lattices are often studied to inform the mechanical behaviour of their more complex 3D counterparts (Gibson and Ashby, 1997). In a similar vein, this thesis will focus on planar/prismatic lattices and reference to 3D lattices will be made only where appropriate.

At the mesoscale, the cell micro-architecture of a lattice (2D or 3D) is either *periodic* or *non-periodic*. The former is characterised by geometrical symmetries so that its macroscopic response is readily analysed through judicious use of a representative unit-cell. It is worth noting here that the analysis of a unit-cell does not account for any edge (or boundary) effects. By contrast, the cell micro-architecture in non-periodic lattices are characterised by varying degree of randomness so that their cells may have different shapes and sizes. It is instructive to examine each category in greater detail; particularly, on how they are to be categorised and their effects upon the bulk mechanical response of a lattice.

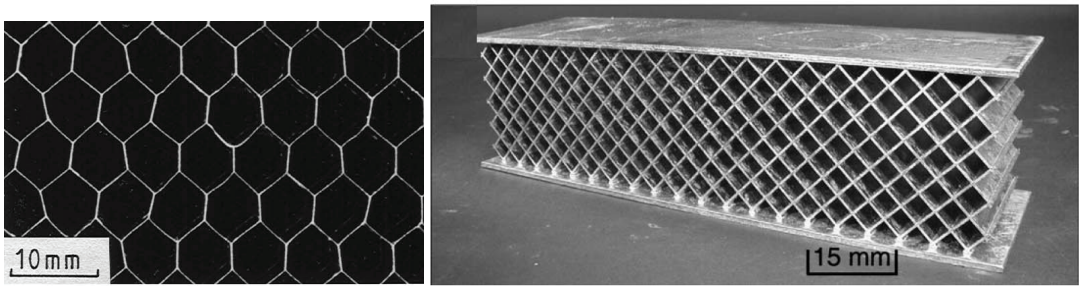

(a) 2D Hexagonal lattice

(b) 3D Prismatic lattice

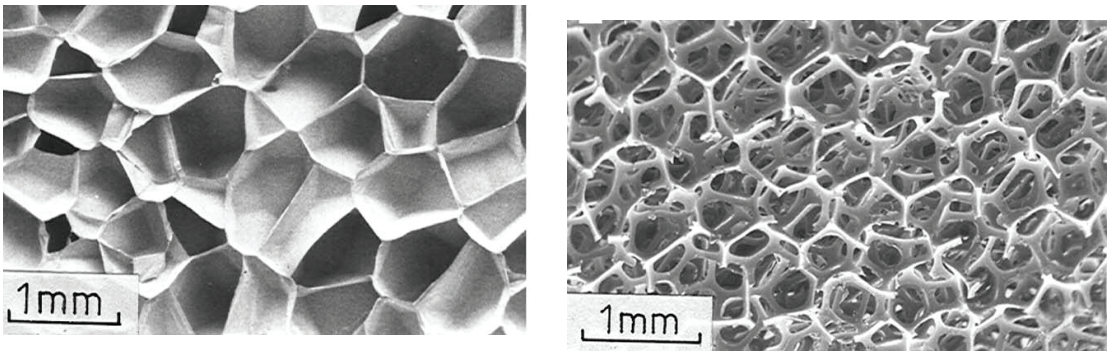

(c) Closed-cell foam

(d) Open-cell foam

Figure 1.2: Cellular solids with different topological features at the mesoscale (Source: Cote et al., 2006; Gibson and Ashby, 1997)

1.1.1 Periodic lattices

If a single regular polygon – equiangular and equilateral – is used to tessellate a plane, the resulting 2D lattice is *regular*. Only three polygons – square, regular hexagon and equilateral triangle – can be used to generate a *regular* lattice (Fleck et al., 2010). These are shown in Figs. 1.3a-c and their resulting lattice in Figs. 1.4a-c, respectively. The square polygon is also commonly used in its 45° rotated version to give the Diamond lattice, as shown in Fig. 1.4d. On the other hand, if two or more regular polygons are used for tessellation, subject to the constraint that its nodal connectivity is identical for every node (or joint), the resulting lattice is *semi-regular*. Only eight independent semi-regular lattices can be constructed. An example is the Triangular-Hexagonal lattice shown in Fig. 1.4e; it is commonly known as a Kagome lattice (Hyun and Torquato, 2002) which is constructed using polygons shown in Fig. 1.3d. By relaxing the aforesaid constraint imposed on nodal connectivity, other periodic lattices may be generated

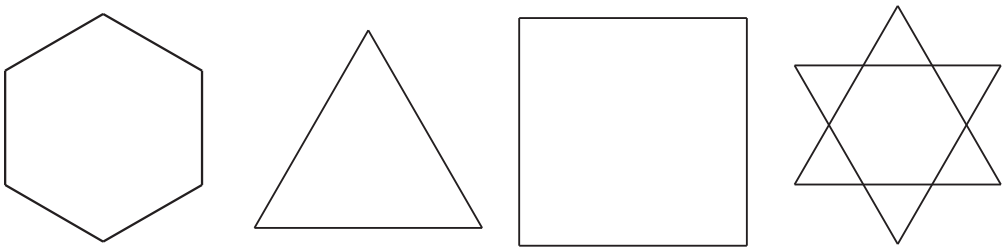

(a) Hexagonal (b) Triangular (c) Square (d) Kagome

Figure 1.3: Regular 2D polygons used to construct regular (a,b,c), and semi-regular (d) lattices.

although they are of no interest to the present study.

Periodic 3D lattices may be generated in a similar fashion. Unlike its 2D counterpart, the polygons now form the faces of 3D cells. Regular 3D lattices can only be generated by tessellating either cubic or dodecahedral cells (Gibson and Ashby, 1997). Semi-regular 3D lattices are much more common. An octet-truss lattice is one example that combines tetrahedra and octahedra cells (Deshpande et al., 2001a).

Regular and semi-regular lattices are either *bending-* or *stretch-dominated* depending on the dominant mode of deformation experienced by its cell walls on the mesoscale. To distinguish them, consider an equivalent pin-jointed framework by replacing all rigid joints of the original lattice with pin-joints. If this pin-jointed equivalent has a macroscopic strain-producing collapse mechanism under remote external loading, then the original rigid-jointed lattice must resist collapse, primarily, through bending of its struts, i.e. it is a bending-dominated micro-architecture. If, on the other hand, the pin-jointed equivalent has no, or only periodic, collapse mechanisms, then the original lattice is stretch-dominated (Deshpande et al., 2001b; Fleck et al., 2010).

The dominant mode of deformation experienced by the cell walls is dictated by its nodal connectivity. Following Maxwell (1864) and Calladine (1978), the necessary but not sufficient conditions for a pin-jointed framework with b struts and j frictionless joints to be just rigid is

$$b - 2j + 3 = s - m \quad \text{(2D)} \tag{1.1}$$

$$b - 3j + 6 = s - m \quad \text{(3D)} \tag{1.2}$$

where s and m corresponds to the number of states of self-stress (a self-equilibrated state in the absence of external load) and mechanisms, respectively. For a large pin-jointed framework with j joints and an average nodal connectivity of Z, the total number of struts is given by $b \approx jZ/2$ (Deshpande et al., 2001b). Thus, according to Maxwell's rule, the necessary *but not sufficient* condition for the pin-jointed framework to remain rigid is $Z = 4$ in the 2D case and $Z = 6$ in the 3D case. The sufficient condition for a macroscopically rigid lattice was found to be $Z = 6$ for 2D and $Z = 12$ for 3D (Deshpande et al., 2001b). Only the Triangular lattice (Fig. 1.4b) and the 3D octet-truss lattice meet this condition (Deshpande et al., 2001a). Thus the rigidly-jointed Triangular lattice deforms primarily by stretch. If the minimum condition for rigidity is not met – the Hexagonal lattice with $Z = 3$ in Fig. 1.4a for example – the pin-jointed framework has a macroscopic strain producing mechanism, and is collapsible. Hence, its rigidly-jointed counterpart deforms primarily by bending.

Now consider the Square, Diamond and Kagome lattices in Fig. 1.4c,d,e. All satisfy the necessary criterion for rigidity given by Eq.(1.1) since their nodal connectivity is $Z = 4$. The pin-jointed Square and Diamond lattices possess a macroscopic strain-producing mechanism and thus its rigidly-jointed counterpart is a bending-dominated lattice. By contrast, a pin-jointed Kagome lattice has no strain producing collapse mechanisms and it can only collapse by a periodic mechanism that does not produce macroscopic strain; i.e. it is a rigid pin-jointed framework. Henceforth the rigidly-jointed Kagome lattice is a stretch-dominated lattice (Hutchinson and Fleck, 2005).

To summarise, both Triangular and Kagome lattices have stretch-dominated micro-architecture whilst that of the Hexagonal lattice is bending-dominated. The Square, and the closely related Diamond, lattice can be either depending on whether a macroscopic strain producing mechanism is triggered in its pin-jointed equivalent. As shall be revealed in the following sections, the dominant mode of deformation at the mesoscale plays a key role in determining the macroscopic mechanical properties of a lattice.

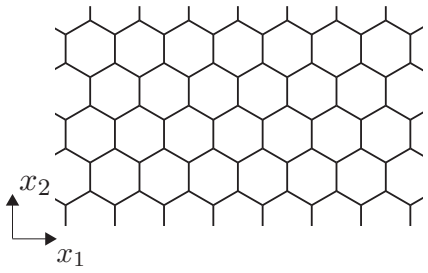

(a) Hexagonal

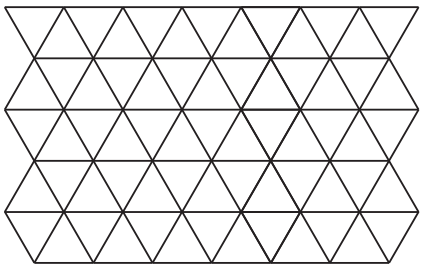

(b) Triangular

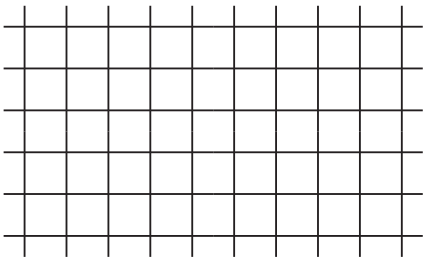

(c) Square

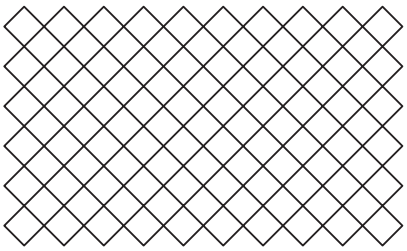

(d) Diamond

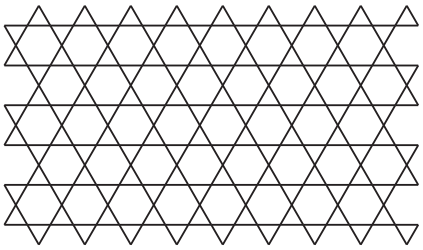

(e) Kagome

Figure 1.4: Periodic lattices: regular (a-d) and semi-regular (e).

Since the five lattices – Triangular, Kagome, Square, Diamond and Hexagonal – cover the entire range of possible deformation mechanisms, they are interesting subjects of investigation from which comparisons can be made. These five lattice micro-architectures, together with their non-periodic counterparts, where appropriate, will be the focus of this thesis.

1.1.2 Imperfections in periodic lattices

In reality, no man-made lattices – thus far – are ever strictly periodic. Even small errors in the manufacturing process can introduce imperfections resulting in slightly distorted cells, uneven cell wall length, etc. The *vertex perturbation* technique is often employed to introduce imperfections into, an otherwise, periodic lattice for the purpose of numerical modelling.

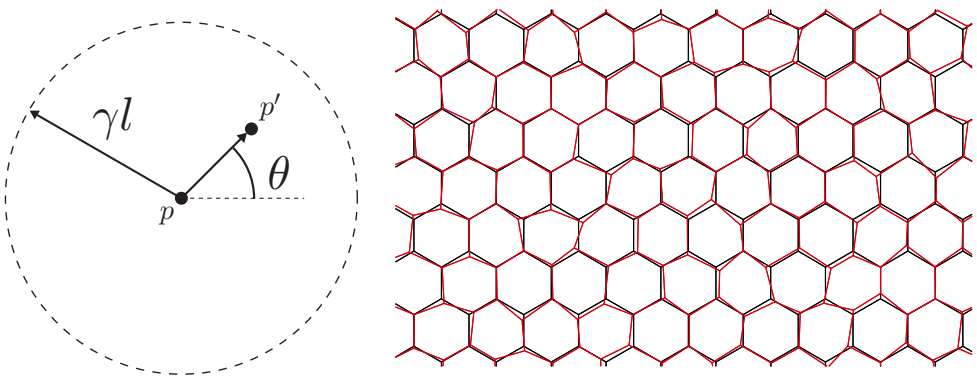

(a) (b)

Figure 1.5: (a) Schematic of the vertex perturbation technique; and (b) regular Hexagonal lattice with perturbed vertices of $\kappa_v = 0.2$.

Starting with a periodic lattice of uniform cell wall length l, each vertex is translated by a random distance $\kappa_v l$ along a random direction θ measured with reference to the horizontal; Fig. 1.5a shows a schematic of this process. An original vertex p at (x_1, x_2) is moved to a new location p' given by

$$x_1^{p'} = x_1^p + \kappa_v l \cos\theta \quad \text{and} \quad x_2^{p'} = x_2^p + \kappa_v l \sin\theta \quad . \tag{1.3}$$

The scalar parameter κ_v $(0 < \kappa_v < 0.5)$ controls the extent of the 'node perturbation'. Figure 1.5b gives an example of a 'perturbed' regular Hexagonal lattice using $\kappa_v = 0.2$. Note that the shape of the cells remain relatively uniform – this is the case even for $\kappa_v \to 0.5^+$ – and is of the same type of polygon, but not regular, as the original lattice although the 'perturbed' lattice is now non-periodic. Importantly, the nodal connectivity remains identical for all nodes – this is identical to the pre-perturbed periodic lattice. The perturbed lattice shown in Fig. 1.5b has a nodal connectivity of $Z = 3$.

1.1.3 Non-periodic lattices

Man-made foams and natural cellular solids fall within the 'non-periodic' category. Their topological characteristics, such as cell-size and cell wall length, follow some forms of statistical distribution and are often known as *stochastic*. The exact nature of its distribution depends on the manufacturing process or the intended use by the natural cellular solid.

Most natural cellular solids evolve in a manner that optimise their load bearing capacity. Consequently, their cell microstructure differs vastly from one another since it depends on their structural function (Gibson, 2005). For instance, wood has a honeycomb-like microstructure in its radial-tangential plane and is also, to a first approximation, an irregular prismatic lattice along its longitudinal direction: this leads to strong anisotropic macroscale properties. Trabecular bone, on the other hand, has a much more complex micro-architecure that evolves in response to external loadings and their topological characteristics can vary substantially from one part of the body to another.

Man-made foaming techniques, by contrast, impose no artificial restrictions on its final cell shape. Some foaming techniques naturally give rise to closed-cell foams. For instance, Alulight foams are manufactured by introducing a foaming agent (e.g. titanium hydride $\mathrm{TiH_2}$) into an aluminium melt. Duocel foams, on the other hand, with its open-cell microstructure is produced by using a polymer foam template for investment casting. The gas bubble nucleation process that governs the final cell shape of man-made foams is, itself, a stochastic process.

To model the gas bubble nucleation process, consider the random positioning of the gas particles that grow to form the final cell shapes. If one assumes that all particles grow at the same linear rate, then the resulting microstructure is similar to a *Voronoi diagram or lattice*. The simplicity of generating Voronoi lattices and their similarities to real foam microstructure makes them an attractive tool for scientists to model the microstructure of foams and natural cellular solids: the same approach is also employed in this thesis. Since only planar lattices are studied here, we shall restrict our attention to 2D Voronoi construction, although the same method can be applied in 3D.

A Voronoi diagram is defined by the random positioning of a set of m points, or nuclei, $P := \{p_1, p_2, \ldots, p_m\}$ in a plane of area A. The positioning of each nucleus in P relative to the other $m-1$ nuclei defines the final shape of the Voronoi diagram. The Voronoi cell k which has point p_k as nucleus, is defined as the set of points in space that are closer to p_k than any other nuclei within A (de Berg et al., 2000; Gibson and Ashby, 1997). The procedure of generating the Voronoi cell of nucleus p_k can be more readily understood if one considers all the perpendicular bisectors of p_k with all its neighbouring nuclei. The closed polygon formed by these lines is the Voronoi cell k

with point p_k as its nucleus.

The standard Voronoi construction places no restriction(s) on the final cell shape and size, or its distribution. It assumes that all cells nucleate at the same time and grow with the same linear rate. A 3D Voronoi lattice has an *average nodal connectivity* of $\overline{Z} = 4$, the same for 3D foams. Likewise, the average nodal connectivity of 2D Voronoi lattices is $\overline{Z} = 3$ which is, also, the case for a regular Hexagonal lattice. The Hexagonal lattice itself is a special case of Voronoi diagram as will be shown later on. All Voronoi lattices, and indeed all stochastic foams, have a bending-dominated micro-architecture since the conditions given in Eqs.(1.1) and (1.2) are not met.

The dispersion of cell-shapes and sizes obtained from a Voronoi construction is significantly wider compared to real foams (Gibson and Ashby, 1997). The regularity of a 2D Voronoi lattice can be controlled by introducing an exclusion distance between any pair of cell nuclei in A. To introduce such an exclusion distance in a meaningful manner, first consider a periodic Hexagonal lattice which is a special case of a 2D Voronoi lattice. All of its nuclei are surrounded by 6 immediate neighbours arranged, in a Hexagonal-close pack, at equi-distance to one another given by

$$d_0 = \sqrt{\frac{2A}{m\sqrt{3}}}. \tag{1.4}$$

If this equi-distance condition is relaxed, and no two nuclei are coincident, then the resulting Voronoi diagram would contain irregular polygons. Following Zhu et al. (2001), one may introduce a non-dimensional constant

$$\Lambda \triangleq \frac{d_{\text{min}}}{d_0} \tag{1.5}$$

in the interval $(0, 1]$, where d_{min} is the minimum permissible distance between any two adjacent nuclei. The parameter Λ is referred to as the *cell-regularity* parameter.

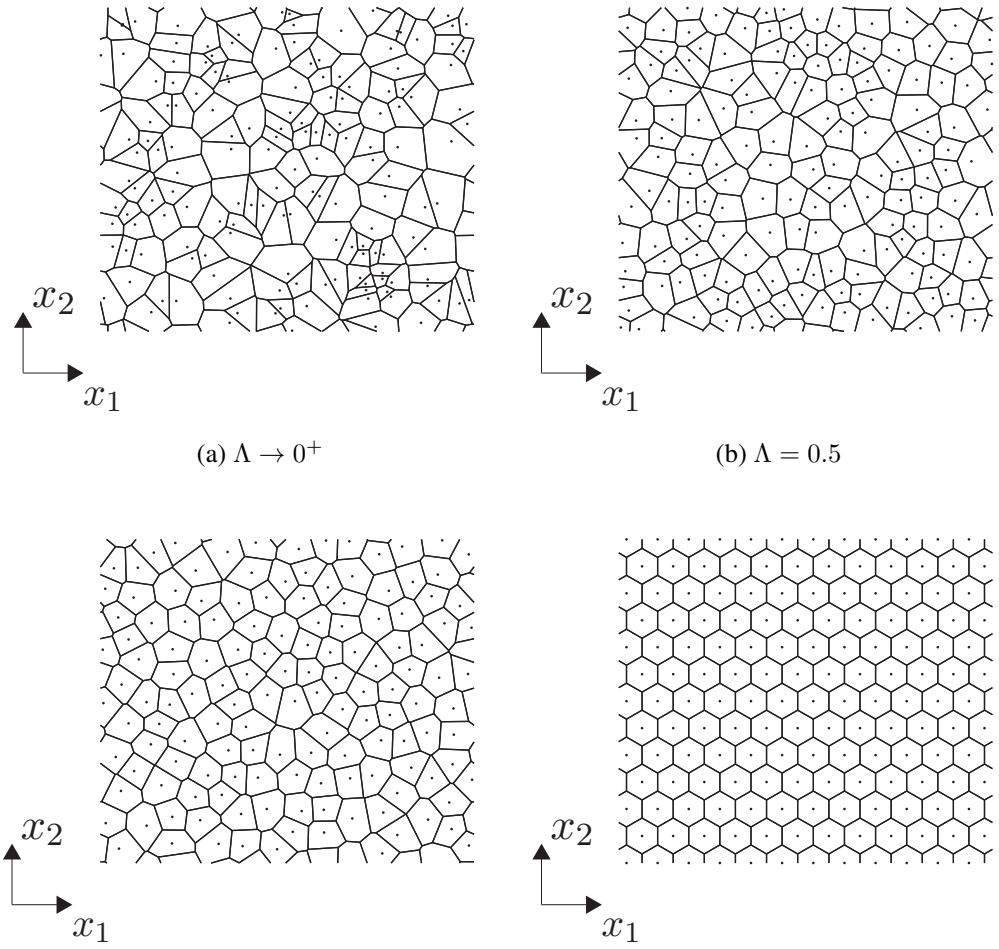

(a) $\Lambda \to 0^+$ (b) $\Lambda = 0.5$

(c) $\Lambda = 0.7$ (d) $\Lambda = 1$

Figure 1.6: Voronoi lattices with different cell-regularity Λ. Each lattice comprises of approximately 150 cells. The nucleus of each cell is indicated by a dot.

The two limiting cases of $\Lambda \to 0^+$ and $\Lambda = 1$ correspond to a completely stochastic Voronoi and a regular Hexagonal lattice, respectively. By relaxing the equi-distant condition, the uniform nodal connectivity of a regular Hexagonal lattice ($Z = 3$) is now lost. However, as previously mentioned above, the nodal connectivity of Voronoi lattices remains, on average, $\overline{Z} = 3$. Figure 1.6 gives a few examples of lattices with different Λ that are generated by the Voronoi assignment model. It is evident that as Λ increases, the distribution of cell shapes and size becomes increasingly narrower. The introduction of Λ provides a useful means, via a scalar parameter, to describe, an otherwise, randomly generated 2D Voronoi lattice. This allows a systematic investigation into the effects of cell-regularity on the macroscopic mechanical properties of such lattices.

1.2 Mechanical properties of infinite-sized lattices

1.2.1 Relative density

The single most important parameter that characterises the bulk mechanical properties of a lattice is its *relative density* given by

$$\overline{\rho} \triangleq \frac{\rho^*}{\rho_{\mathrm{s}}} \tag{1.6}$$

where $*$ and s denotes property on the macroscale and mesoscale (cell wall), respectively. $\overline{\rho}$ typically ranges from 0.001 to 0.3 depending on the type of lattice material and its function (Gibson and Ashby, 1997). For regular and semi-regular 2D lattices of *uniform* cell wall length l and wall thickness t, $\overline{\rho}$ is a linear function of the cell wall slenderness ratio t/l given by

$$\overline{\rho} \approxeq a\frac{t}{l} \tag{1.7}$$

where a is a constant that depends on the lattice micro-architecture. Table 1.1 lists the value of a for the five lattice micro-architectures shown in Fig. 1.4. For closed and open-cell 3D lattices, $\overline{\rho}$ is a linear and quadratic dependence on t/l, respectively. Note that Eq.(1.7) holds only if the cell walls are sufficiently slender, i.e. $t \ll l$. For stocky cell walls, multiple counting at the node (or joint) leads to increased error and a correction term must be applied. For 2D lattices, Eq.(1.7) is corrected to give

$$\overline{\rho} = a\frac{t}{l}\left(1 - a_1\frac{t}{l}\right) \tag{1.8}$$

where a_1 is micro-architecture dependent. For 3D lattices, the correction factor is a much more elaborate function of t/l - see Gibson and Ashby (1997, p.42) for details. The additional term in Eq.(1.8) presents an unnecessary complication and can often be neglected without introducing significant errors if $\overline{\rho}$ is low. This error is $< 5\%$ for Hexagonal lattices if $\overline{\rho} < 0.2$. There is no analogous expression to Eq.(1.8) for irregular lattices. Hence, in numerical analyses, $\overline{\rho}$ is computed explicitly by calculating the total length of all the struts in a lattice assuming, again, that $t \ll l$ for each strut.

1.2.2 Scaling laws

The bulk mechanical properties of *infinite-sized*, regular and semi-regular, 2D lattices are relatively straightforward to derive through the judicious use of a representative unit-cell and utilising geometric symmetries - see, for example, Gibson and Ashby (1997). In general, they are power-law functions of $\overline{\rho}$ and the cell wall material property from which a lattice is made as follows:

$$\frac{E^*}{E_s} = B\bar{\rho}^b \quad , \quad \frac{G^*}{E_s} = C\bar{\rho}^c \quad , \quad \frac{\sigma_y^*}{(\sigma_y)_s} = B_y\bar{\rho}^{b_y} \quad , \quad \frac{\tau_y^*}{(\sigma_y)_s} = C_y\bar{\rho}^{c_y} \tag{1.9}$$

where E and G are the elastic and shear moduli, respectively; and, σ_y and τ_y are the uniaxial and shear yield strength, respectively. The superscript $*$ denotes macroscopic property whilst subscript s denotes cell wall property. It is worth noting that G^* and τ_y^* are functions of the uniaxial, rather than shear, properties of the cell wall material. Parameters B, b, B_y, b_y are related to uniaxial loading whilst C, c, C_y, c_y to shear (Cote et al., 2006; Fleck et al., 2010; Gibson and Ashby, 1997; Wang and McDowell, 2004): Table 1.1 lists the value of each parameter corresponding to the five micro-architectures shown in Fig. 1.4. Their corresponding macroscopic Poisson's ratio, ν^*, is also listed for completeness.

	Z	a	B	b	C	c	B_y	b_y	C_y	c_y	ν^*
Hexagonal	3	$2/\sqrt{3}$	3/2	3	1/3	3	1/2	2	0.217	2	1
Square	4	2	1/2	1	1/16	3	1/2	1	0.125	2	$0.5\nu_s\overline{\rho}$
Diamond	4	2	1/4	1	1/4	1	1/2	1	1/2	1	1
Triangular	6	$2\sqrt{3}$	1/3	1	1/8	1	1/3 (x_1) 1/2 (x_2)	1	0.289	1	1/3
Kagome	4	$\sqrt{3}$	1/3	1	1/8	1	1/3 (x_1) 1/2 (x_2)	1	0.289	1	1/3

Table 1.1: Coefficients of the scaling laws in Eq.(1.9)

The exponent of $\overline{\rho}$ in Eq.(1.9) is an indicator of whether a lattice is stretch- or bending-dominated. A stretch-dominated micro-architecture, such as that found in Triangular, Diamond and Kagome lattices, is typified by a linear dependence of both its bulk elastic moduli and yield strength on $\overline{\rho}$ ($b = c = b_y = c_y = 1$). By contrast, a bending-dominated micro-architecture, such as the Hexagonal lattice, have bulk elastic moduli and yield strength which has a cubic ($b = c = 3$) and quadratic ($b_y = c_y = 2$) dependence on $\overline{\rho}$, respectively. The Square lattice, on the other hand, is an anomaly since the dominant mode of deformation at its mesoscale switches from stretch to bending depending on loading type. Under remote uniaxial tension/compression, it deforms by stretch so $b = b_y = 1$. Under remote shear, however, the dominant deformation mode switches from stretch to bending; hence, $c = 3$ and $c_y = 2$.

It is worth noting that some of the aforementioned lattices are anisotropic. The Square and Diamond lattices have orthotropic in-plane bulk properties since remote in-plane loadings along any directions, apart from x_1 or x_2, causes bending of its struts instead of stretch. The other three lattices are in-plane isotropic in their linear elastic response. However, the non-linear response, including yield strength, of Triangular and Kagome lattices are, in general, anisotropic: hence, Table 1.1 lists two different values of B_y corresponding to uniaxial loading in x_1 and x_2 directions. For the Hexagonal lattices, the difference is marginal and can be neglected.

The Poisson's ratio of a lattice depends on its micro-architecture and the dominant deformation at the mesoscale. For regular Hexagonal and Diamond lattices, $\nu^* = 1$: this is an oddity compared to solid materials. By contrast, the Poisson's ratio of a Square lattice is $\nu^* = 0.5\nu_s\overline{\rho}$ - this is nearly zero for typical values of ν_s and $\overline{\rho}$. For Triangular and Kagome lattices, their macroscopic Poisson's ratio is $1/3$. It is clear Hexagonal, Triangular and Kagome lattices obey the standard relationship that exists between elastic constants given by

$$G^* = \frac{E^*}{2\left(1+\nu^*\right)} \tag{1.10}$$

whereas a Square and Diamond lattices do not since they are orthotropic.

The scaling laws of Eq.(1.9) were derived assuming an Euler-Bernoulli beam ideali-

sation of constituent struts. Consequently, their predictions are accurate only if $\bar{\rho}$ is sufficiently low, say $\overline{\rho} < 0.01$, and the lattice is comprised of slender cell walls where $l >> t$. As $\overline{\rho}$ increases, the contributions from axial and shear stresses in the cell walls become increasingly significant, leading to increased error in the predictions by Eq.(1.9). To account for the axial and shear stresses, Silva et al. (1995) and Gibson and Ashby (1997, p.160) derived expressions for the moduli and Poisson's ratio of Hexagonal lattices within a small-strain context following Timoshenko beam theory (Timoshenko and Goodier, 1970). They are broadly similar to Eq.(1.9) but contain an additional 'correction' term – a function of $\overline{\rho}$ and the Poisson's ratio of the wall material ν_s – as follows:

$$\frac{E^*}{E_\mathrm{s}} = \frac{3}{2}\overline{\rho}^3 \left[\frac{1}{1 + 0.75\overline{\rho}^2(5.4 + 1.5\nu_s)}\right] \quad , \tag{1.11a}$$

$$\frac{G^*}{E_\mathrm{s}} = \frac{3}{8}\overline{\rho}^3 \left[\frac{1}{1 + 0.75\overline{\rho}^2(3.3 + 1.75\nu_s)}\right] \quad \text{and} \tag{1.11b}$$

$$\nu^* = \frac{1 + 0.75\overline{\rho}^2(1.4 + 1.5\nu_s)}{1 + 0.75\overline{\rho}^2(5.4 + 1.5\nu_s)} \quad . \tag{1.11c}$$

As an example, if $\overline{\rho} < 0.15$, the difference in predictions by Eq.(1.9) and Eq.(1.11) is no greater than 10%. Hence, the correction factor is often neglected. The same as above applies to open and closed cell 3D foams (Gibson and Ashby, 1997; Grenestedt, 1999); however, they are not within the scope of this thesis and will not be reviewed.

1.2.3 Non-periodic lattices

Scaling laws, such as Eq.(1.9), derived for periodic Hexagonal lattice are routinely used to understand the response of stochastic foams on the basis that they deform primarily by bending. However, they cannot be borrowed for all types of loading. As an example, a Hexagonal lattice is stretch-dominated under hydrostatic loading since no bending stresses are induced because of its perfectly symmetric micro-architecture. In reality, however, the hydrostatic strength of stochastic foams is nearly an order of magnitude lower than that predicted for a Hexagonal lattice (Gibson and Ashby, 1997). Chen et al. (1999) showed that the vertex perturbation technique, or Voronoi tessellations,

can successfully model a reduction in the hydrostatic strength of Hexagonal lattices.

The bulk mechanical properties of non-periodic lattices, such as Voronoi or the 'perturbed' periodic lattices, cannot be modelled using a unit-cell approach since their micro-architecture violates strict periodicity conditions. The usual approach is to model them numerically using finite elements but applying the appropriate boundary conditions to the FE mesh of the lattice. Romijn and Fleck (2007) and Symons and Fleck (2008) investigated the elastic properties of periodic 2D lattices with varying degree of vertex perturbation. Hexagonal and Triangular lattices were found to deform by bending and stretch, respectively, even with highly perturbed vertices. Consequently, their macroscopic uniaxial and shear moduli are insensitive to imperfections. However, vertex perturbation introduces bending into the struts of a Kagome lattice that would otherwise deform in stretch and this is reflected by a significant drop in both moduli. The Square lattice, on the other hand, weakens under remote uniaxial loading but strengthens under remote shear; this is due to contributions from both bending and axial stresses when subjected to remote uniaxial and shear loadings. The reverse is observed for Diamond lattice. It is worth noting that all isotropic lattices remain isotropic after the introduction of irregularities: this is to be expected. Introducing perturbations in the orthotropic Square and Diamond lattices lead to a more isotropic response, however Eq.(1.10) is still not satisfied.

The response of Voronoi lattices is found to be slightly different compared to the perturbed Hexagonal lattice. As Λ decreases, leading to a more random lattice micro-architecture, the elastic moduli of Voronoi lattices are found to increase (Chen et al., 1999; Li et al., 2005; Silva et al., 1995; Zhu et al., 2001). In a similar vein with the Hexagonal lattice, the response of Voronoi lattices is isotropic and obeys Eq.(1.10).

1.3 Finite-sized (or finite) lattices

The scaling laws of Eq.(1.9) were derived by exploiting geometric symmetries in a lattice micro-architecture: a direct consequence is that they predict the bulk properties of infinite-sized lattices. For *finite-sized* specimens, Eq.(1.9) is applicable only if a lattice has macroscale dimensions that are significantly greater than its characteristic length at the mesoscale (exemplified by their average cell size d_0).

Lakes (1983, 1986) was the first to report a dependence of torsional and bending stiffnesses on the specimen size for polymeric foams. Brezny and Green (1990) also reported a significant reduction in the bending stiffness and strength of reticulated vitreous carbon foams in smaller-sized specimens. In a nutshell, *edge effects* cause a significant deviation of macroscopic properties from their bulk value when one, or more, critical macroscale dimension(s) of a lattice approaches its average cell size d_0. Under uniaxial loading, the *weak boundary layers* that develop along the stress-free edges, parallel to the direction of loading, is responsible for the observed edge effects. Figure

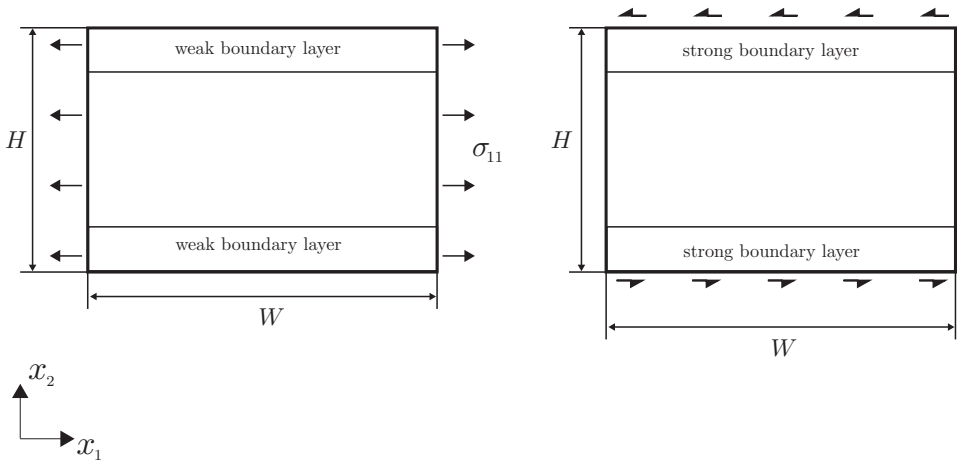

(a) (b)

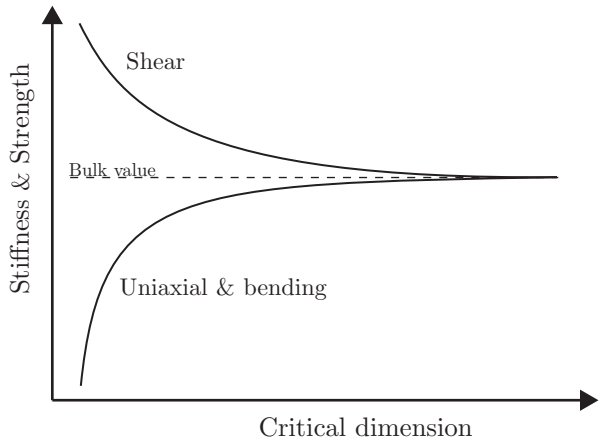

(c)

Figure 1.7: Weak and strong boundary layers induced by remote (a) uniaxial and (b) shear loadings; (c) Schematic of effective stiffness & strength versus the critical macroscale dimension of a lattice specimen.

1.7a shows a schematic of a lattice subjected to remote uniaxial loading in the x_1 direction; for this case, the critical macroscale dimension is the specimen height H. In a similar vein, the critical dimension is W (width) if loading is in the x_2 direction. The boundary layers that develop at the stress-free edges reduce the load bearing ability of a specimen, leading to a knock-down in its bulk stiffness and strength. The extent of this knock-down depends on the area (for 2D) or volume (for 3D) fraction of weakened cells – these are, generally, incomplete cells with reduced nodal connectivity – abutting the lattice boundary. If the macroscale dimension of a specimen is sufficiently large compared to its average cell size d_0, then the relative impact of the boundary layers would be insignificant so that its effective properties approach that of the *bulk* properties of an infinite-sized lattice. Figure 1.7c shows a schematic of how edge effects influence effective properties of lattices; the same were also reported for Alporas (closed-cell) and Duocel (open-cell) foams by Bastawros et al. (2000) and Andrews et al. (2001). They found that a minimum of 8 cells ($H > 8d_0$) are needed to measure its bulk value if subjected to remote uniaxial loading. For bending, twice as many cells, $H > 15d_0$ are typically needed because of compressive and tensile regions that develop at the top/bottom surfaces of the specimen.

Unlike during uniaxial stretch and bending, the effective properties of a stochastic foam are enhanced (or strengthened) under remote simple shear if the critical macroscale dimension – perpendicular distance, or specimen height H, separating the two loaded surfaces – approaches its average cell size d_0 (Andrews et al., 2001; Chen and Fleck, 2002). Rakow and Waas (2004, 2005) employed an optical strain measurement technique to reveal stiffer response by those cells abutting the loading surface compared to its bulk when subjected to pure shear. The rigid bonding of the foam specimen to the two horizontal loading plates was found to provide a greater constraint effect than the cells in the bulk of the foam. This generates strong boundary layers that leads to the apparent enhancement of the effective shear stiffness and strength as shown schematically in Fig. 1.7b. As H increases, the relative impact of these boundary layers on G^* and τ_y^* diminishes, see schematic in Fig. 1.7c.

Edge effects in stochastic foams were modelled analytically by Onck et al. (2001) - using an idealised 2D regular Hexagonal micro-architecture – where expressions for

their effective uniaxial and shear moduli were derived for specimens containing finite number of cells along its width and height, respectively. Diebels and Steeb (2002) and Tekoglu et al. (2011) further investigated this by adopting a stochastic Voronoi lattice and using the finite element method. Both analytical and numerical predictions were consistent with experimental data suggesting that the development of weak boundary layers in tension/compression and strong boundary layers in shear are, indeed, responsible for the observed edge effects in finite-sized specimens.

Notwithstanding, similar studies on edge effects in periodic micro-architectured lattices are rather limited and results exist only for Hexagonal (Onck et al., 2001) – highlighted previously – and Diamond lattices (Cote et al., 2006; Queheillalt et al., 2007; Zupan et al., 2004). The mechanism responsible for the observed edge effects in the Diamond lattice are significantly different to the Hexagonal or Voronoi lattices. The struts near the four corners of the specimen are not 'directly' connected to both horizontal loading surfaces, thus they are not axially loaded. Consequently, four bending 'bending-dominated regions' emanate from each corner that contribute to a significantly reduced load bearing ability of the specimen. This is schematically shown in Fig. 1.8a under remote σ_{22}. The extend of these regions along x_1 depend on H, thus the effective lattice

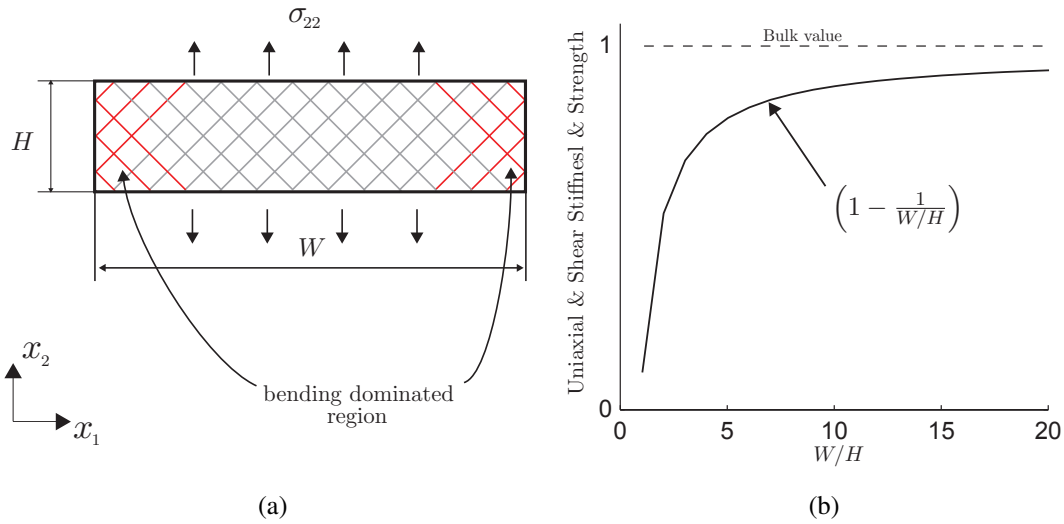

(a) (b)

Figure 1.8: (a) Bending-dominated region emanating from the four corners of a finite-sized Diamond lattice; and (b) Influence of critical dimension W/H upon the effective uniaxial, and shear, stiffness & strength of a Diamond lattice.

properties are a function of both W and H as follows:

$$E^*, G^*, \sigma_y^*, \tau_y^* \propto \left(1 - \frac{1}{(W/H)}\right) \overline{\rho} \tag{1.12}$$

and this is shown schematically in Fig. 1.8b.

It is as yet unknown whether, and to what extent, other periodic micro-architectures – viz. Square, Triangular and Kagome – are affected by the presence of boundaries. A Square lattice is expected to be influenced by edge effects only under remote shear, but it is unknown whether the dependence of effective properties on lattice dimensions is similar to Hexagonal and Voronoi lattices. For Triangular lattices, with its high nodal connectivity and highly redundant micro-architecture, it is of interests to investigate whether edge effects, and the mechanism responsible for its development, are present at all. Furthermore, a Kagome micro-architecture is known to switch from a stretch-only lattice to 'local' bending in the presence of discontinuities and constraints (Fleck and Qiu, 2007; Wicks and Guest, 2004) but the precise physical mechanism and how much it influence the effective properties of a specimen remains unknown. The presence of edge effects in the Square, Kagome and Triangular lattices – and their influence on its effective properties – will be investigated in Chapter 3 and their results will be compared to existing results from the literature for other lattice micro-architectures.

1.4 Fatigue

The performance of lattice materials under cyclic loading are of interests to many applications. In general, factors that influence the fatigue performance of conventional solid materials also affect lattices at their micro-scale – they include the mean stress ($\bar{\sigma}^*$), max stress (σ^*_{max}), *load ratio* ($R \triangleq \sigma^*_{\text{min}}/\sigma^*_{\text{max}}$) and environmental conditions (temperature, corrosion etc.). Unlike solid materials, however, the additional length-scale at the meso-level, viz. cell-scale, is likely to affect the fatigue performance of lattices and requires further investigation.

Existing literature on fatigue performance of lattices are mostly concerned with stochastic metal foams – they are mainly experimental investigations – whilst studies on periodic lattices are fairly limited. The use of the fatigue crack propagation method

is deemed unhelpful for lattices because of the high sensitivity of crack propagation rate on applied stress – the Paris law exponent for foams was found to be in the range 8–20 (Motz et al., 2005; Olurin et al., 2001), compared to $\approx$ 3–5 for solid metals. Hence, most studies chose to investigate the strain accumulation process in uncracked specimens up to failure (ε_{max}–N) in order to produce the associated stress-life curves (S-N). A summary of the available papers with experimental S-N data for various foams and lattices is presented in Table 1.2, along with the estimated endurance strength values, σ_e^*, for each data set. Typically, σ_e^* is normalised either by yield stress σ_y^*, plateau stress σ_{pl}^* or peak stress σ_p^*; here we will use a common indicator of σ_0^*.

Typically, the fatigue life of stochastic metal foams can be divided into three stages as follows (Sugimura et al., 1999): (I) inelastic strain accumulation; (II) gradual-slow strain accumulation; and, (III) rapid strain accumulation that leads rapidly to complete specimen failure, i.e. the lattice is unable to withstand any further load. The transition from stage II to III is associated with the number of cycles to failure (N_{f}^*) and is found to begin at approximately $\varepsilon_{\text{max}}^{\text{III}} \approx$ 2–3% (Banhart and Brinkers, 1999; Sugimura et al., 1999). Due to the stochastic nature of the cell microstructure in foams, it is not uncommon to encounter variations in N_{f}^* by almost a decade. A strong dependence on $\sigma_{\text{max}}^*/\sigma_0^*$ has been noted – higher values lead to shorter cycles-to-failure. On the other hand, $\bar{\sigma}^*$ is found to have insignificant effect on the S-N curve (Harte et al., 1999).

Furthermore, the type of fatigue loading, such as uniaxial compression-compression (C-C) or tension-tension (T-T), was found to have a significant effect upon N_{f}^*. McCullough et al. (2000) showed that the endurance strength (σ_e^*/σ_0^*) of Alulight foams under C-C loading is significantly higher ($= 0.85$) compared to T-T loading ($= 0.5$). Similar observations were also reported by Harte et al. (1999), although the differences are smaller: 0.85 (C-C) and 0.7(T-T) for Duocel foams; 0.7 (C-C) and 0.6 (T-T) for Alulight foams. McCullough et al. (2000) and Harte et al. (1999) also reported that failure under T-T loading initiates at a much lower strain of $\varepsilon_{\text{max}}^{\text{III}} \approx 1\%$.

Harte et al. (2001) found that Alporas foams have a much lower fatigue endurance strength in shear compared to uniaxial loadings (C-C or T-T): $\tau_{\text{max}}^*/\tau_0^* \cong 0.35$ as opposed to $\sigma_{\text{max}}^*/\sigma_0^* = 0.52$ and 0.6 for T-T and C-C loadings, respectively. However, for both shear and uniaxial loadings, the rapid strain accumulation stage begins at ap-

	Foam/Lattice	Material	$\overline{\rho}$	Load type	R	$\varepsilon^{\text{III}}_{\text{max}}$	σ^*_e/σ^*_0
Banhart and Brinkers (1999)	Fraunhofer foam	AL	0.23	C-C	0.1	3%	0.5
Sugimura et al. (1999)	Alporas	AL	0.08	C-C	0.1	2%	0.58
Harte et al. (1999)	Duocel	AL	0.07	C-C	0.1,0.5	2%	0.85
				T-T	0.1	1%	0.7
	Alporas	AL	0.11	C-C	0.1,0.5	2%	0.7
				T-T	0.1	1%	0.6
McCullough et al. (2000)	Alulight	AL	0.15-0.18	C-C	0.1	1%	0.65
			0.29-0.35	C-C	0.1	2%	0.85
				T-T	0.1	1%	0.5
Harte et al. (2001)	Alporas	AL	0.11	S	0.1	2%	0.35
				C-C		=	0.6
				T-T		=	0.52
Cote et al. (2007a)	Diamond	304 Stainless steel	0.08	S	0.5	1%	0.42
			0.15	S	0.5	$< 0.5\%$	0.4
					0.1	$< 0.5\%$	0.32
Cote et al. (2007b)	Pyramidal	AL6XN Stainless steel	0.07	S	0.5	-	0.4
					0.1	-	0.3

Table 1.2: Summary of literature on the fatigue of lattice materials. $\varepsilon^{\text{III}}_{\text{max}}$ refers to the max strain for phase II/III transition. σ^*_e/σ^*_0 is the normalised endurance strength. S refers to shear loading.

proximately $\varepsilon^{\text{III}}_{\text{max}} \approx 2\%$. The rapid strain accumulation stage is associated with the coalescence of tensile microcracks in the cell walls, resulting in fractured struts that eventually form a single macroscopic failure surface.

The effects of $\overline{\rho}$ were investigated experimentally, in a cursory manner, by McCullough et al. (2000) for Alulight foams of relative density $\overline{\rho} \approx 0.15$ and 0.3 subjected to C-C loading ($R = 0.1$). Foams at the higher $\overline{\rho}$ (≈ 0.3) were found to have a significantly higher N_{f} and, also, higher $\varepsilon^{\text{III}}_{\text{max}}$ of 2% compared to 1% at the lower $\overline{\rho}$ (≈ 0.15). Consequently, the higher density Alulight foams have endurance strength that are approximately 20% greater than its lower density counterpart. Note, however, that the gradient of the S-N curves is nearly identical for both densities.

Unlike for stochastic foams, the fatigue performance of periodic lattices is not currently well understood and very limited experimental data are available. Cote et al. (2007a) studied the shear fatigue performance of prismatic Diamond lattices at two relative densities of $\overline{\rho} = 0.08$ and 0.15 where they were found to fail through different mechanisms. The lower density (0.08) exhibit slow, but, progressive strain accumulation followed by a near instantaneous failure at $\varepsilon^{\text{III}}_{\text{max}} \approx 1\%$. Cell walls near specimen boundaries – note that they suffer from edge effects – are always the first to fail by fatigue, followed by those within the core. For specimens at $\overline{\rho} = 0.15$, strain accumulation prior to N_f is negligible and failure is typically through interfacial debonding between the joints of the Diamond core and the face-sheets to which they were bonded. Even though the two aforesaid mechanisms are different, their resulting S-N curves are largely similar and, more surprisingly, their endurance strength is also similar to Alporas foams ($\tau^*_{\text{e}}/\tau^*_0 \cong 0.35$). The interfacial debonding failure mechanism was also noted for $\overline{\rho} = 0.07$ pyramidal lattice cores; these are shown schematically in Fig. 1.9 (Cote et al., 2007b). Additionally, the resulting S-N curve of pyramidal and Diamond lattices are largely similar, leading to a general conclusion that the fatigue response of lattices must be insensitive to their relative density $\overline{\rho}$ and micro-architecture.

As with above, there is also fairly limited numerical studies. Guo et al. (1994) proposed a finite elements model to simulate sequential cell wall fatigue fractures in 2D Hexagonal lattices subjected to cyclic loading. Microcrack propagation in cell walls is modelled using Paris-law. Fully damaged cell walls were deleted from the lattice

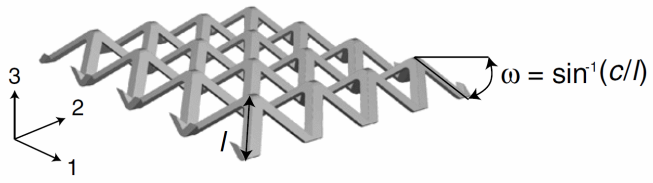

Figure 1.9: Pyramidal truss core (Source: Cote et al., 2007b)

until significant macroscopic strain accumulation is achieved. Schaffner et al. (2000) extended this approach to simulate fatigue damage in stochastic Voronoi lattices where they were found to have significantly reduced fatigue life compared to Hexagonal lattices. This is attributed to the bigger range of stress distribution in the cell walls of these non-periodic lattices.Two key limitations exist in both of these studies. First, the pre-existing microcracks were located at a distance $l/4$ from the mid-span of all cell wall, while their length followed a beta statistical distribution. Second, a cell wall with a developing micro-cracks were assumed to have intact elastic modulus up until the micro-crack reached a critical length, that lead to complete cell wall fracture.

More recently, Abad et al. (2013) modelled the fatigue response of Square and Hexagonal lattice unit-cells using finite elements and numerical homogenisation. Their FE model used 2D eight-node elements, instead of beam elements, to capture the stress distribution in a representative unit-cell with smooth curvature transition from one cell wall to the next. The predicted endurance strength is broadly similar to those of Pyramidal and Diamond core Cote et al. (2007a,b), lending further support to previous conclusions that the S-N curves of lattices are not significantly affected by micro-architecture. However, their method fails to address the presence of edge effects that trigger fatigue failure in low-density Diamond cores Cote et al. (2007a).

In the present thesis, one of the objectives is to develop a numerical method – by improving on the approach of Guo et al. (1994) and Schaffner et al. (2000) – to simulate the fatigue performance of periodic lattices. Specimens of finite size will be modelled so that edge effects are taken into account since they are anticipated to play a key role in fatigue damage initiation. The five different lattice micro-architectures shown in Fig. 1.4 will be modelled in order to establish, and to compare, any differences between the fatigue failure response of stretch- and bending-dominated lattices.

1.5 Fracture

If the ligaments of a lattice are elastic-brittle so that fracture occurs when the stress state at any point along a cell wall reaches its critical fracture strength σ_f, then – just like its elastic moduli – the bulk strength of the lattice can be expressed as a power-law function of its relative density given by

$$\frac{\sigma_f^*}{\sigma_f} = B_f \overline{\rho}^{b_f} \tag{1.13}$$

where the parameters B_f, b_f are listed in Table 1.3 (Fleck and Qiu, 2007; Gibson and Ashby, 1997). Notice that $\sigma_f^*/(\sigma_f)_s$ scales linearly and quadratically with $\overline{\rho}$ for stretch and bending-dominated lattices, respectively: this is similar to Eq.(1.9).

	Hexagonal	Square	Triangular	Kagome
B_f	1/3	1/2	1/3	1/2
b_f	2	1	1	1

Table 1.3: Coefficient values for brittle fracture strength, Eq.(1.13) (Fleck and Qiu, 2007; Gibson and Ashby, 1997)

Equation (1.13) is valid for lattices in the absence of any macroscopic crack. Following the brittle fracture of a cell wall, the redistribution of stresses in neighbouring cell walls leads to further failures. Under compression, this leads to the progressive crushing. Whilst in tension, several fractured cell walls may coalesce to form a continuous macro-crack that can propagate in catastrophic manner which is best analysed using a fracture mechanics method.

The stress field around a crack tip of a *solid material* is given by the following asymptotic expansion (Williams, 1957):

$$\sigma_{ij} = \underbrace{C_1 g_{ij}^{(1)}(\theta)\frac{1}{\sqrt{r}}}_{K\text{-field}} + \underbrace{C_2 g_{ij}^{(2)}(\theta)}_{T\text{stress}} + \underbrace{C_3 g_{ij}^{(3)}(\theta) r^{1/2} + \sum_{n=4}^{\infty} C_n g_{ij}^{(n)}(\theta) r^{(n-2)/2}}_{\text{Higher order terms}} \tag{1.14}$$

where σ_{ij} is the stress tensor, (r, θ) are polar coordinates centred at the crack tip, $g_{ij}^{(n)}(\theta)$ are dimensionless functions of θ; and, C_n is the stress amplitude corresponding to the

n^{th} term. In the immediate crack-tip region, the singular stress field given by the leading term of Eq.(1.14) can be decomposed additively into contributions from remote tensile (Mode I) and in-plane shear (Mode II) loadings as (Kanninen and Popelar, 1985)

$$\sigma_{ij} = \frac{K_{\text{I}}}{\sqrt{2\pi r}}\hat{\sigma}^{\text{I}}_{ij} + \frac{K_{\text{II}}}{\sqrt{2\pi r}}\hat{\sigma}^{\text{II}}_{ij} \tag{1.15}$$

where K_{I} and K_{II} are the mode I and mode II stress intensity factors (SIF), respectively. For mixed-mode loading, the relative composition of K_{I} and K_{II} is controlled by means of an elastic mode-mixity parameter M defined by Shih (1974):

$$M = \frac{2}{\pi}\tan^{-1}\left(\frac{K_{\text{II}}}{K_{\text{I}}}\right) \quad ; \quad 0 \leq M < 1 \tag{1.16}$$

where the limiting values of $M = 0$ and $M \to 1^{-}$ corresponds to the mode I and mode II fracture toughness, respectively.

1.5.1 Periodic lattices

Maiti et al. (1984) applied standard fracture mechanics principles to estimate the mode I toughness (K_{IC}) of lattices. Using an example of a regular Hexagonal lattice, they showed that the K_{IC} of lattices depends not only on its relative density and cell wall material properties (σ_f) but, crucially, on its characteristic cell size, l. This dependence on l arises as a direct consequence of the leading $1/\sqrt{r}$ term in Eq.(1.14) and the resulting scaling law takes the following form:

$$K_{\text{IC}} = D_{\text{I}}\overline{\rho}^{d_{\text{I}}}\sigma_f\sqrt{l} \tag{1.17}$$

where the exponent $d_{\text{I}} = 2$ for the bending-dominated Hexagonal lattice (Gibson and Ashby, 1997). Since the Triangular and Square lattices have a stretch-dominated micro-architecture, it follows that their corresponding exponent $d_{\text{I}} = 1$ (Fleck and Qiu, 2007; Romijn and Fleck, 2007). Unlike the other stretch-dominated micro-architectures, a Kagome lattice has an exponent $d_{\text{I}} = 1/2$ which suggests that it has superior fracture tolerance. Note that Eq.(1.17) is equally valid for mode II loading (Fleck and Qiu, 2007; Romijn and Fleck, 2007). All lattices, apart from Square, have the same $\overline{\rho}$ exponents,

i.e. $d_{\mathrm{I}} = d_{\mathrm{II}}$, for both mode I and II loadings. The Square lattice, on the other hand, has an exponent of $d_{\mathrm{I}} = 1$; this is because of a switch from axial to bending-dominated deformation when subjected to remote shear, as discussed in Section 1.2.

Using the finite element method, Fleck and Qiu (2007) and Romijn and Fleck (2007) performed *boundary layer analysis*, or BLA for brevity, to validate the predictions by Eq.(1.17) and to evaluate the pre-exponents (D_{I} and D_{II}) which were listed in Table 1.4. For all lattice micro-architectures, the pre-exponent (D_{II}) for mode II was found to be substantially lower than their mode I (D_{I}) counterpart. The differences in the predicted D_{I} value between Fleck and Qiu (2007) (1) and Romijn and Fleck (2007) (2) in Table 1.4 are due to the different beam element types used in the FE simulations; the first (1) neglects shear stresses in cell walls whilst the second (2) does not. The same reason applies to the D_{II} predictions.

Topology	D_{I}		d_{I}	D_{II}		d_{II}
	(1)	(2)		(1)	(2)	
Hexagonal	0.800	0.902	2	0.370	0.408	2
Triangular	0.500	0.607	1	0.380	0.404	1
Kagome	0.212	0.205	0.5	0.133	0.115	0.5
Square		0.278	1		0.121	1.5
Diamond		0.216	1		0.225	1

Table 1.4: Tabulation of results from (1) Fleck and Qiu (2007) and (2) Romijn and Fleck (2007).

Fleck and Qiu (2007) investigated the location of incipient cell wall fracture for the different lattice micro-architectures: their findings are summarised in Fig. 1.10. The location of incipient fracture under pure mode I loading is indicated with I. For all lattices, other than Triangular, the crack path does not propagate along the x_1 direction: this is contrary to assumption made in the derivation of Eq.(1.17). Moreover, the crack path, and its propagation, is not contiguous: a jump of 3 cells is predicted for a Kagome lattice. For mixed mode loading, as M increases from 0 to 1, the location of incipient fracture is observed to switch to a different cell wall. A switch of fracture location is witnessed once for the Hexagonal and Square lattices but twice for the Triangular and Kagome. Thus, the former have two possible incipient fracture locations whereas the

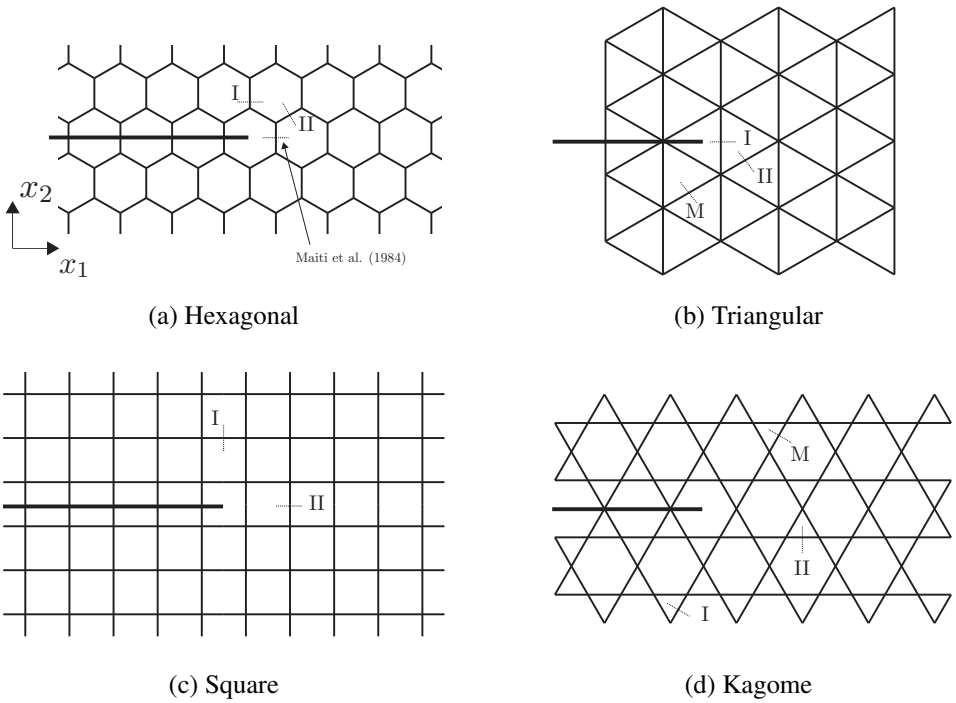

(a) Hexagonal (b) Triangular

(c) Square (d) Kagome

Figure 1.10: Location of incipient wall fracture in periodic lattices. I and II denoted the location for pure mode I and mode II, whilst M for mixed-mode loading

latter three; the active location depends on mode mixity M. These are shown in Fig. 1.10.

1.5.2 Non-periodic lattices

Romijn and Fleck (2007) investigated the sensitivity of the predicted lattice toughness to cell-scale imperfections in the form of perturbed vertices by using the technique described in Section 1.3. Hexagonal lattices were found to be the least sensitivity to imperfections with approximately 40% reduction in K_{IC} and, rather surprisingly, a small increase for K_{IIC} for $\kappa_v = 0.5$, see Eq.(1.3). Even though a Kagome lattice is the toughest in its pristine form, it is also the most sensitive to imperfections. Results show a $\approx 90\%$ decrease in its mode I and II toughness for $\kappa_v = 0.5$, substantially more than the Triangular lattice. The work of Romijn and Fleck (2007), however, did not investigate the impact of micro-architecture imperfections on the exponent d for the entire range of κ_v but only for $\kappa_v = 0$ and 0.5. Their results for the most perturbed case, $\kappa_v = 0.5$ – although this hardly represents a physically realistic lattice – shows that both Kagome and Square lattices are no longer stretch-dominated, as opposed to the Triangular that

remains stretch-dominated. This explains why the decrease in toughness observed for Triangular lattice is significantly less than for the Kagome and Square lattices.

Results on the fracture toughness of stochastic Voronoi lattices are not available in literature. Some parallels between the response of Voronoi lattices can be drawn from experimental results obtained real stochastic foams. Crack-bridging and discontinuous crack propagation are widely observed and a fully-developed *fracture process zone* (FPZ), extending approximately 6-8 cells, is usually encountered in both polymeric (Saenz et al., 2011) and metal foams (Motz and Pippan, 2002; Olurin et al., 2000). The fracture toughness of stochastic Voronoi lattice of different cell regularity will be addressed in the present thesis with special emphasis paid to the effects of cell regularity, relative density and mode mixity on the estimated fracture toughness and the location of incipient cell wall fracture.

1.5.3 Higher order terms - Eq.(1.14)

The results presented in previous Sections (1.5.1 and 1.5.2) only apply if the K-field is dominant, i.e. contributions by all higher order terms in Eq.(1.14) are negligible. The second term in Eq.(1.14) corresponds to a uniform stress parallel to the crack plane; known commonly as the T-stress. In continuum solid materials, T-stress is a measure of the constraint effects surrounding a crack tip (Larsson and Carlsson, 1973; Rice, 1974). All standard test specimen geometries – for example the compact tension (CT) and the single-edge notched in bending (SEN(B)) – used in fracture toughness testing induce a non-negligible T-stress (Leevers and Radon, 1982). Its magnitude depends on the applied stress intensity factor (SIF) and crack length α which can be expressed in non-dimensional form as (Leevers and Radon, 1982; Smith et al., 2006)

$$B = \frac{T\sqrt{\pi\alpha}}{K_{\mathrm{I}}}, \tag{1.18}$$

also known as the *stress biaxiality ratio*. Note that B depends only on test specimen geometry.

Fleck and Qiu (2007) have investigated the effects of T-stress on the predicted toughness of Hexagonal, Triangular and Kagome lattices, by modelling a centre-cracked

panel (CCP) in finite elements subjected to remote uniaxial tension, equi-biaxial tension and remote shear. A CCP specimen is known to induce a stress biaxiality ratio of $B \approx -1$ under remote axial tension and by applying an equi-biaxial load, the T-stress is nearly eliminated. They found that under mode I loading, the Hexagonal lattice to be sensitive to T-stress but not the Triangular and Kagome lattices. Although, all three lattices were found to be insensitive to T-stress under mode II loading.

In this thesis, the effect of higher order terms in Eq.(1.14) will be investigated using two approaches. First, the influence of T-stress on the predicted toughness and the location of incipient cell wall fracture is studied by incorporating the 2$^{\text{nd}}$ term of Eq.(1.14) into the BLA method. Second, two standard specimen geometries – the CT and SEN(B) – will be modelled using FE to compare their predicted toughness against the aformentioned idealised BLA method. Additionally, the CT and SEN(B) test specimens will also be used to investigate the presence of edge effects in *finite-sized* specimens, and how they influence the predicted fracture toughness.

1.6 Aims and Objectives

It is evident from the review of pertinent literature that the mechanical response of lattices to remote macroscopic loadings are dictated, to a large extent, by their topology at the mesoscale. The dominant deformation mechanism for each lattice microarchitecture are as follows:

1. Hexagonal and Voronoi: bending-dominated under remote uniaxial or shear loadings

2. Triangular: stretch-dominated under remote uniaxial or shear loadings

3. Square: stretch-dominated under remote uniaxial loading but switches to bending-dominated under remote shear

4. Kagome and Diamond: stretch-dominated in its pristine and *infinite-sized* form, but affected by significant bending if boundaries and/or imperfections are included.

Five periodic lattice micro-architectures and the stochastic Voronoi lattice – introduced in Sections 1.1.1 and 1.1.3 – will be the subject of detailed investigation in this thesis in order to highlight/compare and quantify the differences in their mechanical response to macroscopic loadings. There exists a number of significant gaps in our current state of knowledge concerning the mechanical performances of micro-architectured lattices as opposed to the more widely-adopted stochastic foams. The main objectives of this thesis is to address some of these issues as follows:

1. Formulate fully-validated FE models to be used as a platform for predicting the mechanical response - properties and mechanism(s) of deformation - of periodic and Voronoi lattices;

2. Elucidate the mechanisms responsible for edge-effects in *finite-sized* Square, Kagome and Triangular lattices subjected to remote uniaxial and shear loadings, and to quantify their effects upon their bulk mechanical properties;

3. Investigate/Quantify the shear and compression fatigue response of the five periodic lattices, and to elucidate the mechanism(s) responsible for the differences in their predicted endurance strength and fatigue life;

4. Quantify the effects of cell-regularity and relative density upon the fracture behaviour of stochastic Voronoi lattices using an idealised BLA approach; and,

5. Quantify the effects of finite specimen size and the use of standard test specimen configurations on the predicted fracture toughness of Voronoi lattices, and to elucidate the mechanism(s) responsible for their differences.

1.7 Outline of this thesis

The outline of this thesis is as follows. In Chapter 2, the mechanical properties of *infinite-sized* lattices, subjected to remote uniaxial compression and simple shear, are modelled using FE through a judicious choice of representative unit-cells. Five periodic lattices – viz. Square, Diamond, Hexagonal, Triangular and Kagome – in addition to the stochastic Voronoi lattice will be modelled. FE predictions for their elastic moduli and yield strength are subsequently validated against those of well-known scaling laws, which will be shown to be in excellent agreement. This lays the foundation for Chapter

3 which reports a detailed investigation into edge-effects in *finite-sized* Square, Kagome and Triangular lattices. An analytical model is first developed that captures the effects of specimen size on the effective properties of Square lattices subjected to simple shear: its predictions will be shown to be in excellent agreement with those by FE. The effects of finite specimen size for the Kagome and Triangular lattices are investigated using FE, and semi-empirical laws will be developed that captures its influence on the bulk lattice properties. The results of the three periodic lattices in Chapter 3 are then compared to existing ones for the Hexagonal, Voronoi and Diamond lattices in the literature. In Chapter 4, a non-linear continuous damage model that incorporates a nonlocal damage scheme will be coupled to the FE models to investigate the cyclic shear and compression fatigue of the periodic lattices. Predictions by the model are first validated against existing experimental S-N data for Diamond lattices. The predicted S-N data for the five lattices, and their sensitivity on imperfections – in the form of vertex perturbation and buckling modes – will be investigated. Fatigue performance of the five lattices will be assessed by comparing their S-N data, the macroscopic modulus damage accumulation and the location of fatigue damage within the lattice. Chapter 5 investigates the fracture response of elastic-brittle, two-dimensional isotropic lattices. The effects of relative density, cell-regularity, mode mixity and T-stress on the predicted fracture toughness will be quantified for Voronoi lattices using a boundary-layer analysis (BLA) and the location of their incipient wall fracture studied. Two commonly-used test specimen geometries - CT and SEN(B) - will also be modelled using FE and the fracture toughness predicted by these will be compared to predictions by the BLA. The discrepancies in predictions will be explained through a numerical-based 'displacement field analysis' approach. Finally, Chapter 6 provides a general summary of the findings and recommendations for further studies will be proposed.

1.8 Contributions to the archival literature

The work presented in this thesis have been published, submitted and/or currently being prepared for publication as follows:

1. Christodoulou I, Tan PJ. Crack initiation and fracture toughness of random

voronoi honeycombs. *Engineering Fracture Mechanics* 2013a;104:140–61.

2. Christodoulou I, Tan PJ. Role of specimen size upon the measured toughness of cellular solids. *Journal of Physics: Conference Series* 2013b;451:012004.

3. Christodoulou I, Tan PJ. Edge effects in periodic lattices. *Journal of Mechanics of Physics and Solids* 2016 (Under review)

4. Christodoulou I, Tan PJ. Influence of edge effects on the toughness of elastic-brittle two-dimensional isotropic lattices. *International Journal of Solids and Structures* 2016 (Under review)

5. Christodoulou I, Tan PJ. Shear and compression fatigue of periodic lattices. (In preparation, 2016)

Chapter 2

Mechanical properties of infinite-sized lattices

2.1 Introduction

Scaling laws for the bulk mechanical properties of periodic lattices were derived by others and reviewed in Chapter 1. Here, finite element (FE) models of periodic lattices – Triangular (T), Kagome (K), Square (S), Diamond (D) and Hexagonal (H) – will be developed and their predictions validated against those of the scaling laws presented in Chapter 1: this lends confidence to the accuracy of the FE models which would allow them, and their predictions, to be used in subsequent Chapters.

Since the micro-architecture of each lattice is strictly periodic, geometric symmetries are easily exploited to derive their intensive (bulk) properties, one that are unaffected by edge effects; in other words, for *infinite-sized* lattices. The analysis of a representative unit-cell (UC) – this is analogous to a representative volume element (RVE) for solid materials – would suffice to estimate their bulk mechanical properties. However, a judicious choice of unit-cell, and the application of correct boundary conditions, is critical and this will be addressed in this chapter.

For purpose of comparisons, lattices with a stochastic cell micro-architecture are also modelled. FE calculations will be performed to establish how their bulk elastic properties vary with relative density $\overline{\rho}$ (Eq.(1.6)) and cell-regularity Λ (Eq.(1.5)). Since the bulk properties of stochastic lattice are of interests, applying the appropriate boundary conditions are again critical – this will also be addressed here – in order to avoid any influence by edge effects.

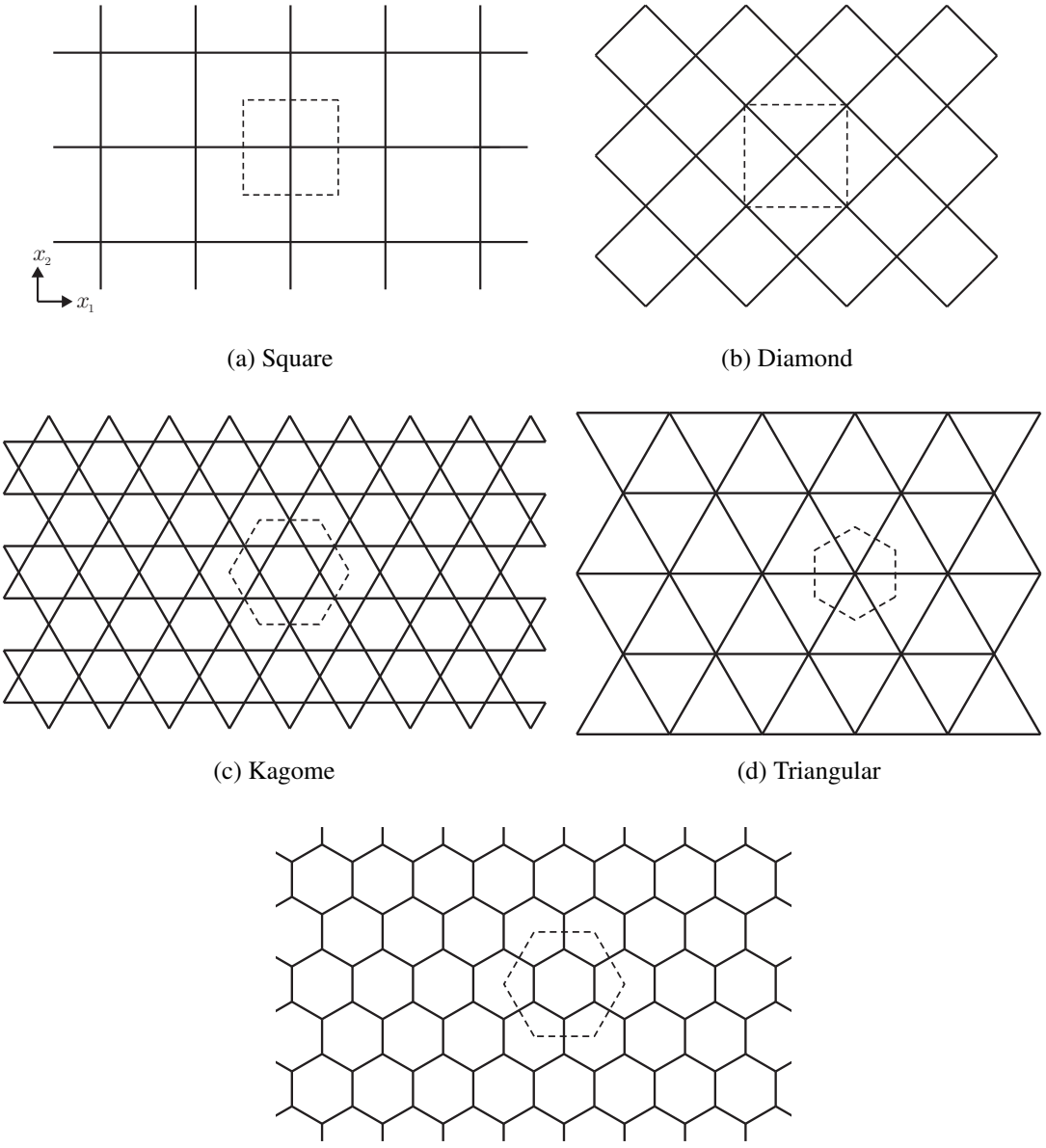

(a) Square

(b) Diamond

(c) Kagome

(d) Triangular

(e) Hexagonal

Figure 2.1: The five periodic lattices to be investigated. Dotted lines indicate the appropriate unit-cell (square or hexagonal) representation of each lattice.

2.2 Periodic lattices

Li (1999, 2000) have previously shown that a square unit-cell packing induces significant in-plane anisotropy. As reviewed in Chapter 1, in-plane anisotropy arises naturally for the Square and Diamond lattices because of their micro-architecture. By contrast, the Hexagonal, Triangular and Kagome lattices are well-known to possess isotropic in-plane properties; therefore, the use of a square unit-cell to model these lattices would

lead to an artefact, in the form of an 'artifical' anisotropic response. Consequently, a regular hexagonal unit-cell packing will need to be employed for the Hexagonal, Triangular and Kagome lattices in order to give the correct isotropic response (Li, 1999, 2000). For this study, both unit-cell packing arrangements will be utilised to model the five lattices as follows:

1. Square unit-cell to model the Square and Diamond lattices

2. Regular hexagonal unit-cell to model the Triangular, Kagome and Hexagonal lattices

Unit-cells with translational symmetries are used here, since reflectional symmetries are best avoided due to complications that might arise from antisymmetric loading conditions associated with shear (Li, 2008). Consequently, unit-cells with reflectional boundary conditions cannot be used for generic loading types and require separate formulations for remote uniaxial and shear loadings. Figure 2.1 shows the five lattice micro-architectures and their corresponding unit-cell (either square or regular hexagonal) to be used for analysing their bulk response. Note that each lattice is assumed to have a uniform cell wall length l and thickness t.

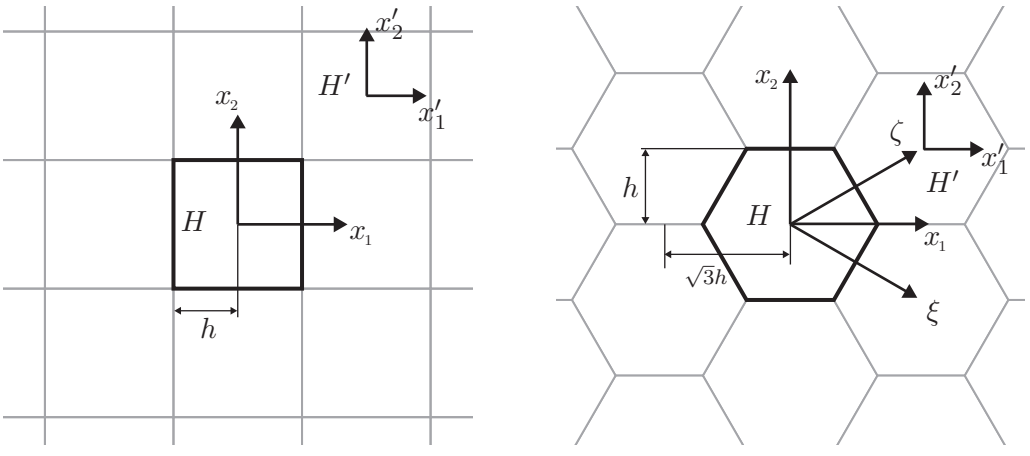

(a) (b)

Figure 2.2: Schematic showing a packing of (a) square and (b) regular hexagonal unit-cell. Note that the schematic shows a packing of unit-cells rather than the square and hexagonal lattices.

Figure 2.2 shows a packing of square and regular hexagonal unit-cells. A square unit-cell has two translational symmetries, along the x_1 and x_2 directions; whilst, a regular hexagonal unit-cell has three, along the x_2, ζ and ξ directions. The axes ζ and ξ are obtained by rotating x_1 through $+/-30°$, respectively. A square unit-cell is bounded by two side-pairs given by

$$x_1 = \pm h \quad , \quad x_2 = \pm h \tag{2.1}$$

as shown in Fig. 2.2, whilst a hexagonal unit-cell, on the other hand, is bounded by three side-pairs of

$$x_2 = \pm h \quad , \quad \zeta = \pm h \quad \text{and} \quad \xi = \pm h \quad . \tag{2.2}$$

The characteristic size of the unit-cell h depends on the micro-architecture of each lattice and is a function of its cell wall length l as shown in Figs. 2.3 and 2.4: they are summarised in Table 2.1. Under remote loadings, the relative displacement of each side-pair is governed by a set of equations to be developed in the next two sub-sections (2.2.1 and 2.2.2).

	Square	Diamond	Kagome	Triangular	Hexagonal
h/l	1/2	$\sqrt{2}/2$	$\sqrt{3}$	1/2	3/2

Table 2.1: Characteristic size of unit-cell (either square or regular hexagon) for each lattice.

2.2.1 Square unit-cell

The mapping of any point on a square unit-cell H, including along its peripheral, defined in a local $x_1 - x_2$ frame to an equivalent point on another unit-cell H' in the $x_1' - x_2'$ frame – see Fig. 2.2a – is given by

$$x_1 = x_1' + 2hk \quad , \quad x_2 = x_2' + 2hj \tag{2.3}$$

where the parameters $k, j = 0, \pm 1, \pm 2, \pm 3, \ldots$ define the translation of the original unit-cell H to the new unit-cell H'. For example, the unit-cell H' in Fig. 2.2a is obtained by setting $k = j = 1$.

For a set of prescribed remote loadings given by $\varepsilon_{11}^{\infty}$, $\varepsilon_{22}^{\infty}$ and γ_{12}^{∞}, the relative displacements between a node in unit-cell H and its corresponding node in H' are as follows:

$$\begin{aligned} u_1' - u_1 =& \varepsilon_{11}^{\infty}(x_1' - x_1) + \gamma_{12}^{\infty}(x_2' - x_2)/2 \\ u_2' - u_2 =& \varepsilon_{22}^{\infty}(x_2' - x_2) + \gamma_{12}^{\infty}(x_1' - x_1)/2 \end{aligned} \tag{2.4}$$

where $\varepsilon_{11}^{\infty}$ and $\varepsilon_{22}^{\infty}$ denotes remote uniaxial straining in the x_1 and x_2 directions, respectively; γ_{12}^{∞} is the remote shear strain; and, u_1' and u_2' are the nodal displacements measured in the local $x_1' - x_2'$ frame. The relationships given by Eq.(2.4) are, however, non-unique. Depending on the manner by which rigid body rotations are constrained, they may also be expressed as follows:

$$\begin{aligned} u_1' - u_1 =& \varepsilon_{11}^{\infty}(x_1' - x_1) \\ u_2' - u_2 =& \varepsilon_{22}^{\infty}(x_2' - x_2) + \gamma_{12}^{\infty}(x_1' - x_1) \end{aligned} \tag{2.5}$$

or

$$\begin{aligned} u_1' - u_1 =& \varepsilon_{11}^{\infty}(x_1' - x_1) + \gamma_{12}^{\infty}(x_2' - x_2) \\ u_2' - u_2 =& \varepsilon_{22}^{\infty}(x_2' - x_2) \quad . \end{aligned} \tag{2.6}$$

Equation (2.4) gives rise to a unit-cell that deforms in pure shear whilst Eqs.(2.5) and (2.6) to simple shear. Even though the deformation of the unit-cell is different for each of the aforementioned formulations, the bulk stiffness and strength predicted by them were found to be identical; likewise, Li (2008) also reported the same for unidirectional composites.

Combining the translational transformation of Eq.(2.3) with the relative displacement equations of Eq.(2.4), the necessary boundary conditions for each side-pair are obtained by evaluating along the boundaries of the unit-cell. For the side-pair $x_1 = \pm h$, the parameters (k, j) are set to $(1, 0)$. Similarly, for side-pair $x_2 = \pm h$, one sets $(k, j) = (0, 1)$. Subsequently, two equations must exist that relate the relative translational degrees of freedom – given by u_1 and u_2 – of each side-pair to any combination of remote strains $\varepsilon_{11}^{\infty}$, $\varepsilon_{22}^{\infty}$ or γ_{12}^{∞} as follows:

$$\begin{aligned} u_1|_{x_1=-h} - u_1|_{x_1=h} &= -2h\varepsilon_{11}^{\infty} \quad , \quad u_2|_{x_1=-h} - u_2|_{x_1=h} = -h\gamma_{12}^{\infty}/2 \\ u_1|_{x_2=-h} - u_1|_{x_2=h} &= -h\gamma_{12}^{\infty}/2 \quad , \quad u_2|_{x_2=-h} - u_2|_{x_2=h} = -2h\varepsilon_{22}^{\infty} \quad . \end{aligned} \tag{2.7}$$

Since the two boundary nodes of each side-pair are coupled, an additional set of equations must be imposed on their rotational degree of freedom as follows:

$$\omega_{12}|_{x_1=-h} - \omega_{12}|_{x_1=h} = 0 \quad \text{and} \quad \omega_{12}|_{x_2=-h} - \omega_{12}|_{x_2=h} = 0. \tag{2.8}$$

Figure 2.3a shows the square unit-cell of a Square lattice. Each side-pair consists of a boundary node on each side upon which the boundary conditions given by Eqs.(2.7) and (2.8) are imposed.

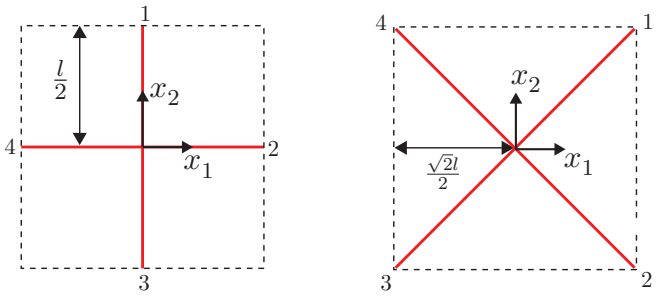

(a) (b)

Figure 2.3: Square unit-cell for the (a) Square and (b) Diamond lattices.

In the case of Diamond lattices, a boundary node is located at each corner of its square unit-cell as shown in Fig. 2.3b. Since each node is a member of two different sides-pairs, the boundary conditions must be reformulated as the displacement field at all four corners is inter-related (Li, 2000). Boundary node 1 is related to nodes 2, 3 and 4 via the translational transformation of Eq.(2.3) by setting the parameters (k, j) to $(0, 1)$, $(1, 1)$ and $(1, 0)$, respectively. The necessary displacement boundary equations thus become:

$$\begin{aligned} u_1|_2 - u_1|_1 &= -2h\gamma_{12}^{\infty} \quad , \quad u_2|_2 - u_2|_1 = -2h\varepsilon_{22}^{\infty} \\ u_1|_3 - u_1|_1 &= -2h\varepsilon_{11}^{\infty} - 2h\gamma_{12}^{\infty} \quad , \quad u_2|_3 - u_2|_1 = -2h\varepsilon_{22}^{\infty} \\ u_1|_4 - u_1|_1 &= -2h\varepsilon_{11}^{\infty} \quad , \quad u_2|_4 - u_2|_1 = 0 \end{aligned} \tag{2.9}$$

where $u_i|_j$ corresponds to the displacement of node j along direction i.

As above, the rotational degree of freedom at opposite corners of the square unit-cell are coupled via

$$\begin{aligned} &\omega_{12}|_1 - \omega_{12}|_3 = 0 \quad , \quad \omega_{12}|_2 - \omega_{12}|_4 = 0 \\ &\omega_{12}|_4 + \omega_{12}|_1 = 0 \end{aligned} \tag{2.10}$$

where $\omega_{12}|_j$ corresponds to the rotation of node j.

2.2.2 Hexagonal unit-cell

Boundary conditions for a hexagonal unit-cell can be derived in a similar manner to its square counterpart. However, because of the three side-pairs and the non-orthogonal translational transformations, the displacement boundary equations are more complicated than previously. Similar to the square unit-cell, the three translational transformations can also be described by just two parameters k and j. A point on the hexagonal unit-cell H defined in a local $x_1 - x_2$ frame can be mapped to an equivalent point on another unit-cell H' in the $x'_1 - x'_2$ frame by

$$x_1 = x'_1 + \sqrt{3}hk \quad , \quad x_2 = x'_2 + 2hj + hk \tag{2.11}$$

where the parameters $k, j = 0, \pm 1, \pm 2, \pm 3, \ldots$ are as before. The new reference frame $x'_1 - x'_2$ of unit-cell H' can be obtained by setting $j = 0$ and $k = 1$ in Eq.(2.11), see Fig. 2.2b. The equations for relative displacements are the same as before in Eq.(2.4). Combining Eq.(2.4) with (2.11), the requisite boundary conditions are obtained. For the side-pair $x_2 = \pm h$, the parameters (j, k) are set to $(1, 0)$; for both $\zeta = \pm h$ and $\xi = \pm h$, they are set to $(-1, 1)$. In total, six displacements and three rotational boundary equations must be imposed to enforce strict periodicity of deformation given by

$$
\begin{aligned}
u_1|_{x_2=-h} - u_1|_{x_2=h} &= -h\gamma_{12}^{\infty} \quad , \quad u_2|_{x_2=-h} - u_2|_{x_2=-h} = -2h\varepsilon_{22}^{\infty} \\
u_1|_{\zeta=-h} - u_1|_{\zeta=h} &= -\sqrt{3}h\varepsilon_{11}^{\infty} - \frac{h}{2}\gamma_{12}^{\infty} \quad , \quad u_2|_{\zeta=-h} - u_2|_{\zeta=h} = -h\varepsilon_{22}^{\infty} - \frac{\sqrt{3}}{2}h\gamma_{12}^{\infty} \\
u_1|_{\xi=-h} - u_1|_{\xi=h} &= -\sqrt{3}h\epsilon_{11}^{\infty} + \frac{h}{2}\gamma_{12}^{\infty} \quad , \quad u_2|_{\xi=-h} - u_2|_{\xi=h} = h\varepsilon_{22}^{\infty} - \frac{\sqrt{3}}{2}h\gamma_{12}^{\infty} \\
\omega_{12}|_{x_2=-h} - \omega_{12}|_{x_2=h} &= 0 \quad , \quad \omega_{12}|_{\zeta=-h} - \omega_{12}|_{\zeta=h} = 0 \\
\omega_{12}|_{\xi=-h} - \omega_{12}|_{\xi=h} &= 0 \quad .
\end{aligned}
\tag{2.12}
$$

Figure 2.4 shows the Kagome, Triangular and Hexagonal lattices where the hexagonal unit-cell is appropriate. Each side-pair consists of one node on each side. Since none of our lattices require a hexagonal unit-cell with nodes that are coincident with the six corners, no special formulation is required here. For the Triangular lattice, a rotated version of the unit-cell is used; note the differences in orientation of the unit-cell in Figs. 2.1c and 2.4b. The necessary modifications for the rotated version are straight forward and are not shown.

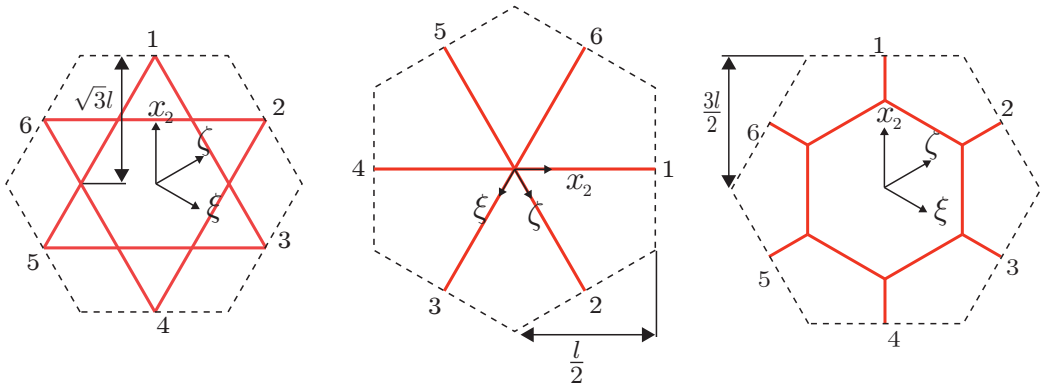

(a) (b) (c)

Figure 2.4: Hexagonal unit-cell of the (a) Kagome, (b) Triangular, and (c) Hexagonal lattices. Note the rotated version of the unit-cell for the Triangular lattice.

2.3 Voronoi lattices

2.3.1 Periodic 'unit-cell' for Voronoi lattices

To obtain the bulk properties of stochastic Voronoi (V) lattices, correct boundary conditions must again be prescribed in the FE analysis. Zhu et al. (2001) and Chen et al.

(1999) have previously shown that the use of mixed boundary conditions – representative of frictionless grips – are known to underestimate the bulk elastic modulus of Voronoi lattices because they do not constrain the rotational degree of freedom at the boundaries of the lattice (Chen et al., 1999; Zhu et al., 2001). To avoid this, periodic boundary conditions must be imposed to a packing of representative square unit-cell. However, unlike previously, the representative unit-cell now contains many cells where the stochastic distribution of cell characteristics averages-out over the entire unit-cell; a square unit-cell comprising of 50×50 cells was found to be sufficient for this purpose.

The square unit-cell of Section 2.2.1 has four boundary nodes in total. Here, a representative square unit-cell, comprising of 50×50 Voronoi cells, has approximately 50 nodes per side. In order to impose periodic boundary conditions, nodes on opposite sides of the representative unit-cell must appear in pairs: in other words, each node on $x_1 = -h$ should have a corresponding node on $x_1 = h$ with the same x_2 coordinate. Likewise, corresponding nodes on the side-pair $x_2 = \pm h$ must also have the same x_1 coordinates.

In periodic lattices, there is always a corresponding pair(s) of nodes for every side-pair since a square unit-cell always intersects the lattice at the correct position. However, this is not the case for Voronoi lattices unless a constraint is introduced to 'force' the Voronoi tessellation process to produce corresponding node-pairs. A commonly-used method is to position the set of nuclei for cells closest to the boundaries, e.g. within two cells from the lattice boundary, in the same manner as a regular periodic lattice, whilst those in the inner core are randomly positioned. This ensures that cells on opposite boundaries are identical so that node-pairs can exist. The perfect nature of the cells is not a realistic one and may lead to inaccurate estimates of the bulk moduli. To circumvent this drawback, another method is developed in the present thesis. The procedure takes the following steps:

1. Within the given area A, randomly position the set of m nuclei P in accordance to the requirements of Eq.(1.5);

2. The set of P nuclei is mapped 9 times for each possible combinations of $j, k = 0, 1$ and -1 of Eq.(2.3). This gives a lattice with a total area of $9A$ and $9 \times m$

nuclei;

3. The minimum distance requirement of Eq.(1.5) is checked and, if violated, Steps 1 and 2 are repeated until an admissible case is obtained;

4. Generate the Voronoi lattice; and,

5. Trim lattice to the required area A which would now have identical node-pairs for side-pairs $x_1 = \pm h$ and $x_2 = \pm h$.

Even though this procedure is lengthy - Step 1 and 2 may have to be repeated up to ≈ 20 times, depending on the Λ value - it gives corresponding node-pairs on opposing sides of the unit-cell whilst ensuring, at the same time, that all nuclei are randomly positioned. The presence of corresponding node pairs is clearly evident from the examples shown in Fig. 1.6 which were generated using this procedure; for the purpose of illustration, lattices with less than 50×50 cells are shown.

2.3.2 Relative density

As $\Lambda \rightarrow 0^+$, the spread of the distribution for cell size and cell shape increases in a Voronoi lattice; note that the special case of $\Lambda = 1$ corresponds to a regular Hexagonal lattice. Unlike for periodic lattices, it is not possible to express $\bar{\rho}$, for Voronoi lattices where $\Lambda \neq 1$, in closed-form such as by Eq.(1.7). Instead, $\bar{\rho}$ would need to be independently calculated for each of the Voronoi lattice generated by summing up the total length of all its cell walls, and assuming uniform cell wall thickness t, as follows:

$$\overline{\rho} = \frac{t \sum_{i=1}^{N} l_i}{A} \tag{2.13}$$

where l_i is the length of the i^{th} cell wall in a lattice and N is the total number of cell walls that make up the lattice. It was found that the *average* cell wall length $\hat{l}$ increases with decreasing Λ as shown in Table 2.2. Even though this variation is small – typically less than 8% – it will be corrected for by adjusting the wall thickness t accordingly in order to eliminate any $\overline{\rho}$ effects when comparing lattices of different Λ.

Λ	$\rightarrow 0^+$	0.25	0.5	0.6	0.7	0.8	1
$\hat{l}/l$	1.0775	1.0754	1.0636	1.0575	1.0484	1.0374	1

Table 2.2: Typical average cell wall length $\hat{l}$ for Voronoi lattices of different cell-regularity Λ.

2.4 Finite element models

Finite element (FE) models of the various unit-cells were generated using the commercial package Abaqus/Standard®; an overview of the numerical method(s) employed by the package can be found in Appendix D. The lattice micro-architecture is modelled using Timoshenko beam elements, or B21 in Abaqus notation. The beam elements, also, take into account shear deformation which is important for lattices with high $\overline{\rho}$, as previously discussed in Section 1.2. Mesh sensitivity studies revealed that four elements per cell wall are sufficient to achieve a converged response for all lattice micro-architectures, with the exception of the Square lattice subjected to remote shear. However, a much more refined mesh of fifteen B21 elements per cell wall are needed to achieve converged post-yield response for the Square lattice under shear.

It is important to emphasize that all finite element models presented in this thesis assume an idealised node/vertex design. Tacitly, this implies that the predicted stress distribution in every cell-wall - converging at a common vertex/node - is independent of each other. A more realistic nodal design is expected to give rise to a different stress distribution for each cell wall near the vertex. Whether the overall stress is higher or lower compared to the ideal node depends on the specifics of the nodal design which is outside the scope of this work. Notwithstanding, this simplification is not expected to limit the validity of the results presented in this thesis since the cell wall deflection, and not the stress distribution within them, is utilised to estimate the macroscopic strain of a lattice. Thus small changes in the estimated stress within the cell wall is not expected to alter significantly the results presented in subsequent Chapters.

The choice of material for the lattice ligament (or struts) is unimportant, since the predicted bulk lattice properties will be normalised by the material properties of the ligament. In the FE simulations, the struts are assumed to be made of an aluminium

alloy with a bi-linear stress-strain relationship, with an elastic modulus of $E_s = 70$GPa, yield strength $(\sigma_y)_s = 130$MPa, Poisson's ratio $\nu_s = 1/3$ and a linear hardening slope $\mathrm{d}\sigma/\mathrm{d}\varepsilon = 735$MPa – they are the same as that used by Tekoglu et al. (2011). Since only planar lattices are of interests, its out-of-plane thickness d is set to unity without any loss of generality.

2.4.1 Consistent estimate of yield strength

Figure 2.5a shows the predicted bulk stress-strain response for each lattice – they all have identical relative density of $\overline{\rho} = 0.01$ – subjected to uniaxial straining $\varepsilon_{11}^{\infty}$. A sharp transition to the non-linear regime is evident in these curves except for that corresponding to a Hexagonal lattice. Hence, an offset method in accordance to the ASTM E8/E8M-13a (2013) – a 0.1% offset is adopted in the present thesis – will be employed to extract the bulk uniaxial and shear modulus/strength of each lattice. It is worth noting that the choice of offset (others might choose 0.2%) has virtually no effect upon the general trend of the results reported here or in subsequent chapters.

The strain energy U absorbed by a lattice when compressed up to a nominal uniaxial strain of ε_i is given by

$$U_{\varepsilon_i} = \int_0^{\varepsilon_i} \sigma(\varepsilon)\,\mathrm{d}\varepsilon \quad . \tag{2.14}$$

Following Tan et al. (2005), the energy absorption efficiency of a lattice $\eta(\varepsilon_i)$ - defined as the ratio of energy absorbed up to a nominal strain ε_i to its corresponding nominal stress - is given by

$$\eta(\varepsilon_i) = \frac{U_{\varepsilon_i}}{\sigma|_{\varepsilon=\varepsilon_i}} \quad . \tag{2.15}$$

If a body is deforming in the linear stress-strain regime, then its energy absorbing efficiency is always exactly $0.5\varepsilon_i$ but when its response deviates from linearity, then $\eta(\varepsilon_i)$ starts increasing. Hence, the energy absorption efficiency can be modified to give

$$\psi(\varepsilon_i) = \eta(\varepsilon_i) - 0.5\varepsilon_i \quad . \tag{2.16}$$

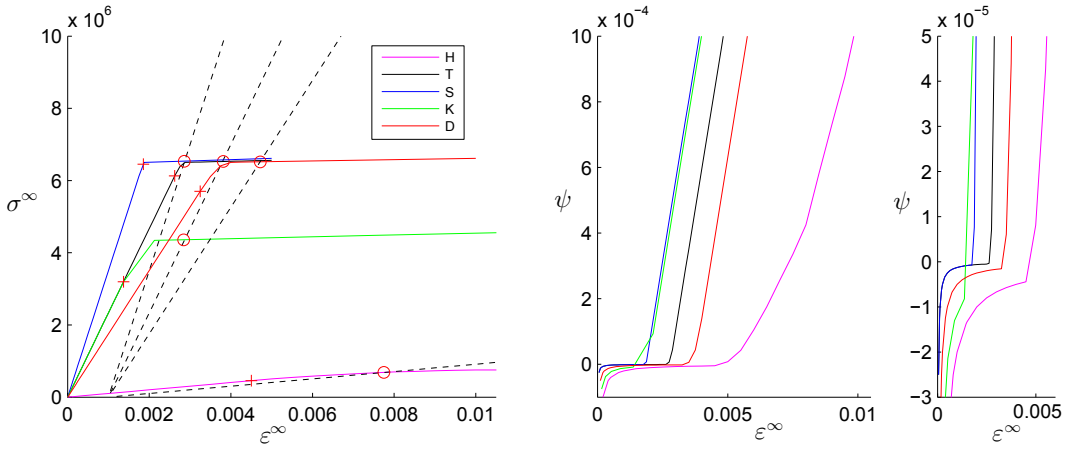

(a) (b)

Figure 2.5: (a) Uniaxial stress vs strain responses; and (b) Energy absorption efficiency curves of the five periodic lattices. The start of non-linear regime is indicated by $+$ and the corresponding estimate of its yield strength by $\circ$. 0.1% offset lines are shown as dashed lines.

The modified form of Eq.(2.16) ensures that $\psi(\varepsilon) = 0$ in the linear stress-strain regime and $\psi(\varepsilon) > 0$ corresponds to the onset of non-linear bulk response. However, the numerical nature of the FE method meant that ψ is never strictly zero in the linear regime. Figure 2.5b plots the ψ-ε^{∞} curves corresponding to the five periodic lattices; note the 'zoomed-in' version, with its different vertical scale for ψ, highlights the shift from linear to non-linear regime. Notice that for all lattices, ψ is negative initially but there is always a steep increase in ψ when the bulk response of the lattice is non-linearly: hence, the corresponding transition strain is easily determined. This point is indicated with a $+$ in Fig. 2.5a, which is used to estimate the bulk modulus E^* of the lattice. Finally, the 0.1% offset is used to estimate its yield strength σ_y^*, commonly known as the proof stress, which is indicated by $\circ$ in Fig. 2.5a.

2.5 Results

2.5.1 Periodic lattices

For each lattice, the cell wall thickness t is adjusted accordingly to achieve the desired relative density between the range of $10^{-3} \leq \overline{\rho} \leq 0.3$. The length l of each strut, or cell wall, in a lattice is uniform, and set to unity, throughout unless otherwise specified; this

does not affect the generality of the results. Three separate analyses were performed for each lattice: uniaxial compressions ($\varepsilon_{11}^{\infty}$ and $\varepsilon_{22}^{\infty}$) and shear ($\gamma_{12}^{\infty}$). All simulations were performed within a small-strain context and neglects non-linear geometry. Examples of deformed unit-cell are shown in Fig. 2.6 for each lattice micro-architecture; note that the deformation of each lattice is exaggerated for the purpose of visualisation. Results from the analyses are used to determine the uniaxial moduli (E_1^* and E_2^*) and strength ($(\sigma_y^*)_1$ and $(\sigma_y^*)_2$) along the two principal directions, shear modulus (G^*), shear strength (τ_y^*) and Poisson's ratio (ν^*). Finally, the modulus and strength predicted by FE is fitted to the scaling laws of Eq.(1.9) for each lattice. Their coefficients are tabulated, and compared to those obtained from existing literature, in Table 2.3.

Since the analyses were carried out within a small-strain context, elastic buckling is excluded and a note of caution on interpreting the predicted yield strength of lattices with a low relative density is necessary. It is well known that elastic buckling precedes plastic buckling if the constituent cell walls are sufficiently slender. This transition from elastic to plastic buckling depends on the ratio of the yield strength of the cell wall material to its elastic modulus $(\sigma_y)_s/E_s$ (Gibson and Ashby, 1997). The transition relative density ($\overline{\rho}_{\text{trans}}$) for each micro-architecture was previously derived by Wang and McDowell (2004) - they are also listed in Table 2.3. Therefore, if a lattice has relative density of $\overline{\rho} < \overline{\rho}_{\text{trans}}$, then its yield strength predicted by Eq.(1.9), and the corresponding coefficients in Table 2.3, is likely to be an over-prediction. Notwithstanding, the macroscopic moduli of a lattice remains valid for the entire range of $\overline{\rho}$.

For each row in Table 2.3, the first line corresponds to analytical predictions by Eq.(1.9) and the second by the FE models, up to three decimal places. In general, there is an excellent agreement. The biggest differences are noted for the yield properties of the Hexagonal lattice. This is unsurprising since the scaling laws of Eq.(1.9) were derived based on fully plastic moment of rigid-perfectly plastic struts and assuming slender cell walls; whereas, the current FE models take into account the effects of axial and shear stresses, including strain hardening (linear) of the ligaments.

An anomaly is encountered for the Triangular lattice subjected to remote $\varepsilon_{22}^{\infty}$ loading. To obtain the correct deformed shape, shown in Fig. 2.6h and the coefficients listed of Table 2.3, two additional boundary conditions must be imposed to relate the x_1

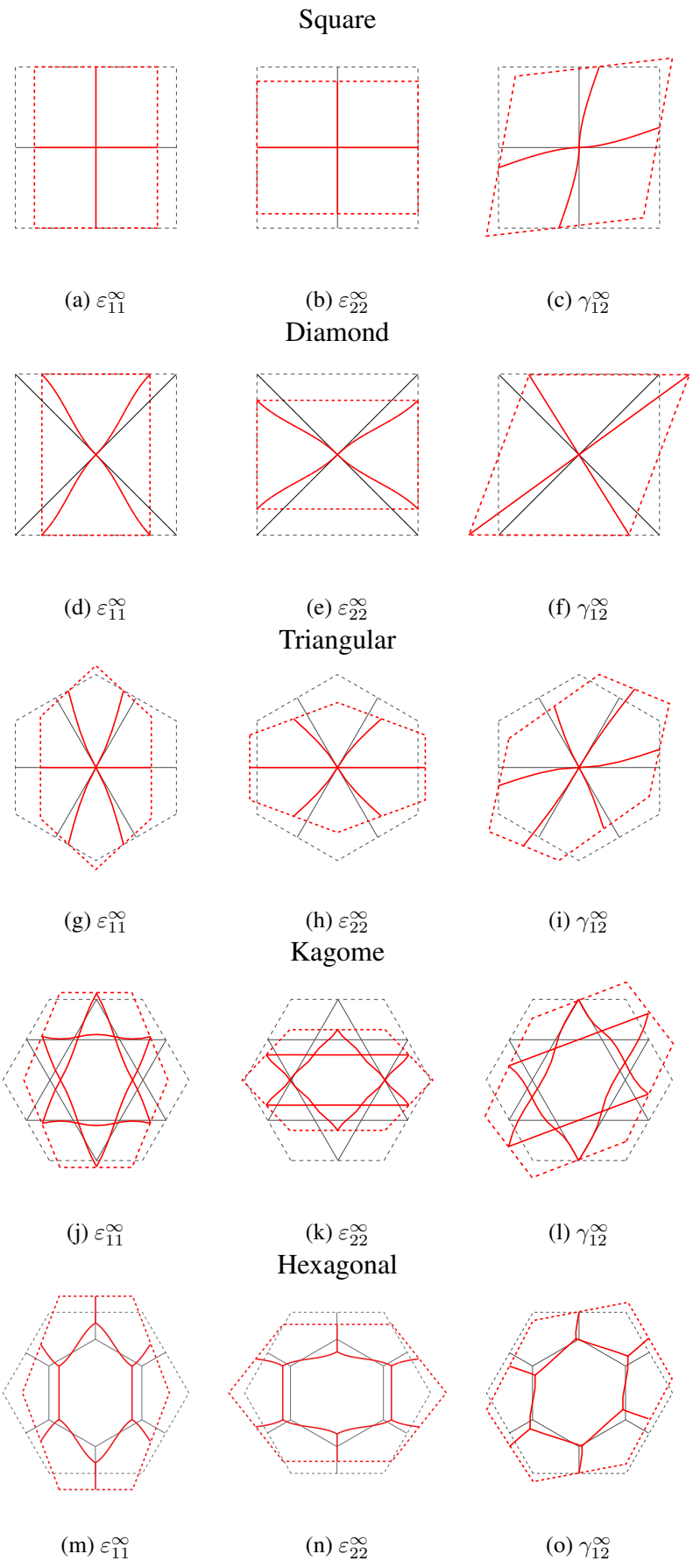

Figure 2.6: Deformed unit-cell of each lattice micro-architecture. Red (deformed) and black (undeformed). Note that the deformation shown has been exaggerated for visualisation purposes.

		B	b	C	c	B_y	b_y	C_y	c_y	ν^*	$\overline{\rho}_{\text{trans}}$
Square	Lit	$1/2$	1	1/16	3	1/2	1	1/8	2	≈ 0	0.070
	FE	0.500	1	0.062	3	0.503	1	0.125	2	0	
Diamond	Lit	$1/4$	1	1/4	1	1/2	1	1/2	2	≈ 0	0.070
	FE	0.253	1	0.250	3	0.501	1	0.501	1	0	
Kagome	Lit	1/3	1	1/8	1	1/3 (x_1) 1/2 (x_2)	1	0.289	1	1/3	0.030
	FE	0.335	1	0.126	1	0.336 (x_1) 0.502 (x_2)	1	0.289	1	0.333	
Triangular	Lit	1/3	1	1/8	1	1/3 (x_1) 1/2 (x_2)	1	0.289	1	1/3	0.060
	FE	0.333	1	0.125	1	0.333 (x_1) 0.502 (x_2)	1	0.290	1	0.333	
Hexagonal	Lit	3/2	3	1/3	3	1/2	2	0.217	2	1	0.003
	FE	1.444	2.992	0.366	2.995	0.549(x_1) 0.604 (x_2)	2.050 (x_1) 2.064 (x_2)	0.246	2.061	0.989	

Table 2.3: Coefficients corresponding to Eq.(1.9). For each lattice micro-architecture, existing analytical results (Cote et al., 2006; Fleck et al., 2010; Gibson and Ashby, 1997; Wang and McDowell, 2004) from the literature (Lit) are compared to predictions by the FE models, denoted by (FE).

displacement of side pairs $\zeta = \pm h$ and $\xi = \pm h$ to that of side pair $x_2 = \pm h$ as follows:

$$u_1|_{\zeta=-h} - u_1|_{\zeta=h} = -u_1|_{x_2=h} \quad , \quad u_1|_{\xi=h} - u_1|_{\xi=-h} = u_1|_{x_2=-h} \quad . \tag{2.17}$$

Without imposing the additional constraints in Eq.(2.17), the boundary conditions for side pair $x_2 = \pm h$ is found to be $u_1|_{x_2=-h} - u_1|_{x_2=h} = 0$ and $u_2|_{x_2=-h} - u_2|_{x_2=h} = 0$ which causes the loss of continuity of the displacement field in the *deformed* hexagonal unit-cell packing. As a result, a bending, instead of stretch, dominated deformation ensues if Eq.(2.17) is not imposed.

2.5.2 Voronoi (Stochastic) lattices

Due to the stochastic nature of a Voronoi lattice micro-architecture, a sufficiently large sample of Voronoi tessellations must be analysed to obtain an average response. Numerical checks have been performed that show a sample size of twenty tessellations is needed at each cell-regularity Λ to obtain representative results. Table 2.4 shows the *average* elastic properties and the percentage variation, from their respective mean values, for a Voronoi lattice of cell-regularity $\Lambda = 0.5$ and relative density $\overline{\rho} = 0.1$. The elastic moduli are normalised by $\overline{\rho}^3 E_s$ to give $\overline{E}^*$ and $\overline{G}^*$; hence, $\overline{E}^* = 3/2$ for a $\Lambda = 1$ lattice. The differences between the average bulk properties in the x_1 and the x_2 directions are insignificant; <2% for all combinations of $\overline{\rho} - \Lambda$ considered in this thesis. These results are not surprising since the cells in a Voronoi lattice have no preferred orientation. Therefore, the $\overline{E}_1^*$ and $\overline{E}_2^*$ values for each Λ are combined into a single sample set of 40 lattices – the same also applies to their corresponding Poisson's ratio – as follows:

$$\overline{E}_1^* = \overline{E}_2^* = \overline{E}^* \quad , \quad \nu_{12}^* = \nu_{21}^* = \nu^* \tag{2.18}$$

Figures 2.7 and b show the variation of the elastic moduli with $\overline{\rho}$ and Λ. The theoretical estimates by Silva et al. (1995) are nearly identical to the present FE results for regular Hexagonal lattices of $\Lambda = 1$. At the lower values of $\overline{\rho}$, cell-irregularities lead to an increase in $\overline{E}^*$ and $\overline{G}^*$, by up to 20%, as $\Lambda \to 0^+$. This trend is reversed for relative densities $\overline{\rho} > 0.2$. The variations of each data point plotted in Fig. 2.7 and b are less than one standard deviation and this also agrees well with the results of Silva et al. (1995) and Zhu et al. (2001).

	$\overline{E}_1^*$	$\overline{E}_2^*$	$\overline{G}^*$	ν_{12}^*	ν_{21}^*
Mean	1.5866	1.5910	0.4152	0.9689	0.9668
% deviation	1.5674	1.5658	1.3934	0.2081	0.4376

Table 2.4: Average elastic bulk moduli and Poisson's ratio estimated from a sample of twenty Voronoi tessellations of identical cell-regularity $\Lambda = 0.5$ and relative density $\overline{\rho} = 0.1$.

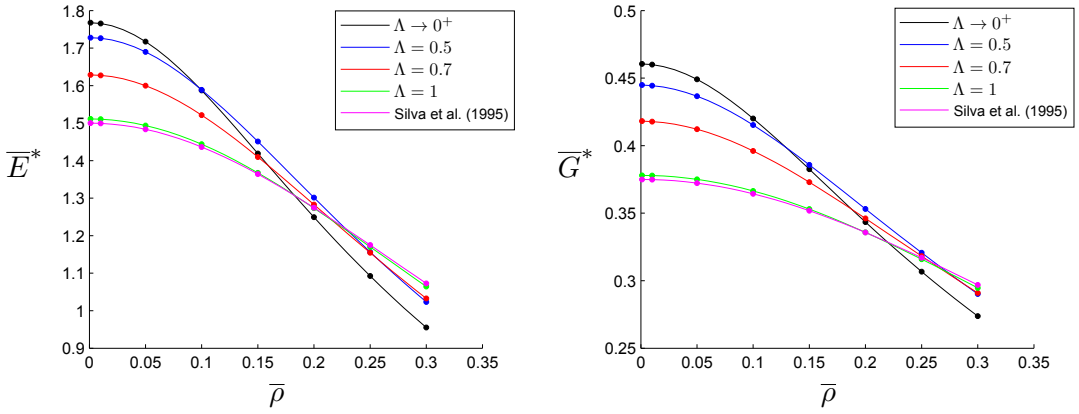

(a) (b)

Figure 2.7: In-plane elastic properties as a function of relative density $\overline{\rho}$ for different cell-regularity Λ. Theoretical estimates by Silva et al. (1995) for a regular Hexagonal lattice are included for comparison.

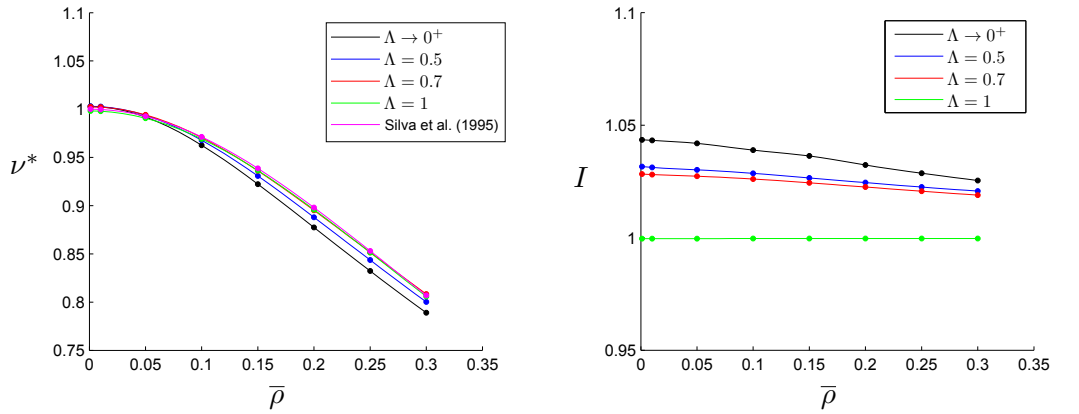

(a) (b)

Figure 2.8: Poisson's ratio and isotropy parameter as a function of relative density $\overline{\rho}$ for different cell-regularity Λ. Theoretical estimate of ν^* for a Hexagonal lattice by Silva et al. (1995) are included for comparison.

The Poisson's ratio ν^* of a Voronoi lattice decreases with increasing $\overline{\rho}$ as shown in Fig. 2.8a; this trend is similar to the theoretical estimate in Silva et al. (1995) for

regular Hexagonal lattices. Cell-regularity does not appear to have a significant effect on ν^*, leading only to a slightly reduced ν^* as $\Lambda \to 0^+$; this reduction becomes more pronounced at higher values of $\overline{\rho}$. Note that a similar trend is also reported by Zhu et al. (2001). Figure 2.8b shows the variation of

$$I = 2G^*(1 + \nu^*)/E^*, \tag{2.19}$$

an isotropy parameter, against $\overline{\rho}$. As expected, I is always unity for a Hexagonal lattice regardless of its relative density. For non-periodic lattices, I is only slightly raised ($<$ 5%). Therefore, the assumption of an isotropic 2D lattice for all cell-regularity Λ is, to a first approximation, valid.

2.6 Summary

In this chapter, the finite element method was employed to determine the bulk elastic and yield properties of regular and semi-regular *infinite-sized* periodic lattices using representative unit-cells. Five lattice micro-architectures were studied, viz. Hexagonal, Triangular, Square, Diamond and Kagome lattices. The correct choice of unit-cell packing was discussed in detail and equations for the appropriate boundary conditions developed. There is excellent agreement between the FE results and predictions by scaling laws developed elsewhere by others. The results presented suggest that the unit-cell method, with its minimal model size, is capable of capturing the bulk response of *infinite-sized* periodic lattices.

In addition, Voronoi lattices with a stochastic micro-architecture were also modelled. The application of periodic boundary conditions were discussed in detail and the FE models used to determine the bulk properties of Voronoi lattices for a range of cell-regularity Λ; excellent agreement with results from the literature is, again, demonstrated.

Last, the results presented in this chapter confirms that the finite element models of the various lattices were correctly developed which would allow them, and their predictions, to be used in subsequent Chapters.

Chapter 3

Edge effects in periodic lattices

3.1 Introduction

The mechanical properties predicted by the scaling laws of Eq. (1.9) apply only to lattices of *infinite-size*, i.e. they give bulk (or intensive) properties. Edge effects in *finite-sized* lattices are a well-known phenomenon - this was reviewed in Section 1.3 - which leads to either an enhancement or a reduction in their bulk properties. In this chapter, the effects of boundaries upon the effective modulus and strength of *finite-sized* lattices subjected to remote uniaxial compression and shear will be studied for three periodic lattice micro-architectures, viz. Square (S), Kagome (K) and Triangular (T). A Square lattice has a simple micro-architecture that allows the problem to be treated analytically whilst the other two are much more complicated and will be solved numerically using finite elements. Their results are compared to those of other lattices, viz. Voronoi (V), Hexagonal (H) and Diamond (D), from existing literature. This chapter aims to elucidate the underlying intrinsic mechanisms responsible for the observed edge effects in bending and stretch-dominated lattice micro-architectures, and to quantify how the effective properties of finite-sized lattices compare to their corresponding bulk counterparts.

3.2 Methodology

Finite-sized lattices were generated, in a manner similar to that described in Chapter 2.4 and is not repeated here, on which numerical experiments will be performed. Appropriate displacement boundary conditions, to be discussed later in Section 3.2.2, are imposed to simulate remote uniaxial compression and simple shear loadings where the moduli and strength of these *finite-sized* lattices will be extracted. The predicted results will be normalised by their corresponding *infinite-sized* counterparts – they will be de-

noted by $(\,)_{\mathrm{UC}}$ – that were previously determined in Chapter 2 by a unit-cell approach.

3.2.1 Lattice size in terms of *complete* cells

Examples of *finite-sized* lattices are shown in Fig. 3.1 for each micro-architecture. Note that all cell walls (struts) are of identical length l with the exception of the overhanging ones along the peripheral of the Square lattice where they each have the same overhanging length λl where $0 \leq \lambda \leq 1$. In order to relate the overall dimensions of a *finite-sized* lattice – W (width) $\times$ H (height) – to the number of cells it contain, the counting of *complete* cells would need to be made clear. Let $\overline{W}$ and $\overline{H}$ be the total number of *complete* cells along each row (horizontal x_1 - direction) and column (vertical x_2 - direction) of a lattice, respectively. For the examples shown in Fig. 3.1, the Square and Triangular lattices would comprise of 7×3 and 9×4 *complete* cells, respectively - their counting is straightforward. The Kagome lattice, on the other hand, is trickier

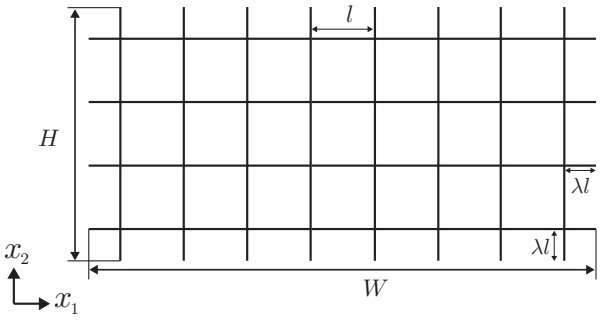

(a) Square (7×3)

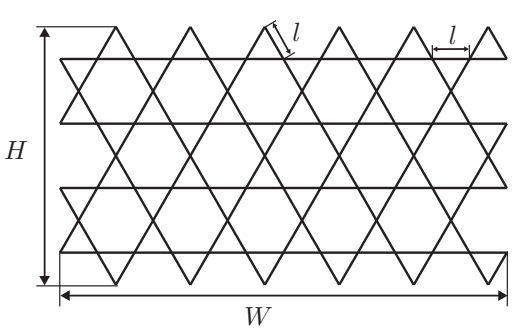

(b) Kagome (5×3)

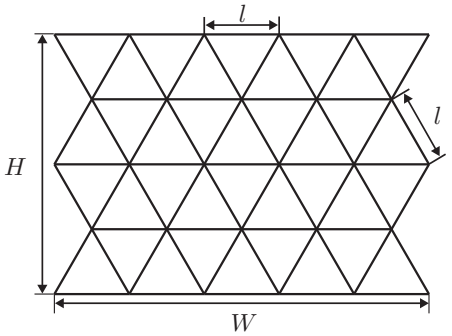

(c) Triangular, (9×4)

Figure 3.1: Examples of *finite-sized* lattices where the number of *complete* cells ($\overline{W} \times \overline{H}$) are shown within brackets. For the Kagome lattice, each intact regular hexagon, excluding its contiguous equilateral triangles, is counted as a *complete* cell.

	W/l	H/l	$\overline{W}$	$\overline{H}$	
Square	$\overline{W}+2\lambda$	$\overline{H}+2\lambda$	$1,3,5,\ldots$	$1,3,5,\ldots$	$0\leq\lambda\leq 1$
Kagome	$2\left(\overline{W}+1\right)$	$\sqrt{3}\left(\overline{H}+1\right)$	”	$1,3,5,\ldots$	-
Triangular	$\left(\overline{W}+1\right)/2$	$\sqrt{3}\left(\overline{H}/2\right)$	”	$2,4,6\ldots$	-

Table 3.1: Relationships between the overall dimensions of finite-sized lattices and their number of *complete* cells

to count due to its micro-architecture: consequently, each complete regular hexagon, excluding its contiguous equilateral triangles, shall be counted here as a *complete* cell. Therefore, the Kagome lattice in Fig 3.1b would comprise of 5×3 *complete* cells. For convenience, all the lattices generated for subsequent parametric studies shall always contain odd number of complete cells $\overline{W}$ and $\overline{H}$; the only exception is an even number of cells $\overline{H}$ for the Triangular lattice. In this manner, the overall dimensions ($W/l\times H/l$) of a lattice are readily expressed as functions of the number of *complete* cells in each row or column: they are tabulated in Table 3.1 for each lattice micro-architecture.

The Square lattices, unlike the other two, were deliberately generated to contain incomplete, open, cells along its boundary expect when $\lambda=0$. This is because finite-sized Hexagonal lattices containing open cells along their boundaries are known to have a profound effect upon their shear modulus and strength (Onck et al., 2001); the same will need to be investigated here for the Square lattice. The length of each overhanging cell wall is given by λl where $0\leq\lambda\leq 1$, as shown in Fig 3.1a. If $\lambda=0$, all cells along the boundary are closed; otherwise, they are always open. In the limiting case of $\lambda=1$, the lattice has open boundary cells with overhanging cell walls of length l.

3.2.2 Displacement boundary conditions

The boundary ∂V of each *finite-sized* lattice can be divided into ∂V^T (Top), ∂V^B (Bottom), ∂V^L (Left) and ∂V^R (Right) as shown in Fig. 3.2: for brevity, they are denoted by T, B, L and R, respectively.

To simulate macroscopic uniaxial compression, the vertical translation of all nodes in B is constrained, i.e. $u_2^B=0$, and the set of nodes in T is displaced by $u_2^T=\varepsilon_{22}^* Hd$ in the negative x_2 direction, where d is the unit out-of-plane thickness. With the exception

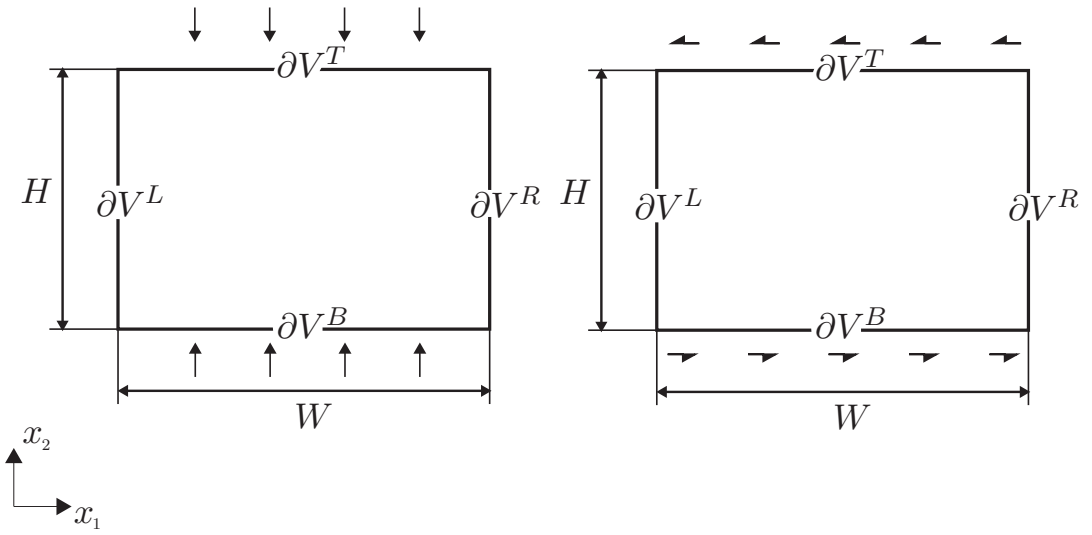

(a) (b)

Figure 3.2: *Finite-sized* specimens subjected to remote (a) uniaxial compression and (b) simple shear loadings.

of a middle node in B, that has been constrained to prevent rigid-body translation, all nodes in T and B are free to translate along x_1. Additionally, just like in Tekoglu et al. (2011), the nodes (or cell walls) in T and B are assumed to be perfectly bonded to the loading 'platens' so their rotational degree of freedom is also restrained, i.e. $\omega_{12}^T = \omega_{12}^B = 0$. All nodes along L and R are unconstrained, i.e. they are stress-free. The compressive stress is defined as the reaction force, per unit specimen width, in the x_2 direction given by $\Sigma RF_2/Wd$ where d is the unit out-of-plane thickness. It follows that the macroscopic elastic modulus is $E^* = \Sigma RF_2/Wd\varepsilon_{22}^*$. The compressive yield strength is estimated using the procedure described in Section 2.4.1, beyond which the lattice is no longer deforming in the linear-elastic regime.

To simulate simple shear, both translational degree of freedoms in B are constrained, i.e. $u_1^B = u_2^B = 0$, and nodes in T are displaced horizontally along x_1 through $u_1^T = \gamma_{12}^* Hd$. All nodes in T are allowed to translate freely along x_2 so that T always remains horizontal, and parallel, to B. Just as for uniaxial loading, both B and T are tied rigidly to the loading 'platens' so that $\omega_{12}^T = \omega_{12}^B = 0$. All nodes in L and R remain stress free. The shear stress is calculated by dividing the total reaction forces in the x_1 direction (ΣRF_1) along T with the specimen width to give $\Sigma RF_1/Wd$. The shear

modulus follows from $G^* = \Sigma RF_1/Wd\gamma_{12}^*$ and the shear strength is estimated using the procedure described in Section 2.4.1.

It is worth highlighting that, previously in Chapter 2, the 'bulk' shear properties predicted are identical irrespective of whether simple or pure shear is applied to the unit-cell. Here, however, care must taken not to assume that the results - for remote simple shear - also apply to pure shear loading, since the mechanism(s) responsible for edge-effects may not be identical.

3.3 Square (S) lattice

3.3.1 Uniaxial loading

Under uniaxial compression, a *finite-sized* Square lattice responds in exactly the same manner as its *infinite-sized* counterpart where all the vertical cell walls aligned with the loading direction are compressed axially whilst the rest remain stress-free. Strictly speaking, this is ***only*** possible if the perfect Square micro-architecture is maintained throughout deformation.

Consider two *finite-sized* lattices with identical column and row ($\overline{W} = n$) of *complete* cells but with either $\lambda = 0$ or $\lambda = 1$. According to Table 3.1, the lattice width would be $W = nl$ if $\lambda = 0$, and $W = (n+2)l$ if $\lambda = 1$. Since they both contain exactly $n+1$ vertical cell walls, see Fig 3.1a, their load carrying capacity is identical. However, the effective stressed area of the $\lambda = 1$ lattice is greater by $2l$, which leads to a more compliant response because of the lower nominal stress. Unsurprisingly, the decrease in nominal stress due to λ becomes more pronounced as $\overline{W}$ reduces.

The bulk modulus of an *infinite-sized* lattice is reached when $\lambda = 1/2$ - this is irrespective of $\overline{W}$ - since these lattices would have exactly one load-carrying cell wall per l and is equivalent to the representative unit cell of Fig. 2.3. Therefore, the size dependency of the effective elastic modulus and yield strength for a Square lattice is simply

$$\frac{E^*}{(E^*)_{\text{UC}}} = \frac{\sigma_y^*}{\left(\sigma_y^*\right)_{\text{UC}}} = \frac{\left(\overline{W}+1\right)}{\left(\overline{W}+2\lambda\right)} \tag{3.1}$$

which is, in reality, just an 'area correction' of the stressed surfaces to a corresponding

$\lambda = 1/2$ lattice. As to be expected, lattice height H does not affect the results and a representative case of $\overline{H} = 51$ is plotted in Fig. 3.3a.

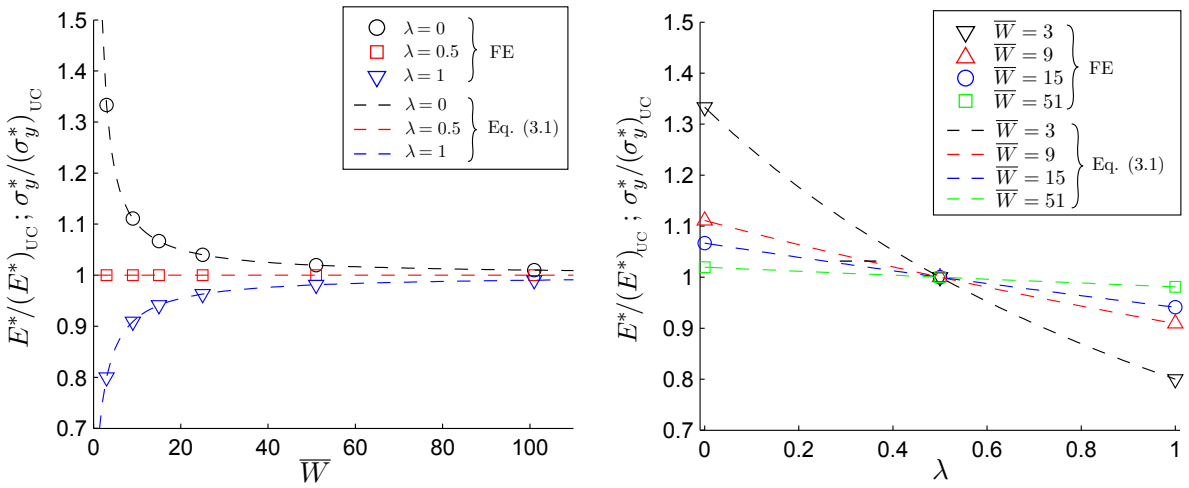

(a) (b)

Figure 3.3: Effects of $\overline{W}$ and λ on the normalised effective elastic modulus $E^*/\left(E^*\right)_{\mathrm{UC}}$ and yield strength $\sigma_y^*/\left(\sigma_y^*\right)_{\mathrm{UC}}$ of Square lattices. All results plotted are for $\overline{H} = 51$ and $\overline{\rho} = 0.1$.

Predictions by Eq. (3.1) are plotted, alongside the FE results, in Fig. 3.3a for $\lambda = 0, 1/2$ and 1: they are in exact agreement. If $\lambda > 0.5$, the effective modulus and strength values are below their 'bulk' values; the reverse occurs if $\lambda < 0.5$. The closer λ is to 0.5, the less sensitive are the properties to $\overline{W}$ as shown in Fig 3.3b. At $\lambda = 0.5$, the 'bulk' properties are reached irrespective of $\overline{W}$. The effective properties are within 10% of its predicted bulk values if $\overline{W} \geq 9$, beyond which they are relatively insensitive to λ, see Fig 3.3b. If, on the other hand, $\overline{W} < 9$, then the properties are highly sensitive to λ. Additionally, the relative density $\overline{\rho}$ of a lattice does not influence the results here since the deformation in a perfect lattice is entirely by stretch; hence, only a representative case of $\overline{\rho} = 0.1$ need to be shown. A note of caution: this 'apparent' size effect is merely a consequence of 'area correction' and is distinct from all subsequent cases later on that arise from a switch in the deformation mechanism at the cell-scale.

3.3.2 Simple shear

Unlike in uniaxial compression, a Square lattice subjected to macroscopic shear deforms predominately by bending of its constituent struts. A three-step procedure is employed here to model analytically the edge effects experienced by a *finite-sized* Square lattice subjected to simple shear. First, a lattice of finite $\overline{H}$, but of infinite $\overline{W}$, is modelled to capture the effects from the two horizontal stressed surfaces T and B in Section 3.3.2.a. Second, a lattice of finite $\overline{H}$ and single cell width ($\overline{W} = 1$) is modelled: this captures the influence from the lateral stress-free boundaries L and R in Section 3.3.2.c. Last, results from both models will be combined in Section 3.3.2.d, using a ***rule-of-mixtures***, to derive an overall expression that quantifies how the effective properties of *finite-sized* Square lattices are affected by edge effects. Slender cell walls are assumed in the model formulations where axial stresses are neglected. Predictions by the analytical model will be compared to FE models for lattices of relative density $\overline{\rho} = 0.1$; comparison is not made for higher relative densities since this would invariably increase any discrepancies between the analytical and FE results.

3.3.2.a Infinitely-wide lattices ($\overline{W} \to \infty$) - Modelling

Case A: $\overline{H} = 1$

Figure 3.4a shows the representative model of an infinitely-wide lattice, but with $\overline{H} = 1$, that is loaded in simple shear. It suffices to analyse only a representative unit cell with appropriate periodic boundary conditions applied to its lateral boundaries (L and R). The representative unit cell comprises only a single column of vertical struts and the corresponding horizontal struts of length $l/2$; there is no necessity to model complete cells because of symmetry. Figure 3.4b shows the corresponding forces and moments associated with each strut. Since all struts are assumed to be slender, then bending is the dominant deformation and axial forces can be neglected. On the contrary, the shear forces F in all vertical struts are important and must be taken into account. By considering force equilibrium at the joints, F can easily be related to the applied macroscopic shear stress through $F = \tau_{12}^{*} ld$. The shear forces S in the horizontal members of Fig 3.4b are not important so they are neglected.

The nodes at the stressed surfaces are denoted by T and B, whilst the nodes corre-

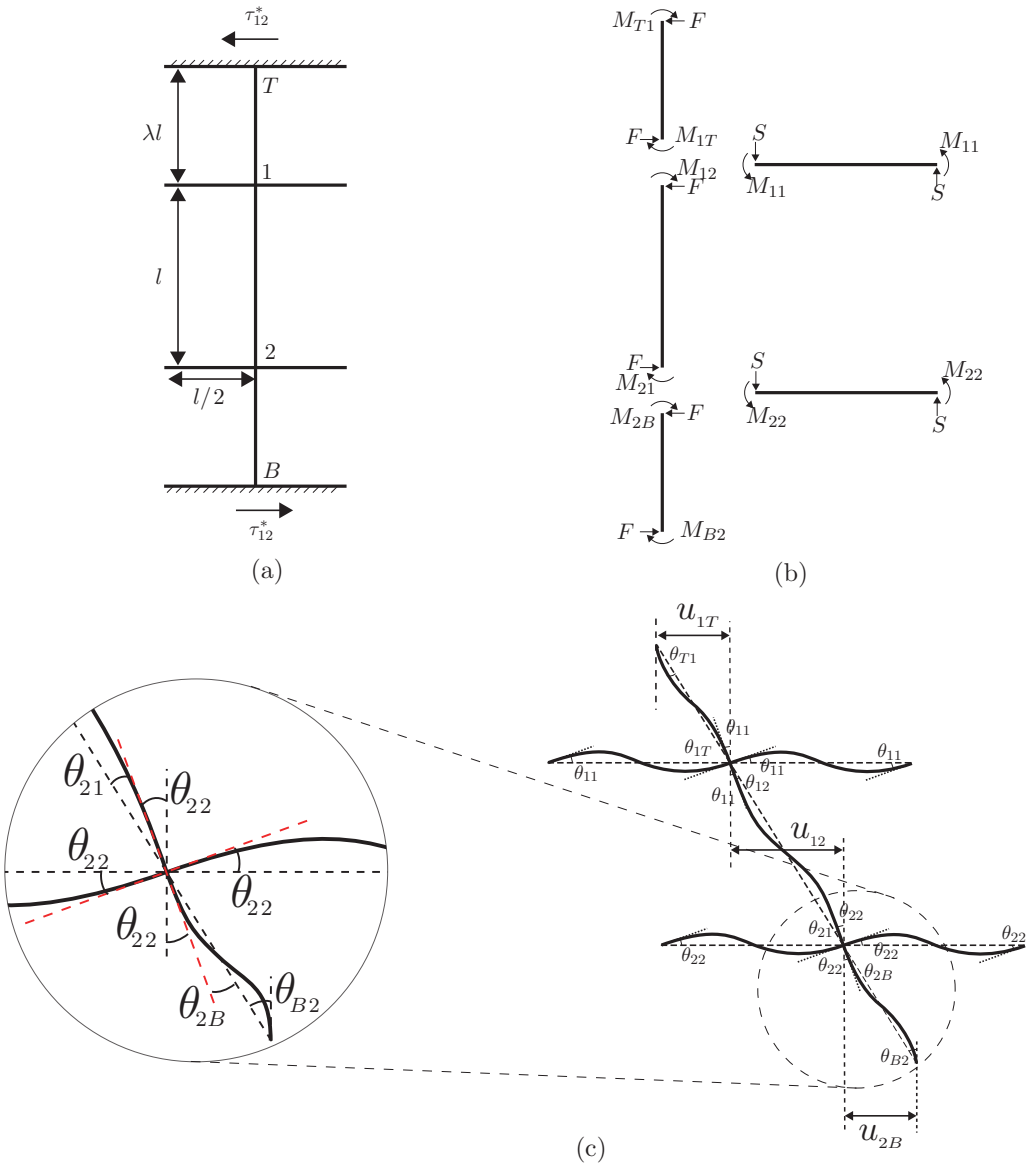

Figure 3.4: Model of an infinitely-wide Square lattice with $\overline{H} = 1$.

sponding to the two joints are numbered, top-down, as 1 and 2, respectively. The moments experienced by the strut $T1$ at nodes T and 1 are denoted by M_{T1} and M_{1T}, respectively; the same notation is also adopted for their corresponding angles shown in Fig 3.4c. To model an infinitely-wide lattice ($\overline{W} \to \infty$), the moments and angles of rotation at the corresponding end of each horizontal strut - of which there are a total of two in the representative model shown in Fig 3.4a - must be identical. Hence, the number of unknowns reduces from four to two in each horizontal strut; for definiteness, the total number of unknowns corresponding to the two horizontal struts are, therefore, M_{11}, θ_{11}, M_{22} and θ_{22}. Assuming joints 1 and 2 are rigid, i.e. the perpendicular con-

nectivity of all members must be preserved even after deformation, this leads to a total of 8 independent degrees of freedom with 8 unknown moments. Moment equilibrium for the three vertical struts gives

$$M_{T1} + M_{1T} = \lambda l F \quad , \tag{3.2}$$

$$M_{B2} + M_{2B} = \lambda l F \quad \text{and} \tag{3.3}$$

$$M_{12} + M_{21} = l F; \tag{3.4}$$

and, the same for the two joints gives

$$M_{1T} + M_{12} - 2M_{11} = 0 \quad \text{and} \tag{3.5}$$

$$M_{2B} + M_{21} - 2M_{22} = 0 \quad . \tag{3.6}$$

Three additional equations are needed which are obtained by considering the rotational compatibility of struts T-1, B-2 and 12 – refer to Fig 3.4c – as follows:

$$\theta_{T1} = \theta_{1T} + \theta_{11} \quad , \tag{3.7}$$

$$\theta_{B2} = \theta_{2B} + \theta_{22} \quad \text{and} \tag{3.8}$$

$$\theta_{12} + \theta_{11} = \theta_{21} + \theta_{22} \quad . \tag{3.9}$$

The unknown rotations in Eqs (3.7)–(3.9) can be expressed as functions of the unknown moments, via their slope-deflection relationships, as follows:

$$\begin{aligned}
\theta_{T1} &= \frac{M_{T1}\lambda l}{3E_sI} - \frac{M_{1T}\lambda l}{6E_sI} & \qquad \theta_{1T} &= \frac{M_{1T}\lambda l}{3E_sI} - \frac{M_{T1}\lambda l}{6E_sI} \\
\theta_{B2} &= \frac{M_{B2}\lambda l}{3E_sI} - \frac{M_{2B}\lambda l}{6E_sI} & \qquad \theta_{2B} &= \frac{M_{2B}\lambda l}{3E_sI} - \frac{M_{B2}\lambda l}{6E_sI} \\
\theta_{11} &= \frac{M_{11} l}{6E_sI} & \qquad \theta_{22} &= \frac{M_{22} l}{6E_sI} \\
\theta_{12} &= \frac{M_{12} l}{3E_sI} - \frac{M_{21} l}{6E_sI} & \qquad \theta_{21} &= \frac{M_{21} l}{3E_sI} - \frac{M_{12} l}{6E_sI} \quad .
\end{aligned} \tag{3.10}$$

where E_sI is the flexural rigidity of the struts and $I(= dt^3/12)$ is the second moment of area. Substituting Eqs (3.10) into Eqs (3.7)–(3.9), and re-arranging, gives

$$3\lambda M_{T1} - 3\lambda M_{1T} - M_{11} = 0 \quad , \tag{3.11}$$

$$3\lambda M_{B2} - 3\lambda M_{2B} - M_{22} = 0 \quad \text{and} \tag{3.12}$$

$$3\lambda M_{12} - 3\lambda M_{21} + M_{11} - M_{22} = 0 \quad . \tag{3.13}$$

The eight independent moment equations, viz. Eqs. (3.2)–(3.6) and (3.11)–(3.13), can be re-cast into a matrix format of $\mathbf{Mm} = \mathbf{F}$ where

$$\mathbf{m} = [M_{T1} \quad M_{1T} \quad M_{B2} \quad M_{2B} \quad M_{12} \quad M_{21} \quad M_{11} \quad M_{22}]^{\mathrm{T}} \tag{3.14}$$

$$\mathbf{F} = [0 \quad 0 \quad \lambda lF \quad \lambda lF \quad lF \quad 0 \quad 0 \quad 0]^{\mathrm{T}} \tag{3.15}$$

and

$$\mathbf{M} = \begin{pmatrix} -3\lambda & 3\lambda & 0 & 0 & 0 & 0 & 1 & 0 \\ 0 & 0 & -3\lambda & 3\lambda & 0 & 0 & 0 & 1 \\ 1 & 1 & 0 & 0 & 0 & 0 & 0 & 0 \\ 0 & 0 & 1 & 1 & 0 & 0 & 0 & 0 \\ 0 & 0 & 0 & 0 & 1 & 1 & 0 & 0 \\ 0 & 1 & 0 & 0 & 1 & 0 & -2 & 0 \\ 0 & 0 & 0 & 1 & 0 & 1 & 0 & -2 \\ 0 & 0 & 0 & 0 & 3 & -3 & 1 & -1 \end{pmatrix} \tag{3.16}$$

Inverting to get $\mathbf{m} = \mathbf{M}^{-1}\mathbf{F}$, one arrives at four unique moments that are re-labelled M_1, M_2, M_3 and M_4 as follows:

$$\begin{aligned} M_1 = M_{T1} = M_{B2} &= \frac{6\lambda^2 + \lambda + 0.5}{c} Fl \quad , \\ M_2 = M_{1T} = M_{2B} &= \frac{6\lambda^2 - 0.5}{c} Fl \quad , \\ M_3 = M_{11} = M_{22} &= \frac{3\lambda^2 + 3\lambda}{c} Fl \quad \text{and} \\ M_4 = M_{12} = M_{21} &= \frac{Fl}{2} \quad . \end{aligned} \tag{3.17}$$

where $c = 12\lambda + 1$. It is no surprise that the eight unknown moments reduces to just four unique pairs; this is due to symmetry about the horizontal mid plane.

According to Fig. 3.4c, the macroscopic shear strain γ_{12}^{*} is given by

$$\gamma_{12}^{*} = \frac{u_{1T} + u_{2B} + u_{12}}{l + 2\lambda l} \tag{3.18}$$

where u_{ij} denotes the relative displacement, along the x_1 direction, between nodes i and j. Assuming small rotations, these relative displacements can be related to the unknown angles through $u_{T1} = \lambda l\theta_{T1}$, $u_{B2} = \lambda l\theta_{B2}$ and $u_{12} = l(\theta_{11} + \theta_{12})$ so that Eq. (3.18) becomes

$$\gamma_{12}^{*} = \frac{\lambda\left(\theta_{T1} + \theta_{B2}\right) + \theta_{12} + \theta_{11}}{1 + 2\lambda}. \tag{3.19}$$

Equation (3.19) can be expressed as a function of F, l and λ by substituting the various angles for the corresponding expressions in Eq. (3.10) and the eight moments of Eq. (3.17).

Given that $\tau_{12}^{*} = F/ld$, and using Eq. (3.19) with $\overline{\rho} = 2t/l$ and $I = dt^3/12$, the effective shear modulus can be obtained as follows:

$$G^{*}\big|_{\overline{H}=1} = \frac{\tau_{12}^{*}}{\gamma_{12}^{*}} = \frac{2(2\lambda+1)(12\lambda+1)}{(24\lambda^4 + 8\lambda^3 + 12\lambda^2 + 18\lambda + 1)}\frac{\overline{\rho}^3 E_s}{16} \tag{3.20}$$

where $\overline{\rho}^3 E_s/16$ corresponds to the bulk shear modulus of an *infinite-sized* Square lattice given by Eq.(1.9), whilst the polynomial fraction adjusts for the effects of λ.

Case B: $\overline{H} = 3$ and 5

The above model can be readily extended to $\overline{H} > 1$; here, corresponding expressions for lattices with $\overline{H} = 3$ and 5 are derived. The representative models for the $\overline{H} = 3$ and 5 infinite-wide lattices are shown in Fig. 3.5. However, the derivations become onerously lengthy when $\overline{H} > 5$ and such cases will only be modelled using finite elements. The node numbering notation for the taller lattices follows exactly as before. Nodes $T, 1, 2, \ldots, n(= \overline{H} + 1), B$ are numbered top-down where T, B corresponds to the nodes at the loading platens, and $1, 2, \ldots, n$ corresponds to the joints where vertical and horizontal struts meet; the numbering for $\overline{H} = 3$ and 5 is shown in Fig. 3.5. For each additional cell in height, three additional unknown moments - one for the

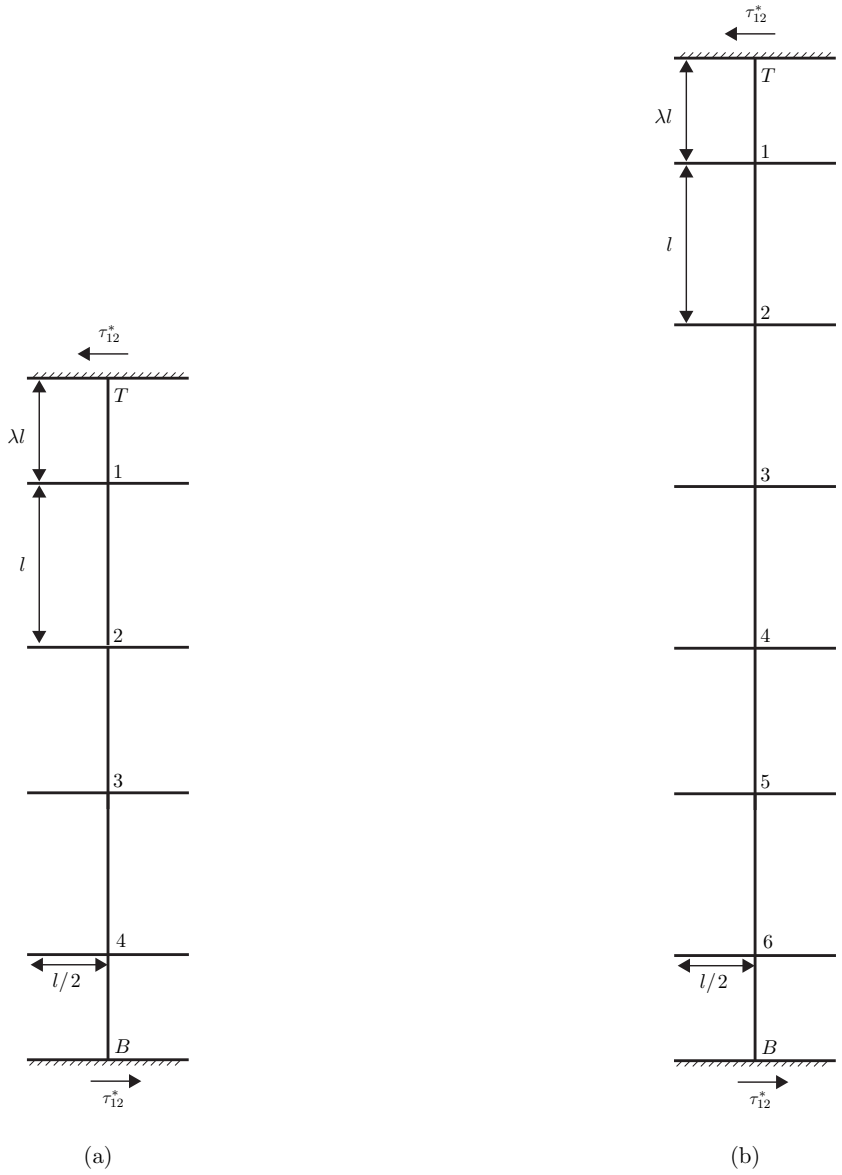

Figure 3.5: Infinitely-wide Square lattice with (a) $\overline{H} = 3$ and (b) $\overline{H} = 5$.

horizontal member and two for the vertical member - are introduced. Consequently, there are 14 and 20 unknown moments for infinitely-wide lattices of $\overline{H} = 3$ and 5, respectively. Their corresponding matrices $\mathbf{m}, \mathbf{M}, \mathbf{F}$ are given in Appendix A, together with the slope-deflection relationships in a matrix format of $\boldsymbol{\theta} = l\boldsymbol{\Theta}\mathbf{m}/(E_s I)$. Also listed are the solutions for the unknown moments and the corresponding expression for shear strain - the equivalent of Eq. (3.19) - for both the $\overline{H} = 3$ and 5 lattices.

In both cases ($\overline{H} = 3$ and 5), the solutions to four of their unknown moments – they listed as M_1, M_2, M_3 and M_4 in Table 3.2 – were found to have a similar functional

form to that of Eq. (3.17), apart from different scalar factors c_1 and c_2, given by

$$\begin{aligned} M_1 &= \frac{6\lambda^2 + c_1\lambda + 0.5c_2}{12\lambda + c_1} Fl \quad , \\ M_2 &= \frac{6\lambda^2 - 0.5c_2}{12\lambda + c_1} Fl \quad , \\ M_3 &= \frac{3c_1\lambda^2 + 3c_2\lambda}{12\lambda + c_1} Fl \quad \text{and} \\ M_4 &= \frac{Fl}{2} \quad . \end{aligned} \tag{3.21}$$

where c_1 and c_2 depends on $\overline{H}$ as listed in Table 3.2. As shown in Eq. (3.17), $c_1 = c_2 = 1$ for an infinitely-wide lattice of $\overline{H} = 1$. The same expressions are also believe to apply to lattices where $\overline{H} > 5$ but with a different set of scalar factors. The three additional moments introduced for a $\overline{H} = 3$ lattice are listed as M_5, M_6, M_7 in Table 3.2. and they have the same functional form as M_5, M_6, M_7 for the $\overline{H} = 5$ lattice; see Appendix A. Likewise, three more, viz. M_8, M_9 and M_{10}, are introduced for the $\overline{H} = 5$ lattice.

	$\overline{H} = 1$	$\overline{H} = 3$	$\overline{H} = 5$
c_1	1	$13/14$	$209/195$
c_2	1	$15/14$	$181/195$
$M_1 \triangleq$	$M_{T1} = M_{B2}$	$M_{T1} = M_{B4}$	$M_{T1} = M_{B6}$
$M_2 \triangleq$	$M_{1T} = M_{2B}$	$M_{1T} = M_{4B}$	$M_{1T} = M_{6B}$
$M_3 \triangleq$	$M_{11} = M_{22}$	$M_{11} = M_{44}$	$M_{11} = M_{66}$
$M_4 \triangleq$	$M_{12} = M_{21}$	$M_{23} = M_{32}$	$M_{34} = M_{43}$
$M_5 \triangleq$	N/A	$M_{12} = M_{43}$	$M_{12} = M_{65}$
$M_6 \triangleq$		$M_{21} = M_{34}$	$M_{21} = M_{56}$
$M_7 \triangleq$		$M_{22} = M_{33}$	$M_{22} = M_{55}$
$M_8 \triangleq$			$M_{23} = M_{54}$
$M_9 \triangleq$		N/A	$M_{32} = M_{54}$
$M_{10} \triangleq$			$M_{33} = M_{44}$

Table 3.2: Moment equivalence between three infinitely-wide lattices of different $\overline{H}$. Note that 'N/A' denotes not-applicable.

Just like the $\overline{H} = 1$ case, the effective shear modulus for each lattice is found by com-

bining their respective shear strain expressions with the appropriate slope-deflection equations and moments - see Appendix A - to give

$$G^*\big|_{\overline{H}=3} = \frac{2(2\lambda+3)(168\lambda+13)}{(336\lambda^4+104\lambda^3+180\lambda^2+918\lambda+63)}\frac{\overline{\rho}^3 E_s}{16} \tag{3.22}$$

$$G^*\big|_{\overline{H}=5} = \frac{2(2\lambda+5)(2340\lambda+181)}{(4680\lambda^4+1448\lambda^3+2508\lambda^2+22146\lambda+1601)}\frac{\overline{\rho}^3 E_s}{16} \tag{3.23}$$

where, as before, the bulk shear modulus are adjusted for the effects of λ through the corresponding polynomial fraction.

3.3.2.b Infinitely-wide lattices ($\overline{W} \to \infty$) – Discussion

Figure 3.6 plots the normalised moments M/Fl in each strut as a function of λ for infinitely-wide lattices with $\overline{H} = 1, 3$ and 5. The bending moment in the strut at the mid-height of the lattice (M_4 in Table 3.2 for all three lattices) is independent of λ and is typically higher than M_1, M_2, M_3; only as $\lambda \to 1$ does $M_1 > M_4$. This is true for all lattices containing $\overline{H} = 1, 3$ and 5 cells since the scalar parameters c_1, c_2 are close to unity and their influence on moments are relatively minor. For lattices with $\overline{H} > 1$

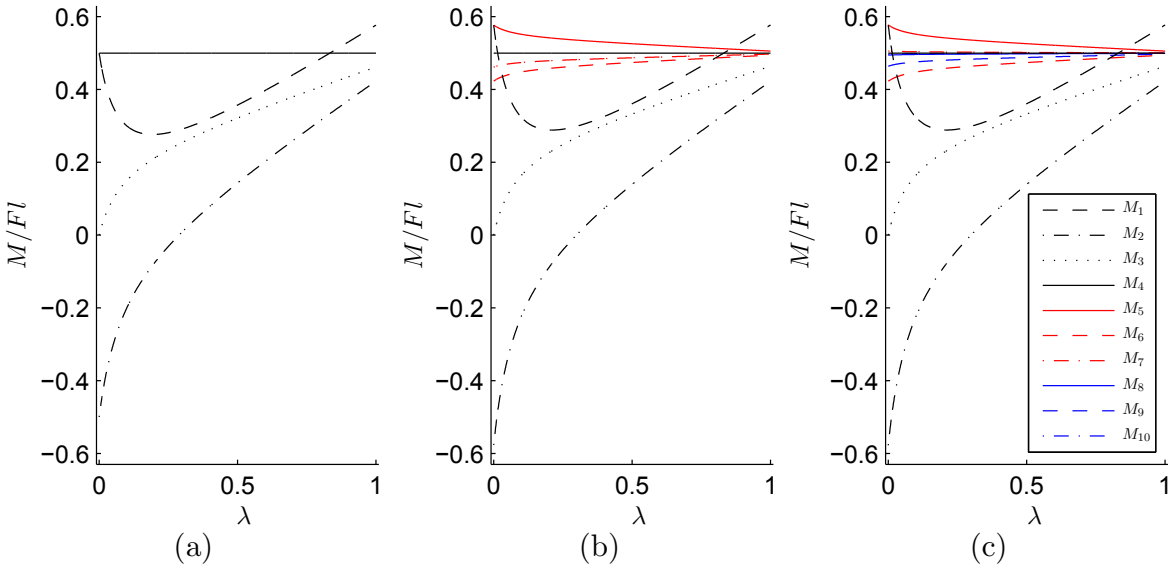

Figure 3.6: Variations of normalised moment M/Fl in each strut as a function of λ for infinitely-wide lattices with $\overline{H}$ = (a) 1 (b) 3 and (c) 5. Moments are labelled as per Table 3.2

cells, the additional moments introduced have magnitude very close to M_4 for the entire range of λ.

M_1, M_2, M_3 are associated with the incomplete cells at the rigid surfaces for all three lattices. The lower magnitude of M_1, M_2, M_3, compared to the other moments, indicates that the *incomplete* cells at the boundaries are stiffer compared to the complete cells in the bulk of the lattice; i.e. the incomplete cells at the boundary form a *stiff horizontal boundary layer*. As λ increases, the differences between M_1, M_2, M_3 and the other moments reduces, hence the stiffening effect of the boundary layer vanishes. The similar values obtained for all other moments - $M_4, M_5, \ldots, M_{10}$ - indicate that the *complete* cells away from the boundaries have similar 'local' stiffness regardless of $\overline{H}$.

Figure 3.7a compares the predictions by Eqs. (3.20), (3.22) and (3.23) to their FE counterparts where they show a perfect match. For the same reason given in Section 3.3.1, the effective modulus predicted by FE had been corrected for area using Eq. (3.1). Note that lattices of $\overline{W} = 101$ were modelled since convergence studies have established this to be sufficient to simulate the response of infinitely-wide lattices. Figure 3.7a shows varying extent of enhancement for the effective shear modulus; this is most pronounced in lattices where the number of row(s) of complete bulk cells $\overline{H}$ are small

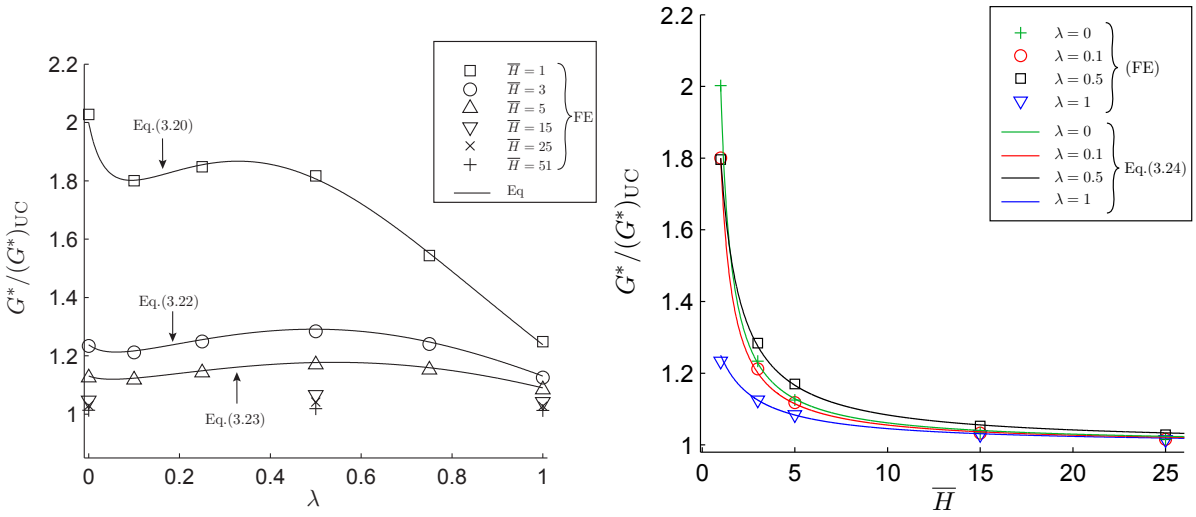

(a) (b)

Figure 3.7: Variation of the normalised effective shear modulus $G^*/(G^*)_{\mathrm{UC}}$ with λ and $\overline{H}$ for infinitely-wide Square lattices.

and/or if the boundary cells, attached to T and B, have a low λ value. As $\overline{H}$ increases, the enhancement diminishes dramatically. The trend of the data plotted in Fig. 3.7a are broadly similar for all $\overline{H}$: a 'down-up-down' response as λ increases. For larger $\overline{H}$, viz. 15, 25 and 51, their effective moduli are close to its corresponding bulk values and they are relatively insensitive to λ.

Figure 3.7b plots the variation of $G^*/(G^*)_{UC}$ against $\overline{H}$ for $\lambda = 0, 0.1, 0.5$ and 1. In all cases, $G^*/(G^*)_{UC}$ diminishes rapidly with $\overline{H}$. The enhancement of the effective modulus is caused by the stiff *horizontal boundary layers* next to T and B surfaces. The additional rows of complete cells diminish the stiffening effect of the boundary layer since, as it was indicated above, they have lower local stiffness compared to the incomplete boundary cells. A value within 5% of $(G^*)_{\text{UC}}$ is reached for lattices that have $\overline{H} > 15$. This asymptotic reduction in the effective shear modulus with $\overline{H}$ may be described using a scaling law of the following form:

$$\left.\frac{G^*}{(G^*)_{\text{UC}}}\right|_{\overline{W}\to\infty} = 1 + \frac{d_1}{\overline{H} + d_2} \tag{3.24}$$

where constants d_1 and d_2 – these are listed in Table 3.3 – are calibrated to the FE predictions.

Figure 3.8 plots the shear strength estimated by FE as a function of lattice height for a $\overline{W} = 101$ wide lattice. Similar to the shear modulus, the shear strength exhibits a strengthening effect for lattices with small $\overline{H}$, a result due to the presence of stiff horizontal boundary layer. Unlike Fig. 3.7b, however, the 'bulk' shear yield strength value from unit-cell method is not approached asymptotically. For a sufficiently large lattice, it was found that $\tau_y^*/(\tau_y^*)_{\text{UC}} \approx 0.8$. An equivalent scaling law, similar to Eq. (3.24), is obtained for the shear yield strength as follows

	$\lambda = 0$	$\lambda = 0.1$	$\lambda = 0.5$	$\lambda = 1$
d_1	0.59	0.54	0.84	0.5
d_2	-0.41	-0.33	0.05	1
d_{y_1}	0.024	0.07	0.15	0.03
d_{y_2}	-0.65	-0.33	0.05	2

Table 3.3: Values of fitted parameters d_1, d_2 in Eq. (3.24) and d_{y_1}, d_{y_2} for Eq. (3.25).

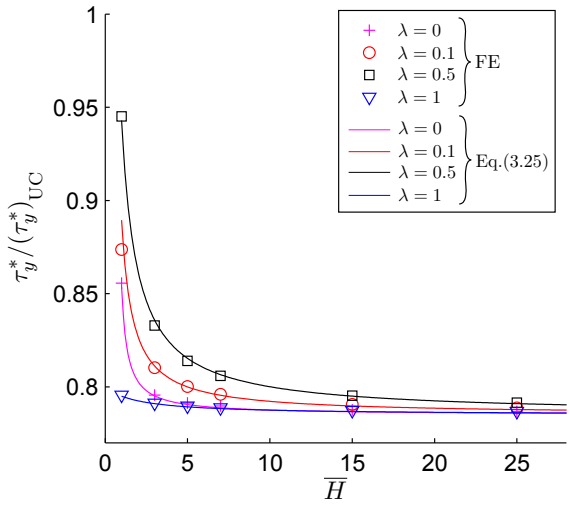

Figure 3.8: Variations of effective normalised shear strength, $\tau_y^*/(\tau_y^*)_{\mathrm{UC}}$ with $\overline{H}$ of a Square lattices with $\overline{W} = 101$.

$$\left.\frac{\tau_y^*}{(\tau_y^*)_{\mathrm{UC}}}\right|_{\overline{W}\to\infty} = 0.785 + \frac{d_{y_1}}{\overline{H} + d_{y_2}} \tag{3.25}$$

where the calibrated constants d_{y_1} and d_{y_2} are listed in Table 3.3. Equations (3.24) and (3.25) are to be used later on in Section 3.3.2.d to develop an expression for the effective properties of a Square lattice of any size.

3.3.2.c Single-cell wide model ($\overline{W} = 1$)

Given a lattice of finite $\overline{W}$, its stress-free lateral boundaries (L and R) gives rise to a more compliant effective response compared to its infinitely-wide counterpart of the same $\overline{H}$ and $\overline{\rho}$. This is due to the absence of moment in the horizontal struts next to the lateral boundaries. The model for the infinitely-wide lattice is now modified to include a single column of complete cells, i.e. $\overline{W} = 1$. First, the smallest Square lattice possible is studied, $\overline{W} = \overline{H} = 1$ (shown in Figure 3.9a), followed by the $\overline{W} = 1, \overline{H} = 3$ lattice. This is to compare the stiffness of cells along the lateral L, R boundaries with the corresponding stiffness of the cells at the bulk of lattice, modelled by the infinite-wide model presented in Section 3.3.2.a. The notation used to label the nodes are the same as in Section 3.3.2.a, apart from an additional subscript introduced to distinguish the different columns; note that the model has two columns of vertical struts, as opposed to one previously.

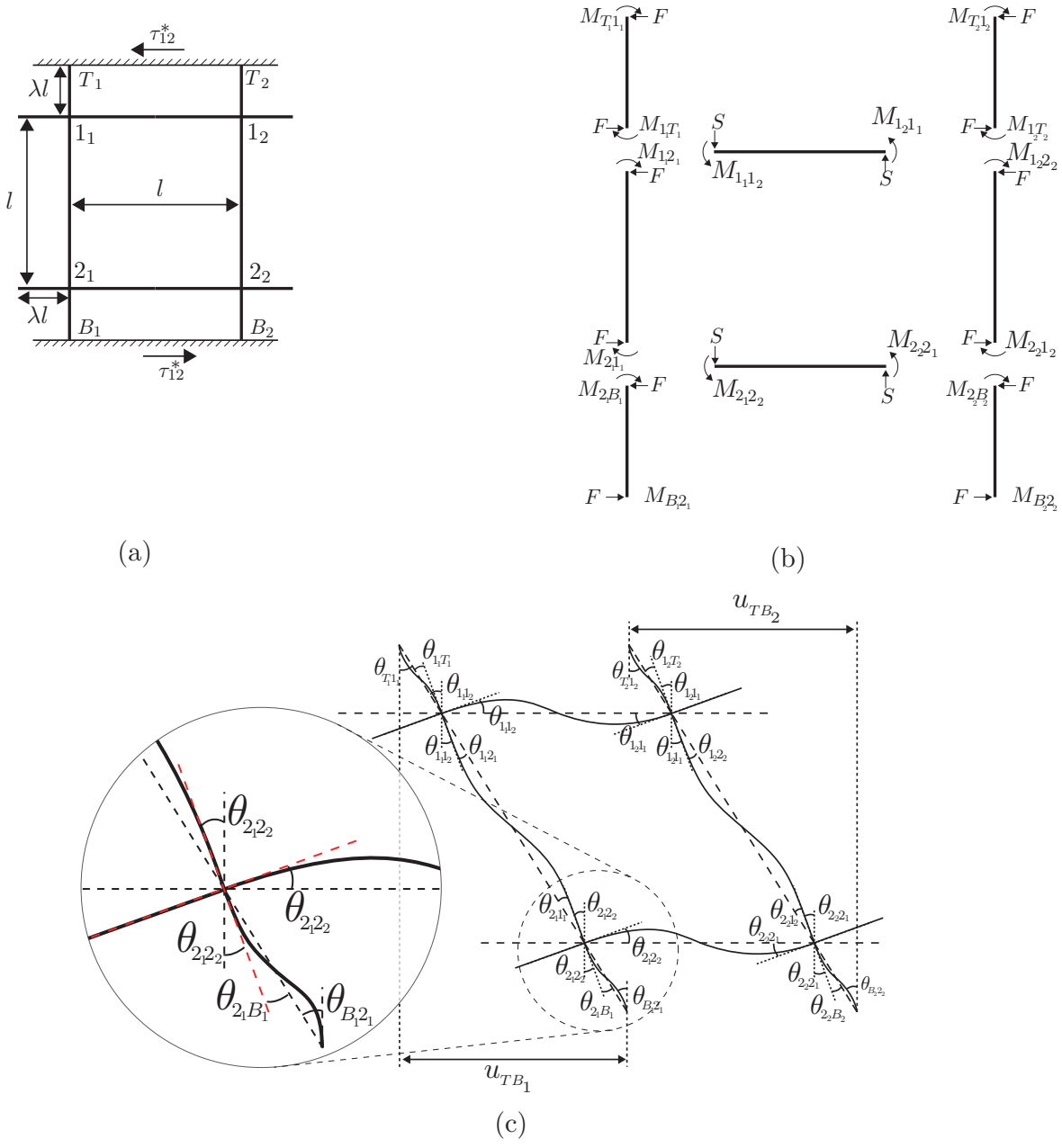

Figure 3.9: Model of a Square lattice with $\overline{W} = \overline{H} = 1$

There are twice as many unknown moments in the model as its infinitely-wide counterpart. Additionally, the shear forces S in the horizontal struts are, too, an unknown; see Fig 3.4b. However, symmetry along the horizontal mid-plane dictates that S is identical in both the horizontal members. Hence, a Square lattice with $\overline{W} = \overline{H} = 1$, as shown in Fig 3.9b, has a total of 17 unknowns. The equations needed to solve for them are derived from the moment balance of each strut (8 in total) and the moment balance at each joint (4 in total). Five additional equations are needed and they come

from rotational compatibility of the struts $T_1 1_1$, $B_1 2_1$,$1_1 2_1$ and $1_1 1_2$ given by

$$\theta_{T_1 1_1} = \theta_{1_1 T_1} + \theta_{1_1 2_1} \quad , \tag{3.26}$$

$$\theta_{B_1 2_1} = \theta_{2_1 B_1} + \theta_{2_1 2_2} \quad , \tag{3.27}$$

$$\theta_{1_1 1_2} + \theta_{1_1 2_1} = \theta_{2_1 2_2} + \theta_{2_1 1_1} \quad \text{and} \tag{3.28}$$

$$\theta_{1_1 1_2} = \theta_{1_2 1_1} \tag{3.29}$$

and by enforcing

$$u_{TB_1} = u_{TB_2} \tag{3.30}$$

where u_{TB_1} and u_{TB_2} are the relative displacements of nodes T and B along the x_1 direction of the first and second column of struts, respectively, as shown in Fig 3.9c. Equation (3.30) ensures that the shear strain is uniform across the surfaces T and B. Assuming small rotations, u_{TB_1} and u_{TB_2} are related to the rotations as follows:

$$u_{TB_1} = (\lambda\theta_{T_1 1_1} + \lambda\theta_{B_1 2_1} + \theta_{1_1 2_1} + \theta_{1_1 1_2})\, l \quad \text{and} \tag{3.31}$$

$$u_{TB_2} = (\lambda\theta_{T_2 1_2} + \lambda\theta_{B_2 2_2} + \theta_{1_2 2_2} + \theta_{1_2 1_1})\, l \quad . \tag{3.32}$$

Similar to Section 3.3.2.a, Eqs. (3.26)–(3.30) can be expressed as functions of the unknown moments, using the appropriate slope-deflection relationship of each strut, to give the following:

$$\begin{aligned}
3\lambda M_{T_1 1_1} - 3\lambda M_{1_1 T_1} - 2M_{1_1 2_1} + M_{2_1 1_1} &= 0 \quad , \\
3\lambda M_{B_1 2_1} - 3\lambda M_{2_1 B_1} - 2M_{2_1 2_2} + M_{2_2 2_1} &= 0 \quad , \\
3M_{1_1 2_1} - 3M_{2_1 1_1} + 2M_{1_1 1_2} - 2M_{2_1 2_2} + M_{2_2 2_1} - M_{1_2 1_1} &= 0 \quad , \\
3M_{1_1 1_2} - 3M_{1_2 1_1} &= 0 \quad \text{and} \\
2\lambda M_{T_1 1_1} - 2\lambda M_{T_2 1_2} + 2\lambda M_{B_1 2_1} - 2\lambda M_{B_2 2_2} - & \\
\lambda M_{1_1 T_1} + \lambda M_{1_2 T_2} - \lambda M_{2_1 B_1} + \lambda M_{2_2 B_2} + & \\
3M_{1_1 1_2} + 2M_{1_1 2_1} + M_{2_2 1_2} - 3M_{1_2 1_1} - 2M_{1_2 2_2} - M_{2_1 1_1} &= 0 \quad .
\end{aligned} \tag{3.33}$$

Solving for the unknown moments and shear stress S gives

$$\begin{aligned} M_{T_1 1_1} = M_{T_2 1_2} = M_{B_1 2_1} = M_{B_2 2_2} &= \frac{6\lambda^2 + 2\lambda + 1}{12\lambda + 2} Fl \quad , \\ M_{1_1 T_1} = M_{1_2 T_2} = M_{2_1 B_1} = M_{2_2 B_2} &= \frac{6\lambda^2 - 1}{12\lambda + 2} Fl \quad , \\ M_{1_1 1_2} = M_{1_2 1_1} = M_{2_1 2_2} = M_{2_2 2_1} &= \frac{3\lambda^2 + 3\lambda}{6\lambda + 1} Fl \quad , \\ M_{1_1 2_1} = M_{1_2 2_2} = M_{2_1 1_1} = M_{2_2 1_2} &= \frac{Fl}{2} \quad \text{and} \\ S &= -\frac{6\lambda(\lambda + 1)}{6\lambda + 1} F \quad . \end{aligned} \tag{3.34}$$

Notice that the moments in Eq. (3.34) have a similar functional form as Eq. (3.21), but with $c_1 = c_2 = 2$ instead of $c_1 = c_2 = 1$. The moments here appear in sets of four since there are two mid planes of symmetry – horizontal and vertical. Following the same procedure as an infinitely-wide model, the shear modulus for a lattice of $\overline{H} = \overline{W} = 1$ is found as follows:

$$G^*\big|_{\overline{H}=1} = \frac{2\,(2\lambda + 3)\,(48\lambda + 7)}{(96\lambda^4 + 56\lambda^3 + 108\lambda^2 + 378\lambda + 45)} \frac{\overline{\rho}^3 E_s}{16} \tag{3.35}$$

If the above model, for a $\overline{W} = \overline{H} = 1$ lattice, is extended to one with $\overline{W} = 1$ and $\overline{H} = 3$, then two additional unknown shear forces are introduced. This leads to a total of 30 unknowns and the shear modulus of a lattice with $\overline{H} = 3$ and $\overline{W} = 1$ is found to be

$$G^*\big|_{\overline{H}=3} = \frac{2\,(2\lambda + 1)\,(6\lambda + 1)}{(12\lambda^4 + 8\lambda^3 + 12\lambda^2 + 12\lambda + 1)} \frac{\overline{\rho}^3 E_s}{16} \tag{3.36}$$

The analytical derivation for the effective shear modulus for $\overline{H} = 5$ lattice involves 43 unknown and is rather cumbersome and it is not repeated here; its shear modulus is expected to have the same form as Eqs.(3.35) and (3.36) but with a different polynomial fraction. Compared to an infinitely-wide lattice of the same $\overline{H}$, its single-cell wide counterpart ($\overline{W} = 1$) is found to have significantly lower shear modulus. This is a direct consequence of the lower moments experienced by their constituent struts because of the reduced constraint from the lateral boundaries L and R. The results from the analytical Eqs.(3.35) and (3.36) will be discussed in detail in Section 3.3.2.e.

3.3.2.d Finite-sized lattices – Modelling

The analytical models developed in Sections 3.3.2.a and 3.3.2.c show that the vertical struts in the bulk of a *finite-sized* lattice are considerably stiffer compared to the first vertical struts near its L and R boundaries. Thus, the cells at the L and R boundaries form a boundary layer to account for the uniform stiffness since the applied shear strain is uniform along the T and B surfaces. By studying the cell deformation and the stress distribution within the struts as predicted by FE, it is observed that a transition zone (or shear-lag zone) does not and thus the boundary layer shows a sharp demarcation and extends for only one cell; this is shown schematically in Fig. 3.10; note that for the reasons given in Sections 3.3.1 and 3.3.2.a, the stressed surfaces are area corrected for $\lambda = 0.5$.

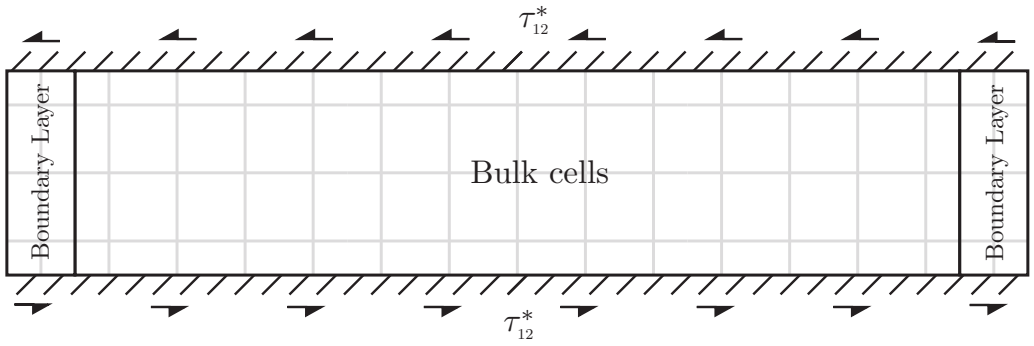

Figure 3.10: Schematic of a Square lattice under shear and the boundary layers that span one cell in width.

Hence, the shear modulus of these *finite-sized* Sqaure lattices may be derived using a 'Mechanics of materials' approach, in a manner analogous to estimating the stiffness of a composite material, comprising of two phases. Let the composite be composed of two distinct phases each with a different elastic modulus E_i and area fraction A_i/A, where $i = 1, 2$ and $A = A_1 + A_2$ is total area of both phases. If the same strain is applied to both phases of the composite, then the sections normal to the loading direction, which were plane before, remains plane after loading. This condition allows the effective modulus of the composite to be estimated by a 'rule-of-mixtures' as follows (Jones, 1999):

$$E = E_1 \frac{A_1}{A} + E_2 \frac{A_2}{A}. \tag{3.37}$$

Equation (3.37) is equivalent to a 'springs-in-parallel' model, where the load is distributed according to each spring stiffness. In the case of a Square lattice under shear, the rule-of-mixtures is applicable since the aforesaid condition is valid, i.e. the shear strain is applied uniformly across the width of the lattice and any section normal to x_2 remains plane for small displacements.

The two constituent phases of a *finite-sized* Square lattice, see schematic in Fig 3.10, are as follows:

1. *bulk cells* with a 'local' modulus of G^*_{blk}, given by the modulus for infinite-wide lattices from Sections 3.3.2.a. For lattices with $\overline{H} > 5$ - for which analytical solutions were not derived - FE models with $\overline{W} = 101$ are used to determine G^*_{blk} ; and,

2. *vertical boundary layers* – of 'local' modulus G^*_{bdy} – emanating from the two stress-free lateral boundaries (L and R), with each extending one cell in width into the bulk. G^*_{bdy} is given by the shear modulus for $\overline{W} = 1$ lattices from Sections 3.3.2.c.

Since all the lattices modelled are of unit depth, the area fractions are also length fractions. For *finite-sized* Square lattices, the area fraction of the bulk cells is $A_1/A = (\overline{W} - 1)l/W$ and $A_2/A = 2l/W$ for the boundary layers; again note that the loading surface area is corrected for $\lambda = 0.5$ using Eq. (3.1), hence λ does not appear in these expressions. Hence, Eq. (3.37) can be written as

$$G^*\left(\overline{W}, \overline{H}, \lambda\right) = \frac{\left(\overline{W} - 1\right) G^*_{\text{blk}} + 2 r_G G^*_{\text{blk}}}{\overline{W} + 1} \tag{3.38}$$

where $r_G(\lambda) \triangleq G^*_{\text{bdy}}(\lambda)/G^*_{\text{blk}}(\lambda)$ is a measure of the loss of stiffness at the boundary layers; this parameter is reminiscent of the ratio of the fibre to matrix stiffness in a composite material. The stiffness of the bulk (G^*_{blk}) and boundary layer (G^*_{bdy}) cells were derived in Sections 3.3.2.a and 3.3.2.c, respectively, for lattices with $\overline{H} = 1$ and 3 cells. These allow $r_G(\lambda)$ to be obtained analytically, as follows:

$$r_G(\lambda)\big|_{\overline{H}=1} = \frac{(48\lambda+7)\,(2688\lambda^4+832\lambda^3+1440\lambda^2+7344\lambda+504)}{8\,(168\lambda+13)\,(96\lambda^4+56\lambda^3+108\lambda^2+378\lambda+45)} \quad \text{and} \tag{3.39}$$

$$r_G(\lambda)\big|_{\overline{H}=3} = \frac{(6\lambda+1)\,(24\lambda^4+8\lambda^3+12\lambda^2+18\lambda+1)}{(12\lambda+1)\,(12\lambda^4+24\lambda^3+12\lambda^2+12\lambda+1)} \quad . \tag{3.40}$$

Recall that closed-form expressions for shear modulus were not derived for $\overline{H} \geq 5$; for such cases, $r_G(\lambda)$ is estimated using FE at selected λ values and these are plotted in Fig 3.13a.

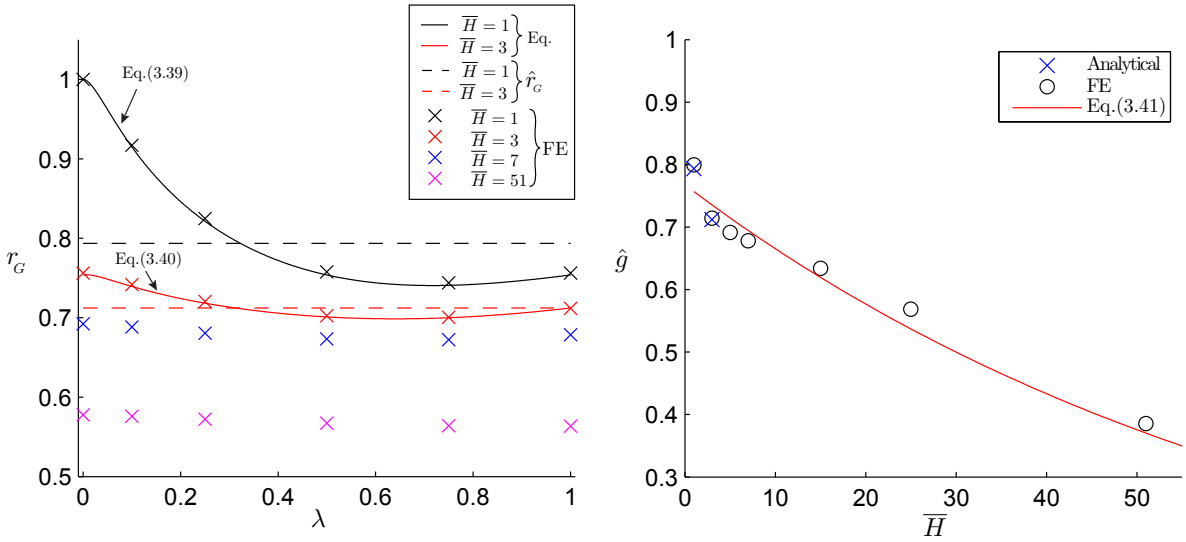

(a) (b)

Figure 3.11: (a) Variation of r_G with λ for different $\overline{H}$; (b) Variation of $\hat{r}_G$ with $\overline{H}$.

Equations (3.39) and (3.40) are plotted in Fig 3.11a where they show a near perfect agreement with predictions by FE. Their close agreement provides further confirmation that no transition zone develops between the boundary layers and the bulk cells. The results in Fig 3.11a shows that $r_G(\lambda)$ is nearly insensitive to λ at higher $\overline{H}$. This suggests that beyond, say, $\overline{H} \geq 7$, it is reasonable to approximate $r_G(\lambda)$ as a constant value, viz. $r_G(\lambda) = \hat{r}_G$, without loss of accuracy. In the cases of $\overline{H} = 1$ and 3, where there are significant variations of r_G with λ, a constant $\hat{r}_G$ could still be defined by using a technique known as the 'equal-area rule' - see Appendix B. The estimated $\hat{r}_G$ values for $\overline{H} = 1$ and 3 are plotted in Fig 3.11a as dashed horizontal lines. Error is

introduced as a consequence of this approximation; the root-mean-square (rms) error is 0.022 and 0.090 for $\overline{H} = 3$ and $\overline{H} = 1$, respectively. Beyond $\overline{H} \geq 7$, the rms error is negligibly small.

Figure 3.11b shows that $\hat{r}_G$ decreases monotonically with $\overline{H}$ for the range of $\overline{H}$ investigated. By neglecting the special case of $\overline{H} = 1$, $\hat{r}_G$ can be fitted to a scaling law of the form

$$\hat{r}_G = \mathrm{e}^{-(0.0143\overline{H}+0.2644)} \quad , \quad \overline{W} > 1; \tag{3.41}$$

this has been plotted, for comparison, in Fig 3.11b.

Equation (3.38) can be extended to account for any $\overline{H}$, by approximating $r_G(\lambda)$ with Eq. (3.41) and G^*_{blk} with Eq. (3.24) to obtain

$$\frac{G^*}{(G^*)_{\text{UC}}}(\overline{W}, \overline{H}) = \frac{\overline{W} - 1 + 2\mathrm{e}^{-(0.0143\overline{H}+0.2644)}}{\overline{W} + 1} \left(1 + \frac{d_1}{\overline{H} + d_2}\right) \tag{3.42}$$

where the parameters d_1, d_2 are listed in Table 3.3 for different λ values. However, as $\overline{H}$ increases the impact of d_1, d_2 on Eq. (3.42) becomes less important as lines for various λ merge together as shown in Fig. 3.7b.

Equation (3.38) is rewritten to account for shear yield strength rather than modulus as follows:

$$\tau_y^*\left(\overline{W}, \overline{H}, \lambda\right) = \frac{\left(\overline{W} - 1\right)(\tau_y^*)_{\text{blk}} + 2r_\tau(\tau_y^*)_{\text{blk}}}{\overline{W} + 1} \tag{3.43}$$

where $(\tau_y^*)_{\text{blk}}$ is the yield strength of an infinitely-wide lattice and r_τ is an equivalent parameter to r_G; r_τ is calculated as the ratio of shear strength of a $\overline{W} = 1$ lattice to that of a $\overline{W} = 101$ lattice. Figure 3.12a plots r_τ for selected values of λ and $\overline{H}$ from FE results. Just like r_G, r_τ is almost insensitive to λ for high $\overline{H}$ and can be approximated with a constant value, viz $\hat{r}_\tau$. Figure 3.12b shows that $\hat{r}_\tau$ monotonically decreases with $\overline{H}$ which can be described using

$$\hat{r}_\tau = 0.54 + \frac{1}{5\overline{H} - 2.5} \quad . \tag{3.44}$$

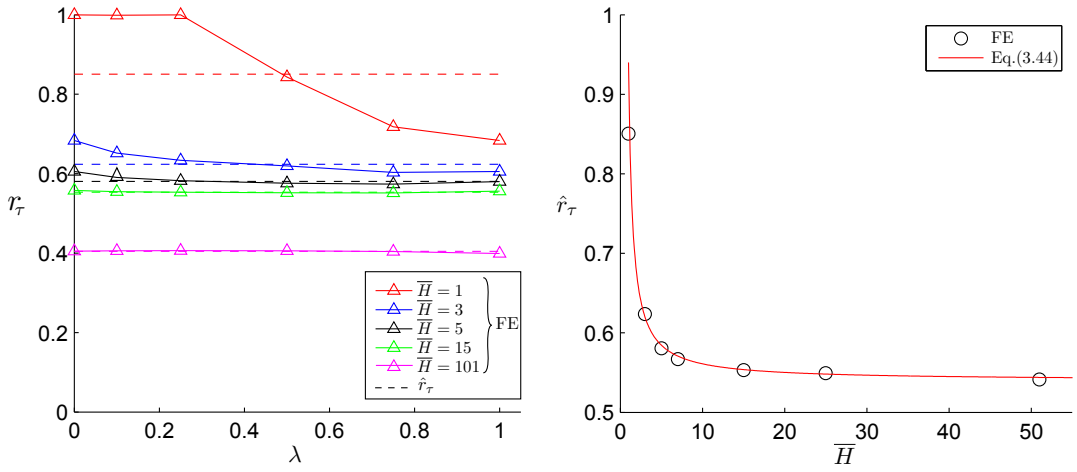

(a) (b)

Figure 3.12: (a) Variation of r_τ with λ for different $\overline{H}$; (b) Variation of $\hat{r}_\tau$ with $\overline{H}$.

To obtain a similar expression to Eq. (3.42) for shear strength, r_τ and $(\tau_y^*)_{\text{blk}}$ are replaced in Eq.(3.43) with Eqs.(3.44) and (3.25), respectively, to obtain:

$$\frac{\tau_y^*}{(\tau_y^*)_{\text{UC}}}(\overline{W},\overline{H}) = \frac{\overline{W}-1+2\hat{r}_\tau}{\overline{W}+1}\left(0.785+\frac{d_{y_1}}{\overline{H}+d_{y_2}}\right) \tag{3.45}$$

where the parameters d_{y_1} and d_{y_2} are listed Table 3.3.

3.3.2.e Finite-sized lattices – Discussion

Figure 3.13 plots the effective shear modulus against λ for $\overline{H} = 1$ and 3 and various $\overline{W}$; the FE and analytical predictions are in excellent agreement. The analytical predictions for $\overline{W} = 1$ are from the single-cell wide model - Eqs.(3.35) and (3.36) - whilst the rest are Eq.(3.38). Additionally, predictions by Eqs.(3.20) and (3.22) for the infinite-wide lattices are also shown. The effects of the weak lateral boundary layer is clearly evident here. In both Figs. 3.13a and b, the effective modulus for $\overline{W} = 1$ lattices is significantly lower compared to the infinite-wide lattices for all λ; the only exception is for $\overline{H} = 1$ and $\lambda = 0$. With increasing $\overline{W}$, the influence of the weak lateral boundary layers is observed to diminish and for very wide specimens, say $\overline{W} = 101$, the effective modulus of an infinite-wide lattice is approached; this validates the use of $\overline{W} = 101$ FE models as an approximation for infinite-wide lattices in Section 3.3.2.d. By comparing the curves for a $\overline{H} = 1$ lattice to the corresponding for $\overline{H} = 3$ lattices of same $\overline{W}$, it is

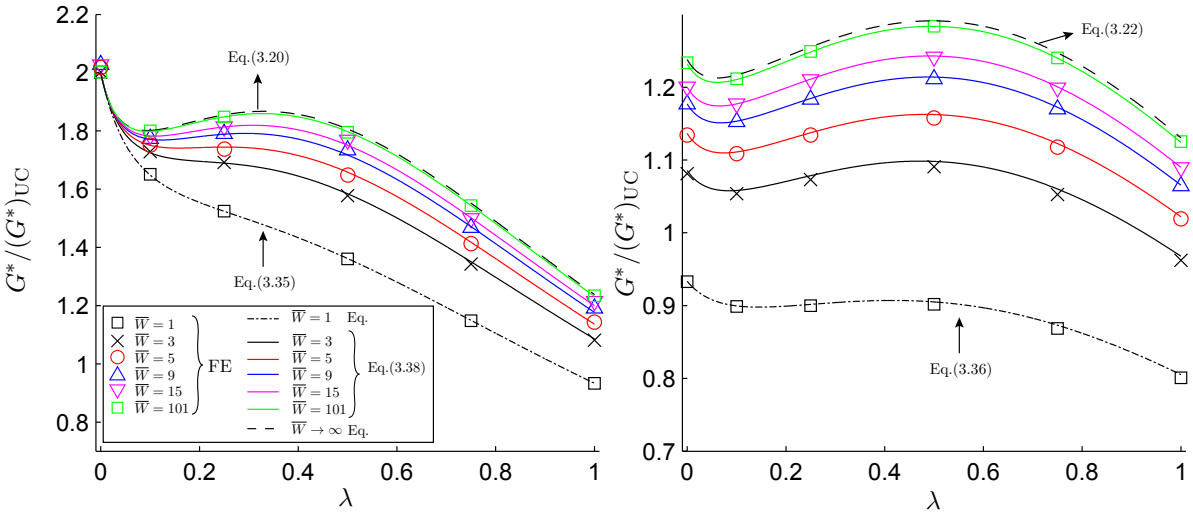

(a) (b)

Figure 3.13: Variations of the normalised effective shear modulus $G^*/(G^*)_{\rm UC}$ with λ for Square lattices with (a) $\overline{H}=1$ and (b) $\overline{H}=3$. Results from the analytical and FE models are plotted for comparison.

clear that the stiffening effect due to the stiff horizontal boundary layer diminishes as $\overline{H}$ increases; note the difference in vertical axis scale; this is the regardless of $\overline{W}$.

Figure 3.14a and b shows the variation of $G^*/(G^*)_{\rm UC}$ against $\overline{W}$, for lattices with $\overline{H}=1$ and with $\overline{H}=3$ and 25, respectively; Eqs.(3.38) is shown for $\overline{H}=1$ and 3 and Eq.(3.42) for $\overline{H}=25$: both are in good agreement with the FE predictions. The effective modulus is found to reduce significantly when $\overline{W}$ is low because of weak lateral boundary layers. As $\overline{W}$ increases, a converged $G^*/(G^*)_{\rm UC}$, depending on $\overline{H}$ and λ, is reached. For higher $\overline{H}$, the closer the converged $G^*/(G^*)_{\rm UC}$ value is to unity because of the diminishing effect of the horizontal boundary layer. The reduced importance of the horizontal boundary layers also means that the choice of λ becomes negligible for high $\overline{H}$, see for example $\overline{H}=25$.

Figure 3.15 plots effective shear yield strength $\tau_y^*/(\tau_y^*)_{\rm UC}$ against $\overline{W}$. Predictions by FE are compared to Eq. (3.45) for $\overline{H}=3$ and 25 and three λ values; for $\overline{H}=25$ only $\lambda=0.5$ is presented since the three curves are indistinguishable. The good agreement justifies the use of the rule-of-mixtures to model the yield strength. Similarly with the shear modulus, the effect of the lateral weak boundary layers is greatest for low $\overline{W}$,

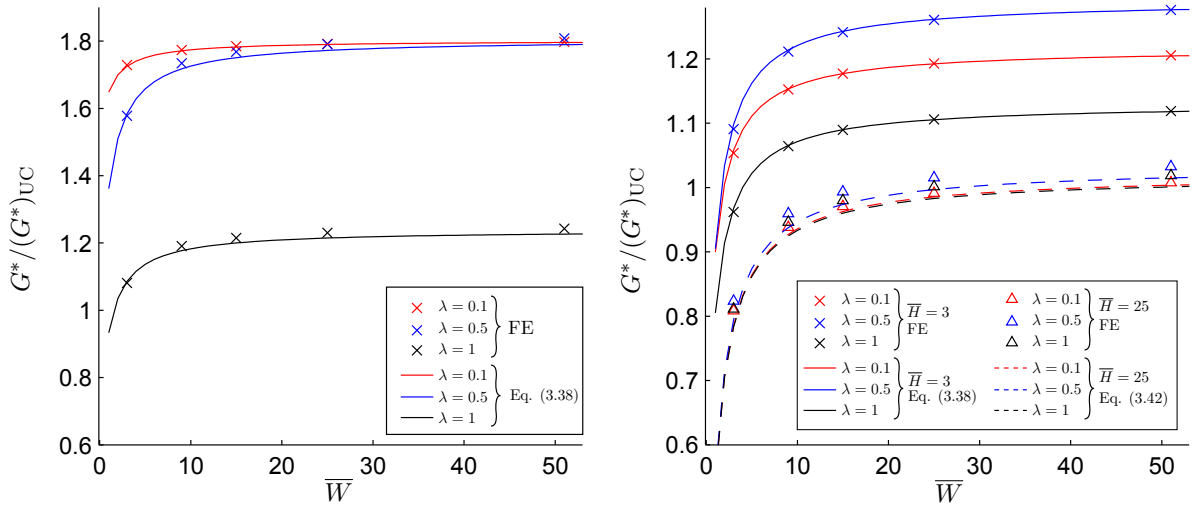

(a) (b)

Figure 3.14: Variation of $G^*/(G^*)_{\mathrm{UC}}$ of a Square lattice with $\overline{W}$ for (a) $\overline{H} = 1$ and (b) $\overline{H} = 3$ and 25. Three values of λ are presented.

and the knock-down on the yield strength is significant. As $\overline{W}$ increases, the effective strength increases and reaches a converged value that depends on $\overline{H}$ and λ. The lower the $\overline{H}$, the lower the converged value of shear strength, because of the diminishing effect from the strong horizontal boundary layer; this is also evident from Fig. 3.12.

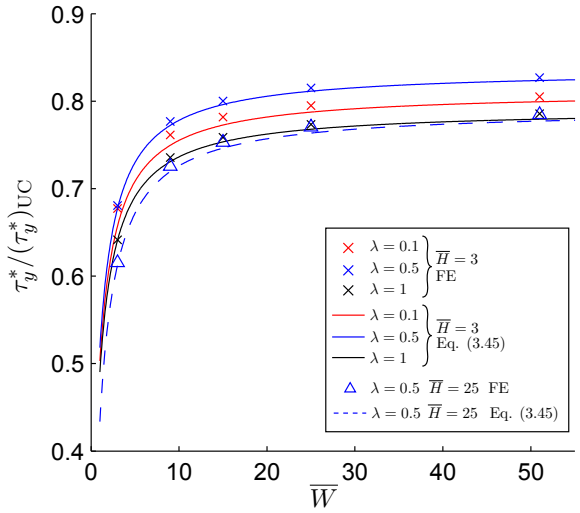

Figure 3.15: Variation of $\tau_y^*/(\tau_y^*)_{\mathrm{UC}}$ of a Square lattice with $\overline{W}$ for $\overline{H} = 3$ and 25. Three values of λ are presented for $\overline{H} = 3$.

3.4 Kagome lattice

3.4.1 Uniaxial loading

Unlike the Square lattice, the micro-architecture of a Kagome lattice does not lend itself amenable to analytical treatment; thus, edge effects in Kagome lattices will be investigated numerically using finite elements. FE models of Kagome lattices with different sizes ($\overline{W}$ and $\overline{H}$) and relative densities ($\overline{\rho}$) were generated and the loading applied as outlined in Section 3.2.2. The FE predictions are presented first.

3.4.1.a Effective Modulus and Yield Strength

Figure 3.16 plots the normalised effective modulus $E^*/(E^*)_{\text{UC}}$ against $\overline{W}$ for three $\overline{\rho}$ values. When $\overline{W}$ is small, there is a significant reduction in its effective modulus $E^*/(E^*)_{\text{UC}}$. FE predictions for the uniaxial strength $(\sigma_y^*/(\sigma_y^*)_{\text{UC}})$ are also plotted in the same figure: they follow a similar trend with $\overline{W}$ as $E^*/(E^*)_{\text{UC}}$. The rate of increase of $E^*/(E^*)_{\text{UC}}$ with $\overline{W}$ depends on $\overline{\rho}$. For the higher densities, e.g. $\overline{\rho} = 0.1, 0.2$, a lattice with $\overline{W} \approx 20$ is adequate to obtain effective properties within 10% of the infinite-sized counterparts. However, lattices with low relative density, e.g. $\overline{\rho} = 0.01$ and $\overline{W} = 20$ show a significant decrease of effective properties; approximately 70%. Lattice height, $\overline{H}$, has not been found to influence the effective properties in any way; all subsequent

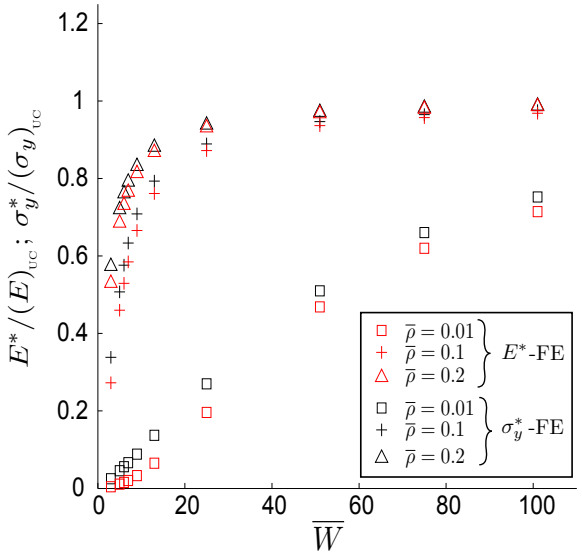

Figure 3.16: Variation of E^* and σ_y^* with $\overline{W}$.

results are for lattices with $\overline{H} = 3$.

Figure 3.17a plots the predicted effective modulus E^*, normalised by the elastic modulus of its cell wall E_s, against relative density $\overline{\rho}$ for lattices of different width $\overline{W} = 25, 51$ and 101. At sufficiently high $\overline{\rho}$, the FE results follow closely the theoretical scaling law for an *infinite-sized* lattice, given by $E^* = E_s\overline{\rho}/3$. As $\overline{\rho}$ reduces, the effective modulus progressively deviates from its *infinite-sized* counterpart. For sufficiently low $\overline{\rho}$, E^*/E_s is found to scale with $\overline{\rho}^3$, suggesting that the lattices are entirely bending-dominated; this is reflected by a huge reduction of effective modulus compared to its infinite-sized counterpart. Lattices of different $\overline{W}$ fall on different lines; unsurprisingly, results for lattice with a higher $\overline{W}$ give higher E^* which reflects the results from Fig. 3.16. The same trend is also observed for the strength of Kagome lattices, shown in Fig. 3.17b. The only difference is that $\sigma^*/(\sigma_y)_s$ now scales with $\overline{\rho}^2$ for sufficiently low relative densities $\overline{\rho}$. At the higher end of $\overline{\rho}$ range, the theoretical scaling law $\sigma^* = (\sigma_y)_s\overline{\rho}/2$ is followed. Since the FE models neglect elastic buckling, the predicted $\sigma^*/(\sigma_y)_s$ are likely to be lower for $\overline{\rho} < 0.03$ than those shown in Fig. 3.17b as they may no longer scale with $\overline{\rho}^2$. Notwithstanding, this should not affect the generality of the results - a significant reduction in effective strength - alluded above. Equally, it is important to note that the transition density $\overline{\rho}$ from elastic buckling to

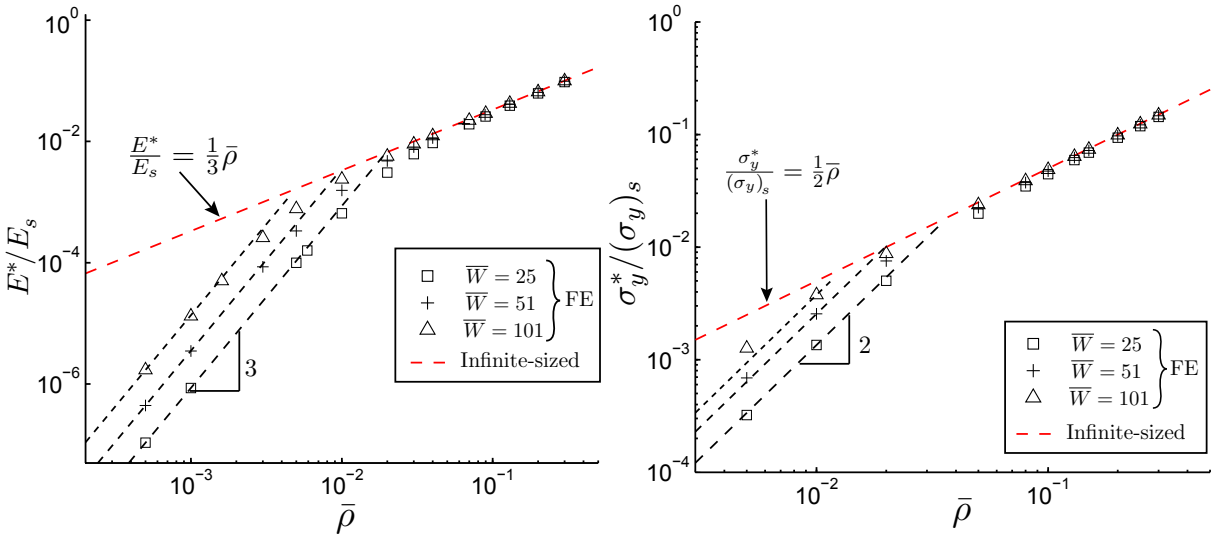

(a) (b)

Figure 3.17: (a) Variation of E^*/E_s with $\overline{\rho}$ and (b) Variation of $\sigma^*/(\sigma_y)_s$ with $\overline{\rho}$ of Kagome lattices.

plastic collapse predicted by Wang and McDowell (2004) was derived using a unit-cell approach. This might not be strictly valid for finite-sized lattices that are affected by edge effects and is the subject matter of a separate on-going study.

3.4.1.b Bending boundary layer

Figure 3.18 shows three deformed Kagome lattices – all have identical height $\overline{H} = 3$ and relative density $\overline{\rho} = 0.1$ – of different width $\overline{W} = 5, 15$ and 101. The deformation of constituent struts of the lattice and their internal stresses, as obtained from the FE simulations, reveal that two regions of deformation develop in *finite-sized* Kagome lattice under remote uniaxial loading as follows:

1. *Bending boundary layer* (BBL) emanate from each of the stress-free lateral boundaries (L and R) with a range of influence l_{BBL} – they are highlighted in red in Fig 3.18; and,

2. *Bulk-region* where their constituent cells deform predominantly by stretch – much like their *infinite-sized* counterparts.

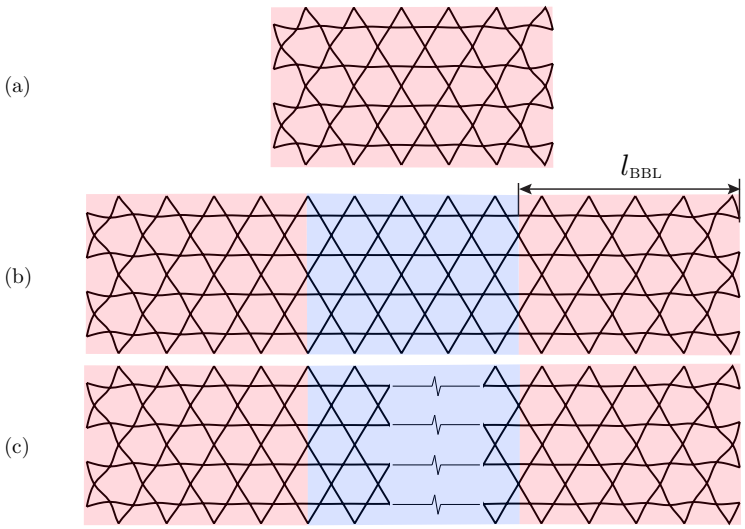

Figure 3.18: Bending boundary layer (BBL) emanating from each end of the stress-free lateral boundaries for Kagome lattices of different width: (a) $\overline{W} = 5$ (b) $\overline{W} = 15$ and (c) $\overline{W} = 101$. All lattices have identical height $\overline{H} = 3$ and $\overline{\rho} = 0.1$. Red and blue denote BBL and stretch-dominated bulk-region, respectively. Bulk-region in (c) is truncated for purpose of presentation.

The deformed lattices of Fig 3.18 suggests that l_{BBL} is identical for the two longer lattices, viz. $\overline{W} = 15$ and 101; thus it can be concluded that l_{BBL} is independent of $\overline{W}$. By contrast, a bulk-region did not develop in the shorter ($\overline{W} = 5$) lattice; hence, their two BBLs intersect and its constituent cell-walls are not stretch-dominated. It has to be noted that the vertical BBL is constant in width along the x_2 direction.

Unlike the Square lattice in shear, a sharp demarcation of the BBL from the bulk is not observed here. However, a transition zone develops and a diffused demarcation of BBL to the bulk cells is obtained. Thus l_{BBL} has to be properly defined to obtain a consistent measure for the range of influence of BBL. In order to do this, the distribution of the nodal reaction force RF_2 (in the x_2-direction) along the loading surface T are investigated - these information have to be extracted from their corresponding FE models. For convenience, RF_2 is normalised by its stretch-dominated, *infinite-sized*, counterpart $(RF_2)_{\text{UC}}$ given by

$$(RF_2)_{\text{UC}} = 2l\varepsilon^*_{22}\,(E^*)_{\text{UC}} \tag{3.46}$$

where ε^*_{22} is the remote uniaxial compressive strain and is chosen such that the macroscopic stress-strain response of the lattice remains in the linear-elastic regime. Following Eq. (3.46), if the reaction force of a node is $RF_2 = (RF_2)_{\text{UC}}$, its corresponding strut deforms entirely by stretch and equal to that expected from an infinite-sized lattice; if $RF_2 < (RF_2)_{\text{UC}}$, then stretch is not the dominant deformation mechanism. Remember that the effective modulus of a lattice is estimated as $E^* = \Sigma RF_2/Wd\varepsilon^*_{22}$; thus if $RF_2 < (RF_2)_{\text{UC}}$ at any of the boundary nodes, then the effective modulus of the lattice is lower than $(E^*)_{\text{UC}}$.

Figure 3.19a plots $RF_2/(RF_2)_{\text{UC}}$ as a function of x_1/W, where W is listed in Table 3.1 as a function of $\overline{W}$. The data plotted are for lattices with different width $\overline{W}$ but of identical relative density $\overline{\rho} = 0.1$ and height $\overline{H} = 3$; the plot is insensitive to the choice of $\overline{H}$. For all $\overline{W}$ lattice, near the lateral L and R boundaries, RF_2 is found to reduce considerably compared to the mid-span of the lattice; this is due to the presence of BBL. It is clear that in the longer lattices, say $\overline{W} \geq 25$, a bulk-region develops within which their constituents cells deform primarily by stretch; as exemplified by

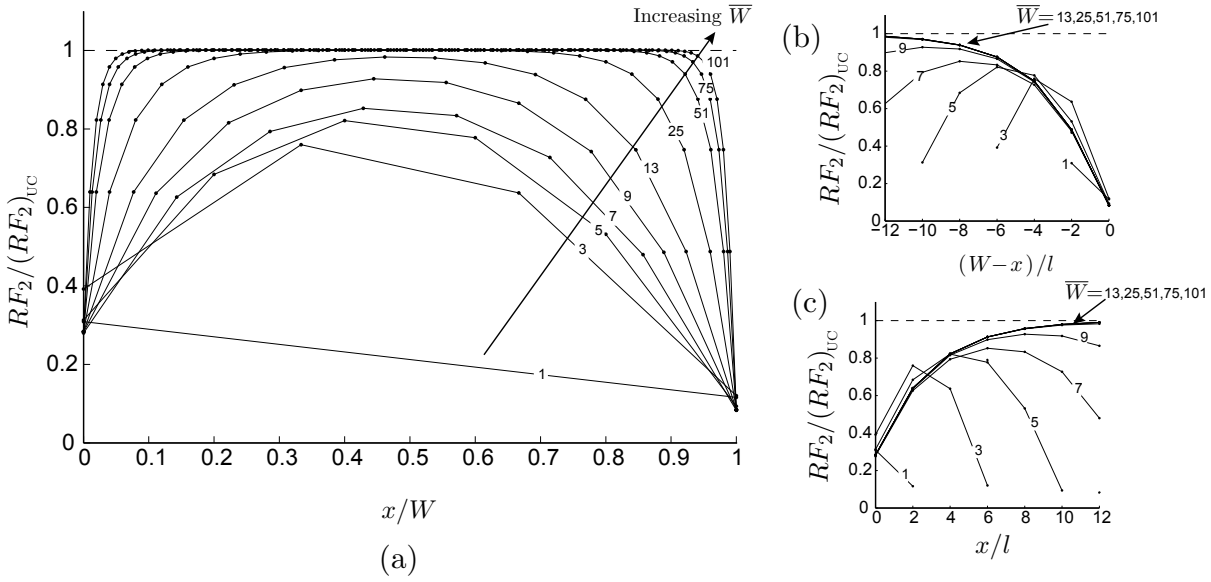

Figure 3.19: Distribution of RF_2 along the stressed surface T of lattices with different width $\overline{W}$. Each dot denotes a boundary node in the FE model. All lattices have identical $\overline{\rho} = 0.1$ and $\overline{H} = 3$.

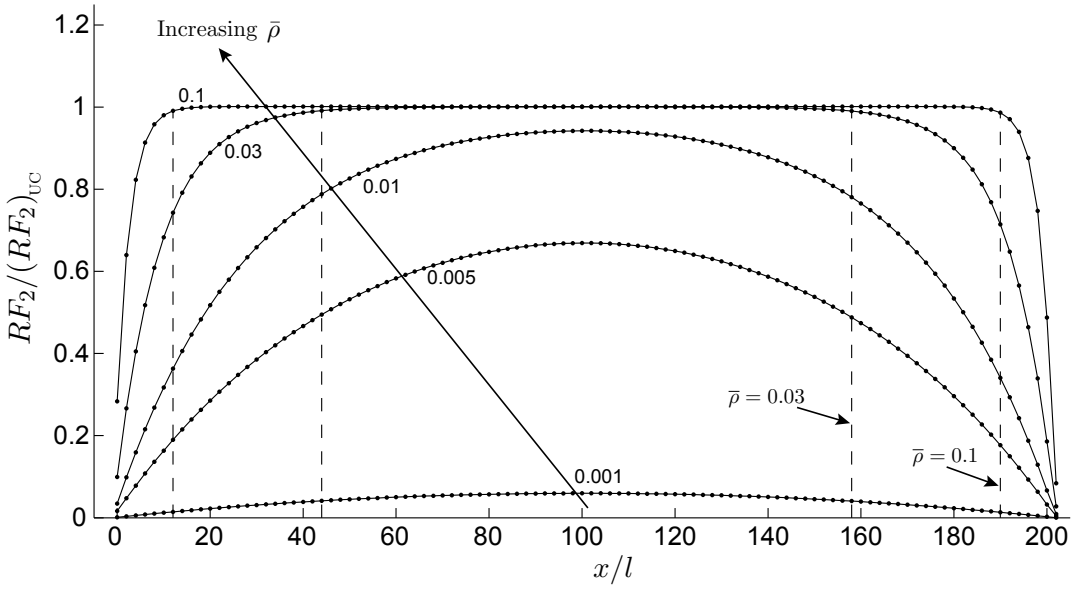

Figure 3.20: Effects on relative density $\overline{\rho}$ on the distribution of RF_2 (all lattices have identical $\overline{W} = 101$ and $\overline{H} = 3$) along the stressed surface T. The vertical dashed lines delineates the border of the BBL region, defined as $RF_2 < 0.99\,(RF_2)_{\rm UC}$.

$RF_2 = (RF_2)_{\text{UC}}$ for their corresponding nodal reaction forces. By contrast, a bulk-region did not develop in the shorter lattices ($1 < \overline{W} < 13$) implying that they are entirely covered by the two BBLs. Figures 3.19b and c show that the rate at which RF_2 falls away as it approaches the lateral boundaries are nearly identical for all the lattices that develop a bulk-region, viz. $\overline{W} \geq 13$. This is not the case in the shorter lattices. The rate of decrease for all lattices - short or long - were found to be insensitive to $\overline{H}$; hence only results for $\overline{H} = 3$ need to be shown here. These results show that l_{BBL} is independent of $\overline{W}$ if a bulk-region develops.

Figure 3.20 plots the distribution of RF_2 for lattices with different relative density $\overline{\rho}$ but of identical size ($\overline{W} = 101$ and $\overline{H} = 3$). To obtain a consistent measure of the range of influence of BBL, l_{BBL} is defined as the distance from a stress-free lateral boundary where $RF_2/\left(RF_2\right)_{\text{UC}} < 0.99$ - this is indicated by the vertical dashed lines in Fig 3.20 for the two relative densities ($\overline{\rho} = 0.03$ and 0.1) where a bulk-region develops. Since the *local modulus* of the BBL scales with $\overline{\rho}^b$ - where $b > 1$, as expected for any non stretch-dominated lattice - whilst that of the bulk-region with $\overline{\rho}$, it is not surprising that the lower density lattices develop a longer range of influence (l_{BBL}) in order to bridge the bigger differences in local modulus between the BBL and bulk-region.

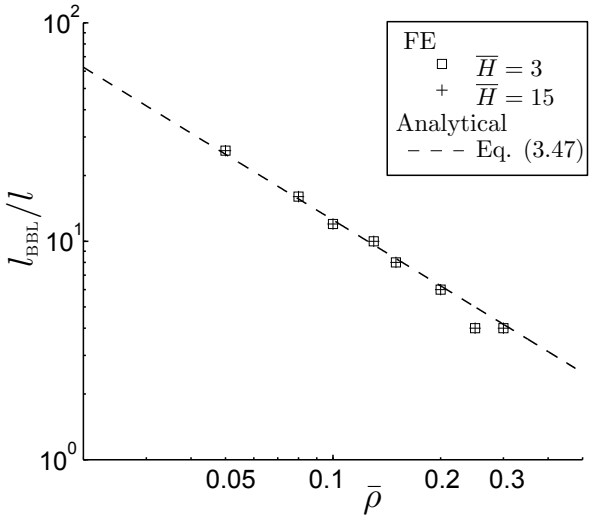

Figure 3.21: Variation of l_{BBL} on $\overline{\rho}$ on a log-log scale.

Figure 3.21 plots l_{BBL}/l versus $\overline{\rho}$ on a log-log scale. The data suggest a scaling law of the following form:

$$\frac{l_{\text{BBL}}}{l} = \frac{10}{8\overline{\rho}} \quad . \tag{3.47}$$

Notice that l_{BBL} is independent of $\overline{H}$ and this is evident in Fig 3.21 where the results for $\overline{H} = 3$ and 15 overlay one another. The scaling law in Eq. (3.47) is similar to the one reported by Fleck and Qiu (2007) for an elastic shear lag region emanating from the crack tip of a Kagome lattice, viz. $l_{\text{shear lag}}/l = 4.5/\overline{\rho}$.

3.4.1.c Deformation mechanism map

As it was already shown in Fig. 3.17, a Kagome lattice is not always a stretch-dominated micro-architecture; depending on its relative density $\overline{\rho}$ and width $\overline{W}$, a shift to a bending-dominated deformation is possible. Figure 3.22a, shows schematically the three region of a $E^*/E_s - \overline{\rho}$ curve, each with a different dominant mode(s) of deformation, as follows

1. Bending, $b \approx 3$
2. Mixed
3. Stretch, $b = 1$

Recall that the parameter b is the exponent of the scaling law in Eq. (1.9). To estimate the transition relative density from stretch-to-mixed region, $\overline{\rho}_{S-M}$, first a the pre-exponent of a scaling law with $b = 1$ is fitted to the numerical results at the higher end of the $\overline{\rho}$ range. The higher $\overline{\rho}$ that gives more than 10% deviation from this scaling law is termed $\overline{\rho}_{S-M}$. Conversely, to estimate $\overline{\rho}_{B-M}$, a scaling law with $b = 3$ is fitted to the numerical results at the lower end of the $\overline{\rho}$ range, and $\overline{\rho}_{B-M}$ is the lowest $\overline{\rho}$ for which the numerical results deviate more than 10% from this scaling law.

The transition relative densities $\overline{\rho}_{S-M}$ and $\overline{\rho}_{B-M}$ are determined from FE results for lattices with various $\overline{W}$; these are plotted in the $\overline{W}$ – $\overline{\rho}$ space in Fig. 3.22b with bold black lines, along with the contour map of $E^*/(E^*)_{\text{UC}}$. The border between axial-mixed and bending-mixed dominated deformation mode coincide with a 10% and 90% drop in modulus respectively; this is a reflection of the definition of the transition $\overline{\rho}$ given above. As already addresses, with increasing $\overline{W}$ and $\overline{\rho}$, $E^*/(E^*)_{\text{UC}}$ approaches

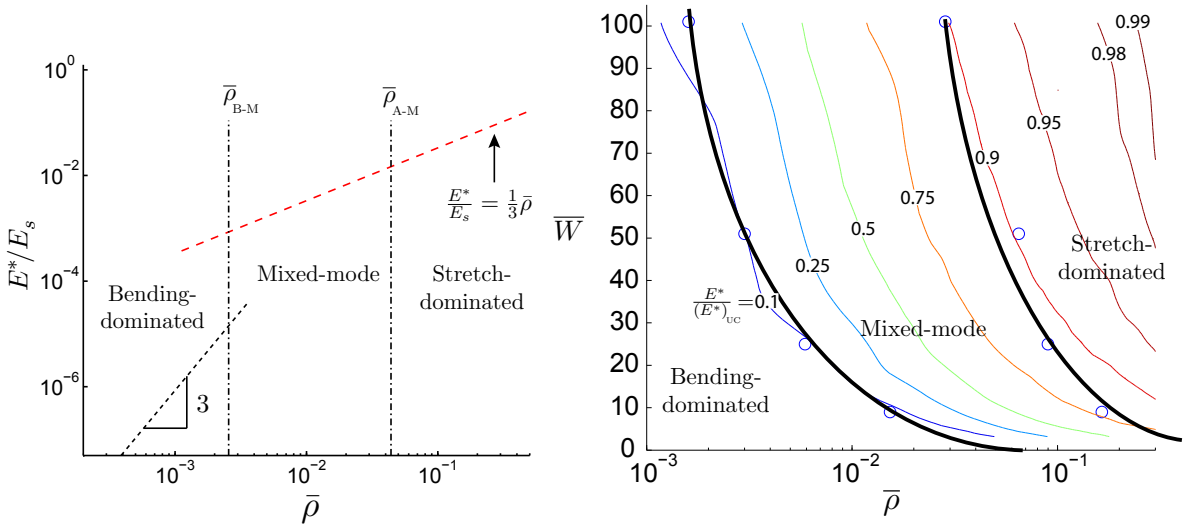

(a) (b)

Figure 3.22: (a) Schematic showing the three regions in a E^*/E_s versus $\overline{\rho}$ diagram for a Kagome lattice. (b) Contour plot of $E^*/(E^*)_{\text{UC}}$ in $\overline{W}$–$\overline{\rho}$ space. The bold black lines indicate the borders for the three deformation mechanism regimes.

1. For high relative densities, say $\overline{\rho} = 0.2$, the Kagome lattice can be considered stretch-dominated for $\overline{W} > 10$. However, for low relative densities, say $\overline{\rho} = 0.02$, the deformation is never stretch-dominated regardless of $\overline{W}$. Reducing $\overline{\rho}$ even further, say $\overline{\rho} = 2 \times 10^{-3}$, the Kagome lattice is always bending-dominated for any $\overline{W}$; however it has to be noted that such low relative densities are unrealistic.

3.4.2 Shear

Under the action of remote shear, bending boundary layers (BBLs) also develop in *finite-sized* Kagome lattices. The extent to which a BBL permeates a lattice, and their consequential impact on the effective response, depends on the lattice width (W) and height (H) – it will be clear later why this is the case. Therefore, it is convenient to first introduce a parameter $\overline{R}$, defined as the ratio of the number of *complete* cells along the width to height of a Kagome lattice, as follows:

$$\overline{R} = \frac{\overline{W}}{\overline{H}} = \frac{3W - 6l}{2\sqrt{3}H - 6l} \quad . \tag{3.48}$$

The case of $\overline{R} \geq 1$, where a stretch-dominated bulk-region is able to develop in a

lattice, is to be addressed first.

3.4.2.a Aspect ratio $\overline{R} \geq 1$

Figure 3.23 shows the estimated effective shear modulus $G^*/(G^*)_{\text{UC}}$ and shear yield strength $\tau_y^*/(\tau_y^*)_{\text{UC}}$ from FE models for lattices of different $\overline{W}$ and $\overline{H}$; constant relative density of $\overline{\rho} = 0.1$ is used for all lattices. As to be expected, the effective shear modulus and yield strength follow the similar general trend. In a similar manner with the Kagome lattice in uniaxial loading, larger lattices in $\overline{W}$ are required to obtain converged values of $G^*/(G^*)_{\text{UC}}$. However, here, the lattice height $\overline{H}$ affects the results significantly; $\overline{\rho}$ has little effect on the results as it will shown further on. If lattice height is small, say $\overline{H} = 1$, the effective shear modulus $G^*/(G^*)_{\text{UC}} > 0.9$ is reached for relatively small $\overline{W} > 10$ lattices. On the contrary, for lattices with high $\overline{H}$, a considerably larger $\overline{W}$ is required to obtain $G^*/(G^*)_{\text{UC}} > 0.9$; for $\overline{H} = 15$, a significantly larger $\overline{W} = 101$ lattice is required.

A typical example of a deformed Kagome lattice ($\overline{W} = 25$; $\overline{H} = 15$; $\overline{R} = 1.7$; $\overline{\rho} = 0.001$) under shear is shown in Fig 3.24; this example is for applied shear strain

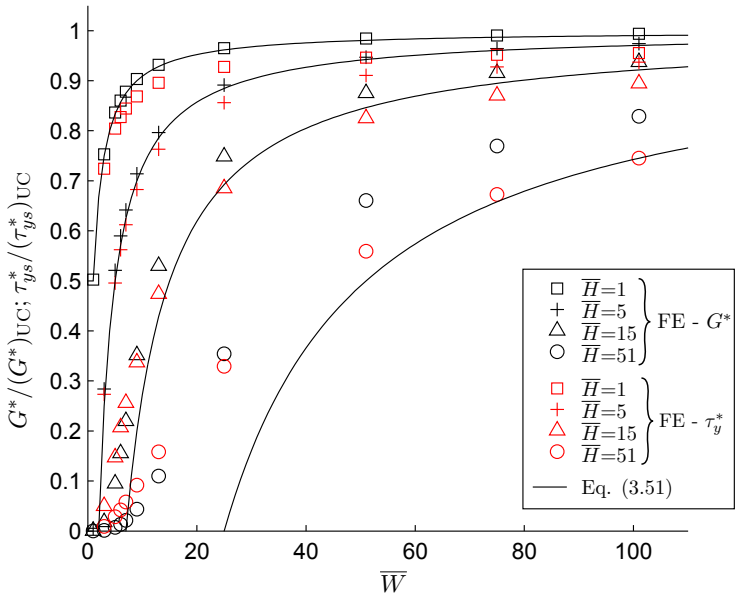

Figure 3.23: Predicted effective shear modulus and strength for lattices of different $\overline{W}$ and $\overline{H}$. All have identical relative density of $\overline{\rho} = 0.1$

.

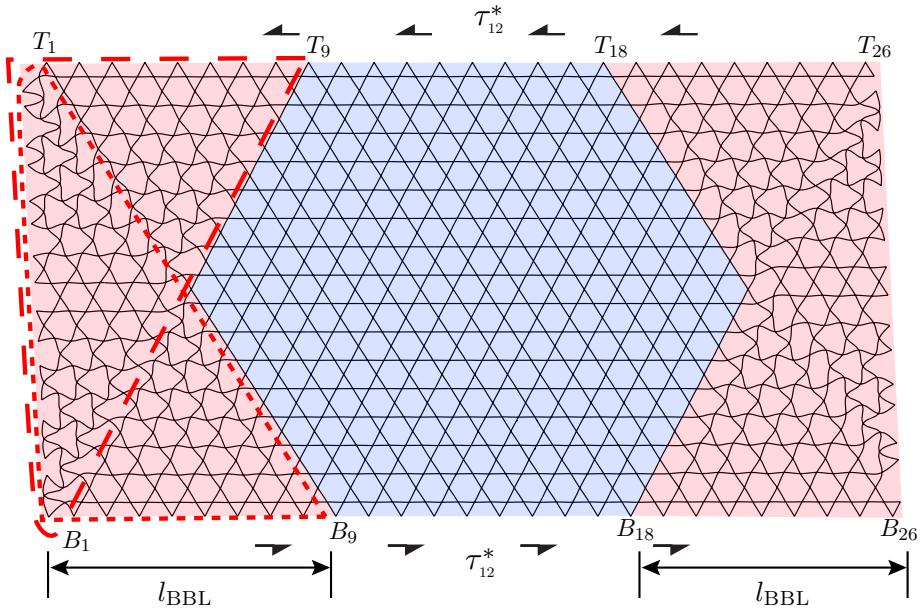

Figure 3.24: A deformed Kagome lattice ($\overline{W} = 25$; $\overline{H} = 15$; $\overline{R} = 1.7$) of relative density $\overline{\rho} = 0.001$ under simple shear. Red and blue area denotes bending boundary layers and bulk-region, respectively.

that falls within the linear regime of the macroscopic response. Two bending-boundary layers (BBLs) are developed- one emanating from each free end - highlighted in red, and a bulk-region in blue. Unlike their uniaxial counterpart, the boundary that separates a BBL from its bulk-region is not vertical. Each 'angular-shaped' BBL, with its sharp boundary, can be thought of as a superposition of two triangular regions of cells that deform with considerable bending; the cells within the bulk-region deform entirely by stretch as to be expected for a Kagome lattice. In Fig. 3.24, the two triangular regions that make up one of the 'angular-shaped' BBL are enclosed by their respective red-dashed lines. The shape of BBL is similar to the one reported by Zupan et al. (2004) for Diamond lattices under uniaxial and shear loading; see review in Section 1.3. It is important to emphasise that a sharp boundary separating the BBLs from the bulk, such as the ones shown here in Fig 3.24, only develops for lattices with low relative density – this shall be the primary focus here. If relative density is sufficiently high, a transition zone (or shear-lag zone) develops which will be discussed later using Fig 3.26.

To delineate the sharp boundary of an 'angular-shaped' BBL from its bulk, one must establish whether there is a continuous series of struts that connects the top (T) to the

bottom (B) surface. Take, for instance, $B_9 - T_1$ and $T_9 - B_1$ in Fig 3.24. All the other series of struts to the immediate left of $B_9 - T_1$ – they are the ones orientated at 120° counter-clockwise to the horizontal – do not connect surfaces T to B: these make up a group of cells for one of the triangular region alluded to above; these cells are found to deform by significantly high bending stresses. Likewise, for those to the immediate left of $T_9 - B_1$, orientated at -120° clockwise to the horizontal, that make up the other triangular region. Collectively, $B_9 - T_1$ and $T_9 - B_1$ defines the boundary of the 'angular-shaped' BBL in Fig 3.24. By the same construction, $B_{18} - T_{26}$ and $T_{18} - B_{26}$ defines the boundary of the other BBL.

This knowledge can now be used to establish the range of influence of the BBL. Thus, a non-dimensional parameter l_{BBL}/l is introduced to locate the boundary of the BBL, measured from either end of the stressed surfaces (T and B), as follows:

$$\frac{l_{\text{BBL}}}{l} = \frac{H}{l}\tan 30^\circ = \overline{H} + 1 \quad . \tag{3.49}$$

where l is the uniform cell wall length that make up a Kagome lattice. $\overline{R} = 1$ corresponds to the limiting case where a lattice is just long enough, viz. $W = 2l_{\text{BBL}}$, for the two BBLs (with sharp boundary) to fully develop. If $\overline{R} < 1$, the lattice does not develop a bulk-region; this will be investigated in Section 3.4.2.b.

To understand the effect of the BBLs on the effective modulus of the lattice, the reaction forces for nodes in and out of BBL are investigated here. By virtue of how the shear

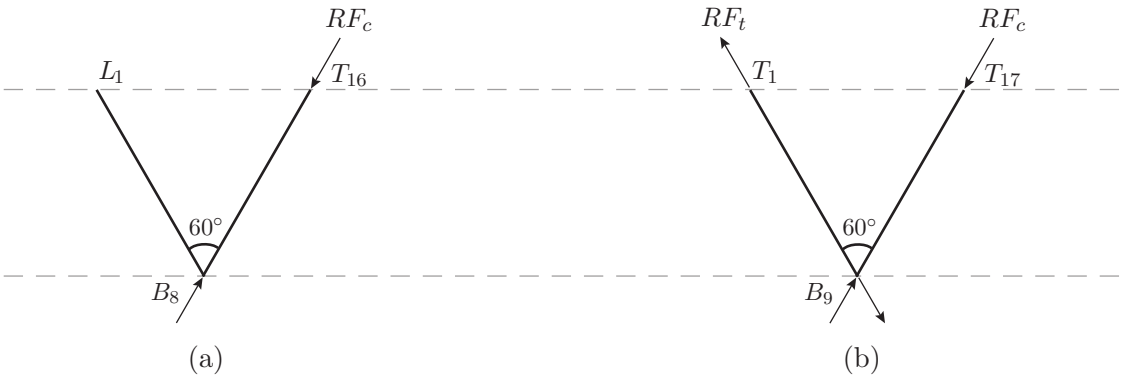

Figure 3.25: Schematic of the reaction forces acting on nodes B_8 and B_9 shown in Fig 3.24.

strain is imposed in the FE model of Fig 3.24, the series of struts orientated at 60° and 120° (both measured clockwise to the horizontal) are loaded in compression and tension, respectively. The reaction forces at selected nodes on the top T and B surfaces are depicted schematically in Fig 3.25, where $|RF_c| = |RF_t|$ are the axial load in the series of struts that connect T and B surfaces.

For every surface node that lie within the bulk region, say B_9 in Fig 3.25c, their resultant reaction force along the horizontal x_1 direction is given by $RF_1 = |RF_c|/2 + |RF_t|/2 = (RF_1)_{\text{UC}}$ where

$$(RF_1)_{\text{UC}} = 2l\gamma^*_{12}\,(G^*)_{\text{UC}} \tag{3.50}$$

and γ^*_{12} is the applied shear strain. Using a lower bound approach, it is assumed that the series of struts that fall within a BBL are not loaded; i.e. either $|RF_c| = 0$ or $|RF_t| = 0$. If a surface node lies within the BBL, such as nodes B_8 their corresponding reaction force along the x_1 direction is $RF_1 = (RF_1)_{\text{UC}}/2$. Consequently, the 'local' stiffness of cells within a BBL is $(G^*)_{\text{UC}}/2$, whilst for the bulk region is $(G^*)_{\text{UC}}$.

Figure 3.26 plots the $RF_1/(RF_1)_{\text{UC}}$ - as obtained from FE simulations - against x/W, for lattices with different combinations of $\overline{W}\,(= 51$ and $101)$ and $\overline{H}\,(= 5, 15$ and $51)$ at different $\overline{\rho}\,(= 0.001, 0.01$ and $0.1)$. First consider the results for the lower relative density; $\overline{\rho} = 0.001$. As it was already addressed from Eq.(3.49), l_{BBL}/l increases with $\overline{H}$; this is best observed for lattices of fixed $\overline{W}$, compare either Figs 3.26a & c or b,d & f. Also, as expected, within a BBL, the reaction force are exactly $RF_1/(RF_1)_{\text{UC}} = 0.5$ and for the rest of the lattice $RF_1/(RF_1)_{\text{UC}} = 1$. For small $\overline{H}$, say 5, the BBLs cover a very small portion of the length of the lattice, thus the knock-down on the effective modulus is not significantly; this is especially true for high $\overline{W}$, say 101. For constant $\overline{W}$, as $\overline{H}$ increases, the proportion of lattice covered by BBL increases and the knockdown on effective modulus increases; this is also reflected by Fig. 3.23. For the limiting case where $\overline{W} = \overline{H}$, i.e. $\overline{R} = 1$, a bulk-region does not develop in the lattices, see Fig 3.26e; consequently, the effective shear modulus is $G^* = (G^*)_{\text{UC}}/2$.

Recall that the mechanistic explanation presented above for the the presence of BBL - and its effect on the effective modulus - uses a lower bound estimate and is strictly

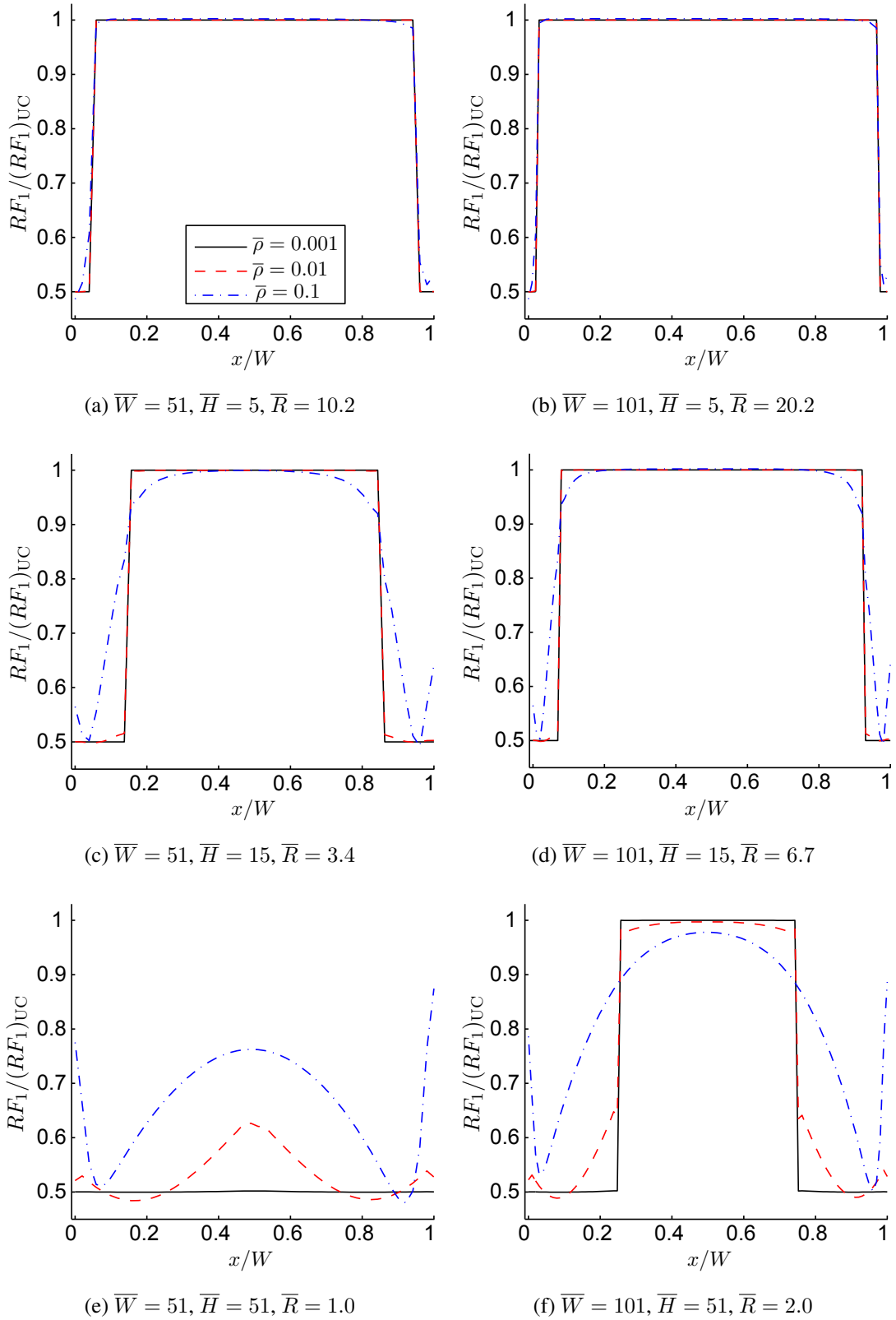

(a) $\overline{W} = 51$, $\overline{H} = 5$, $\overline{R} = 10.2$

(b) $\overline{W} = 101$, $\overline{H} = 5$, $\overline{R} = 20.2$

(c) $\overline{W} = 51$, $\overline{H} = 15$, $\overline{R} = 3.4$

(d) $\overline{W} = 101$, $\overline{H} = 15$, $\overline{R} = 6.7$

(e) $\overline{W} = 51$, $\overline{H} = 51$, $\overline{R} = 1.0$

(f) $\overline{W} = 101$, $\overline{H} = 51$, $\overline{R} = 2.0$

Figure 3.26: Normalised nodal reaction forces, $RF_1/(RF_1)_{\mathrm{UC}}$ along the top surface T of lattices with different $\overline{W}$ and $\overline{H}$. Three relative densities are shown $\overline{\rho} = 0.001, 0.01, 0.1$.

correct for lattice with slender cell walls; i.e. for sufficiently low relative density $\overline{\rho}$. From the FE results of Fig 3.26, it becomes clear that for higher $\overline{\rho}$, a transition (or shear-lag) zone develops, and as a result a smooth transition is observed between $RF_1/(RF_1)_{\text{UC}} = 1/2$ and $= 1$ for nodes in and out of a BBL, respectively. The reason behind the presence of a transition zone for high $\overline{\rho}$ is the increased contribution from axial stretch in stockier cell walls; thus the assumption that struts within the BBL are not loaded is not strictly true for high $\overline{\rho}$. As $\overline{\rho}$ increases, the angular boundary becomes increasingly diffused, resulting to higher $RF_1/\left(RF_1\right)_{\text{UC}} > 1/2$ within the a BBL and $RF_1/\left(RF_1\right)_{\text{UC}} < 1$ in the bulk region; this is clear in Fig 3.26f. Consequently, an increase in $\overline{\rho}$, does not fundamentally affect the edge effects mechanism and the presence of a diffused BBL boundary does not affect $G^*/(G^*)_{\text{UC}}$ significantly.

To quantify the overall effect of the BBLs on the effective shear modulus of a *finite-sized* Kagome lattice with $\overline{R} \geq 1$, one may again use the rule-of-mixtures in Eq. (3.37). By concentrating only for lower $\overline{\rho}$ - and thus neglecting the presence of a diffused BBL boundary for high $\overline{\rho}$ - the two constituent phases are as follows:

1. BBLs of total length $2l_{\text{BBL}}$ and 'local' modulus $G^* = (G^*)_{\text{UC}}/2$
2. the 'bulk' region with length $(W - 2l_{\text{BBL}})$ and 'local' modulus $G^* = (G^*)_{\text{UC}}$

Substituting Eq. (3.49) into (3.37), and using the above, gives

$$\frac{G^*}{(G^*)_{\text{UC}}} = \frac{2\overline{W} + 1 - \overline{H}}{2\left(\overline{W} + 1\right)}. \tag{3.51}$$

The predictions by Eq. (3.51) are plotted in Fig. 3.23 against the results for FE lattices of relative density of $\overline{\rho} = 0.1$; a reasonable agreement is obtained. The discrepancies are down to the two basic assumption made upon deriving Eq. (3.51). Firstly, it was assumed that the BBL boundary is sharp. Even though that this is violated for $\overline{\rho} = 0.1$ - as shown from Fig. 3.26 - Eq. (3.51) gives a very good approximation for higher $\overline{\rho}$. This is especially true for lattice of high $\overline{R}$, because the length of the transition zone relative to the lattice length is negligible; compare Fig. 3.26a and 3.26f for $\overline{R} = 10.2$ and 2.0 respectively. Secondly, Eq. (3.51) was developed for aspect ratios $\overline{R} \geq 1$, however Fig. 3.23 plots data for the whole range of $\overline{R}$. The largest discrepancies are

obtained for cases where $\overline{R} < 1$; e.g. for $\overline{H} = 51$ and $\overline{W} < 50$. Lattices with aspect ratios $\overline{R} < 1$ will be investigated further in Section 3.4.2.b.

3.4.2.b Aspect ratio $\overline{R} < 1$

As already addressed above, Kagome lattices with aspect ratio $\overline{R} \leq 1$ do not develop a bulk region, and the lattice deformation involves considerable bending in all of its cell walls. Because of this, $\overline{\rho}$ becomes the dominant parameter for $\overline{R} < 1$ lattices, whilst, as it will become apparent further down, $\overline{W}$ and $\overline{R}$ play a minor role. Figure 3.27 plots the FE predictions for the shear modulus G^*/E_s and shear strength $\tau^*/(\sigma_y)_s$ against $\overline{\rho}$ for various aspect ratios $\overline{R}$; for each $\overline{R}$, data for two lattices with different $\overline{W}$ are shown.

In a similar vein as the Kagome lattice in uniaxial loading, a shift of the dominant deformation mechanism is observed for lattices with $\overline{R} < 1$; this is exemplified by the non-linear dependence on $\overline{\rho}$. For $\overline{R} < 1$ and sufficiently low $\overline{\rho}$, G^*/E_s is found to scale with $\overline{\rho}^3$, whilst $\tau^*/(\sigma_y)_s$ with $\overline{\rho}^2$; this observation signifies bending-dominated deformation. Since elastic collapse - this is expected to precede plastic collapse if $\overline{\rho} < 0.03$ - is ignored in the FE models, the knock down in shear strength might be even greater than what is shown in Fig. 3.27b. On the other hand, for lattices with $\overline{R} \geq 1$,

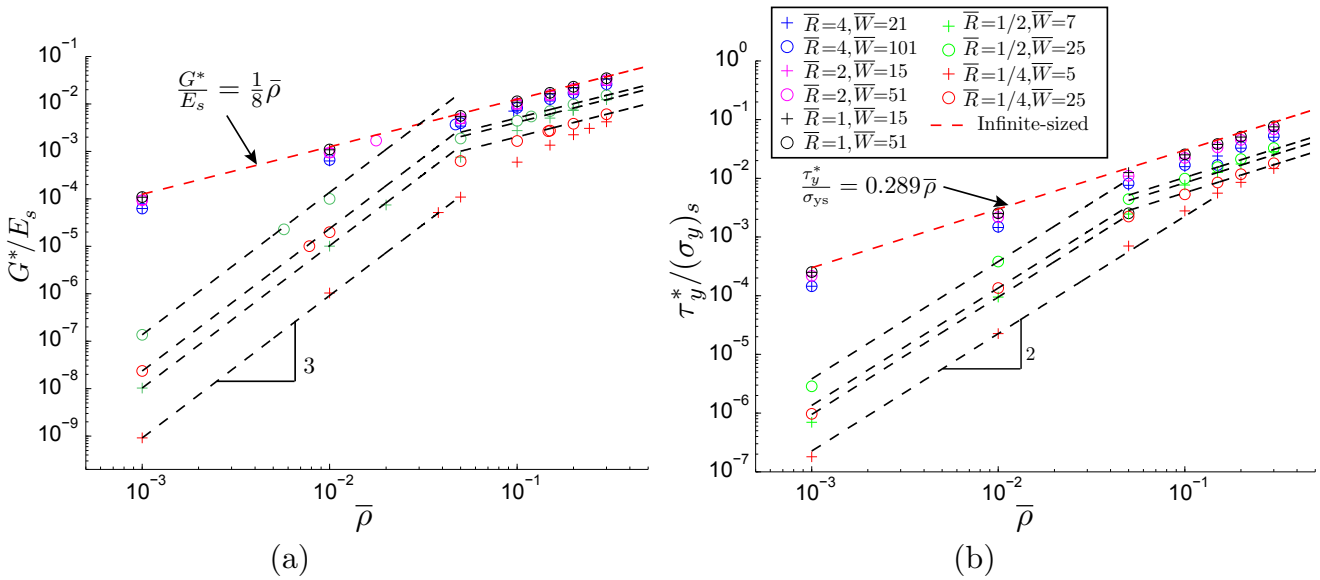

Figure 3.27: (a) Shear modulus and (b) yield strength as a function of relative density for Kagome lattices of various $\overline{R}$ and $\overline{W}$.

the linear dependence on $\overline{\rho}$ is maintained throughout the range of $\overline{\rho}$; this strengthens the conclusion made in Section 3.4.2.a that $\overline{\rho}$ does not plays a significant role in the edge effects for Kagome lattices with $\overline{R} \geq 1$.

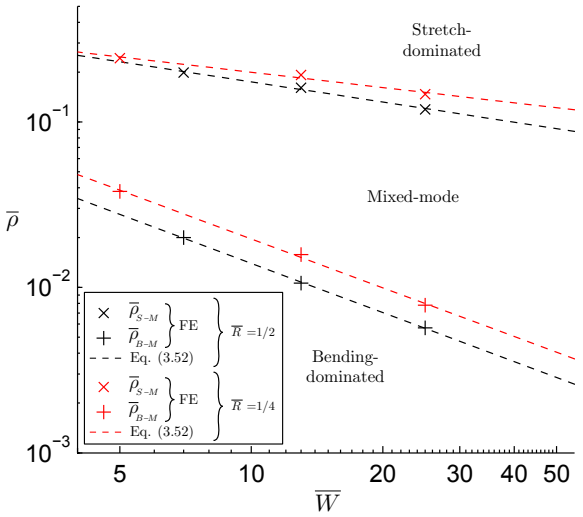

Figure 3.28: Transition relative density for bending-mixed and axial-mixed as the dominant deformation mechanism. Note the log-log scales.

Transition	$\overline{R}$	c_1	c_2
Bending-Mixed	1/2	0.1350	0.9857
	1/4	0.1868	0.9791
Stretch-Mixed	1/2	0.4429	0.4045
	1/4	0.4054	0.3075

Table 3.4: Table of coefficients for Eq.(3.52).

By following the same approach as with the Kagome lattice in uniaxial loading, the transition relative densities from stretch-dominated to mixed and bending-dominated to mixed response are estimated. Figure 3.28 plots $\overline{\rho}_{S-M}$ and $\overline{\rho}_{B-M}$, for two aspect ratios, in the ($\overline{\rho}$–$\overline{W}$) space, in log-log scales. Since the estimated transitions $\overline{\rho}$ for each ($\overline{W}$, $\overline{R}$) combination fall into straight lines, they can be describe by a scaling law of the form

$$\overline{\rho} = \frac{c_1}{\overline{W}^{c_2}} \tag{3.52}$$

where the parameters c_1 and c_2 are calibrated to the FE results and given in Table 3.4.

The transition from stretch-to-mixed deformation is found to have a weak dependency on $\overline{W}$ whilst $\overline{R}$ is insignificant. However, the transition $\overline{\rho}$ from bending-to-mixed has a much stronger dependence on $\overline{W}$ and a weak dependence on $\overline{R}$.

3.5 Triangular lattice

3.5.1 Uniaxial loading

In a similar manner to the Kagome lattice, the edge effects will be investigated by employing numerical finite element models. The competing influences of lattice width $\overline{W}$, height $\overline{H}$ and relative density $\overline{\rho}$ are presented first and then a model is developed to explain these observations.

3.5.1.a Effective Modulus and Yield Strength

Figure 3.29a plots the normalised $E^*/(E^*)_{\text{UC}}$, estimated from finite elements, against lattice height $\overline{H}$ for various $\overline{W}$. All results are for $\overline{\rho} = 0.1$. For constant $\overline{W}$, as $\overline{H}$ increases, $E^*/(E^*)_{\text{UC}}$ decreases from > 1 to a converged value < 1; the higher the $\overline{W}$, the closer the converged value is to $E^*/(E^*)_{\text{UC}} = 1$. For constant $\overline{H}$ and varying $\overline{H}$, the reverse trend is observed; see Fig. 3.29b. As $\overline{W}$ increases, $E^*/(E^*)_{\text{UC}}$ converge to a value > 1; only for lattices with sufficiently high $\overline{H}$ – e.g. $\overline{H} = 32$ – the

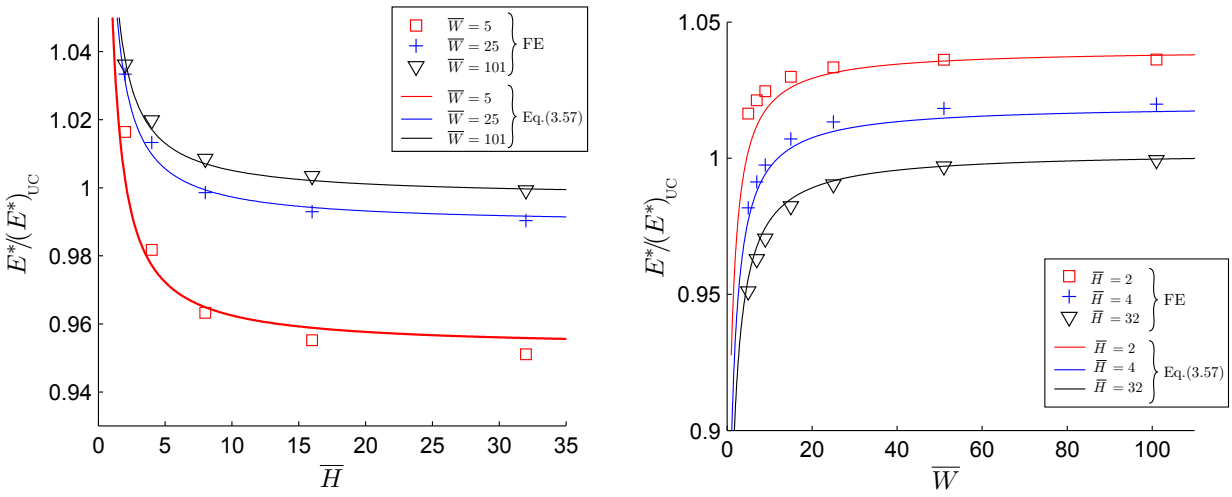

Figure 3.29: (a) Variation of $E^*/(E^*)_{\text{UC}}$ with $\overline{H}$ and (b) Variation of $E^*/(E^*)_{\text{UC}}$ with $\overline{W}$. All results are for $\overline{\rho} = 0.1$.

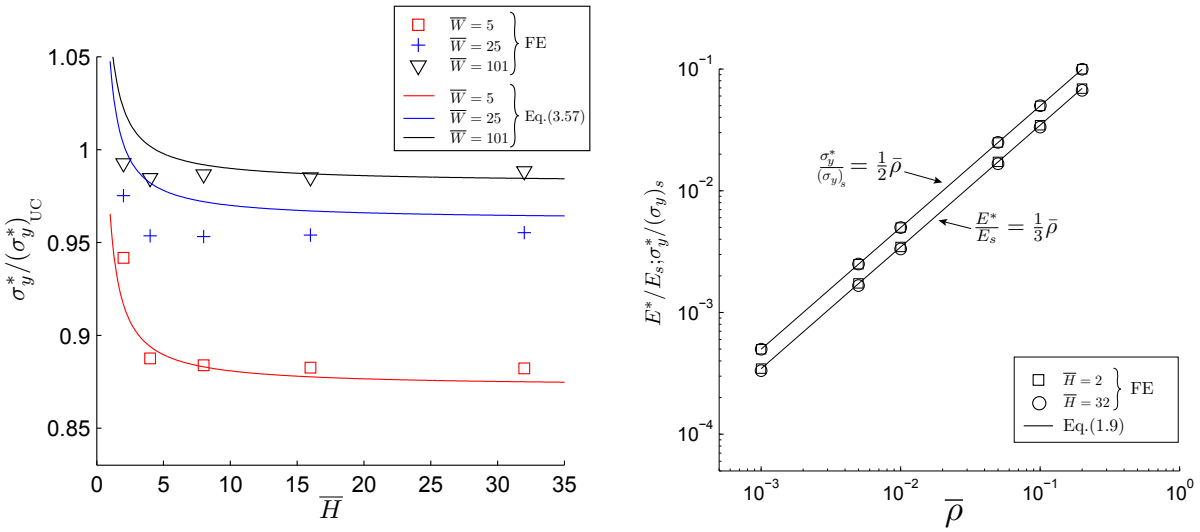

Figure 3.30: (a) Variation of $\sigma_y^*/(\sigma_y^*)_{\mathrm{UC}}$ with $\overline{H}$ for Triangular lattices. (b) Variation of E^*/E_s and $\sigma_y^*/(\sigma_y)_s$ with $\overline{\rho}$ for lattices with $\overline{W} = 15$.

converged value is $E^*/(E^*)_{\mathrm{UC}} \approx 1$. Similar trend is also observed for yield strength as shown in Fig. 3.30a. Figure 3.30b shows the variation of E^*/E_s and $\sigma_y^*/(\sigma_y)_s$ with $\overline{\rho}$; lattices with $\overline{W} = 15$ and $\overline{H} = (2, 32)$ are shown. Both lattices are found to maintain the stretch-dominated deformation for the entire range of $\overline{\rho}$, exemplified by the linear dependence on $\overline{\rho}$. This allows us to safely conclude that $\overline{\rho}$ does not affect the edge effect mechanism in any way. However, elastic buckling might lead to a significant reduction in the predicted $\sigma_y^*/(\sigma_y)_s$ if $\overline{\rho} < 0.06$ (Wang and McDowell, 2004); note that only plastic collapse is considered in this thesis.

3.5.1.b Edge effects model

The dependence of the effective properties on lattice dimensions, as shown in Fig. 3.29, signify the presence of weak vertical and strong horizontal boundary layers. To investigate this, consider a typicaly deformed Triangular lattice - of $\overline{W} = 15$ and $\overline{H} = 8$ - as shown in Fig. 3.31. Upon closely investigating the stress distribution in struts, from the finite element results, the cells at the L and R surfaces are found to deform by higher contribution from bending stresses compared to the 'bulk' cells; this is attributed to the reduced connectivity of the cells at the boundaries. The finite element results also indicate that a transition zone does not develop to diffuse the difference in 'local' stiffness in and out of the boundary layer, and each vertical boundary layer extends for

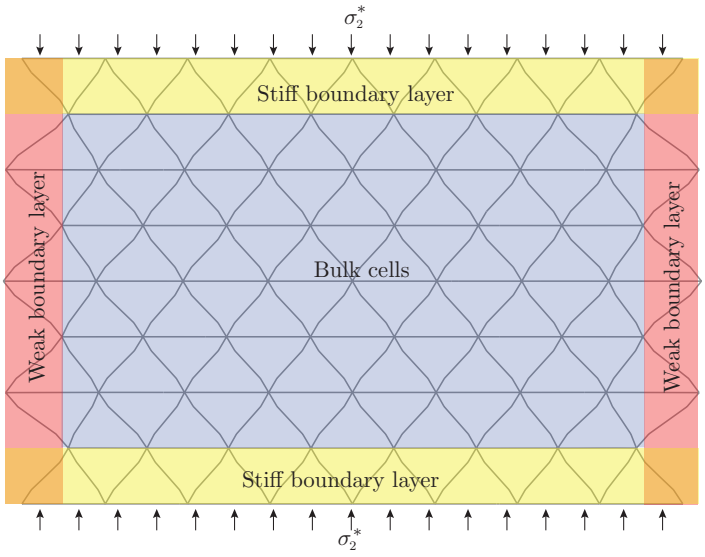

Figure 3.31: Schematic of the boundary layers that develop in a Triangular lattice under uniaxial loading. The lattice shown has $15(\overline{W}) \times 8(\overline{H})$ complete cells.

half cell, $l/2$, along the x_1 direction. Additionally, the cells at the immediate vicinity of the T and B surfaces show slightly stiffer response compared to the 'bulk' cells; from FE models, the bending stresses of the struts within the stiff boundary layer are found to be lower compared to the bulk region. The presence of the horizontal boundary layer is believed to be due to the additional constraint induced from to the loading platens T and B. Each horizontal boundary layer was found to extend for exactly one cell along the x_2 direction; i.e. its range of influence is $\sqrt{3}l/2$. At the four corners of the lattice, the horizontal and vertical boundary layers 'merge' and the 'local' stiffness is a combination of the effects from both, as it will become clear further on. Note that the term bending boundary layer (BBL) is not employed here, since under no circumstances the presence of boundary layers can lead to a macroscopic bending-dominated response.

To capture the overall effect of the boundary layers on the lattice effective properties, a model is proposed based on the rule-of-mixture. The effect of the vertical boundary layers is modelled by Eq. (3.37), in the same spirit as the one developed for the Square and the Kagome lattices in shear. However, since the horizontal boundary layers develop perpendicular to the loading direction, their effect has to be modelled using the rule-of-mixture for the transverse stiffness of unidirectional composites, given by

(Jones, 1999)

$$E = \frac{E_1 E_2 A}{A_1 E_2 + A_2 E_1} \tag{3.53}$$

where E_i and A_i/A, $i = 1, 2$, are the modulus and area fractions for the two phases in a composite; this is equivalent to the 'springs-in-series' model. For the purpose of the edge effects model, the role of the two constituent materials are taken by

1. two horizontal boundary layers of total area fraction $A_1/A = \sqrt{3}l/H$ and 'local' modulus $E_1 = \beta_1 (E^*)_{\text{UC}}$, where the scalar parameter $\beta_1 > 1$ is to be calibrated later using numerical results; and,

2. the 'bulk' region with area fraction $A_2/A = (H - \sqrt{3}l)/H$ and 'local' modulus $E_2 = (E^*)_{\text{UC}}$.

By substituting the above into Eq. (3.53) and using $H = \sqrt{3}(\overline{H}/2)$, the following scaling law is obtained

$$\frac{E^*}{(E^*)_{\text{UC}}} = \frac{\beta_1 \overline{H}}{2 + \beta_1 (\overline{H} - 2)} \quad . \tag{3.54}$$

Now consider the vertical boundary layers; the role of the two constituent materials in Eq. (3.37) are taken by

1. two weak vertical boundary layers of total area fraction $A_1/A = l/W$ and elastic modulus $E_1 = \alpha (E^*)_{\text{UC}}$, where $\alpha < 1$ is to be calibrated from numerical FE experiments; it will shown that α is not a scalar but a function of $\overline{H}$; and,

2. the 'bulk' region with area fraction $A_2/A = (W - l)/W$ and 'local' modulus $E_2 = (E^*)_{\text{UC}}$.

By substituting the above in Eq. (3.37) and using $W = (\overline{W}+1)/2$ the following scaling law is obtained:

$$\frac{E^*}{(E^*)_{\text{UC}}} = \frac{\overline{W} - 1 + 2\alpha}{\overline{W} + 1} \quad . \tag{3.55}$$

To obtain α, consider lattices with $\overline{W} = 1$, which are totally covered by the two weak boundary layers; it follows from Eq. (3.55) that $E^*/(E^*)_{\rm UC} = \alpha$. However, as it was hinted above and from Fig. 3.31, the horizontal boundary layers also extend within the vertical boundary layers; thus, the response of a lattice with $\overline{W} = 1$ should be a function of $\overline{H}$. The response due to the presence of horizontal boundary layers within the vertical boundary layers is modelled using Eq. (3.54); however $(E^*)_{\rm UC}$ is substituted with $\beta_2(E^*)_{\rm UC}$, where the scalar parameter $\beta_2 < 1$ is introduced to capture the reduced 'local' stiffness of the weak boundary layer, compared to the 'bulk' cells. Thus, the following scaling law is reached

$$\left.\frac{E^*}{(E^*)_{\rm UC}}\right|_{\overline{W}=1} = \alpha = \beta_2 \left(\frac{\beta_1 \overline{H}}{2 + \beta_1(\overline{H} - 2)}\right) \tag{3.56}$$

where the scalar parameters β_1 and β_2 remain to be calibrated from numerical results for $\overline{W} = 1$ lattices.

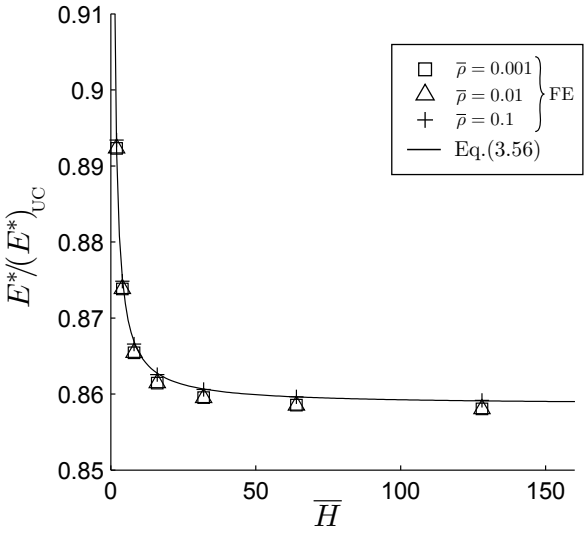

Figure 3.32: Variation of $E^*/(E^*)_{\rm UC}$ with $\overline{H}$ for lattices with $\overline{W} = 1$. Three relative densities are shown $\overline{\rho} = 0.001, 0.01, 0.1$.

Figure 3.32 plots $E^*/(E^*)_{\rm UC}$ against $\overline{H}$, as estimated from FE models, for lattices with $\overline{W} = 1$. As $\overline{H}$ increases, $E^*/(E^*)_{\rm UC}$ is found to converge to 0.8585; this is the value for parameter β_2. By calibrating for best fit, $\beta_1 = 1.04$ is obtained. The scaling law, Eq. (3.56), with the calibrated scalar parameters is also presented in Fig.3.32; an excellent agreement with FE results is demonstrated. Additionally, results for three different rela-

tive densities are shown, which are found to be nearly identical; this observation further supports the earlier statement that $\overline{\rho}$ is insignificant in the edge effects mechanism for Triangular lattices under uniaxial loading.

Finally, to obtain an expression for the combined influence from the presence of horizontal and vertical boundary layers in a lattice of any $\overline{W}$ and $\overline{H}$, Eq. (3.55) is multiplied by (3.54) to give

$$\frac{E^*}{(E^*)_{\text{UC}}} = \left[\frac{\overline{W} - 1 + 2\alpha}{\overline{W} + 1}\right]\left[\frac{\beta_1 \overline{H}}{2 + \beta_1(\overline{H} - 2)}\right] \tag{3.57}$$

where α is given by Eq. (3.56), $\beta_1 = 1.04$ and $\beta_2 = 0.8585$. Equation (3.57) is plotted in Fig. 3.29 against the results from FE models, showing a very good agreement for the entire range of $\overline{W}$ and $\overline{H}$ investigated here.

Equation(3.57) is also plotted for the effective uniaxial strength in Fig. 3.30a; a reasonable agreement with the FE results is obtained. However, the scalar parameter β_2 is found to require adjustment; $\beta_2 = 0.65$ is found to be a more appropriate value. This indicates that the knockdown in effective properties due of the vertical weak boundary layer is more prominent for yield strength compared to stiffness. For example, consider the $\overline{W} = 5$ lattice in Figs. 3.29a and 3.30a; the converged value at high $\overline{H}$ is 0.96 for $E^*/(E^*)_{\text{UC}}$ but only 0.88 for $\sigma_y^*/(\sigma_y^*)_{\text{UC}}$. The loss in accuracy of Eq. (3.57) to predict the effective strength is not surprising, since it is known that the rule-of-mixtures is not very well suited for modelling the strength of composites materials (Jones, 1999). Therefore, in order to model the uniaxial strength of Triangular lattice in a more detailed and accurate manner, alternative theories will have to be used.

3.5.2 Shear

Similarly with the Triangular lattice under axial loading, shear is also studied by employing numerical finite element models. The competing influences of lattice width $\overline{W}$, height $\overline{H}$ and relative density $\overline{\rho}$ are presented first followed by a model to capture the edge effects mechanism.

3.5.2.a Effective Modulus and Yield Strength

Finite element models of Triangular lattices subjected to shear are used to investigate the effect of lattice height $\overline{W}$ and height $\overline{H}$ on the effective shear modulus $G^*/(G^*)_{\text{UC}}$ and strength $\tau^*/(\tau^*)_{\text{UC}}$; the results are summarised in Figs. 3.33 and 3.34, respectively. All results are for lattices with relative density $\overline{\rho} = 0.1$. In a similar manner as the Kagome lattice in shear, see Fig. 3.23, with increasing lattice width, $\overline{W}$, the effective properties approach the corresponding properties of an infinite-sized lattice. Also similarly to the Kagome lattice, the rate of increase of modulus and strength values with $\overline{W}$ depends on $\overline{H}$; the higher the $\overline{H}$, the higher $\overline{W}$ is required to obtain effective properties near the infinite-sized counterparts. These results indicate to a similar edge effects mechanism as the Kagome lattice in shear; i.e. the presence of two vertical weak boundary layers with length l_{BL} and l_{BL} depends on lattice height $\overline{H}$. Consequently, the lattice aspect ratio $\overline{R} = \overline{W}/\overline{H}$ is a significant parameter for the Triangular as well; this will be elucidated later on. A marked difference from the response of the Kagome lattice, is that for $\overline{H} = 2$ lattices, $G^*/(G^*)_{\text{UC}} = \tau^*/(\tau^*)_{\text{UC}} = 1$, regardless of $\overline{W}$.

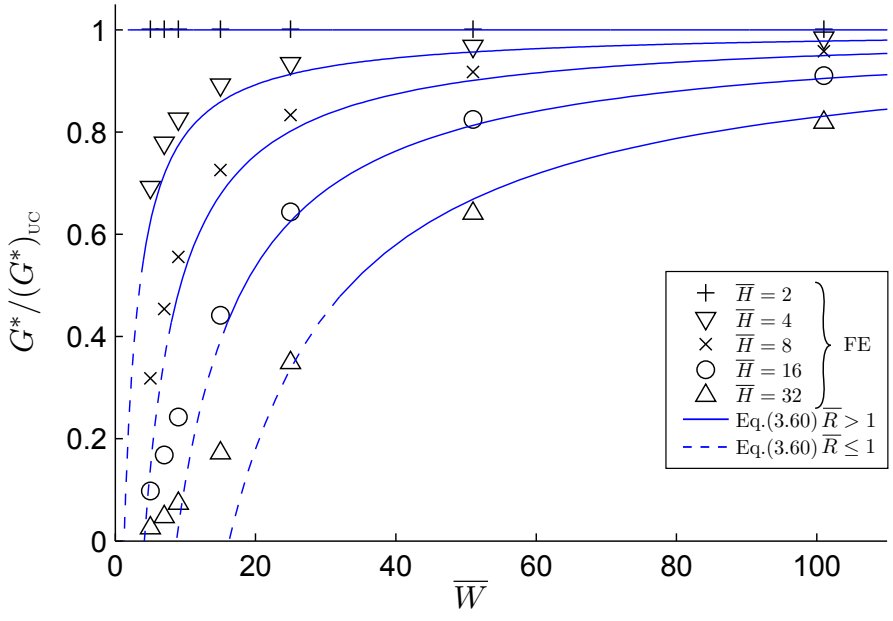

Figure 3.33: Variation of normalised effective shear modulus $G^*/(G^*)_{\text{UC}}$ with $\overline{W}$.

Figure 3.35 shows the variation of G^*/E_s with $\overline{\rho}$ for lattices with $\overline{R} = 1$ and 1/3. The linear dependence for both lattice dimensions is maintained even for $\overline{R} < 1$. This

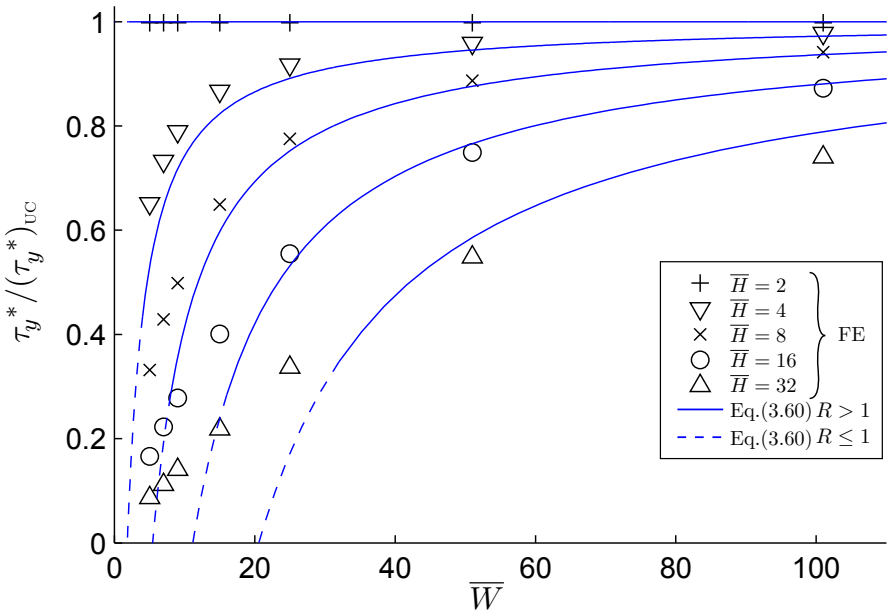

Figure 3.34: Variation of normalised effective shear yield strength $\tau_y^*/(\tau_y^*)_{\rm UC}$ with $\overline{W}$.

indicates that the deformation remains stretch-dominated, even though there is significant knock-down on $G^*/(G^*)_{\rm UC}$; this is also observed from Fig. 3.33, see for example $\overline{H} = 32$ and $\overline{W} < 30$. Consequently, one can safely conclude that $\overline{\rho}$ has absolutely no influence on the edge effects mechanism; this is in contrast with the finding for the Kagome lattice.

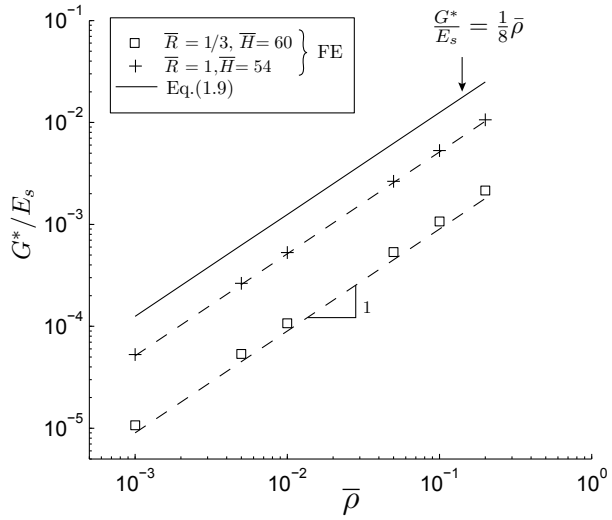

Figure 3.35: Variation of shear modulus G^*/E_s with $\overline{\rho}$ for lattices with low $\overline{R}$.

3.5.2.b Strain maps

To elucidate the mechanism responsible for the dependence of effective properties on specimen size, macroscopic strain maps are generated and shown in Fig 3.36 for lattices of various dimensions. The strain maps plot the effective strain at the cell-scale ($\gamma_{12}^{\text{cell}}$) and not the strain at each individual cell wall. They are generated by using the displacement field estimated from FE; see Appendix C for more details on the procedure. All strain maps are generated for the same applied strain, γ_{12}^{*}, which is within the linear regime of the macroscopic response.

First consider the special case of a lattice with $\overline{H} = 2$; see Fig 3.36a. As it was pointed out above, such lattices are not influenced by edge effects, which is also confirmed here. The macroscopic cell strain is equal to γ_{12}^{*} in all cells of the lattice; this highlights that no boundary layer develops in lattices with $\overline{H} = 2$. The reason behind the lack of boundary layer is believed to be the restricted rotational degree of freedom of all the nodes at the stressed surfaces T and B. By keeping $\overline{W}$ constant and increasing $\overline{H}$, two weak vertical boundary layers at the lateral L and R become evident and their range of influence increases with $\overline{H}$; compare Figs 3.36a, e and b. The weak boundary layers are associated with $\gamma_{12}^{\text{cell}}/\gamma_{12}^{*} < 1$ values, whilst the 'bulk' region with $\gamma_{12}^{\text{cell}}/\gamma_{12}^{*} = 1$.

By studying the deformed FE models of lattices, the cells near the boundaries are found to rotate - similar to a rigid body rotation - without significant deformation. On the other hand, the cells within the bulk of the lattice deform significantly, without any rigid body rotation; however rigid body translation is observed to accommodate the remote applied shear. The difference of the deformation mode between the boundary layers and bulk cells explains why the macroscopic cell strain is significantly lower in the boundary cells.

With further increase of $\overline{H}$, and $\overline{R} < 1$ (see Fig 3.36c and d), the two boundary layers clearly start to interact together and $\gamma_{12}^{\text{cell}}/\gamma_{12}^{*} < 1$ is observed in the entire lattice. The edge effects mechanism for lattices with $\overline{R} < 1$ is clearly different compared to lattices with $\overline{R} > 1$ and it does not involve the presence of weak vertical boundary layers. However, a macroscopic bending mode is superimposed with shear deformation, similarly to what was reported by Diebels and Steeb (2002) for Voronoi lattices. Thus

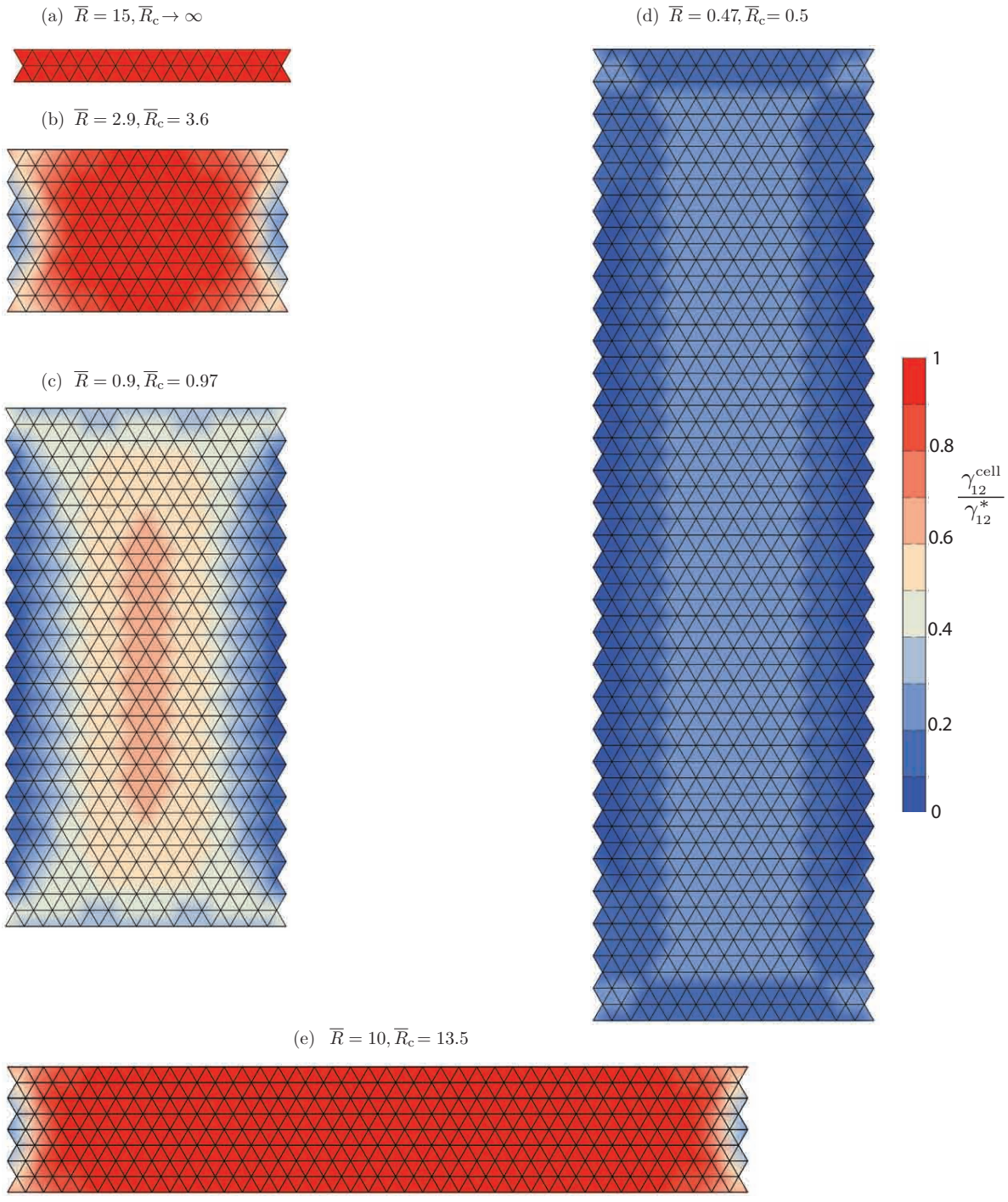

Figure 3.36: Macroscopic strain maps of normalised shear strain $\gamma_{12}^{\text{cell}}/\gamma_{12}^{*}$. The size of the lattices are $\overline{W} = 29$ (a,b,c and d) and $\overline{W} = 59$ (e).

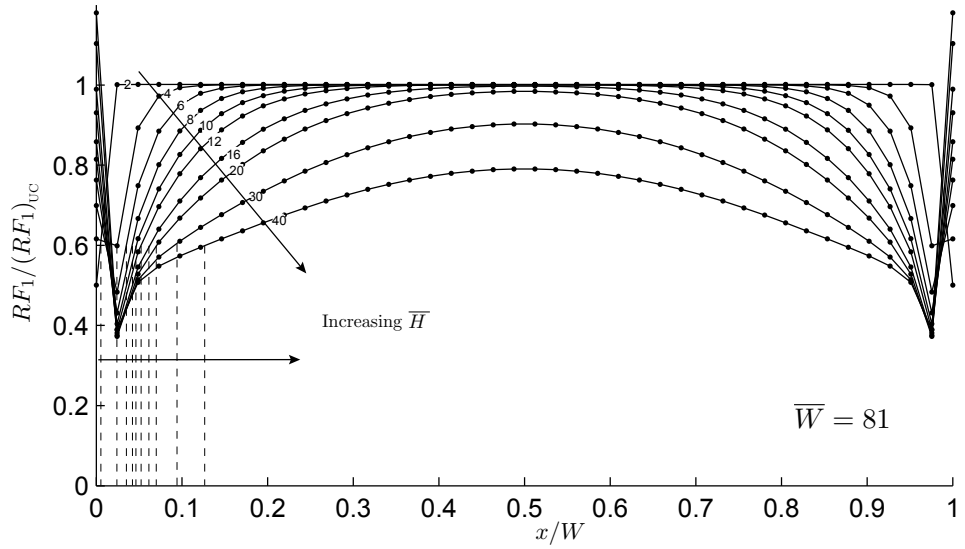

Figure 3.37: Distribution of RF_1 along the stressed surface for lattices of different $\overline{H}$ and constant $\overline{W} = 81$. The dots indicate the presence of boundary nodes. The vertical dashed lines correspond to the border of boundary layer, defined as $RF_1 < 0.6\,(RF_1)_{\rm UC}$.

a significant reduction in $G^*/(G^*)_{\rm UC}$ is observed; Fig. 3.33 shows that the effective modulus of lattices with $\overline{H} = 32$ and $\overline{W} < 30$ is $G^*/(G^*)_{\rm UC} < 0.3$.

3.5.2.c Lattices with $\overline{R} > 1$ - Edge effects model

First, lattices with $\overline{R} > 1$ are considered, in order to develop a model that captures the effect of the weak boundary layers on the macroscopic shear modulus; lattices with $\overline{R} \leq 1$ are considered in Section 3.5.2.d. In a similar manner as the Kagome lattice, the reaction forces along the x_1 direction (RF_1) obtained from finite elements are plotted in Figure 3.37 for the nodes at the T stressed surface. RF_1 is normalised by the corresponding value for an infinite-sized lattice

$$(RF_1)_{\rm UC} = (G^*)_{\rm UC}\, l\gamma_{12}^* \tag{3.58}$$

where γ_{12}^* is the applied remote shear strain, and is chosen in the linear elastic regime. RF_1 is found to be significantly reduced near the L and R surfaces; this is a reflection of the presence of two weak boundary layer emanating from each stress-free surfaces L and R. A smooth increase of RF_1 is observed as one moves from the boundaries

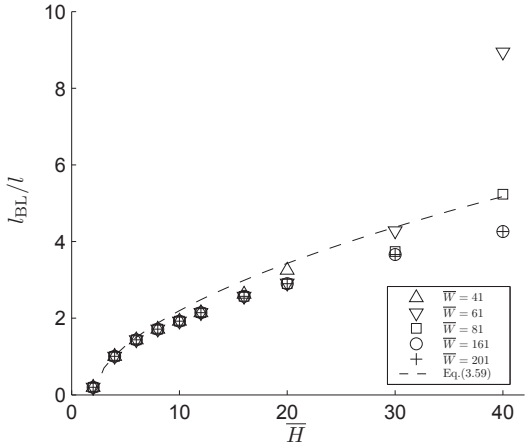

Figure 3.38: Variation of boundary layer length l_{BL} with $\overline{H}$ for Triangular lattice subjected to shear.

into the lattice. In the central part of long enough lattices, $RF_1 = (RF_1)_{\text{UC}}$ as one would expect. In contrast with the Kagome lattice in shear, and Triangular in uniaxial loading, there is no sharp demarcation of the boundary layer. The range of influence of the vertical boundary layer, l_{BL}, is defined here as $RF_1/\left(RF_1\right)_{\text{UC}} < 0.6$; this is shown with dotted lines in Fig. 3.37. As already noted from Fig. 3.36, l_{BL} increases with lattice height $\overline{H}$; however for $\overline{H} = 2$, no boundary layer is obtained, i.e. $l_{\text{BL}} = 0$.

The boundary layer length l_{BL} is plotted against $\overline{H}$ in Fig. 3.38. Lattices with different $\overline{W}$ are found to develop identical boundary layers for the same $\overline{H}$. The dependence of l_{BL} on $\overline{H}$ is modelled using a power law of the form

$$\frac{l_{\text{BL}}}{l} = a(\overline{H} - 2)^b \tag{3.59}$$

where the scalar parameters are calibrated from the numerical FE results; $a = 0.7$ and $b = 0.55$. As $\overline{H} \to \overline{W}$, significant deviation between the FE results and Eq.(3.59) is observed. This indicates that the two vertical boundary layers interact together resulting to a higher l_{BL}; for example the data point for $\overline{W} = 61$ and $\overline{H} = 41$ is well higher than what expected from Eq. (3.59).

An exact scaling law to capture the size effects - in the manner introduced for the Triangular lattice under uniaxial loading - is not possible to be developed here, because of the diffused, rather than sharp, boundary layer. However, the rule-of-mixtures from

Eq. (3.37) is used to give an approximation. The role of the two constituent materials are taken by

1. two vertical boundary layers of total area fraction $A_1/A = 2l_{\text{BL}}/W$ and 'local' modulus $G^* = \beta(G^*)_{\text{UC}}$, where β is a scalar parameter to be calibrated in the range $0 < \beta < 1$; and
2. the 'bulk' region with area fraction $A_2/A = (W - 2l_{\text{BL}})/W$ and 'local' modulus $G^* = (G^*)_{\text{UC}}$

By substituting the above in Eq. (3.37) and using $W = (\overline{W} + 1)/2$, the following scaling law is obtained:

$$\frac{G^*}{(G^*)_{\text{UC}}} = 1 - \frac{4l_{\text{BL}}(1-\beta)}{\overline{W}+1} \tag{3.60}$$

where β is to be determined from calibrating to FE results.

Equation (3.60) is shown in Fig. 3.33 along with the FE results, for the calibrated parameter $\beta = 0.6$; the value of β agrees favourably with the definition of l_{BL}. A reasonably good agreement is achieved, considering that the scaling law captures very roughly the effect of the diffused boundary layers. Additionally, Eq. (3.60) is also found to give a good prediction for the effect of lattice dimensions on the shear yield strength $\tau^*/(\tau^*)_{\text{UC}}$, as shown in Fig. 3.34; however the calibrated parameter needs to be $\beta = 0.3$.

3.5.2.d Lattices with $\overline{R} \leq 1$

Figures 3.33 and 3.34 also plot results for $\overline{R} \leq 1$ lattices; estimates using the scaling law for $\overline{R} \leq 1$ are shown with dashed line. It is not surprising that Eq. (3.60) fails to accurately predict the FE results for $\overline{R} \leq 1$ lattices and large deviation are observed. To quantify the edge effects for lattices of any $\overline{R}$, the results from FE models are presented on a contour plot of $G^*/(G^*)_{\text{UC}}$ in the $\overline{W}$ and $\overline{H}$ space, shown in Figure 3.39a. As expected, the contour line $G^*/(G^*)_{\text{UC}} = 1$ coincides with a horizontal line passing through $\overline{H} = 2$. All the other contour lines fall on straight lines with origin at $\overline{W} = \overline{H} = 0$; for example for lattices with $\overline{W} = \overline{H}$, the knockdown in modulus is $G^*/(G^*)_{\text{UC}} \approx 0.45$, regardless of $\overline{W}$. As $\overline{R}$ decreases < 1, there is no lower bound

for $G^*/(G^*)_{\text{UC}}$; however, as it was noted above, a bending-dominated response is never obtained for the Triangular lattice in shear, regardless of $\overline{R}$, see Fig. 3.35.

3.6 Comparison of lattice micro-architectures

The responsible mechanisms for the edge effects presented in this Chapter are compared with the corresponding mechanisms for other lattice micro-architectures, for which results already exist in literature. For the bending dominated micro-architectures – periodic Hexagonal and stochastic Voronoi – the impact of edge effects was quantified for the uniaxial modulus against $\overline{W}$ and for shear modulus against $\overline{H}$; the combined effect of both $\overline{W}$ and $\overline{H}$ has not been reported. Onck et al. (2001) investigated edge effects for periodic Hexagonal lattices analytically whilst the stochastic Voronoi lattices were studied numerically by Tekoglu et al. (2011). Lastly, results for the presence of edge effects in Diamond lattices, subjected to uniaxial and shear loading have been addressed by (Zupan et al., 2004); both E^* and G^* were found to exhibit a dependence on aspect ratio W/H. Hence, the comparison that follows does not directly compare the Diamond lattice with Hexagonal and Voronoi lattices.

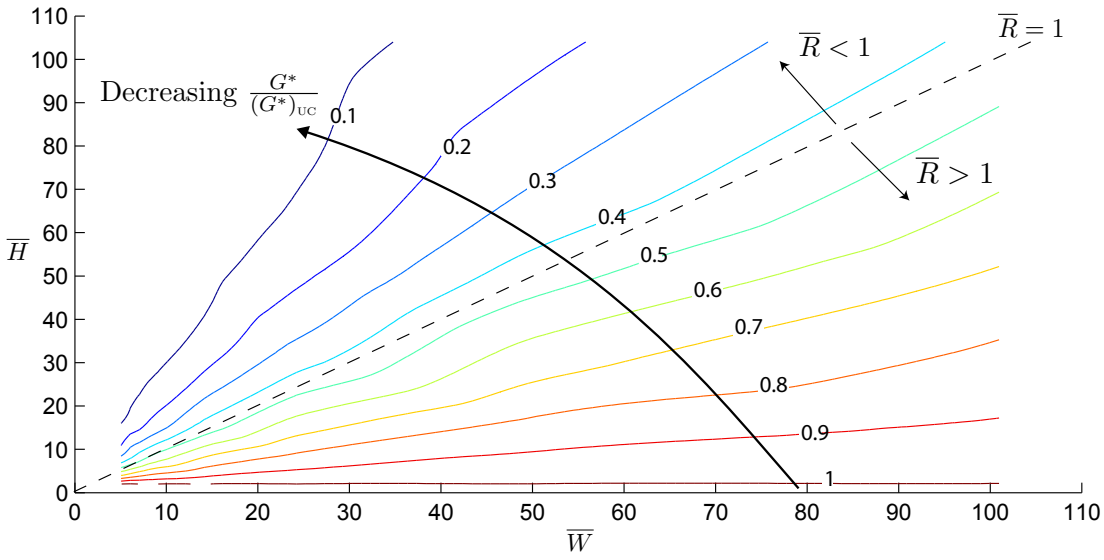

Figure 3.39: Contour plot of $G^*/(G^*)_{\text{UC}}$ in the ($\overline{W}$–$\overline{H}$) space.

3.6.1 Bending dominated lattices

3.6.1.a Uniaxial loading

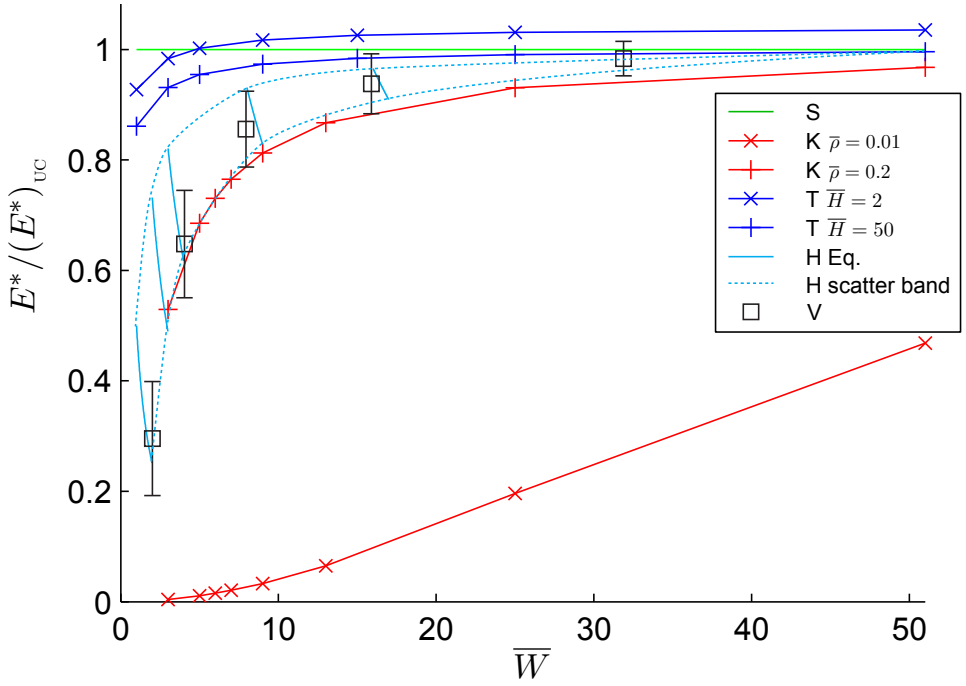

Figure 3.40: Effect of lattice width $\overline{W}$ on the uniaxial modulus for Square (S), Kagome (K), Triangular (T), Hexagonal (H) and Voronoi (V) lattices. For Voronoi lattices, the mean and $\pm$ one standard deviation are shown.

Figure 3.40 plots the effective uniaxial modulus $E^*/(E^*)_{\mathrm{UC}}$ against $\overline{W}$ for the three periodic lattices studied here, along with the results for Hexagonal and Voronoi lattices. The size effects equation for Hexagonal lattices given by Onck et al. (2001) is a discontinuous function for different $\overline{W}$; these are listed in Table 3.5 and reproduced in Figure 3.40. Consequently, a 'scatter-band' is formed that captures the influence of $\overline{W}$ on E^*; this is plotted with dotted lines. The numerical results for Voronoi lattices follow a similar trend; the error-bars indicates the standard deviation. Both Hexagonal and Voronoi lattices are found to develop a weak boundary layer at the two stress-free surfaces, L and R, of fixed length, which are responsible for the decrease of $E^*/(E^*)_{\mathrm{UC}}$ for lattices with low $\overline{W}$.

Of the three periodic lattices investigated here, only the Kagome lattice shows similar weak boundary layers that span several cells from the L and R surfaces. The length of the boundary layer in a Kagome lattice, l_{BBL}, is found to depend on $\overline{\rho}$ (Eq.

	$1 \leq \overline{W} < 2$	$2 \leq \overline{W} < 3$	$3 \leq \overline{W} < 4$	$8 \leq \overline{W} < 9$	$16 \leq \overline{W} < 17$
$\frac{E^*}{(E^*)_{\mathrm{UC}}}$	$\frac{1}{2\overline{W}}$	$\frac{41}{28\overline{W}}$	$\frac{165}{67\overline{W}}$	$\frac{7.45}{\overline{W}}$	$\frac{15.45}{\overline{W}}$

Table 3.5: Size effect for $E^*/(E^*)_{\mathrm{UC}}$ of periodic Hexagonal lattices as a function of $\overline{W}$ (Onck et al., 2001).

(3.47)), unlike the bending dominated lattices. For Kagome lattice of high relative density, say $\overline{\rho} = 0.2$, the influence of edge effect is similar, quantitatively, to the bending dominated lattices. On the other hand, low density Kagome lattices, say $\overline{\rho} = 0.01$, show a completely differently response, with much greater reduction in $E^*/(E^*)_{\mathrm{UC}}$, because the weak boundary layers has a much larger range of influence. For the stretch-dominated Triangular lattice, the edge effects are significantly less pronounced than any other lattice micro-architecture; both $\overline{W}$ and $\overline{H}$ have little influence over its effective $E^*/(E^*)_{\mathrm{UC}}$. The mechanism behind the edge effects in Triangular lattices is associated with the presence of vertical weak boundary layers that span half-cell in width and horizontal stiff boundary layer of one cell in height. Lastly, the Square lattice is unaffected by edge effects.

3.6.1.b Shear loading

For the Hexagonal lattice, an analytical solutions for $G^*/(G^*)_{\mathrm{UC}}$ is presented by Onck et al. (2001) for lattice with $1 \leq \overline{H} \leq 3$; shown in Fig 3.41. Only values for $c = 0.5$ are shown, since $c = 0.5$ is the case for which edge effects have the most influence on $G^*/(G^*)_{\mathrm{UC}}$; c is the equivalent to parameter λ for the Hexagonal lattice as studied by (Onck et al., 2001, p.692). Significant stiffening of the Hexagonal lattice is reported, with up to $G^*/(G^*)_{\mathrm{UC}} = 4.2$ for $\overline{H} = 1$. A similar trend is reported for Voronoi lattices. The edge effect mechanism, for both Hexagonal and Voronoi lattices, is associated with the presence of strong boundary layers at the stressed surfaces T and B.

Among the three periodic lattices studied here, the Square lattice exhibits the most similar edge effect mechanism to the Hexagonal and Voronoi lattices. This is not surprising, since the Square lattice subjected to shear is a bending-dominated micro-architecture. However, the stiffening effect for the Square lattice is significantly less

pronounced compared the Hexagonal lattice, only $G^*/(G^*)_{\mathrm{UC}} = 1.8$; this is for $\lambda = 0.5$ and $\overline{W} \to \infty$.

For Kagome and Triangular lattices subjected to shear, the aspect ratio $\overline{R}$ – and not $\overline{H}$ – is the most important dimensional measure that characterises edge effects. For both lattices, the mechanism responsible for edge effects is the weak boundary layers that emanate from the stress-free surfaces, L and R, with range of influence that depends on $\overline{H}$. The boundary layer induced in a Kagome lattice exhibits a clear demarcation for sufficiently low $\overline{\rho}$, while a transition zone appears for higher $\overline{\rho}$. In a Triangular lattice, $\overline{\rho}$ is found to have no influence on the edge effect mechanism. For lattices where $\overline{R} >> 1$, the size of the boundary layers is rather small for both lattice mirco-architectures, and the influence of edge effects is negligible, hence $G^*/(G^*)_{\mathrm{UC}} \approx 1$. For $\overline{R} = 1$, the weak boundary layers cover the entire length of the lattice, and $G^*/(G^*)_{\mathrm{UC}} \approx 0.5$ with decreasing $\overline{\rho}$; this is observed both Kagome and Triangular lattices.

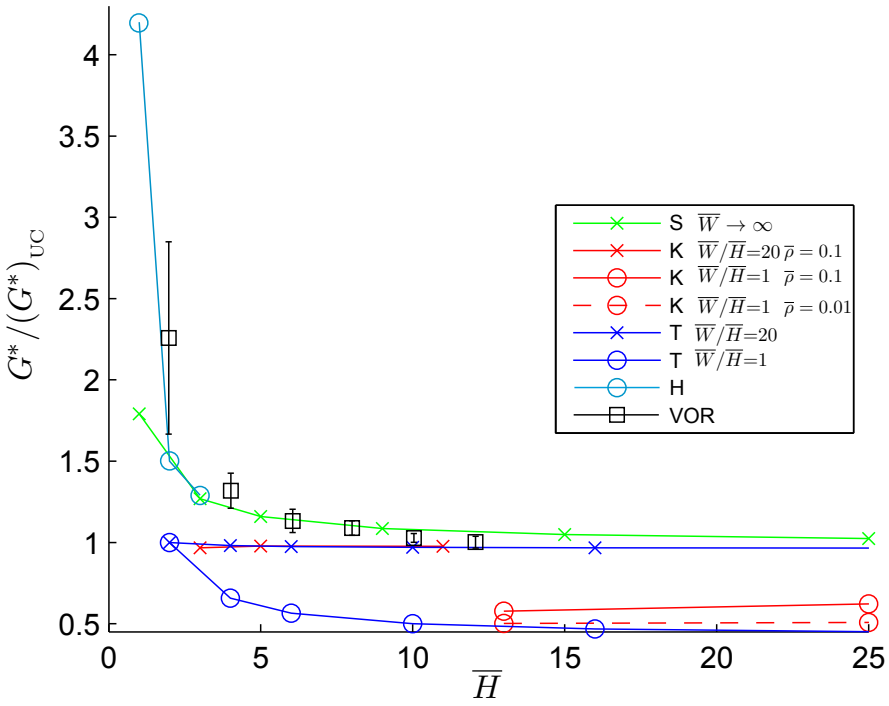

Figure 3.41: Effect of lattice height $\overline{H}$ on the shear modulus for Square (S), Kagome (K), Triangular (T), Hexagonal (H) and Voronoi (V) lattices. For Voronoi lattices, the mean and $\pm$ one standard deviation are shown.

3.6.2 Diamond lattice

The edge effects mechanism in a Diamond lattice is in the form of an angular boundary layer at the lateral L and R stress free boundaries of the lattice. The length of these regions, along x_1 axis, is $l_{\text{BBL}} = H$. Consequently, the uniaxial and shear moduli, $E^*/(E^*)_{\text{UC}}$ and $G^*/(G^*)_{\text{UC}}$, of a Diamond lattice dependent on both $\overline{W}$ and $\overline{H}$. The dependence of effective properties on lattice size is described by (Zupan et al., 2004)

$$\frac{E^*}{(E^*)_{\text{UC}}} = \frac{G^*}{(G^*)_{\text{UC}}} = \left(1 - \frac{1}{(\overline{W}/\overline{H})}\right) \quad \overline{W}/\overline{H} > 1 \tag{3.61}$$

The three lattice studied here, subjected to shear, are compared with the Diamond lattice in Fig 3.42.

The edge effects mechanism in a Diamond lattice is also observed in Kagome lattices subjected to shear. Due to the differences in micro-architecture, $l_{\text{BBL}} = \sqrt{3}H/3$ in a Kagome lattice. As a result, the reduction in $G^*/(G^*)_{\text{UC}}$ with decreasing $\overline{R}$ is lower compared to a Diamond lattice. The Triangular lattice subjected to shear also shows a dependence on $\overline{R}$, however the responsible mechanism is different. Two vertical weak boundary layers emanate from the L and R surfaces, whose range of influence depends on $\overline{H}$ and have no sharp border with the 'bulk' region. The Square lattice subjected to shear is also found to have a minor dependence on $\overline{R}$. The mechanism behind it is completely different than the other three lattices. The dependence on $\overline{W}$ arises from the presence of weak boundary layers at the L and R surfaces, that span for only one cell, whilst the dependence on $\overline{H}$ is due to the stiff boundary layer at the stressed surface that diminishes after one cell. Consequently, the size effect becomes considerable only for $\overline{R} << 1$.

For Kagome and Triangular lattices with $\overline{R} < 1$, the macroscopic bending mode becomes dominant, and $G^*/(G^*)_{\text{UC}}$ decreases significantly with decreasing $\overline{R}$. For sufficiently low $\overline{\rho}$, the Kagome lattice becomes a bending-dominated micro-architecture, and G^*/E_s scales with $\overline{\rho}^3$. On the other hand, the Triangular lattice is always a stretch-dominated micro-architecture, regardless of the knockdown on $G^*/(G^*)_{\text{UC}}$.

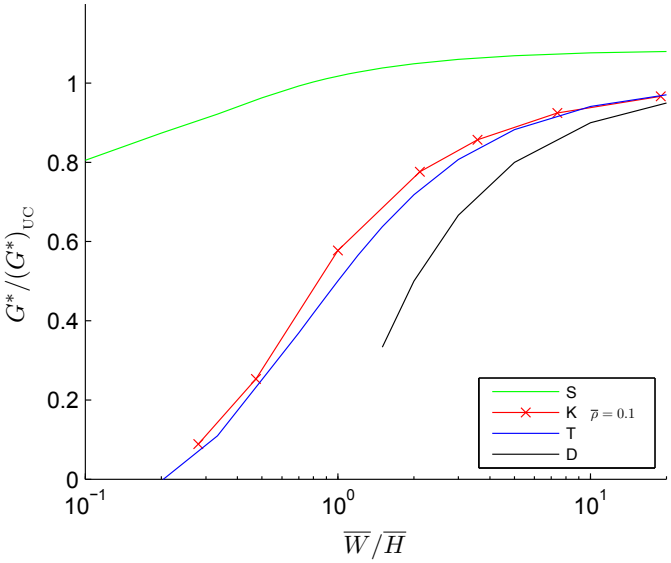

Figure 3.42: Variation of $G^*/(G^*)_{\mathrm{UC}}$ with $\overline{R}$ for Square (S), Kagome (K), Triangular (T) and Diamond (D) lattices

3.7 Summary

In conclusion, a brief comparison between the mechanisms responsible for edge effects for each of the lattices is presented here. Universally, horizontal and vertical boundary layers are found to emanate from the stressed (T and B) and stress-free (L and R) surfaces, respectively. The range of influence of these boundary layers in some cases is constant or may vary with lattice dimensions and/or relative density, depending on the lattice micro-architecture and the imposed loading. Table 3.6 summarises the range of influence of the boundary layers for all three lattice micro-architectures. Their size is noted by l_{H} and l_{V} for the horizontal and vertical boundary layers respectively.

The presence of vertical boundary layers results to a size dependence on lattice width $\overline{W}$. On the other hand, horizontal boundary layers result to a size dependence on lattice height $\overline{H}$, respectively. The vertical boundary layers that originate from the stress-free surfaces, are always weaker than the bulk region of the lattice. Conversely, the horizontal boundary layers are found to always be stiffer than the bulk region. Also listed in the Table 3.6 is which of the lattice dimensional measures influence the macroscopic response of a finite-sized lattice compared to its infinite-sized counterpart. These are classified as of major or minor importance, indicated by ● and • respectively.

Lattice	Loading	$\overline{W}$	$\overline{H}$	$\overline{R}$	$\overline{\rho}$	l_{V}/l	l_{H}/l	Notes
Square	σ^*_{22}							
	τ^*_{12}	•	●			1	>1	The majority of contribution in the horizontal boundary layer is confined to a single cell.
Kagome	σ^*_{22}	●			●	$10/(8\overline{\rho})$		For low $\overline{\rho}$, the deformation is bending dominated; $E^*/E_s \propto \overline{\rho}^3$.
	τ^*_{12}			●	•		$(\overline{H}+1)$	This is only strictly applicable for very low $\overline{\rho}$; for moderate to high $\overline{\rho}$, strong transition zones are formed that reduces the impact of the boundary layer. For $\overline{R} < 1$, the deformation is bending dominated; $G^*/E_s \propto \overline{\rho}^3$.
Triangular	σ^*_{22}	•	•			1/2	1	
	τ^*_{12}		•	●		>1		Vertical boundary layers form only for $\overline{R} > 1$ and $\overline{H} > 2$. For $\overline{R} \leq 1$, the macroscopic bending mechanism is dominant.

Table 3.6: Summary of the dimensions of vertical l_{V} and horizontal l_{H} boundary layers and which lattice dimensions are influential in edge effects, classified as of ● major or (•) minor importance.

Chapter 4

Fatigue response of periodic lattices

4.1 Introduction

In this Chapter, the *constant amplitude* fatigue response of periodic lattices – Triangular (T), Kagome (K), Diamond (D), Square (S) and Hexagonal (H) – to cyclic shear and uniaxial compression-compression (C-C) loadings will be investigated. Finite element simulations are carried out using ABAQUS/Standard (a commercial FE package) where a non-linear continuous fatigue damage model, modified to incorporate nonlocal material damage, is implemented into the FE models of the lattices from previous Chapters.

Existing experimental data on the fatigue life of lattices deals primarily with stochastic (non-periodic) foams; various authors have studied the shear, compression-compression (C-C) and tension-tension (T-T) fatigue response of stochastic foams – both closed and open cells – and their key results are summarised in Table 1.2. The exceptions are recent works by Cote et al. (2007a,b) on the cyclic shear response of sandwich beams with a Diamond and Pyramidal core. Based on their results, Cote et al. (2007a) concluded that micro-architecture plays an insignificant role on the fatigue performance of periodic lattices. A numerical approach, using FE, will be employed here to establish whether this is indeed the case by simulating the fatigue response of other periodic micro-architectures. Harte et al. (2001) has previously shown that stochastic foams exhibit significantly shorter fatigue life and lower endurance strength under cyclic shear compared to C-C loading; it is, as yet, unclear whether the same, and to what extent, also applies to periodic lattices.

Five different periodic micro-architectures are investigated in this study. The current work will also establish how the presence, and severity, of imperfections affect the fatigue performance and endurance strength of these periodic lattices; the results will be

used to define upper and lower limits for the fatigue life of real periodic lattices (lattices with slight imperfections). The mechanisms that are responsible for the differences in fatigue life and endurance strength between the different lattice micro-architectures, and the effects of imperfections, will be elucidated in this work.

4.2 Methodology

In this section, the methodology employed in this study – including terminologies, FE models set-up, non-linear continuous damage model, and the coupling between the former and latter to account for nonlocal material damage – will be presented.

Table 4.1 lists the dimensions of the lattices that are modelled in FE: they are expressed in terms of the number of *complete* cells along their width and height. The size of each lattice is decided based on a compromise between minimising edge effects (on their modulus and yield strength) – these were addressed in Chapter 3 – and to keep the simulation times manageable.

	Diamond (D)	Triangular (T)	Kagome (K)	Square (S)	Hexagonal (H)
$\overline{W}$	20	21	20	20	15
$\overline{H}$	3	6	5	7	9

Table 4.1: Dimensions of the lattices (in terms of number of *complete* cells along their width and height) modelled in FE for the fatigue simulations

4.2.1 Preliminaries

4.2.1.a Terminologies

Figure 4.1 shows a typical *constant amplitude* stress-time loading history that is used in this study. For regular *constant amplitude* loading cycle of period T, the load varies between a maximum (σ_{max}) and minimum (σ_{min}) value. Note that material strain rate sensitivity and their time-dependent behaviour are not considered here. Hence, the time variable t can be normalised by the period T to give the number of cycles, viz. $N \triangleq t/T$. The exact functional form of the loading/unloading curve is not important in the following analysis since all the parameters that are needed to characterise the cyclic load are functions of σ_{max} and σ_{min}.

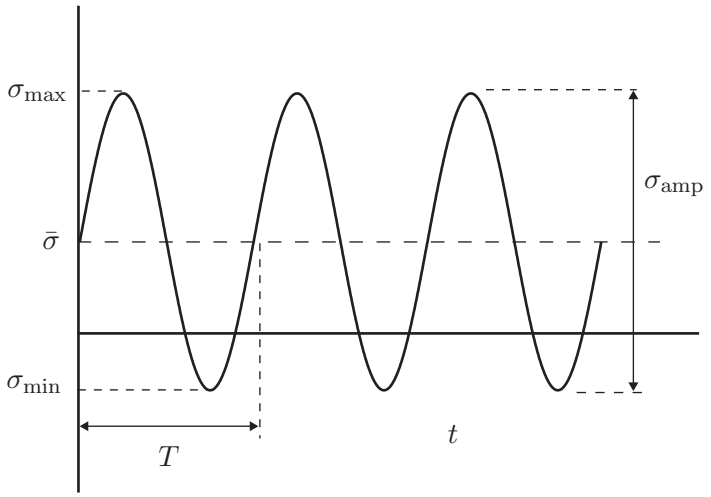

Figure 4.1: A regular *constant amplitude* stress-time loading history with $R < 0$ and $\bar{\sigma} > 0$.

The *load ratio* R is defined as the ratio of the minimum to maximum stress given by

$$R \triangleq \frac{\sigma_{\text{min}}}{\sigma_{\text{max}}} \tag{4.1}$$

where $R > 0$ refers either to compressive-compressive (C-C) or tension-tension (T-T) loading; whilst $R < 0$ refers to alternate compressive-tension cyclic loadings. The parameters σ_{max} and R are sufficient to fully define a regular load cycle. Two additional parameters that are commonly used along with the aforementioned are the *mean stress* ($\bar{\sigma}$) and *stress amplitude* (σ_{amp}) given by

$$\bar{\sigma} \triangleq \frac{\sigma_{\text{min}} + \sigma_{\text{max}}}{2} = \frac{\sigma_{\text{max}}}{2}(1 + R) \tag{4.2}$$

and

$$\sigma_{\text{amp}} \triangleq \frac{\sigma_{\text{max}} - \sigma_{\text{min}}}{2} = \frac{\sigma_{\text{max}}}{2}(1 - R). \tag{4.3}$$

Existing experimental data on the fatigue performance of materials are typically presented in the form of $S - N$ curves that plots σ_{max} against the number of *cycles-to-failure* (N_f) for a given load ratio R. The $S - N$ curve approach is only applicable to high-cycle fatigue situations where the number of cycles to failure, typically, exceeds $N_f > \times 10^3$ (Bannantine et al., 1989): this will be the case in the present study. The

maximum stress σ_{max} that does not cause fatigue failure for $N < N_e$, is termed the *fatigue endurance strength* σ_{e}; in this study $N_e = 2 \times 10^7$ is adopted.

In order to distinguish between macro- and micro- level responses, and their corresponding variables, the superscript $(\,)^*$ is used here to denote macro-level effects, this is the same as with previous Chapters. However, the subscript $(\,)_{\text{s}}$, used previously to denote micro-level effects, is dropped here for the sake of brevity. The maximum stress σ^*_{max} is typically normalised by a reference material strength obtained from monotonic loading. In the case of foams and lattices, their peak stress σ^*_p are often used as the reference material strength. Here, in this study, this peak stress is the yield strength σ^*_y of the lattices, extracted using a method described previously in Chapter 2.

4.2.1.b Damage parameters

Following Kachanov (1986), a scalar isotropic damage parameter is introduced as follows:

$$\omega \triangleq \frac{A}{A_1} \tag{4.4}$$

where A and A_1 is the damaged and initial (undamaged) cross-sectional area of the strut, respectively. By using the concept of actual stress, Eq.(4.4) can be rewritten as

$$\omega = 1 - \frac{E}{E_1} \quad , \quad 0 \leq \omega \leq 1 \quad . \tag{4.5}$$

where E and E_1 is the modulus of the damaged and undamaged strut, respectively. Note that ω is a monotonically increasing parameter; $\omega = 0$ corresponds to an undamaged strut whilst $\omega = 1$ corresponds to a fully damaged (failed) strut that has lost its load carrying capacity completely. Since ω is directly related with a reduction in elastic modulus, it is referred to as the 'modulus damage' parameter.

In a similar vein, a modulus damage parameter may also be defined on the macro-level given by

$$\omega^* = 1 - \frac{E^*}{E^*_1} \qquad 0 \leq \omega \leq 1 \tag{4.6}$$

where E_1^* corresponds the macroscopic modulus of an undamaged lattice at $N = 1$. Similarly, for cyclic shear, it follows that $\omega^* = 1 - G^*/G_1^*$. $\omega^* = 1$ indicates that complete macro-level failure has occurred for the lattice which is no longer able to sustain any further loading. In the present study, complete macro-level failure is assumed to occur when $\omega^* = 0.9$ is reached and the corresponding load cycle at which this occurs is the number of cycles to failure N_f^*.

The non-linear continuous damage model - this is addressed later in Section 4.2.4 - makes use of a 'fatigue damage parameter' D. This should not be confused with ω, even though it will be shown later on that there is a one-to-one correspondence between these two parameters. Note that during cyclic loading, damage accumulation occurs within the constituent struts of a lattice; hence, it is important to stress that, D is only defined at the micro-level. The fatigue damage parameter D is associated with the remaining life of a strut, i.e. cycles to N_f, instead of damaged area used to characterise ω. Thus, $D = 0$ denotes an undamaged (pristine) strut, whilst $D = 1$ indicates that the strut has ruptured and reached the end of its fatigue life.

4.2.2 Overview of approach

Figure 4.2 gives an overview of the approach – details of each individual elements are covered later – adopted in this study. Finite element (FE) models are generated for each lattice micro-architecture in ABAQUS/Standard. Regular cyclic macroscopic loading of *constant amplitude* is imposed to each of these models, which depends on the user-defined macroscopic load ratio R^*, and either $\sigma^*_{\text{max}}/\sigma^*_y$ (C-C loading) or $\tau^*_{\text{max}}/\tau^*_y$ (shear loading). The reference material strength, σ^*_y and τ^*_y, needed for the normalisation are to be determined a priori from their monotonic stress-strain response: this is also obtained using FE. Details of the FE model set-up are given in Section 4.2.3. The stress distribution in each strut are calculated by FE at the two extreme load levels, viz. σ_{max} and σ_{min}. These information are next used to calculate the fatigue damage parameter D and the modulus damage parameter ω in each strut by the non-linear continuous damage (NLCD) model, to be covered in Section 4.2.4. To circumvent the mesh convergence issue that is often associated with numerical simulations of damage, a nonlocal damage scheme – presented in Section 4.2.5 – is implemented. With increasing number of load

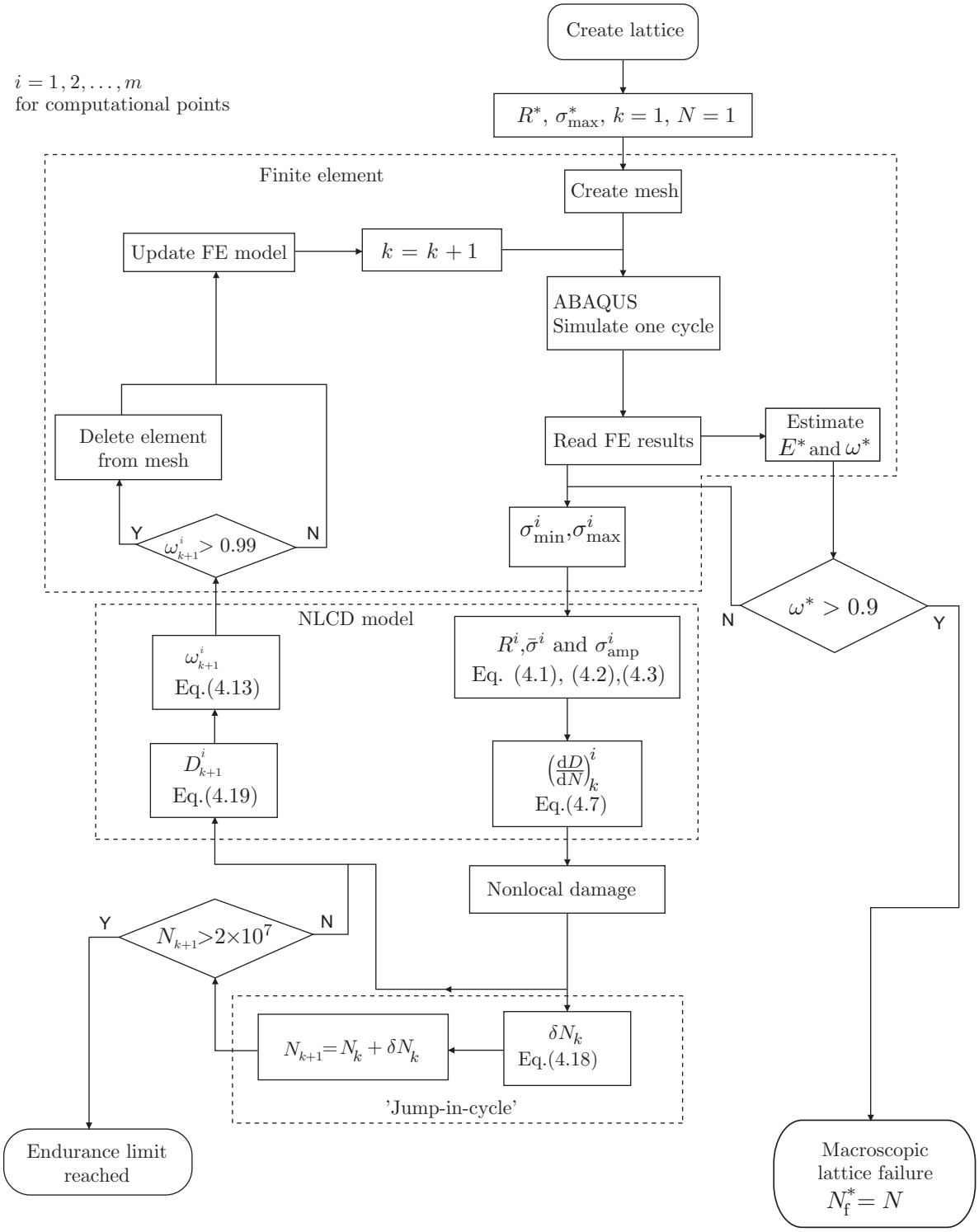

Figure 4.2: Overview of the non-linear continuous damage (NLCD) - finite element (FE) computational scheme.

cycle N, the modulus damage ω in each strut increases monotonically; this leads to a corresponding monotonic increase in macroscopic modulus damage ω^* of the lattice. Simulation continues until complete macro-level failure occurs at $\omega^* = 0.9$. Since it is practically impossible to simulate every load cycle in a fatigue 'numerical experiment', a technique known as a 'jump-in-cycle' has been implemented - details of which are given in Section 4.2.6.

The NLCD-FE scheme was implemented in a DELL workstation equipped with 6-core Intel Zeon 3.33Ghz processor and 24GB of memory. For the specimen sizes that were modelled, the computational time for an analysis for a specified macroscopic load ratio R^* and $\sigma^*_{\text{max}}/\sigma^*_y$ (C-C loading) or $\tau^*_{\text{max}}/\tau^*_y$ (shear loading) varies between 4 hours for a Square lattice to 12 hours for the more complex Kagome lattice. For some analyses involving larger lattices - see Section 4.6.4 - the computational times were found to increase by six fold when doubling the specimen size. Such long computational times were too prohibitive for the current study, thus the specimen sizes were chosen as per Table 4.1.

4.2.3 Set-up of FE models

Finite element (FE) models of the periodic lattices, with dimensions listed in Table 4.1, are generated in ABAQUS/Standard (a commercial FE package): their details were previously described in Chapter 3 and are not repeated here. Cyclic loading is applied to the lattice – in a load-controlled manner – through traction boundary conditions imposed on the surface nodes in ∂V^T (or Top or T), see Fig. 3.2.2. The macro-level stresses, viz. σ^*_{22} or τ^*_{12}, that were applied to the FE models are pre-determined by the user-prescribed load ratio of R^* and the maximum macroscopic stresses of either $\sigma^*_{\text{max}}/\sigma^*_y$ (C-C loading) or $\tau^*_{\text{max}}/\tau^*_y$ (shear loading). The overall fatigue response of a lattice is characterised by monitoring its macroscopic damage parameter ω^* (see Eq.(4.6)) with the number of cycles. Its macroscopic elastic modulus is estimated by measuring the macroscopic strain accumulation $\varepsilon^*_{\text{max}}$ with the number of cycles.

The FE mesh comprises of m number of B22, using standard ABAQUS terminology, beam elements per strut (or cell wall); the number of elements m needed to give converged results will be addressed in Section 4.3.3. Unlike the B21 beam elements used

previously in Chapters 2 and 3, these are also Timoshenko (shear flexible) beam elements but with a quadratic interpolation function and two integration points. Since this is a stress-based fatigue damage analysis, a higher-order element is needed here to accurately model the internal stress state of each strut.

4.2.4 Fatigue damage model

A non-linear continuous damage (NLCD) model, first introduced by Chaboche and Lesne (1988), is coupled to the FE model to capture the cumulative effects of fatigue damage on the micro-scale, for each of the constituent struts that make up a lattice. A generic version of the NLCD model is first presented in Section 4.2.4.a and the specifics of how it is to be coupled with the aforesaid FE models are presented later in Section 4.2.4.c. It is worth emphasising that all the parameters of the NLCD model are micro-level quantities and the material properties are those of the strut (or cell wall) material.

4.2.4.a NLCD model

The NLCD model that has been implemented in this study was originally developed by Chaboche and Lesne (1988) to capture both fatigue damage initiation and fatigue damage propagation. Recall that the fatigue damage parameter D of a strut is associated with its remaining cycles to failure. Hence, the damage accumulation rate $\mathrm{d}D/\mathrm{d}N$ in a strut may be expressed as a function of the state of damage D and the load cycle parameters (σ_{max} and $\bar{\sigma}$) as follows:

$$\frac{\mathrm{d}D}{\mathrm{d}N} = D^{\alpha(\sigma_{\text{max}},\bar{\sigma})} \left[\frac{\sigma_{\text{max}} - \bar{\sigma}}{M(\bar{\sigma})}\right]^{\beta} \tag{4.7}$$

where α and M are functions of the load cycle parameters and β is a scalar parameter to be calibrated to experimental data in Section 4.3.1. Like all continuum damage models, the damage accumulation rate is always positive so that $(\mathrm{d}D/\mathrm{d}N) > 0$. By integrating Eq.(4.7) from $D = 0$ (at $N = 1$) to complete strut rupture when $D = 1$ (at $N = N_f$) the total number of cycles-to-failure of a strut can be found as follows:

$$N_f = \frac{1}{1-\alpha(\sigma_{\max},\bar{\sigma})}\left[\frac{\sigma_{\max}-\bar{\sigma}}{M(\bar{\sigma})}\right]^{-\beta} \quad . \tag{4.8}$$

The function M takes the form of

$$M\left(\bar{\sigma}\right) = M_0(1-b\bar{\sigma}) \tag{4.9}$$

where b and M_0 are scalar parameters to be calibrated in Section 4.3.1. Various forms of the function α have been proposed in the literature; in this study, we adopt the one suggested by Chaboche and Lesne (1988) and Dattoma et al. (2006) as follows:

$$\alpha(\sigma_{\max},\bar{\sigma}) = 1 - c\left\langle\frac{\sigma_{\max}-\sigma_{\mathrm{e}}(\bar{\sigma})}{\sigma_{\mathrm{u}}-\sigma_{\max}}\right\rangle \tag{4.10}$$

where c is, again, another scalar parameter to be calibrated to experimental data in Section 4.3.1, σ_{u} is the ultimate tensile strength and σ_{e} is the fatigue endurance strength of the strut (or parent) material. The piecewise function $\langle g\rangle$ in Eq.(4.10) is defined as:

$$\langle g\rangle = \begin{cases} 0 & g \le 0 \\ g & g > 0 \end{cases} \quad . \tag{4.11}$$

If $\sigma_{\max} < \sigma_{\mathrm{e}}$, it follows from Eq.(4.10) that $\alpha = 1$, and Eq.(4.8) predicts an infinite N_f, as required. The fatigue endurance strength is known to depend on the mean stress $\bar{\sigma}$, which is given by (Chaboche and Lesne, 1988)

$$\sigma_{\mathrm{e}}(\bar{\sigma}) = \bar{\sigma} + (1-b\bar{\sigma})\sigma_{\mathrm{e}_0} \tag{4.12}$$

where b is the same scalar parameter that also appears in Eq.(4.9) and σ_{e_0} is the fatigue endurance strength that corresponds to a fully reversed load cycle of $\sigma_{\max} = -\sigma_{\min}$ and $R = -1$.

4.2.4.b Relationship between ω and D

Equations (4.7)–(4.12) are sufficient to estimate the accumulation of fatigue damage D at the micro-level but the modulus damage parameter ω had not been addressed.

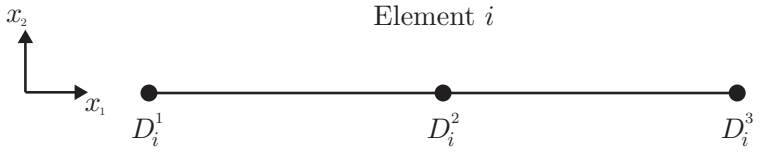

Figure 4.3: The locations in a B22 beam element where the fatigue damage parameter D_i^j are computed.

Chaboche and Lesne (1988) have shown that there is, indeed, a one-to-one correspondence between D and ω given by

$$\omega = 1 - (1 - D)^{\frac{1}{\beta+1}} \quad . \tag{4.13}$$

Equation (4.13) is used to link D and ω in the present study.

4.2.4.c NLCD-FE coupling

The FE model predicts the internal state of stress for each element; this information is used to calculate σ_{max}, σ_{min}, $\bar{\sigma}$ and R for every element in the corresponding FE mesh. For every beam element, these four parameters are computed at three locations, viz. both nodes and the mid-span, as shown in Fig. 4.3. In the computation of the aforementioned, the linear stress variation through the transverse (or thickness) x_2 direction of each element is ignored. Instead, the maximum absolute stress – one that develops along the outermost fibre of each element – is used; this leads to a tacit assumption that tensile and compressive stresses cause the same fatigue damage.

With the load cycle of each element fully defined, the NLCD model estimates the damage accumulation rate $\mathrm{d}D/\mathrm{d}N$ – using Eq.(4.7) – at the three aforementioned locations for every element. To avoid the mesh convergence issues, a nonlocal approach is implemented to perform the 'spatial-averaging' of $\mathrm{d}D/\mathrm{d}N$ across elements: the procedure is described in Section 4.2.5. With $\mathrm{d}D/\mathrm{d}N$ known, D is calculated by integrating Eq. (4.7) over a number of a jump-in-cycle δN. For every ith element, the fatigue damage parameter D_i^j ($j = 1, 2, 3$) is computed at the three locations. Since, a single ω_i parameter is needed to characterise each element, this will be obtained by averaging D_i^j across the i-th element. Hence, Eq.(4.13) is modified to give

$$\omega_i = 1 - \left(1 - \frac{\sum_{j=1}^{3} D_i^j}{3} \right)^{\frac{1}{\beta+1}} \quad . \tag{4.14}$$

Once D and ω are determined, the FE model is updated for the next load cycle by replacing the elastic modulus of each element with the one predicted using Eq.(4.5). A 'jump-in-cycle' procedure will be implemented – see Section 4.2.6 – so that simulations need not be performed for every load cycle in the fatigue analysis.

Recall that an ideal nodal design is assumed in the FE models. Consequently, the stress distribution is each cell wall is not affected by their neighbourhood cell walls that meet at a common vertex. Since the damage law used here is stress-based, the impact of an idealised nodal design is more important compared to the FE models from earlier Chapters 2 and 3. Consequently, the results presented should be treated with caution although they can be considered as the 'average' response of real lattices. The damage accumulation in lattices with a more realistic nodal design can be either more or less rapid leading to shorter or longer fatigue life, respectively. This is a subject that requires further investigation and is not covered here.

4.2.5 Nonlocal damage

It is well known, and it shall be demonstrated in Section 4.3.3.a, that continuum damage models that need to take into account material strain softening are also highly mesh dependent. As the mesh gets progressively finer, the strain-softening damage tends to localise into a zone of vanishing volume, leading to failure at zero damage energy dissipation – this is physically unrealistic but a mathematically possible solution (Pijaudier-Cabot and Bazant, 1987). A direct consequence of strain localisation is spurious mesh sensitivity. A crude way to overcome this is to impose – in an ad-hoc manner – a lower limit on the element size (Bazant, 1976; Bazant and Cedolin, 1976). A more general and fundamental approach to avoid damage localisation into an infinitesimally small volume, and its associated spurious mesh sensitivity issues, is to adopt a *nonlocal continuum* approach, first proposed by Pijaudier-Cabot and Bazant (1987). This approach serves as a damage localisation limiter by imposing a minimum size in form of a mate-

rial property and allows the FE meshes to be successfully refined to achieve converged stress-strain distribution.

4.2.5.a Formulation

Following Pijaudier-Cabot and Bazant (1987), the nonlocal field $\overline{f}$ for a point x in the domain V is defined as

$$\overline{f}(x) = \int_V g'(x,\xi) f(\xi) \mathrm{d}\xi \tag{4.15}$$

where $f(x)$ is the local field and $g'(x,\xi)$ is a prescribed nonlocal weight function to be provided later. In the present study, the domain V refers to each individual strut. As alluded to earlier, the nonlocal approach is applied to the local field $\mathrm{d}D/\mathrm{d}N$ which is calculated by Eq.(4.7).

The point x at which the nonlocal field $\overline{f}$ is calculated is termed an 'effect' point, while all the other points ξ_i are 'source' points, where $i = 1, 2, \ldots, n$ and $n(= 2m + 1)$ is the total number of points in the domain V. Recall that there are m number of beam elements that make up a domain and each beam element has three computational points; the two computational points at the end nodes that belong to two different elements are considered only once.

If the domain is infinite, then the weight function $g'(x,\xi_i)$ depends only on the distance r between the 'effect' and 'source' points where $r_i = |x - \xi_i|$. However, if the domain contains boundaries, which is the case here, then it is necessary to scale the weight function as follows:

$$g'(x,\xi_i) = \frac{g(r_i)}{\int_V g(r_i)\mathrm{d}\zeta} \tag{4.16}$$

where $g(r_i)$ is a monotonically decreasing non-negative function of r_i. The most common choice for $g(r_i)$ in the literature is a Gaussian distribution function given by

$$g(r_i) = \exp\left(-\frac{r_i^2}{2l_{nl}^2}\right) \tag{4.17}$$

where l_{nl} is an internal characteristic length - a material parameter - associated with the nonlocal continuum. Note that l_{nl} - a parameter on the micro-scale - should not be confused with the cell wall length l which is a characteristic length - a meso-scale parameter - of a lattice. For metals, l_{nl} is typically between the range of $0.2 - 0.5$mm (Ahad et al., 2014; Giry et al., 2011; Samal et al., 2009); following the suggestion by Ahad et al. (2014) for 6061-T6 aluminium alloy, $l_{nl} = 0.4$mm is adopted in the present study.

Figure 4.4 shows the variation of $g(r)$ along a strut of length $l = 7.5$mm; this corresponds to the cell wall length of the Diamond lattice investigated by Cote et al. (2007a). The 'effect' point is placed at 1/4 of the strut's length. For the nonlocal scheme to be effective, a number of 'source' points must be located within the range of influence from the 'effect' point. To clarify this point, consider a strut modelled with just two beam elements (this gives a total of five computational points at $x/l = 0\,,\ 1/4\,,\ 1/2\,,\ 3/4\,,\ 1$); their 'source' points are indicated by the red dots in Fig. 4.4. From Fig. 4.4, $g(r) \approx 0$ for all but the 'effect' point at $x/l = 1/4$. By increasing the number of elements in each struts, say to $m = 16$, the number of 'source' points increases and now there are approximately 10 'source' points that can influence the 'effect' point; see blue dots in Fig. 4.4. Hence, a sufficiently fine mesh is required for the nonlocal damage to be effective; this will be addressed later in Section 4.3.3.

4.2.6 Jump-in-cycle procedure

The *jump-in-cycle* procedure - first proposed by Lemaitre (1992) and adopted by Warhadpande et al. (2010) and Weinzapfel and Sadeghi (2013) - is implemented here to speed up the simulations; this procedure negates the need to run a FE simulation for every cycle in the entire life of a lattice. For clarity of explanation, a counter k is introduced here to denote the number of completed FE simulation runs.

A *jump-in-cycle* procedure assumes that the state of stress in each strut, and thus their corresponding $(\mathrm{d}D/\mathrm{d}N)$, predicted at the k^{th} simulation run - and corresponds to cycle N_k - remain the same for a block of cycles δN_k such that

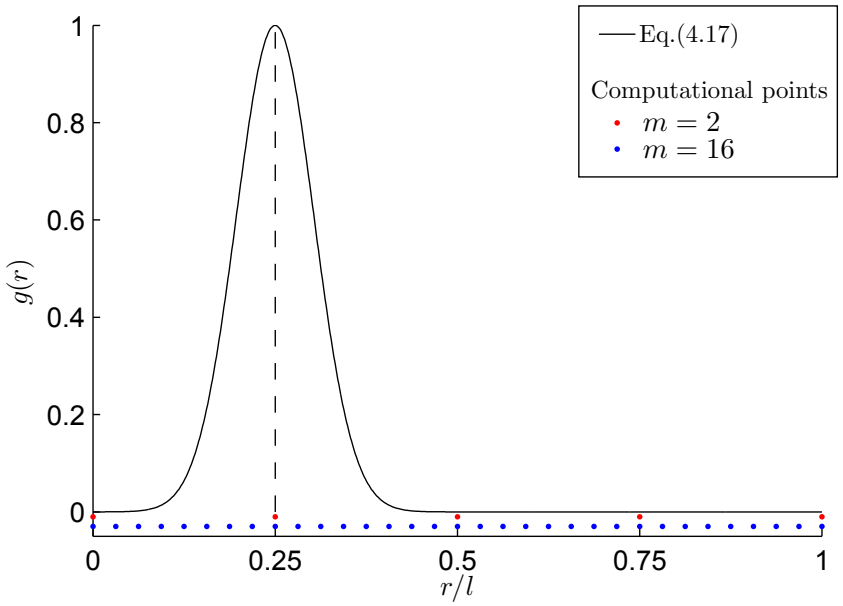

Figure 4.4: The Gauss distribution function along a strut of length $l = 7.5$mm with the 'effect' point located at 1/4 of a strut's length. The locations of the computational points for two example cases (2 and 16 elements per strut) are shown.

$$\max\left[\delta N_k \left(\frac{\mathrm{d}D}{\mathrm{d}N}\right)_k^i\right] = \delta D \quad , \quad \text{for } i = 1, 2, \ldots, m \tag{4.18}$$

where m is the total number of computational points in a given lattice. The $(k+1)^{\text{th}}$ simulation run corresponds to cycle $N_{k+1} = N_k + \delta N_k$. Thus, the 'jump-in-cycle' method gives a piecewise linear approximation of the damage parameters - D, ω and ω^* - with cycles N.

The parameter δD is introduced to control how large each δN_k can be and this is kept constant throughout the fatigue simulation. δD needs to be sufficiently small so that the piecewise linear approximation does not induce significant error in the non-linear dependence of stress- and damage-state, but large enough to ensure that the simulation time is not excessive. As with any strain-softening damage simulation, the solution of the problem is not unique. The choice of δD has a direct influence over the strain accumulation solution given by the NLCD-FE model. A value of $\delta D = 0.1$ was deemed satisfactory and this is chosen based on extensive numerical checks to ensure that the predictions by the NLCD-FE model matches the experimental results as closely as pos-

sible

To better understand how the 'jump-in-cycle' technique is integrated into the NLCD-FE model, the various stages of the fatigue simulation, see also Fig. 4.2, are itemised as follows:

1. Given the desired R^* and σ^*_{max}, an initial FE simulation run ($k = 1$ and $N_k = 1$) is carried out for one load cycle to predict the macroscopic modulus E^*_k.

2. At the two extremes of the load cycle (σ^i_{min} and σ^i_{max}), the stress state at every computational points $i = 1, 2, \ldots, m$ of every struts in the FE model are calculated, as described in Section 4.2.4.c. The parameters $R^i, \bar{\sigma}^i$ and σ^i_{amp} are estimated at each computational point, i, using Eqs.(4.3), (4.1) and (4.2), respectively.

3. The damage accumulation rate at each computational point $(\mathrm{d}D/\mathrm{d}N)^i_k$ is calculated using Eq.(4.7).

4. Apply the nonlocal damage scheme for $(\mathrm{d}D/\mathrm{d}N)^i_k$ as described in 4.2.5.

5. The 'jump-in-cycles' δN_k is estimated using Eq.(4.18).

6. With D^i_k, $(\mathrm{d}D/\mathrm{d}N)^i_k$ and δN_k now known, the fatigue damage in computational point i is calculated for the $(k+1)^{th}$ simulation run as follows:

$$D_{k+1} = D_k + \left(\frac{\mathrm{d}D}{\mathrm{d}N}\right)^i_k \delta N_k \tag{4.19}$$

7. The corresponding modulus damage for each element ω^j_{k+1} are calculated using Eq.(4.14)

8. Update the FE model with the new values for the damage variables, ω_{k+1} and D_{k+1}. Any elements with $\omega_{k+1} > 0.99$ are deleted from the FE mesh.

9. Repeat from Step 1 with the updated FE model and using $N_{k+1} = N_k + \delta N_k$.

As previously reviewed in Chapter 1, most macroscopic strain-cycle curves exhibit a knee where macroscopic failure follows soon after this point. For all lattices investigated here, this point is reached by $\omega^* < 0.5$; hence, this is used as the threshold to

determine the number of cycles to failure N_f^* at the macro-scale. Last, a simulation run is terminated - even if $\omega^* > 0.5$ is not reached - if the total number of cycles exceeds the 'infinite' life limit of $N > 2 \times 10^7$.

4.3 Model calibration and validation

The validation of the NLCD-FE model is carried out in four separate stages as follows:

1. In Section 4.3.1: The NLCD model of Section 4.2.4 is calibrated to the high-cycle fatigue data for Aluminium alloy Al2014-T6 obtained from existing literature.

2. In Section 4.3.2: The coupled NLCD-FE model of Section 4.2.4.c is used to simulate a thin rectangular tensile specimen – this is for a fully dense Aluminium Al2014-T6 specimen rather than a lattice – subjected to cyclic compression-compression (C-C). This is to ensure that the coupled NLCD-FE model can reproduce the output of the NLCD model - one that has not been coupled to the FE model - and that the 'jump-in-cycles' procedure does not induce any error.

3. In Section 4.3.3: The NLCD-FE model is implemented for a single strut (or cell wall) modelled as an end-loaded cantilever beam. Mesh sensitivity study is performed to determine the mesh size that is needed to obtain converged results, before implementing the NLCD-FE model to simulate the high-cycle fatigue response of lattices. Additionally, the need to implement a nonlocal damage scheme will be highlighted here.

4. In Section 4.4: Predictions by the NLCD-FE model are compared against existing experimental data for Diamond lattices subjected to cyclic shear loading by Cote et al. (2007a). The fully-validated NLCD-FE model is subsequently used to study the fatigue behaviour of other lattice micro-architectures.

4.3.1 Calibration of parameters - Stage 1

The material from which the struts are made is characterised by E, σ_y, σ_{e_0} and σ_{u}. Here, four additional scalar parameters, viz. M_0, c, β and b, are introduced by the NLCD model that have to be obtained by calibration, through fitting Eq.(4.8) to the experimental $S - N$ data. Data for fully reversed loading ($R = -1$) are needed to

estimate M_0, c and β whilst data for different R values are needed to estimate b; this makes it challenging to find comprehensive data from the literature. Experimental data for Al2014-T6 given in MIL-HDBK-5H (1998) are used here for the calibration: they are plotted in Fig. 4.5. As to be expected, there is a significant amount of scatter in the experimental data for high cycle fatigue tests.

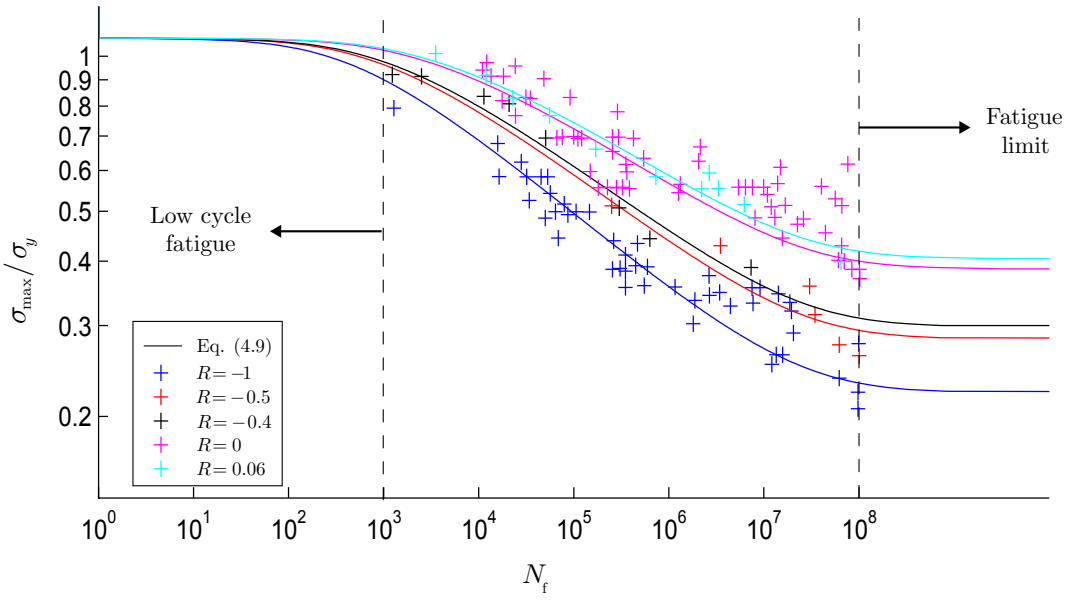

Figure 4.5: Al 2014-T6 stress-life data at various load ratio R and the curves correspond to NLCD model predictions using the calibrated parameters in Table 4.2.

Ideally, the aforementioned parameters would need to be calibrated to as-brazed AISI 304 stainless steel: this is the strut material from which the Diamond lattices in the experimental study by Cote et al. (2007a) were made. However, experimental $S-N$ data for the 304 stainless steel are given only for $R = 0.1$ and 0.5 by Cote et al. (2007b). The lack of $S-N$ data for $R = 0$ makes it impossible to properly calibrate the parameters of the NLCD model. Hence, we shall calibrate the NLCD model using data for Al2014-T6 instead. Since the major purpose of this work is to compare the fatigue performance of various lattice micro-architectures, the choice of strut parent material is not important.

Table 4.2 lists the calibrated parameters M_0, c, β and b alongside material properties for Al2014-T6 given in MIL-HDBK-5H (1998). Predictions by Eq.(4.8), using the calibrated parameters of Table 4.2, is also plotted in Fig. 4.5. The NLCD model captures

E †	σ_{u} †	σ_y †	σ_{e_0} †
69GPa	538MPa	496MPa	105MPa
M_0 ‡	c ‡	β ‡	b ‡
3.2GPA	1.125	4.233	$0.7345/\sigma_{\text{u}}$

Table 4.2: Material properties for Al2014-T6 and the calibrated NLCD model parameters. † indicates property given in MIL-HDBK-5H (1998), whilst ‡ refers to calibrated parameters.

well the effects of R and σ_{max} on N_f. If the maximum stress value $\sigma_{\text{max}}/\sigma_y$ is too high, then the number of cycles to failure $N_f < 10^3$; this is a case of low-cycle fatigue which is beyond the scope of this work. On the other hand, if maximum stress does not exceed the fatigue endurance strength given by Eq.(4.12), then the $\sigma_{\text{max}}/\sigma_y$ vs N_f curve is a horizontal line which indicates 'infinite' life.

Figures 4.6a and b show the predicted damage accumulation of D and ω with N, using the calibrated parameters with Eqs.(4.7) and (4.13). Two load ratios are shown: (a) fully reversed $R = -1$ and (b) $R = 0.1$. When $R = 0.1$, $\sigma_{\text{max}}/\sigma_y = 0.3$ is below the fatigue endurance strength leading to 'infinite' life; this can be inferred from Fig. 4.5. D is seen to accumulate more rapidly than ω due to their non-linear relationship given by from Eq. (4.13): the relationship between D and ω is plotted in Fig. 4.6c. As to be expected, $D = \omega = 1$ at $N = N_f$. The plots of Fig. 4.6 give a general overview of the rate at which fatigue and modulus damage accumulates in the struts of a lattice.

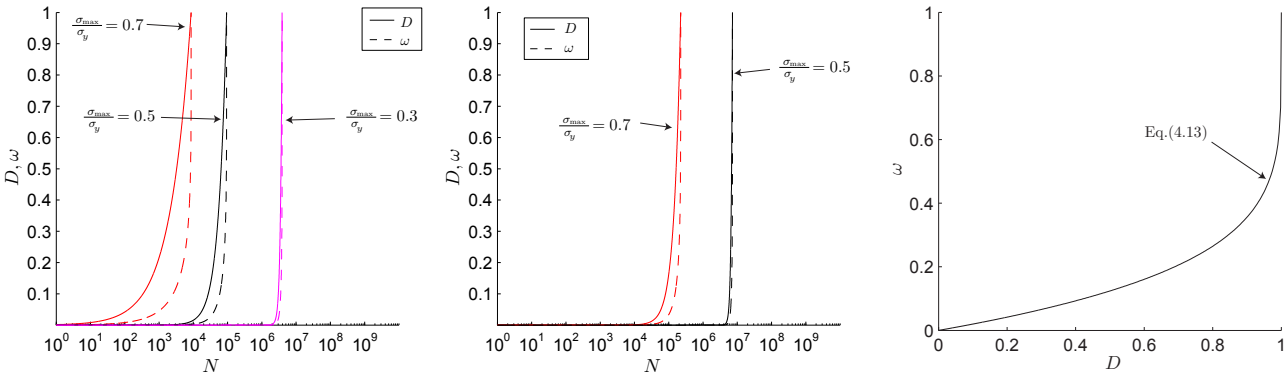

(a) (b) (c)

Figure 4.6: Damage accumulation (D and ω) with number of cycles for (a) $R = -1$ and (b) $R = 0.1$; (c) Variation of ω with D.

The combination of $\sigma_{\max}/\sigma_y$ and R experienced by each strut directly affects the rate at which D and ω increases with N. As ω in the struts increases, it is expected that the macroscopic modulus damage ω^* of the lattice also increases.

4.3.2 Uniaxial loading - Stage 2

In the second stage of the validation process, predictions by the coupled NLCD-FE model of a thin, fully-dense rectangular tensile specimen are compared to those of the NLCD model. The reactangular specimen is modelled with solid (CPS8) finite elements; details of the coupling between the FE and NLCD models were presented in Sections 4.2.4–4.2.6. Since there is a uniform stress distribution in the rectangular specimen, no mesh dependency is observed. The comparison is shown in Fig. 4.7, where D and ω are plotted against N, for the load case of $R = 0.1$ and $\sigma_{\max} = 0.7\sigma_y$. Results for two different values of $\delta D = 0.1$ and 0.2, see Eq. (4.18), are presented. A smaller δD value gives better curve resolution but it requires a higher number of simulation runs. Predictions by the coupled NLCD-FE model is in excellent agreement with those by the analytical NCLD model: the results show a good match for both δD values. The same is true even if a lower value for δD, e.g. 0.01, is used but they are not plotted for brevity. This indicates that the coupling of the NLCD model to FE did not induce any unwanted numerical artefacts; a key objective of the second step in the validation process. The above demonstrates that the coupled NLCD-FE model is able to successfully reproduce the $S - N$ curves of Fig. 4.5 with good accuracy.

4.3.3 Single cell wall in bending - Stage 3

The third stage of the validation process will examine the sensitivity of damage accumulation in a single strut (or cell wall) to bending deformation. A single cell wall is modelled as an end-loaded cantilever beam of length $l = 7.5$ mm and thickness $t = 0.3$ mm; their dimensions are the same as the struts (cell walls) in the Diamond core lattice in Cote et al. (2007a). The cantilever is modelled with m number of B22 beam elements; the element number $i = 1, 2, \ldots, m$ from the fixed end is indicated in Fig. 4.9. Results with and without the inclusion of nonlocal damage will be presented to highlight their differences and the need to considering nonlocal continuum.

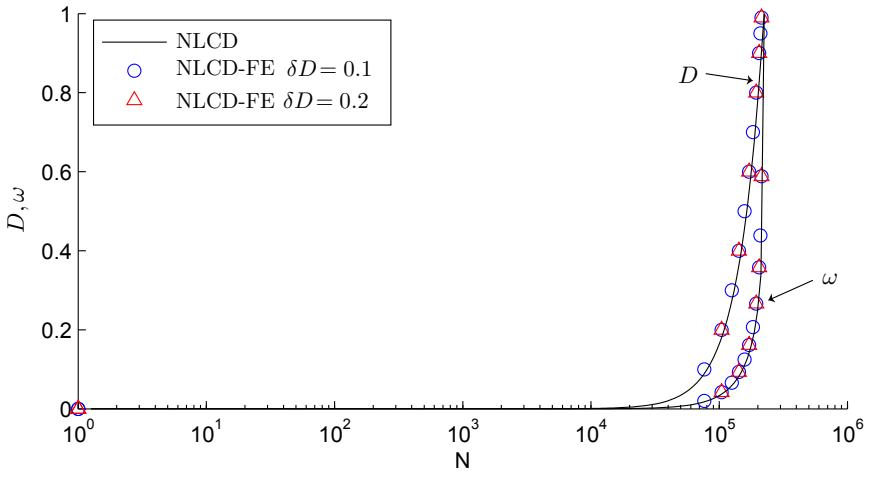

Figure 4.7: Predicted damage-cycle curves, incorporating the *jump-in-cycle* procedure, for the load case of $\sigma_{\max}/\sigma_y = 0.7$ and $R = 0.1$.

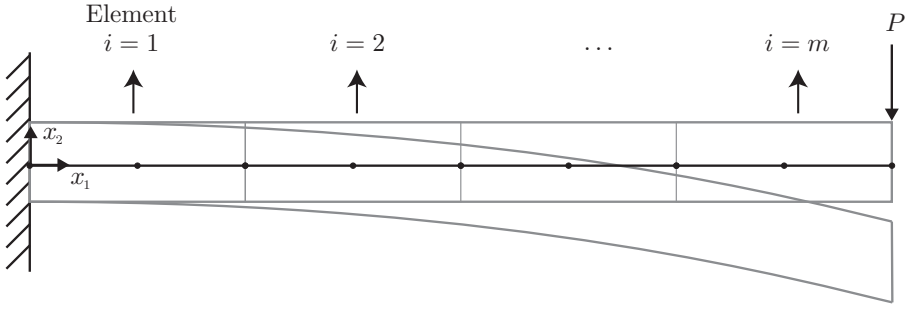

Figure 4.8: End-loaded cantilever beam modelled by four ($m = 4$) B22 beam elements. The dots indicate the three damage computational points of each element.

The end load P that was applied is always aligned in the x_2 direction, i.e. it does not follow the curvature of the beam as it bends, so that its tip deflection is given by

$$\delta_2 = \frac{Pl^3}{3E_sI} \tag{4.20}$$

where $I = t^3 d/12$ is the second moment of area and its out-of-plane depth is $d = 1$. Mesh sensitivity study will be carried out for $R = 0.1$ and $P_{\max} = 0.7P_y$, where P_y is the end-load needed to initiate plastic deformation at the fixed-end. The macro-level damage ω^* is not determined by Eq.(4.6); instead, it is given by

$$\omega^* = 1 - \frac{(\delta_2)_1}{\delta_2} \tag{4.21}$$

where $(\delta_2)_1$ is the end deflection of the undamaged beam.

4.3.3.a Without nonlocal damage

Mesh sensitivity study is performed without taking into account nonlocal damage; this is done by setting $l_{nl} = 0$ in Eq. (4.17). The accumulation of ω^* is plotted against N in Fig. 4.9 for seven FE models with progressively finer mesh. As alluded to earlier, a finer mesh does not lead to converged results. Even though ω^* starts increasing from approximately $N = 2.2 \times 10^5$ for all the meshes shown, their subsequent response varies significantly.

A plateau region develops afterwards; this is a direct consequence of $(\mathrm{d}D/\mathrm{d}N)^{i=1} \to 0$ in step 3 in Section 4.2.6 where the superscript i denotes the element number in Fig. 4.9. This happens because as $\omega \to 1$, the local stress in the element at the fixed-end ($i = 1$) reduces significantly so that $(\mathrm{d}D/\mathrm{d}N)^{i=1} \to 0$, see Eq. (4.7). Consequently, any further increase in ω^*, beyond the first plateau region, must be from contributions by the rest of the elements ($i > 1$) in the FE mesh. For coarser mesh, say $m = 2$, the local stress in the second element ($i = 2$) is not high enough to reach $(\mathrm{d}D/\mathrm{d}N)^i > 0$;

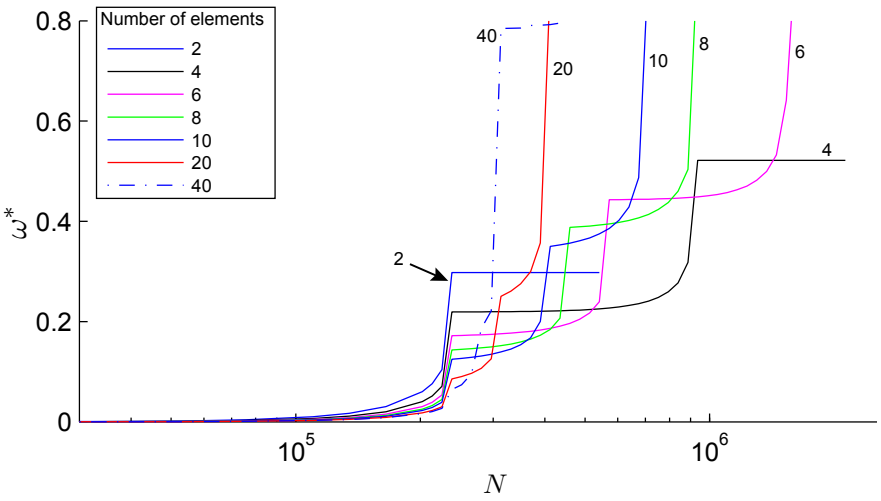

Figure 4.9: Results showing mesh sensitivity for an end-loaded cantilever beam with m number of beam elements without considering nonlocal damage.

hence, $\mathrm{d}\omega^*/\mathrm{d}N = 0$.

With a finer mesh, say 20 elements, the internal stress in the second element ($i = 2$) element is sufficiently high so that $(\mathrm{d}D/\mathrm{d}N)^{k=2} >> 0$ and the plateau region, seen in the coarse mesh, disappears. Notwithstanding, a converged response is not observed with increasingly finer mesh; thus, without considering nonlocal damage, the NLCD-FE model is not useful.

4.3.3.b With nonlocal damage

Figure 4.10 presents the results of the same mesh sensitivity study from previously but, this time, taking into account the effects of nonlocal damage. Results for the two-element ($m = 2$) mesh is nearly identical to the previous one without nonlocal damage. This is because there are insufficient computational points for the nonlocal scheme to be effective. However, if more than 4 elements are used, a significant difference between the predicted $\omega^* - N$ curves begin to emerge. Because of the nonlocal averaging scheme, the rate of initial damage accumulation - $\mathrm{d}\omega^*/\mathrm{d}N$ - is slower and the plateau region observed previously without nonlocal damage disappears. Figure 4.10 shows that a converged response is, indeed, achieved with successively finer mesh. A FE mesh comprising of 20 elements per strut (or cell wall) is deemed to be sufficient to model a converged response for lattices.

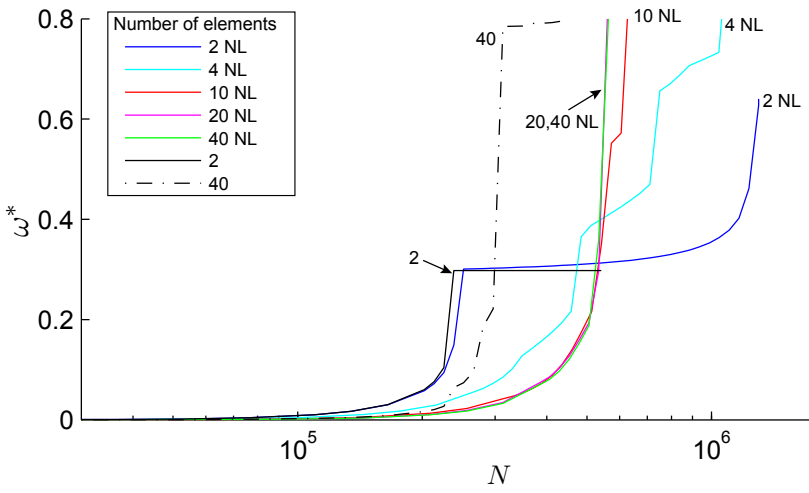

Figure 4.10: Results showing mesh sensitivity for an end-loaded cantilever beam with m number of beam elements. NL indicates that nonlocal damage was implemented.

4.4 Shear fatigue of Diamond lattices - Stage 4

The 4^{th}, and final, stage of validation comprised of two parts: predictions for its monotonic shear response are validated first followed by its cyclic response. To this end, the experimental data of Cote et al. (2007a) on Diamond lattices are used here. It needs to be emphasised that the FE model is used on its own, without the NLCD model, when simulating the monotonic response of a lattice. Ordinarily, the coupled NLCD-FE approach, with nonlocal damage, is always used.

There are two reasons why the monotonic response is first validated. Firstly, the parameter τ^*_{max} (or σ^*_{max} in C-C loading) is to be normalised by τ^*_y (or σ^*_y); this is estimated a priori in a monotonic analysis. Recall that Cote et al. (2007a) uses the peak value τ^*_p to normalise their data (τ^*_{max}). Here, τ^*_y is used in place of τ^*_p, since our FE model does not account for the strain softening regime post τ^*_p. Secondly, it remains to be shown that the FE model of a lattice can accurately predict the monotonic stress-strain response for a load cycle; in particular, for loadings in the range of τ^*_{max} ($\leq 0.8\tau^*_y$) and σ^*_{max} ($\leq 0.8\sigma^*_y$) that will be used in subsequent cyclic simulations.

In the second part of the validation, predictions by the coupled NLCD-FE are compared to the shear fatigue data of Cote et al. (2007a). Recall in Section 4.3.1 that there are insufficient $S-N$ data on the AISI 304 stainless steel to properly calibrate the NLCD model. Instead, the cyclic response of the NLCD-FE model will be validated using the parameters calibrated to Al2014-T6. As Cote et al. (2007a) reported, the fatigue performance of lattice materials is independent of the choice of cell wall material. Thus, the choice of material for the NLCD-FE model is not expected to be the source of any discrepancies in the validation process; which will be shown to be the case.

4.4.1 Monotonic shear loading

4.4.2 Specimen dimensions

The prismatic Diamond lattices in Cote et al. (2007a) were manufactured using AISI 304 stainless steel sheets of thickness $t = 0.3$ mm. Two relative densities of $\overline{\rho} = 0.08$ and 0.15, corresponding to a cell wall length of $l = 7.5$ mm and 4 mm, respectively, were tested. All their specimens are of aspect ratio $\overline{R} = \overline{W}/\overline{H} = 12$ and $\overline{H} = 5$. Ac-

cording to Eq. (3.61) in Chapter 3, these specimens are sufficiently large with minimal influence from edge effects.

4.4.2.a Material properties of cell wall

The face-sheets and diamond-core assembly in Cote et al. (2007a) were brazed together using a Ni-Cr 25-P10 alloy at an elevated temperature. Consequently, the properties of their stainless steel struts are not the same as commercially available ones. However, in a companion paper, Cote et al. (2006) provided the mechanical properties of as-brazed AISI 304 stainless steel alloy; they are listed in Table 4.3 and these were used in our FE model to simulate the monotonic response of the Diamond lattices.

E	σ_y	$\mathrm{d}\sigma/\mathrm{d}\varepsilon$
210GPa	210MPa	2.1GPa

Table 4.3: Material properties for as-brazed AISI 304 stainless steel alloy. (Cote et al., 2006)

4.4.2.b Results

The current FE model matches successfully the linear-elastic response of the diamond lattice but not its non-linear response. It overestimates τ_y^* by up to 30% for both relative densities. The perfect bonding between the Diamond core and the face-sheets, assumed in our FE model, is unlikely to be the key source of discrepancy since Cote et al. (2007a) have noted that their lattice deform by the buckling of its struts at the peak value, while the softening regime - post-peak stress - is associated with fracture of the brazed joints. Instead, the perfect lattice microstructure of the FE model is thought to be the more likely source.

Imperfections are introduced to each strut, in the form of an initial transverse deflection, given by

$$\delta_2(s) = \kappa_b t \sin\left(\frac{\pi s}{l}\right) \tag{4.22}$$

where κ_b is a dimensionless parameter that controls the severity of imperfection and s is the arc length along the strut measured from one end (Cote et al., 2006). The imposed

transverse deflection corresponds to the buckling mode of a pin-ended strut that are estimated a prior in a standard eigenvalue analysis. It is worth emphasising that Cote et al. (2006), too, found this to be necessary in their FE simulations of the Diamond lattices.

Figure 4.11 compares the FE predictions, using $\kappa_b = 0.2$, to the experimental data. The inclusion of strut imperfections lead to a significant reduction in the predicted τ_y^*; they are now within 6% of the τ_p^* values reported by Cote et al. (2007a) which suggests that using τ_y^*, in place of τ_p^*, for normalisation is unlikely to lead any significant error in subsequent fatigue analyses. Even though, there is a significant difference between their corresponding shear strains although they do not affect the fatigue analysis. The imposed macroscopic loading in a fatigue analysis is always within the linear regime - in the range where $\tau^*_{\text{max}} < 0.8\tau_y^*$ - hence the difference between the shear strain for τ_y^* and τ_p^* becomes insignificant. Additionally, the small range of imposed macroscopic loads means that the inability of the FE model to follow the experimental results post τ_p^* is not problematic to the cyclic analyses for the above reason. Therefore, it is deemed acceptable to use τ_y^* and σ_y^* for normalisation.

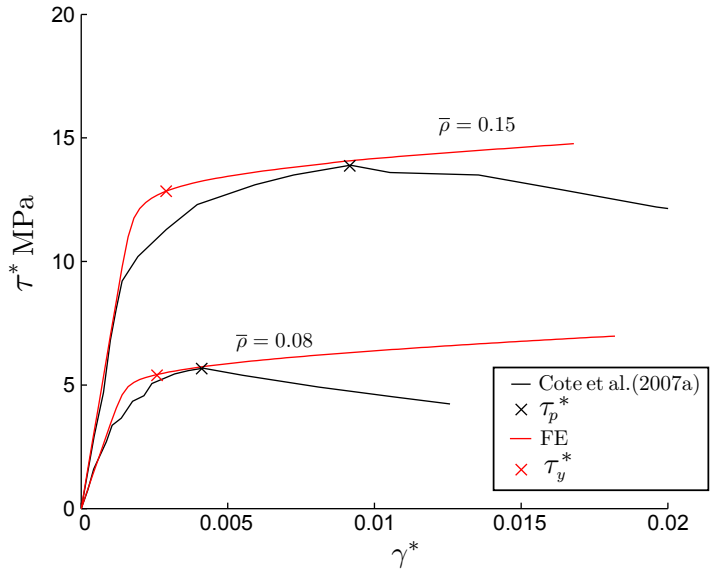

Figure 4.11: Monotonic shear stress-strain curves – predicted by FE and measured experimentally – for Diamond lattices constructed using AISI 304 stainless steel.

4.4.3 Cyclic shear loading

Cote et al. (2007a) presented experimental data on Diamond lattices of relative density $\overline{\rho} = 0.08$ subjected to cyclic shear at a load ratio $R = 0.5$; and, of $\overline{\rho} = 0.15$ at $R = 0.5$ and $R = 0.1$. Fatigue failure in the lower density lattice ($\overline{\rho} = 0.08$) was reported to originate from bending deformation of the constituent struts near the edges of the specimen; these regions are known to be affected by edge effects as previously discussed in Chapter 3. By contrast, the higher density lattices ($\overline{\rho} = 0.15$) fail by shear fatigue at the brazed joint between the core and the face-sheets. Since the NLCD-FE model does not model interfacial failure between core and face-sheets, validation will be limited to those results for $\overline{\rho} = 0.08$ and $R = 0.5$.

4.4.3.a Specimen dimensions

To minimise computational time, since a large number of simulation runs is needed, smaller-sized lattices compared to that used by Cote et al. (2007a) were modelled. The Diamond lattices simulated, here, contain 20 ($\overline{W}$) $\times$ 3($\overline{H}$) *complete* cells, see Table 4.1. Based on Eq.(3.61), this specimen size is only marginally affected by edge effects compared to those of Cote et al. (2007a); under monotonic loading, a slight $\approx 5\%$ reduction in E^* compared to that of Cote et al. (2007a) is expected here. It will be shown later that the larger lattice, under cyclic loading, gives slightly reduced N_f^* for the same τ^*/τ_y^*.

4.4.3.b Material properties of cell wall

To circumvent the lack of data - see Section 4.3.1 - the validation of the cyclic response for Diamond lattices will be performed using material properties, and NLCD parameters, calibrated to Aluminium Al 2014-T6 which are listed in Table 4.2. It will be shown that this does not pose a problem in terms of the predicted results. Moreover, this can be further justified based on one of the key conclusions by Cote et al. (2007a) where it was reported that the normalised shear endurance strength (τ_e^*/τ_p^*) is independent of cell wall material, relative density $\overline{\rho}$ and core topology. Since the main objective of this work is to investigate the influence of lattice micro-architecture on fatigue life, the roles played by cell wall material and relative density may be considered to be negligible.

4.4.3.c Results

Figure 4.12 plots the predicted $S - N$ data by the NLCD-FE model in normalised $\Delta\tau^*/\tau_p^* - N_f^*$ and $\tau_{\max}^*/\tau_p^* - N_f^*$ space. Just like the monotonic case, all the results shown are for imperfect struts with $\kappa_b = 0.2$. The predictions for relative density $\overline{\rho} = 0.08$ and load ratio $R = 0.5$ are close to the experimental data of Cote et al. (2007a). The NLCD-FE model is found to predict slightly longer life, by $\approx 1/5$ of a decade; this can be attributed to simulating smaller-sized lattices compared to that used by Cote et al. (2007a), which will be clear later on.

Experimental data for the higher density ($\overline{\rho} = 0.15$) lattices are also plotted in Fig. 4.12 for two load ratios $R = 0.1$ and 0.5. Since interfacial failure is not modelled, our numerical predictions only capture the influence of increasing $\overline{\rho}$ on the fatigue response; this is unlike in Cote et al.'s experiments where additional fatigue process also occurs at the interface between core and face-sheets. At load ratio $R = 0.1$ and $\overline{\rho} = 0.15$, the NLCD-FE model predicts higher N_f^* compared to experiment, see Fig. 4.12b. The slightly higher N_f^* is due to the smaller specimen size that was simulated and the disregarding of the interfacial failure mechanism. At load ratio $R = 0.5$, and

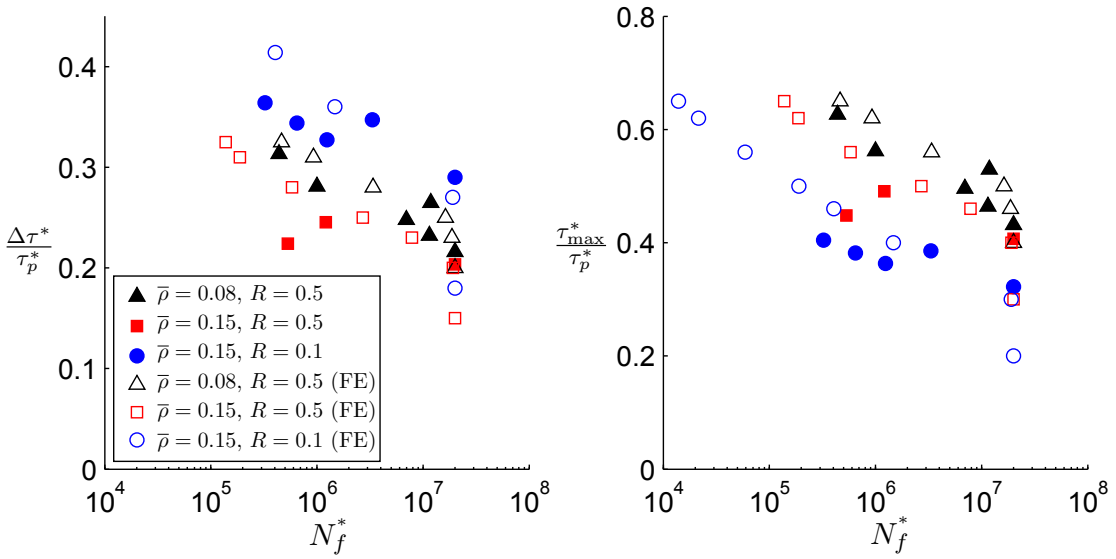

Figure 4.12: Predicted shear $S - N$ data for Diamond lattices using the NLCD-FE model. Experimental data by Cote et al. (2007a) are included for comparison.

$\overline{\rho} = 0.15$, the NLCD-FE model again predicts slightly higher N_f^*; only for $\tau_{\max}^*/\tau_p^* = 0.45$ the difference is significant which is believed to be caused by premature failure due to imperfections in the core and face-sheet brazing. The numerical predictions for $\overline{\rho} = 0.08$ and $\overline{\rho} = 0.15$ at the same load ratio $R = 0.5$ shows that the higher density lattice has a life which is approximately half decade shorter; this is less evident in the experiments since the results for higher $\overline{\rho}$ are affected by interfacial failure and, to some extent, data scatter.

Figure 4.12 shows that the NLCD-FE model is capable of reproducing, with sufficient accuracy, the fatigue response of Diamond lattices. Additionally, the effects of load ratio R and relative density $\overline{\rho}$ on fatigue life are, also, successfully captured by the current NLCD-FE model. It is important to emphasise that the use of Al2016-T6 material properties instead of 304 stainless steel did not appear to have affected the ability of the NLCD-FE model to estimate the normalised fatigue response of Diamond lattices - this is consistent with what was reported by (Cote et al., 2007a) that the normalised shear endurance strength (τ_e^*/τ_p^*) is independent of cell wall material and relative density $\overline{\rho}$.

The four stages of model validation and calibration are now complete, and their predictions were shown to be sufficiently accurate. The fully validated NLCD-FE model is next used to simulate the fatigue response of other lattice micro-architectures.

4.5 Imperfection sensitivity of fatigue response

The fully-validated NLCD-FE model is employed here to simulate the shear and compression-compression (C-C) fatigue response of five periodic lattices with different micro-architectures; their dimensions are listed in Table 4.1. We showed previously that the monotonic and cyclic response of the Diamond lattices measured in experiments can only be accurately predicted if imperfect struts are modelled. Therefore, an imperfection sensitivity analysis is carried out to establish the bounds of the $S - N$ curve for the different micro-architectures. Sensitivity analysis is presented for shear and C-C loading in the Section 4.5.1 and 4.5.2, respectively. For completeness, a sensitivity analysis for the Diamond lattices subjected to cyclic shear is also presented.

Following the approach used during validation, the imperfections introduced by esti-

mating the buckling modes through an eigenvalue analysis; this is carried out for all lattices that deform predominantly in stretch, viz. Diamond, Kagome, Triangular lattices, and for the Square under uniaxial loading (only). The range of κ_b is different for each micro-architecture; this is listed in the corresponding figures as they appear. For the bending dominated lattices - the Hexagonal and the Square in shear - imperfections are imposed via the vertex perturbation method described in Eq.(1.5). Recall that vertex perturbation is controlled by a parameter κ_v. The range of κ_v is kept to moderate levels of between $0 \leq \kappa_v \leq 0.1$ so that the perturbed lattice is not too distorted.

The load ratio and relative density for all subsequent analyses is the same as that used for validation: $R = 0.5$ and $\overline{\rho} = 0.08$. The cell wall length l is kept the same at $l = 7.5mm$ for all lattices because it may influence the predicted fatigue response through the nonlocal continuum length scale $l_{nl} = 0.4mm$; recall that if n_l is too small compared to the size of beam elements, the nonlocal averaging scheme is no longer effective. Consequently, the uniform cell wall thickness t for each lattice will need to be adjusted accordingly to achieve the desired relative density $\overline{\rho}$.

4.5.1 Shear fatigue

Figure 4.13 plots the predicted shear fatigue data, in $\tau^*_{\max}/\tau^*_p - N^*_f$ space, for the five different micro-architectures. The three stretch-dominated micro-architectures - Triangular, Kagome and Diamond - exhibits a significant reduction in fatigue life with increasing κ_b. However, their sensitivity to κ_b - parameter controlling the severity of imperfections - varies. For Kagome, there appears to have no effect on the estimated life beyond $\kappa_b > 0.2$. By contrast, this is not the case for Triangular lattices, at least for the range of κ_b investigated, where N^*_f decreases monotonically with increasing κ_b without a lower bound. Further increase to κ_b results in convergence issues with the FE model. The Diamond lattice was found to be the least sensitive to imperfections, with only a small reduction of estimated life with increasing κ_b. Predictions by the NLCD-FE model is an excellent match to the experimental data of Cote et al. (2007a) in Fig.4.13c. The sensitivity analysis shows that any value of $\kappa_b > 0$ provide a good estimate to the experimental data; however, $\kappa_b = 0.2$ must be used from the monotonic analysis, see Section 4.4.2.b.

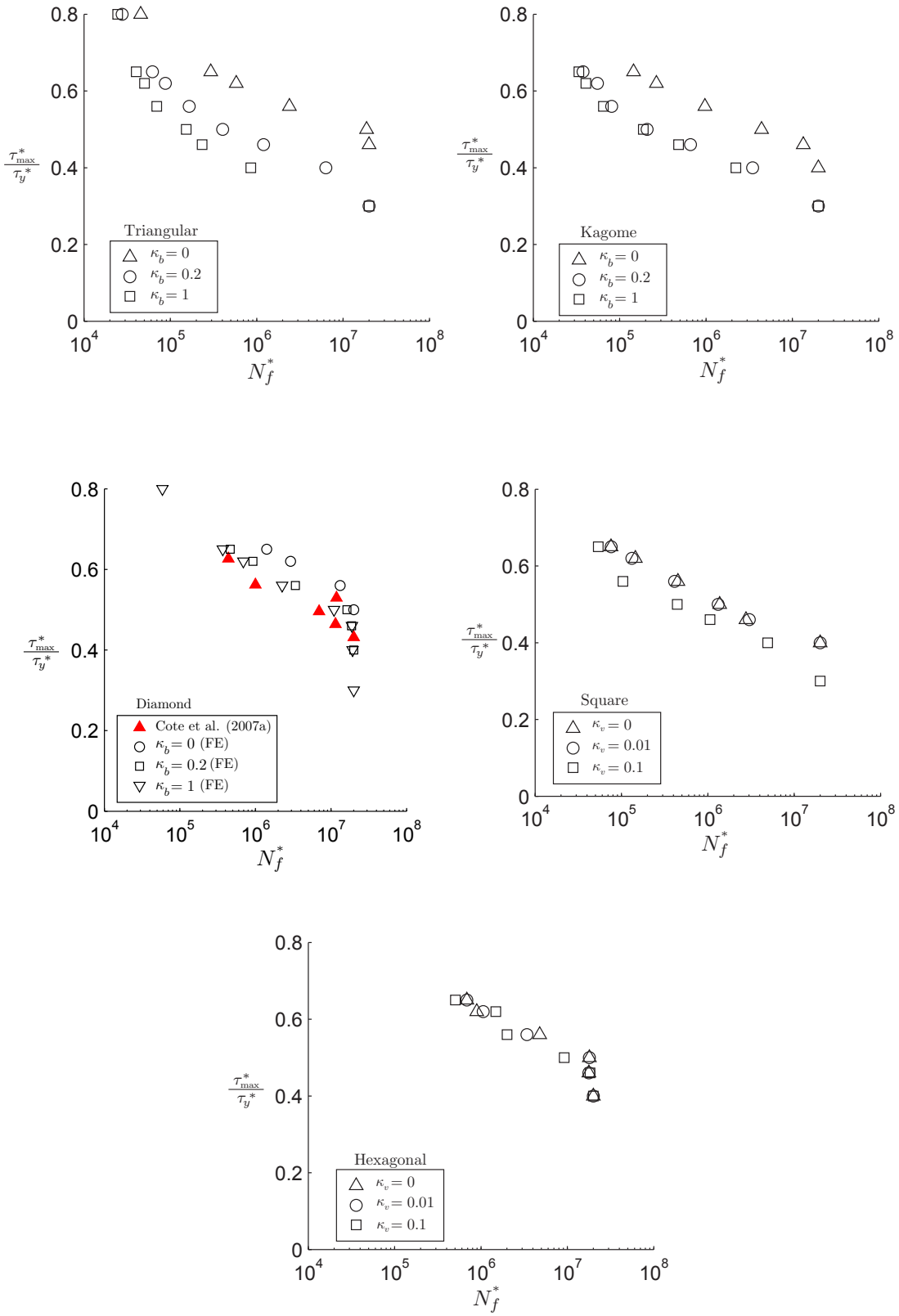

Figure 4.13: Shear fatigue data for stretch-dominated (Triangular, Kagome, Diamond) and bending-dominated (Hexagonal and Square) lattices. Imperfections in the shape of buckling modes were imposed to each strut for the stretch-dominated lattices and by vertex perturbation for the bending-dominated lattices. All data shown are for load ratio $R = 0.5$ and $\overline{\rho} = 0.08$.

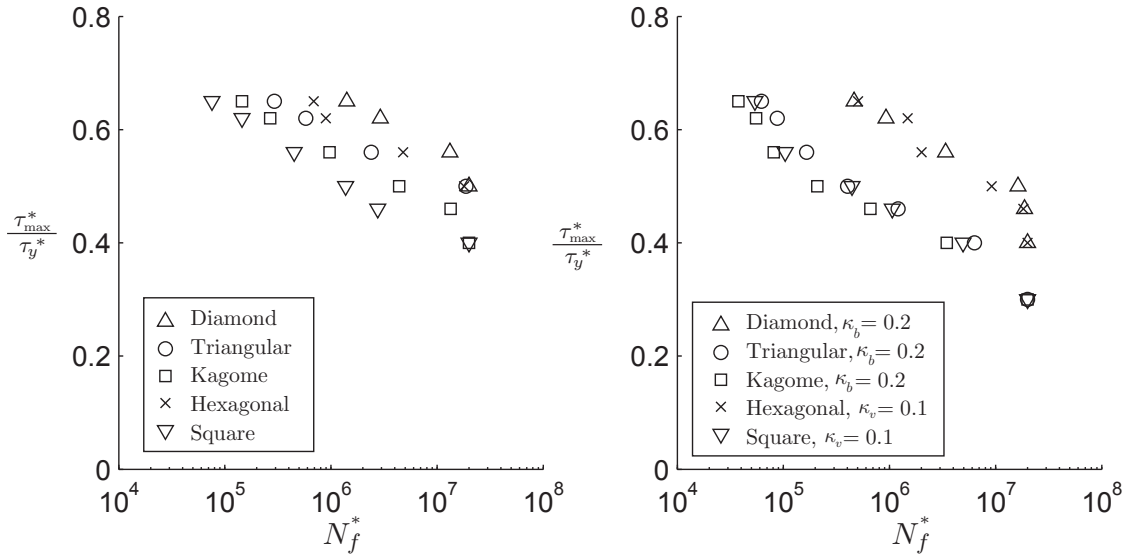

Figure 4.14: Shear fatigue data for lattices (a) without imperfections and (b) with imperfections. All data shown are for load ratio $R = 0.5$ and $\overline{\rho} = 0.08$.

It is evident from Fig. 4.13 that all bending-dominated lattices are nearly insensitive to the presence, and also the extent, of imperfections; only the Square lattice shows a slight decrease in fatigue life when $\kappa_v = 0.1$ - note this is a relatively severe imperfection. The reason for the insensitivity of bending-dominated lattices is that their fatigue failure mode - due to the bending of cell walls - remains the same with and without the introduction of imperfections. By contrast, the stretch-dominated lattices are sensitive to buckling imperfections because their deformation mode switches from axial loading of cell walls, for the perfect lattice, to localised bending at the buckled cell walls for the imperfect.

The predicted $S - N$ data corresponding to their (a) perfect ($\kappa_v = \kappa_b = 0$) and (b) imperfect states are plotted in Fig. 4.14. For the perfect lattices, their fatigue life are different for the different micro-architectures. The Diamond lattice has the longest fatigue life and the Square has shortest. More importantly, there is no evidence to suggest that stretch-dominated lattices have a longer fatigue life compared to their bending-dominated counterpart. In general, the trend in Fig. 4.14a is in contrast to the findings by Cote et al. (2007a) where they concluded that the fatigue life and endurance strength of lattices are insensitive to their micro-architecture.

Data plotted in Fig. 4.14b for the imperfect lattices were generated by using $\kappa_b = 0.2$ (for stretch-dominated) and $\kappa_v = 0.1$ (for bending-dominated). The predicted $S - N$ data collapse into two main clusters, separated by as much as 1.5–2 decades in N_f^*. Imperfections in the Triangular and Kagome lattices lead to a reduction fatigue life, and their $S - N$ data collapses onto the same cluster as with the Square lattice. The imperfect Diamond lattice show similar fatigue response with the Hexagonal lattice. If higher κ_b and κ_v values were used in the simulations, the aforesaid trends are not expected to be altered dramatically, since all except the Triangular lattice are not greatly affected by increased imperfections. For lower imperfection values, the differences between the $S - N$ data of the five lattices will decrease so that the data may no longer fall into the two aforesaid clusters.

Even though the resulting $S - N$ data fall into two clusters, one cannot necessarily conclude that the lattices in each cluster fail by two different mechanisms. For all lattices - in both clusters - fatigue damage were found to initiate and accumulate at the cell walls where bending deformation is most severe before accumulating in other cell walls; this will be discussed in greater detail in Section 4.6.2. The imperfection parameters presented here may not necessarily be representative of commercially-available Triangular and Kagome specimens; experimental data are needed to justify the use of $\kappa_b = 0.2$. Hence the collapse of all $S - N$ data into two clusters may not be witnessed in reality and is a coincidence of the imperfections that were chosen. Nevertheless, Figs. 4.14a and b provides an upper and lower bound in the expected life of the lattice micro-architectures.

4.5.2 Compression-Compression fatigue

Figure 4.15 plots the predicted compression-compression $S-N$ data for different severity of imperfections. Similar to cyclic shear, Kagome and Triangular lattices exhibit a significant reduction in fatigue life with increased imperfections. The Diamond lattice, on the other hand, is relatively insensitive to imperfections; a significant reduction in fatigue life is noted only if an unrealistically high imperfection parameter, say $\kappa_b = 20$ is introduced. This is because the buckling eigenmode shapes estimated by ABAQUS are significantly less severe compared to the other two lattices and to the corresponding

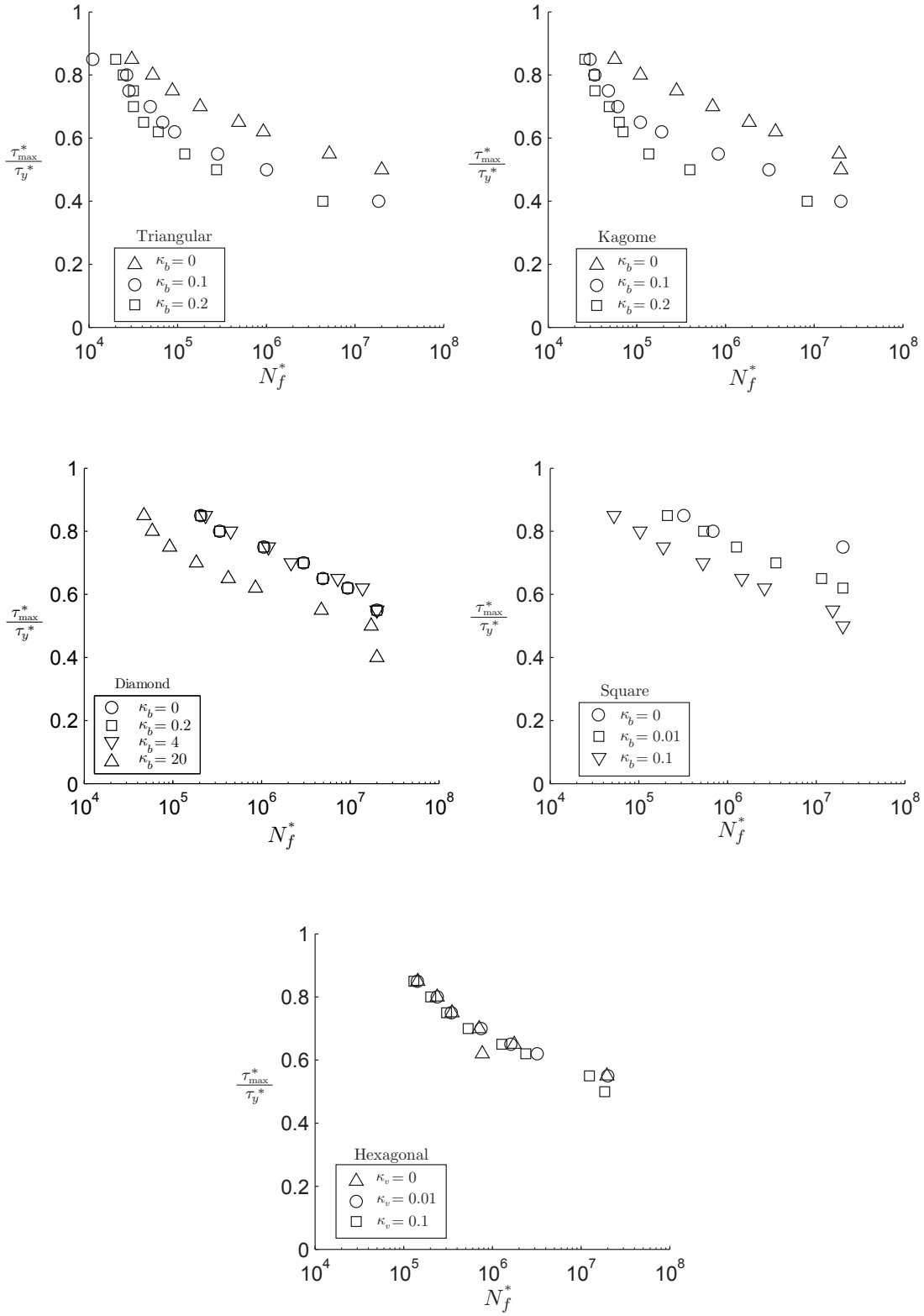

Figure 4.15: Imperfection sensitivity of predicted C-C fatigue data for periodic lattices. All data shown are for load ratio of $R = 0.5$ and $\overline{\rho} = 0.08$.

Diamond lattice subjected to shear. In its perfect state, a Square lattice would exhibit unusually high endurance strength and long fatigue life since all the vertical constituent struts are loaded axially. This is, of course, unrealistic since all real lattices have slight imperfections; therefore the C-C fatigue data for a perfect Square lattice are omitted from the discussion in Section 4.6. Even with a slight amount of buckling imperfection, say $\kappa_b = 0.01$, the fatigue life of the Square lattice is reduced significantly to a level comparable to the other lattices; a further increase of κ_b, leads to further reduction in fatigue life. In contrast to the stretch-dominated lattices, the Hexagonal lattice is insensitive to imperfections; this is in agreement with what is observed for shear cyclic loading.

Figure 4.16 shows the predicted C-C fatigue data for lattices in their (a) perfect ($\kappa_v = \kappa_b = 0$) and (b) imperfect states. Similar to shear, the $S - N$ data for the perfect lattices in Fig. 4.16a do not collapse into a single line indicating the dependence of fatigue life on lattice micro-architecture. In their perfect state, the Diamond lattice is again found to have the longest fatigue life of the four lattices, with the exception of Square which is not representative of real lattices. However, if one ranks the lattices

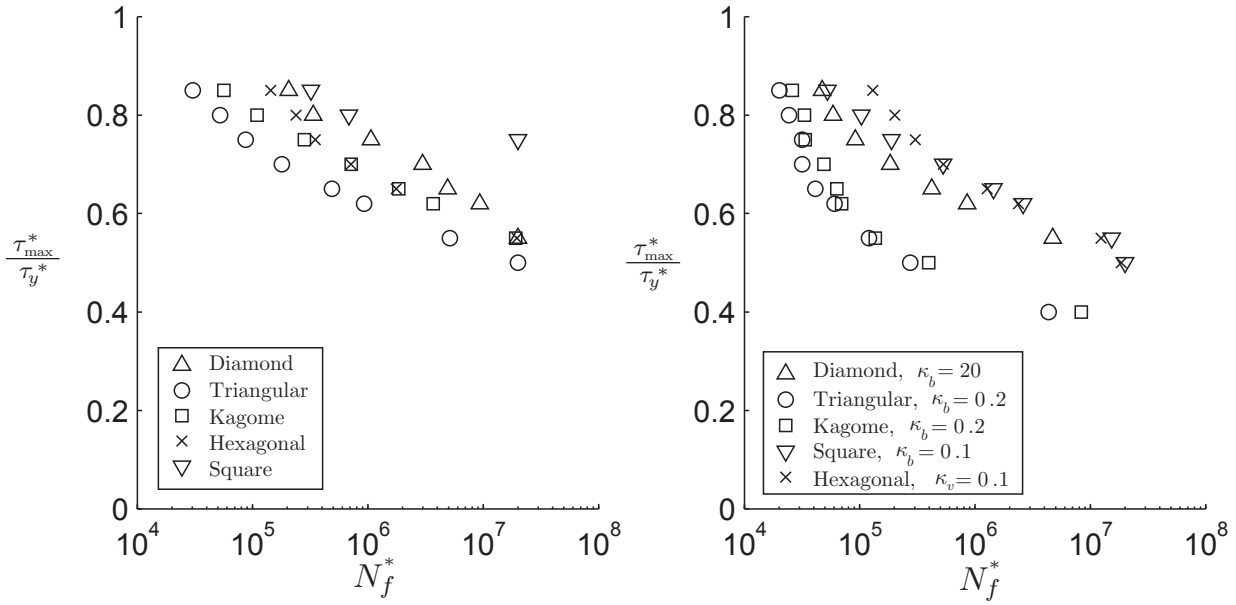

Figure 4.16: C-C fatigue data for lattices (a) without imperfections and (b) with imperfections. All data shown are for load ratio $R = 0.5$ and $\overline{\rho} = 0.08$.

from longer to shorter life, the order is different compared to cyclic shear loading. By introducing imperfections, the $S-N$ data again collapse into two clusters. Unlike for shear, the Kagome and Triangular lattices exhibit similar fatigue response and have the shortest life. Data for the imperfect Square lattice is clustered together with those for Hexagonal and Diamond: this is different to the results for shear in Fig. 4.14. Similar with shear, the initiation and accumulation of fatigue damage is linked to the cell walls that experience the highest bending stresses; this will to be discussed in Section 4.6.2.

Fatigue experiments reported by Harte et al. (2001) have found that the endurance strength of 3D Alporas foams in C-C and T-T is $0.55\sigma_p$ and $0.5\sigma_p$, respectively. However, in cyclic shear, their endurance strength is found to be significantly lower at $0.35\tau_p$. Since stochastic 3D foams are also bending-dominated, comparisons can be made to the Hexagonal lattices here. A similar difference in endurance strength between C-C and shear cyclic loading is also observed here for Hexagonal lattices where the endurance strength is estimated to be $0.5\sigma_y$ and $0.4\tau_y$, respectively. The aforesaid results show that predictions by the NLCD-FE model is able to predict the trend of available experimental data relatively well.

4.6 Discussions

4.6.1 Macroscopic modulus damage accumulation

Figures 4.17 and 4.18 plots the macroscopic modulus damage accumulation (ω^*) against number of cycles N for shear ($\tau^*_{\text{max}}/\tau^*_y = 0.56$) and C-C ($\sigma^*_{\text{max}}/\sigma^*_y = 0.75$), respectively. Note that increasing ω^* corresponds to a reduction in the macroscopic stiffness (E^*) of a lattice through Eq. (4.6). The two applied macroscopic maximum stress were chosen since they give the biggest differences in N^*_f amongst the five lattices. The symbol $\times^k$, in Figs. 4.17 and 4.18, indicates the k^{th} instance when cell wall(s) fail, and the corresponding cycle at which this occurs is denoted by N_k. A cell wall is considered to have failed, and thus deleted from the FE mesh, if its modulus damage parameter $\omega > 0.99$, see Section 4.2.6. Unlike imperfect lattices, cell walls of perfect lattices tend to fail simultaneously in groups of more than one, rather than individually (one at a time), because of geometric symmetries in the micro-architecture.

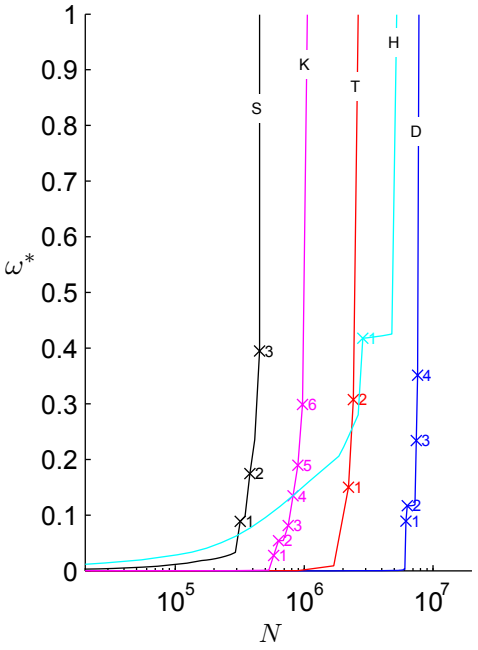

(a)

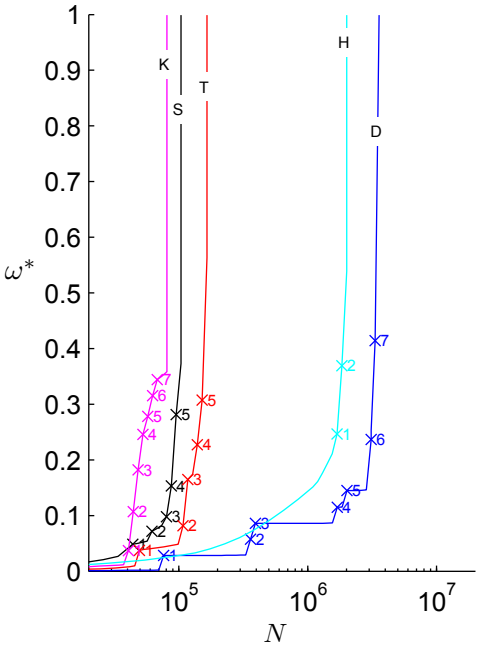

(b)

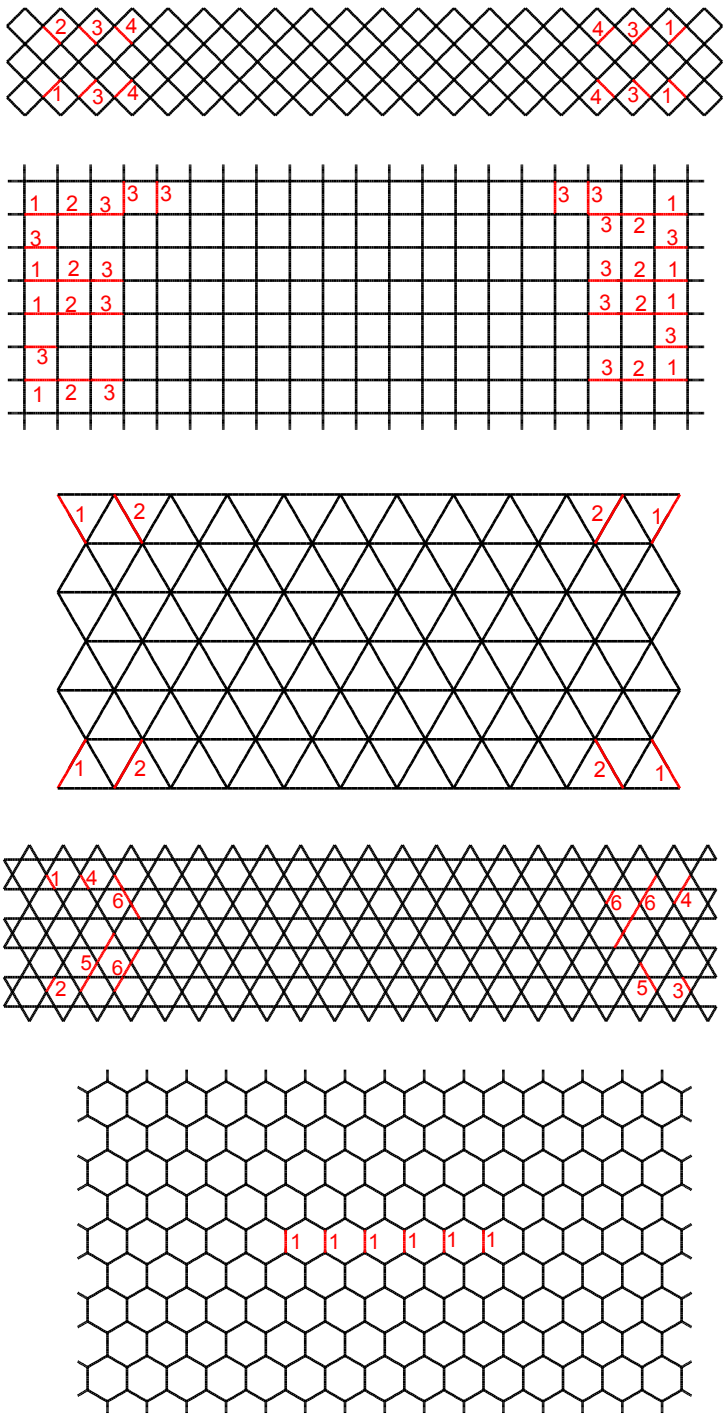

(c)

Figure 4.17: Macroscopic modulus damage accumulation (ω^*) during shear fatigue at load ratio $R = 0.5$ and $\tau^*_{\max}/\tau^*_y = 0.56$ for (a) perfect and (b) imperfect lattices. $\times$ indicates the instance at which cell wall failures are observed. (c) Locations of failed cell wall in lattices that contain no imperfections.

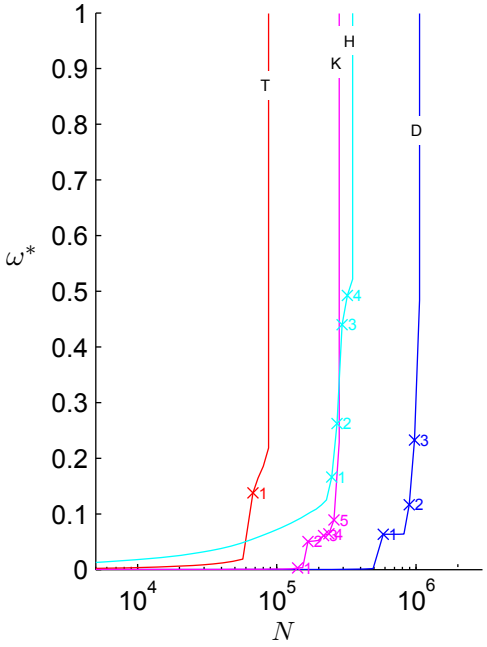

(a)

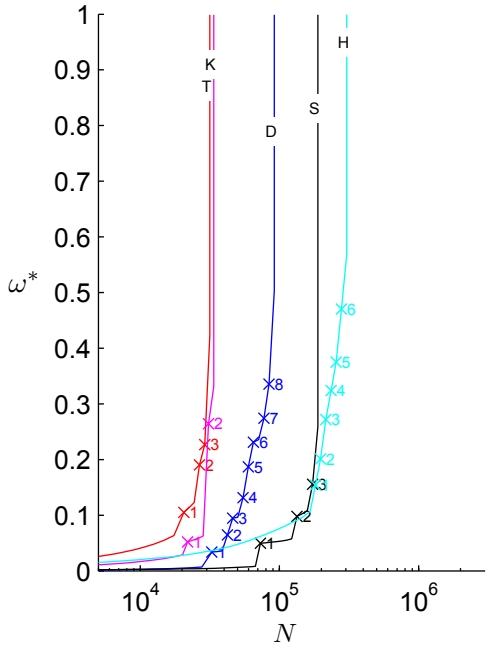

(b)

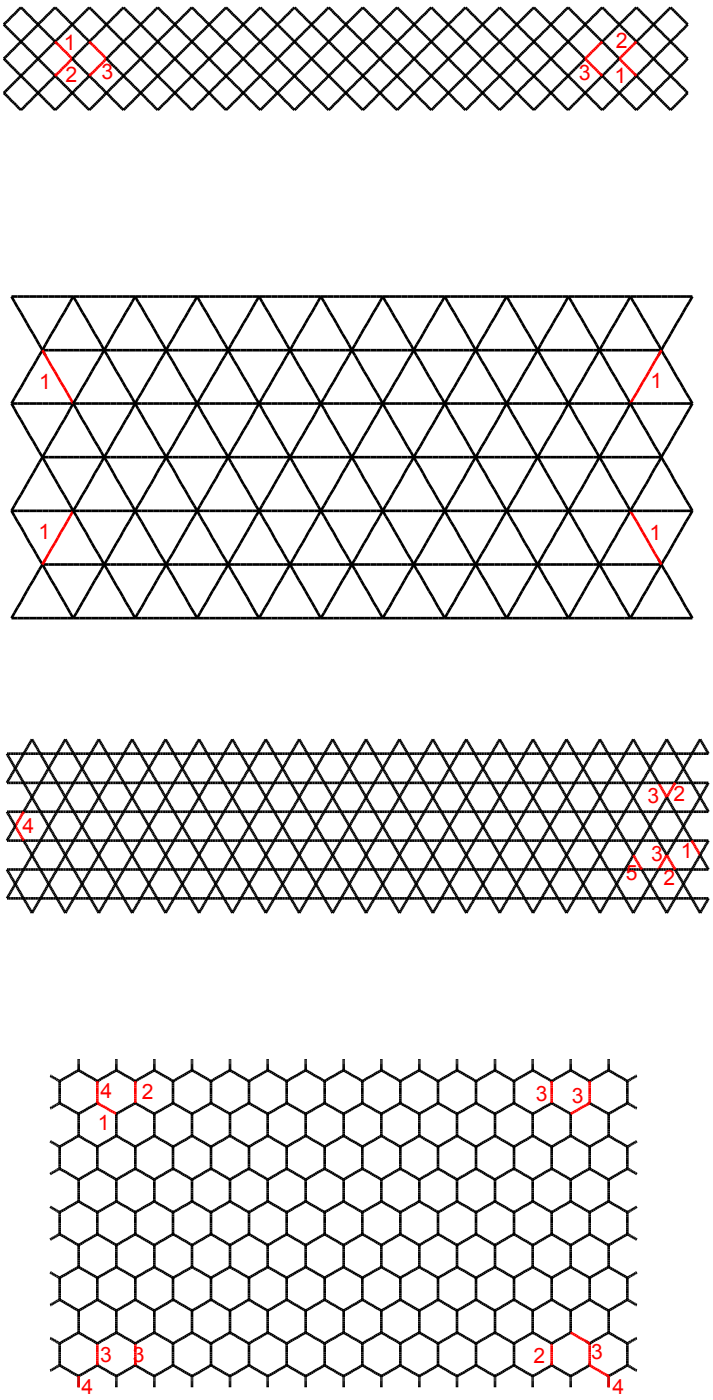

(c)

Figure 4.18: Macroscopic modulus damage accumulation (ω^*) during C-C fatigue at load ratio $R = 0.5$ and $\sigma^*_{\max}/\sigma^*_y = 0.75$ for (a) perfect and (b) imperfect lattices. $\times$ indicates the instance at which cell wall failures are observed. (c) Locations of failed cell wall in lattices that contain no imperfections.

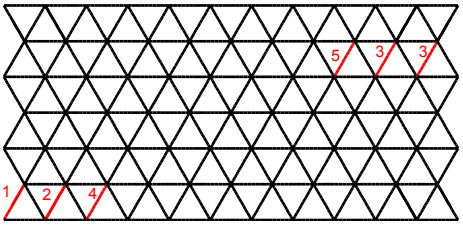

Figure 4.19: Locations of failed cell walls predicted by the NLCD-FE model for an imperfect Triangular lattice subjected to cyclic shear.

The locations of the failed cell walls in a lattice, and the sequence at which this occurs, are also shown in Figs. 4.17 and 4.18 - this is only shown for the perfect lattices.

4.6.1.a Perfect vs imperfect lattices

The fatigue response of a perfect lattice and its imperfect counterpart is compared in Fig. 4.17. Take, for example, the case of a Triangular lattice subjected to shear. In its perfect state, cell wall failures are observed in just two instances. Four cell walls fail simultaneously at N_1 followed by another four at N_2; their locations in the lattice are shown in Fig. 4.17. The NLCD-FE model predicts that the failure of just four cell walls is sufficient to reach $\omega^* \approx 0.3$. Beyond N_2, the next set of cell walls, in total 16, to fail is sufficient to cause failure with $\omega^* \approx 1$; these are not indicated in the lattice diagram for clarity. For the imperfect case, cell walls fail in a progressive manner. The first cell wall to fail occurs much earlier in the load cycle, at $N_1 = 4 \times 10^4$ compared to $N_1 = 2 \times 10^6$ for its perfect counterpart. The location of the first failed cell wall is directly related to the imposed buckling eigenmodes estimated from the FE model. Cell wall failures are observed at five different instances until the final rapid damage accumulation phase causes complete failure. In contrast to a perfect lattice, cell wall tends to fail individually one-by-one, rather than in groups, the location of the failed cell walls is indicated in Fig. 4.19. The first cell wall to fail at N_1 is directly associated with the imposed buckling imperfection in that cell wall. One may conclude that imperfections gives rise to more gradual macroscopic failure in terms of modulus damage accumulation.

Similar observations to the above are also made for the other lattice micro-architectures for both shear and C-C loading. For the stretch-dominated lattices, the presence of

buckling imperfection tends to trigger fatigue failure at a lower N_1 compared to the perfect counterpart; see, for example, Fig. 4.18. The location of the failed cell wall at N_1 is always associated with the location of most severely buckled strut. Even though the presence of imperfections leads to a significant reduction in fatigue life - as previously discussed in Section 4.5 - the more progressive modulus degradation may be preferable in practical applications, instead of the rapid failure, which would allow time for detection of fatigue damage. For bending-dominated micro-architectures - the Hexagonal and Square lattice in shear - the imperfections that were introduced through vertex perturbation hardly affects their fatigue life. Similarly, the way ω^* accumulates in bending dominated micro-architectures is also insensitive to imperfections. However, the loss of perfect periodicity of micro-architecture again means that cell wall do not fail in groups and a slightly more progressive accumulation of ω^* is observed; this is most evident for Square lattices under shear.

A comparison between the location of failed cell walls in an imperfect Diamond lattice subjected to shear, as predicted by the NLCD-FE model, and the experimental results from Cote et al. (2007a) is shown in Fig. 4.20; note that the experimental results are presented for one end of the specimen and is rotated by 90° to the horizontal. The first cell wall to fail is found in exactly the same location for both the numerical and experimental results, which is near one of the four corners of the lattice. The second cell wall to fail is further away from the boundaries; the location between experimental and numerical results do not exactly match because of the different dimensions of the specimen. The next cell wall failures are observed to be increasingly away from the boundary and towards the central part of the specimen. Another important observation that is common between the numerical and experimental results, is that the macroscopic lattice failure is triggered by the failure of few cell walls, while the rest of the specimen remains mostly undamaged. These observations further validate the capabilities of the current NLCD-FE to simulate fatigue damage/failure in the lattices.

4.6.1.b Bending- versus stretch-dominated lattices

Figures 4.17 and 4.18 highlight significant differences in the fatigue response of stretch- and bending-dominated micro-architectures: the latter exhibits greater damage accu-

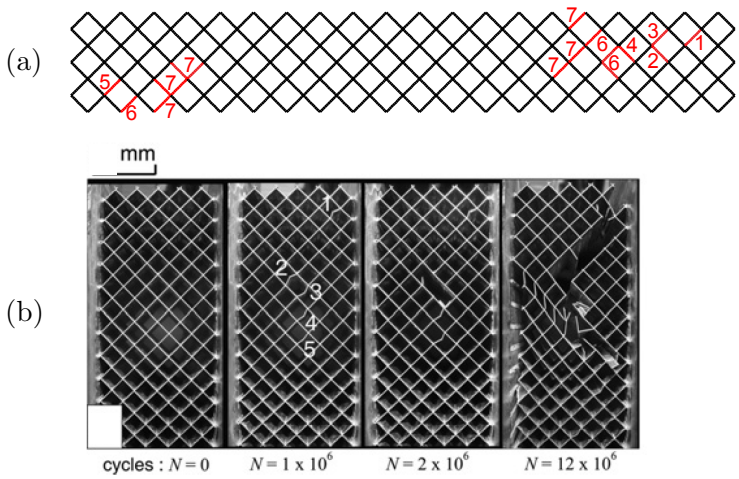

Figure 4.20: (a) Locations of failed cell walls as estimated by the NLCD-FE model for the Diamond lattices subjected to cyclic shear. (b) Photographs of the experimentally observed sequence of failed cell walls in a Diamond lattice subjected to cyclic shear (Cote et al., 2007a). The last photograph, $N = 12 \times 10^6$, corresponds to macroscopic lattice failure.

mulation in the early stages before the first set of cell wall fails ($N < N_1$). On the contrary, the three stretch-dominated lattices, ω^* is nearly zero for $N < N_1$. A potential advantage of bending micro-architectures in real application is the ability to detect the accumulation of fatigue damage relatively early before the onset of catastrophic failure at N_f^*. However, this may interfere with the design requirements of the lattice and thus negate the above benefit. The more progressive ω^* accumulation in bending-dominated lattices (Hexagonal and Square in shear) is associated with a higher percentage of cell walls that experience fatigue damage. This is illustrated in Fig. 4.21, where the percentage of cell walls with damage $\omega > 0.01$, for the analysis step prior to N_1, is plotted against N_f^*. Evidently, the stretch-dominated lattices show significantly lower percentage of damaged cell walls compared to the Hexagonal and Square lattices.

The endurance strength of the cell wall material σ_e^* at a load ratio of $R = 0.5$ is $\approx 0.6\sigma_y^*$, as shown Fig. 4.5; damage accumulate in any cell wall that experience higher stress than σ_e^*. For the same applied normalised remote stress, $\sigma_{\max}^*/\sigma_y^*$ or $\tau_{\max}^*/\tau_y^*$, a considerably higher proportion of cell walls exceed σ_e in bending-dominated lattices - 70% for the Square in shear and 25% for the Hexagonal, see Fig. 4.21 - in comparison to the stretch-dominated counterpart - all $< 2\%$ in shear and $< 8\%$ in C-C. However, this does

not necessarily correlate to lower N_f^* as is clearly seen in Fig. 4.21. This is due to the strain softening in a larger proportion of the cell walls in the bending-dominated lattices that reduces the local cell wall stresses. This subsequently decreases the damage accumulation rate in these cell walls, see Eq.(4.7), and eventually the bending-dominated micro-architectures are found to have comparable N_f^* to their stretch-dominated counterparts.

The observations for the perfect lattices also hold for imperfect ones. The imperfect stretch-dominated lattices accumulate fatigue damage in an even smaller percentage of cell walls prior to N_1 since damage is isolated in the cell walls the buckle the most. On the other hand, for bending-dominated lattices, there is hardly any difference in their fatigue response regardless of whether imperfections are present. However, as previously addressed in Section 4.5, N_f^* is reduced for stretch-dominated lattice but is hardly affected for bending-dominated lattices. Hence, the percentage of damaged cell walls cannot be used to explain the differences in N_f^* among the five micro-architectures.

The percentage of cell walls that accumulate damage is characteristic of the lattice micro-architecture. Additionally, from Fig. 4.17 and 4.18 it becomes apparent that each micro-architecture accumulate damage in cell walls at different regions of the lattice. Naturally, the next question to be addressed is what causes this difference and whether the boundary layers influence these observations in any way; this will be addressed next.

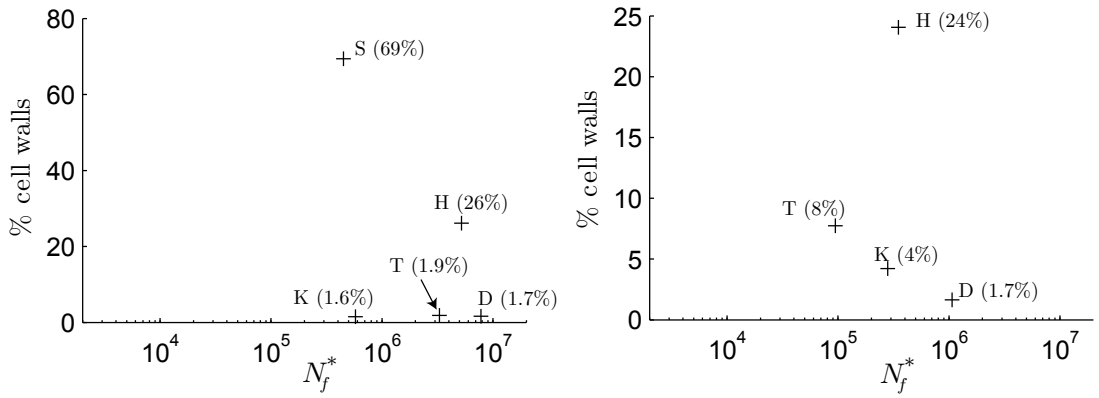

Figure 4.21: Percentage of cell walls in a lattice with damage $\omega_i > 0.01$ prior to $N < N_1$, in (a) shear $(\tau^*_{\text{max}}/\tau^*_y = 0.56)$ and (b) C-C $(\sigma^*_{\text{max}}/\sigma^*_y = 0.75)$.

From Section 4.6.2 onwards, we shall focus only on perfect lattices unless otherwise stated. This allows us to isolate the role of micro-architecture on fatigue response without the influence from random imperfections and buckled cell walls.

4.6.2 Damage distribution maps

Damage maps are generated for the lattices in a similar manner as the strain maps of Fig. 3.36 by replacing shear strain γ_{12}^* with element modulus damage ω; see Eq.(4.13). To construct these maps, ω is interpolated across the lattice area to generate a continuous map – instead of plotting ω along individual cell walls – that would provide a better visualisation of the damage distribution of an entire lattice. The damage map serves two purposes: (1) to highlight differences in the percentage of damaged cell walls between bending- and stretch-dominated lattices; and, (2) highlight region(s) within a lattice where damage had occurred and/or with the greatest accumulation of damage.

First, the micro-level damage (ω) distribution is plotted for the cycle that corresponds to macroscopic modulus damage $\omega^* \approx 0.02$, in Fig. 4.22. The two extreme cases - in terms of the percentage of damaged cell walls - of Hexagonal and Triangular lattices are shown; note that the number of cycles needed to reach $\omega^* \approx 0.02$ varies significantly which depends on loading and micro-architecture. Even though both lattices have identical knocked-down in macroscopic modulus ($\omega^* \approx 0.02$), their internal damage distribution, and percentage of damaged cell walls, are very different. For the Triangular lattice, damage is highly localised in just a few cell walls of between 4 and 8 depending on micro-architecture; we will show later that this applies to all stretch-dominated lattices. By contrast, damage is highly diffused and affect a large region of the bending-dominated lattices. Note that the severity of damage are different in each case; the damaged cell walls in the Triangular lattice reach a maximum $\omega = 0.4$, although for the Hexagonal lattice is just $\omega = 0.1$.

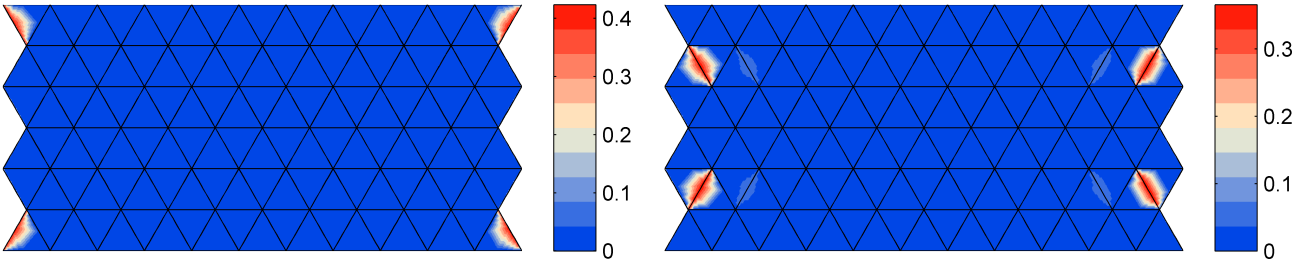

(a) Shear, $N = 1.9 \times 10^6$ (b) C-C, $N = 6.1 \times 10^4$

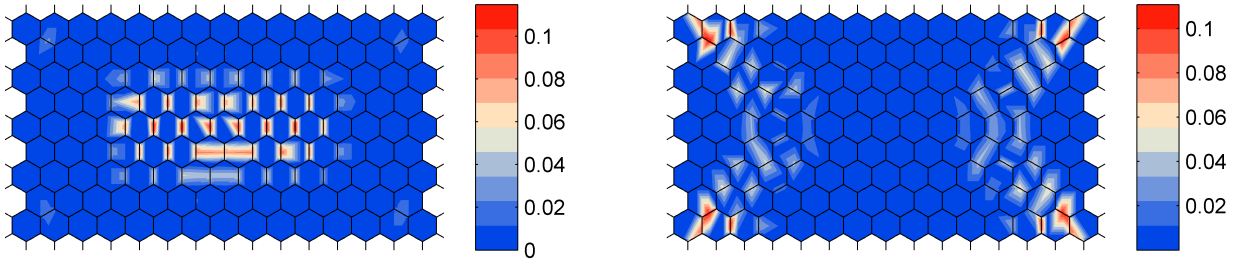

(c) Shear, $N = 3.7 \times 10^4$ (d) C-C, $N = 9.6 \times 10^3$

Figure 4.22: Damage distribution maps in (a,c) shear $(\tau^*_{\max}/\tau^*_y = 0.56)$ and (b,d) C-C $(\sigma^*_{\max}/\sigma^*_y = 0.75)$. The state of damage is plotted for the indicated cycle N, for which the macroscopic modulus damage is $\omega^* \approx 2\%$.

Figures 4.23 and 4.24 show the damage maps for each lattice micro-architecture subjected to cyclic shear $(\tau^*_{\max}/\tau^*_y = 0.56)$ and C-C $(\sigma^*_{\max}/\sigma^*_y = 0.75)$; the case of a perfect Square lattice in C-C is not considered which was explained earlier. The maps are plotted for just before $N = N_1$, where N_1 corresponds to the cycle when cell wall(s) first fail, see Fig. 4.17 and 4.18. This means that the maximum ω is similar in all lattices, however ω^* varies substantially between bending- and stretch-dominated lattices, as already discussed previously. These maps clearly show that damage is highly localised for the Diamond, Triangular and Kagome lattices compared to Hexagonal and Square lattices. For all three stretch-dominated lattices, considerable ω is accumulated in only four cell walls, while the rest of cell walls have $\omega \approx 0$. By contrast, ω is spread to significantly greater proportion of the cell walls in the two bending-dominated lattices. For the Hexagonal lattice, nearly all of its cell wall are damaged, with the exception of those near its boundaries. The reverse is observed for the Square lattice - the specimen remains undamaged at its bulk cells, whilst damage occurs next to the lattice boundaries.

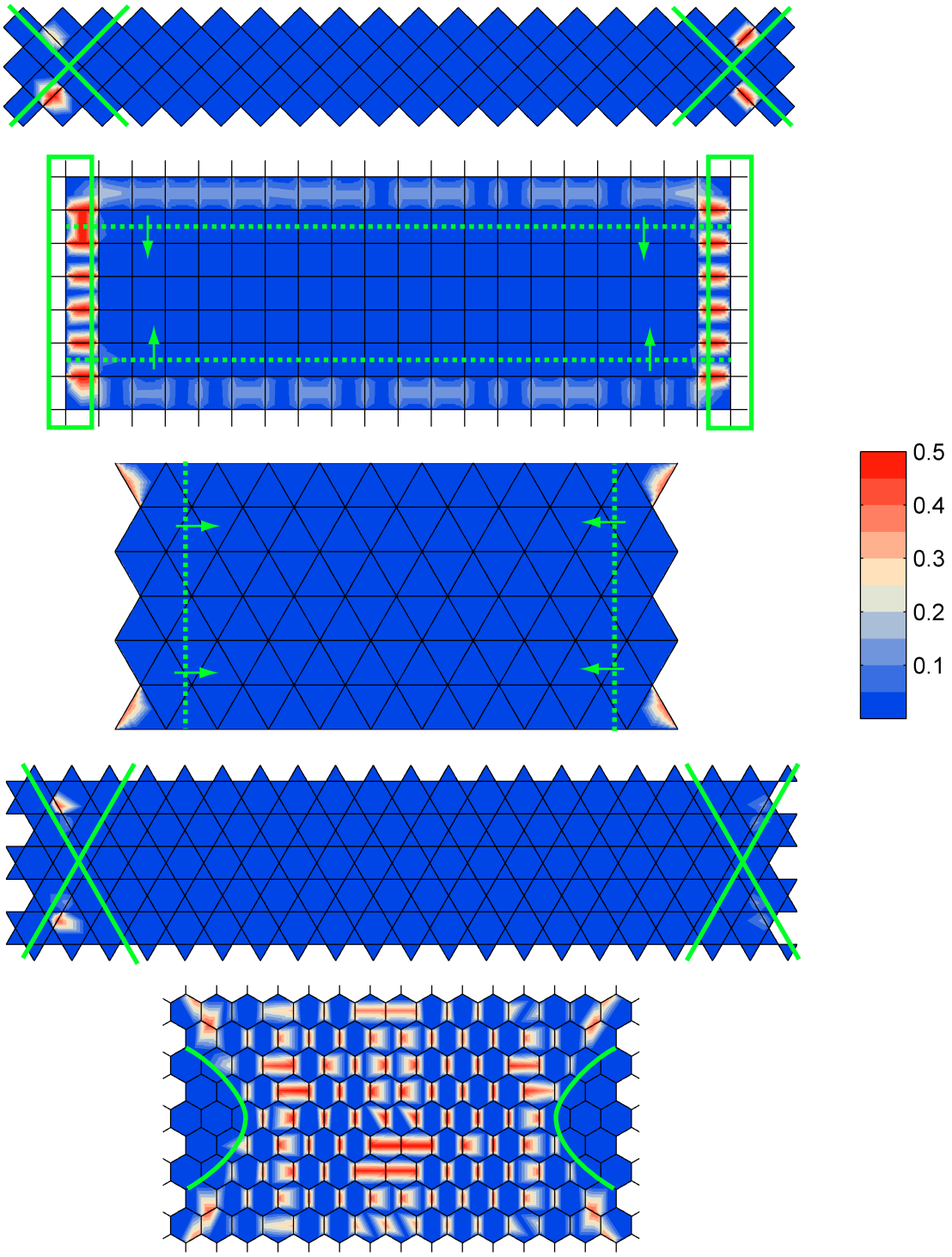

Figure 4.23: Damage distribution maps of lattices under cyclic shear. Damage levels shown correspond to just before $N = N_1$, where N_1 corresponds to the cycle when cell wall(s) first fail. Data shown is for $R = 0.5$ and $\tau^*_{\max}/\tau^*_y = 0.56$. The borders of boundary layers are shown with green colour. For diffused boundary layers, the arrows indicate the direction of decreasing boundary layer influence.

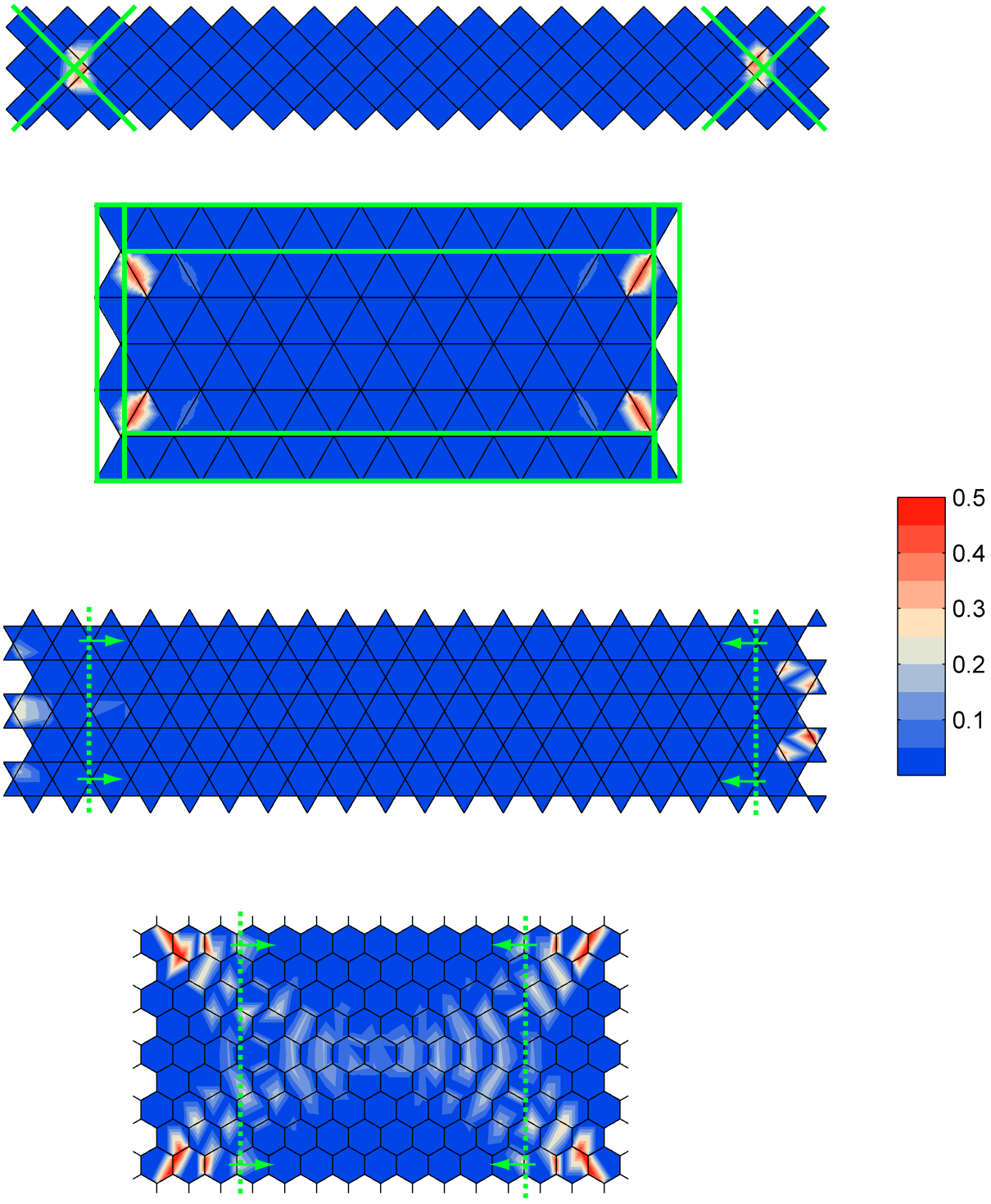

Figure 4.24: Damage distribution maps of lattices under cyclic shear. Damage levels shown correspond to just before $N = N_1$, where N_1 corresponds to the cycle when cell wall(s) first fail. Data shown is for $R = 0.5$ and $\sigma^*_{\max}/\sigma^*_y = 0.75$. The borders of boundary layers are shown with green colour. For diffused boundary layers, the arrows indicate the direction of decreasing boundary layer influence.

The regions in a lattice where elevated damage is observed, e.g. $\omega \approx 0.5$ in the damage maps, is a consequence of edge effects. The cell walls within these regions are the first to fail at cycle $N = N_1$. In Figs. 4.23 and 4.24, the border between a boundary layer and 'bulk' cells is indicated with green lines; these are described in detail in Chapter 3. However, for some lattices - the Kagome and Hexagonal in compression and the Triangular and Square in shear - there is no clear border between a boundary layer and the bulk cells; an approximate boundary is shown using dotted lines and the direction towards which its influence decreases is indicated with arrows. For the lattices that have a clear border between boundary layer and bulk cells, the location of maximum ω occurs along the border; this is also the location of the first cell wall failure. For the lattices without a definite border, the location of high damage is within the boundary layers. These results are not surprising. The cell walls within the boundary layers experience higher local stresses compared to the bulk of the lattice cells because the 'local' lattice modulus within the boundary layers is reduced compared to the 'bulk' modulus, see Chapter 3. The only exception the Hexagonal lattice in shear where the cell walls in the bulk of the lattice are highly damaged, rather than in the boundary layers. This is believed to be due to the bending mode superimposed on shear for specimens of low aspect ratio ($\overline{W}/\overline{H}$), which induces stiffer boundary layers relative to the bulk cells (Diebels and Steeb, 2002).

4.6.3 Fatigue response of *infinite-sized* lattices

Even though all three stretch-dominated lattices, in their perfect state, fail by the same macroscopic damage accumulation mechanism - i.e. by rapid complete lattice failure following N_1 - the estimate N_f^* for each lattice vary significantly. The next point to be investigated is the fatigue response in the absence of boundary layers, by addressing two questions: (1) does a finite- and infinite-sized lattice of the same stretch-dominated micro-architecture have the same N_f^* and (2) is the differences in N_f^*, among the different stretch-dominated micro-architectures, also witnessed for the infinite-sized lattices? To investigate this, the FE models used in the unit-cell approach of Chapter 2, are adopted here and coupled with the NLCD-FE model. By using the necessary boundary conditions, Eqs.(2.9) and (2.12), the effects of finite boundaries are eliminated, so the role of lattice micro-architecture is isolated.

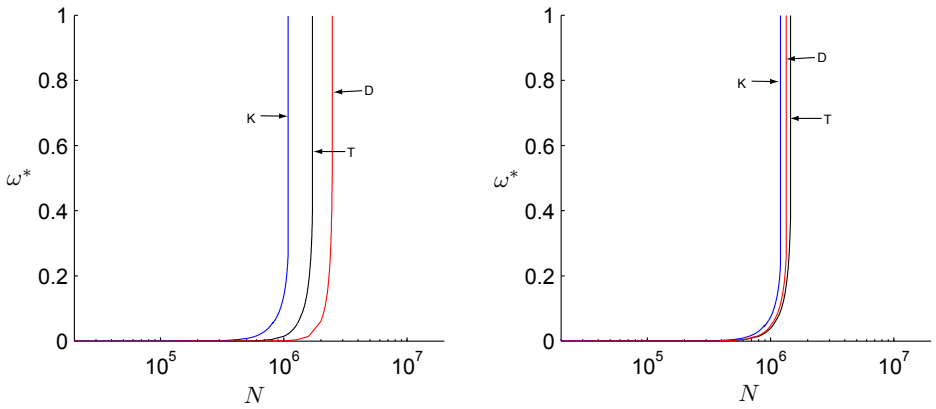

Figure 4.25: Macroscopic modulus damage accumulation, ω^*, under (a) shear ($\tau^*_{\text{max}}/\tau^*_y = 0.75$) and (b) C-C ($\sigma^*_{\text{max}}/\sigma^*_y = 0.75$).

Figure 4.25 shows the macroscopic modulus damage accumulation, ω^*, for Kagome, Triangular and Diamond lattices in shear and C-C loading. The infinite-sized lattices were found to have substantially longer N^*_f compared to their finite-sized counterparts. In shear loading, the applied macroscopic stress shown is $\tau^*_{\text{max}}/\tau^*_y = 0.75$; the value of $\tau^*_{\text{max}}/\tau^*_y = 0.56$ used in Fig. 4.17, gives no damage, since the stress in all cell walls are below the endurance strength σ_e.

By comparing the three infinite-sized lattice micro-architectures together, a different picture emerges compared to their finite-sized counterparts; the differences among the three micro-architectures are significantly less pronounced here. For shear loading and finite-sized lattices N^*_f ranges from 5×10^4 for the Kagome lattice to 3×10^5 for the Diamond lattices; see Fig. 4.14a. However for the infinite-sized lattices, the range in fatigue life is $10^6 < N^*_f < 3 \times 10^6$; interestingly, the order of shorter to longer N^*_f is the same. In C-C loading, the differences among the three infinite-sized lattices are negligibly small with $N^*_f \approx 10^6$, contrary to what is observed for finite lattices where N^*_f ranges from 8×10^4 for the Triangular to 10^6 for the Diamond lattice. The small differences in N^*_f for shear fatigue can be explained by looking at cell wall stresses. Figure 4.26 plots the normalised maximum stress in cell walls for each lattice, $\sigma_{\text{max}}/\left(\sigma_s\right)_y$, with N^*_f. For shear loading, a near linear correlation is found. For compression, all three lattices are found to have similar $\sigma_{\text{max}}/\left(\sigma_s\right)_y$, which is unsurprising since there are no differences in N^*_f.

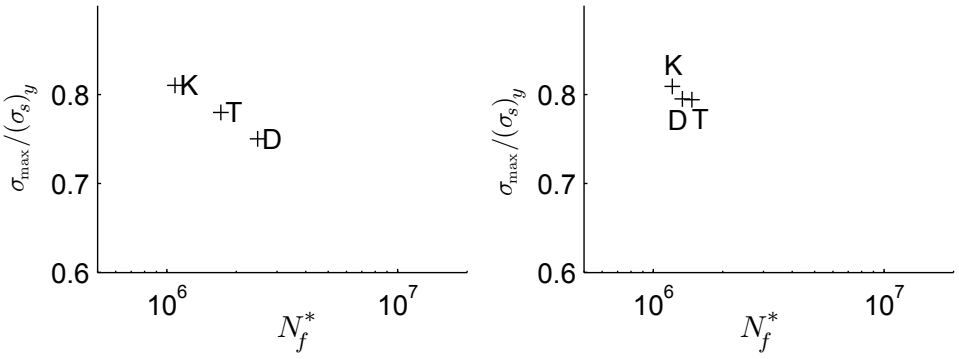

Figure 4.26: Variations of maximum normalised cell wall stress, $\sigma_{\max}/\left(\sigma_s\right)_y$, with N_f^* for infinite-sized stretch-dominated lattices in (a) shear and (b) C-C loading.

4.6.4 Effects of specimen size

From the results in Section 4.6.3 above, it can be deduced that cells in the bulk of a lattice play a secondary role in the fatigue response of periodic micro-architectures whilst the boundary layers have the dominant role. The nature, size and the influence of the boundary layers is directly linked to the lattice micro-architecture and the remote loading as already discussed in detail in Chapter 3. One would expect that the fatigue response of a very large finite lattice would approach the corresponding response of an infinite-sized lattice, as is the case with the monotonic properties.

In order to investigate the above hypothesis, a set of preliminary results are produced as a basis for further future work. Figure 4.27 plots $\omega^* - N$ curves for Diamond and Triangular lattices in shear, where specimens of various sizes - without any imperfections - are shown. The fatigue response of both lattices is found to be sensitive to specimen size. For the Diamond lattice, their fatigue life is found to reduce as the specimens gets bigger, despite that the specimens are of similar $\overline{R} = \overline{W}/\overline{H}$ - hence their monotonic properties have very similar values. A similar trend is also observed for the Triangular lattice, where the larger the lattice the lower the N_f^*. This is observed for both aspect ratio $\overline{W}/(\overline{H}-2)$ presented; from Fig. 3.39, Triangular lattices of the same $\overline{R}_c$ have the same shear monotonic properties. Further work is thus required to better understand the mechanisms that leads to this specimen size dependency. A likely explanation for this, is that the local stresses within the boundary layers are higher for the larger specimens, hence fatigue damage initiates at an earlier cycle, leading to reduced N_f^*.

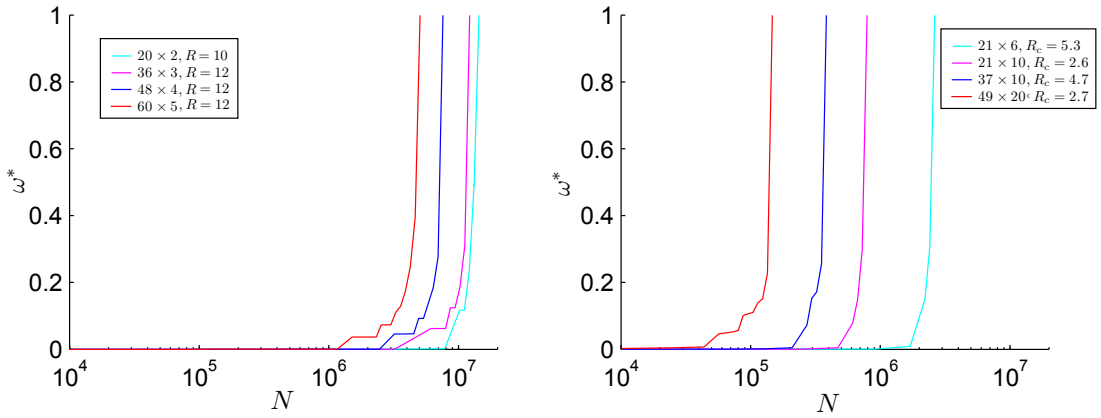

Figure 4.27: Macroscopic modulus damage accumulation, ω^*, for (a) Diamond and (b) Triangular lattices of various sizes $\overline{W} \times \overline{H}$. The loading is cyclic shear with $\tau^*_{\max}/\tau^*_y = 0.56$ and load ratio $R = 0.5$.

4.7 Summary

In this Chapter, the fatigue performance of periodic lattices was investigated by adopting a fatigue damage model coupled with lattice finite element models. Initially, the method is validated using experimental results for Diamond lattices subjected to shear fatigue, showing very good agreement. The effect of load ratio R and $\tau^*_{\max}/\tau^*_y$ are shown to be adequately captured by the model.

The fatigue response of Diamond, Triangular, Kagome, Square and Hexagonal lattices in shear and compressive cyclic loading and its sensitivity on the presence, and severity, of imperfections is investigated. For the stretch-dominated lattices, imperfections are introduced based on the buckling of the constituent struts - as given by eigenvalue analysis - whilst for the bending-dominated lattices the vertex perturbation method. The fatigue life and endurance strength of stretch-dominated micro-architectures, are found to be significantly reduced by the presence of imperfection; the extend of the reduction depends on the lattice and the severity of buckling modes considered. On the other hand, the bending dominated micro-architectures are insensitive to the presence of imperfections.

For perfect lattices, the estimated fatigue life is found to depend on lattice micro-architecture, but there is no indication that the stretch-dominated micro-architectures

hold any advantage over the bending-dominated ones. For imperfect lattices, some lattices are found to give similar fatigue response and cluster together in the estimated $S - N$ diagrams. However, this is only intended to give an approximate lower bound of the fatigue life in real lattices.

The bending-dominated lattices are found to accumulate damage in a greater percentage of cell walls as opposed to stretch-dominated lattices, where significant damage is observed in only few cell walls; in some cases only four. This leads to a more progressive macroscopic damage accumulation rate in the bending-dominated lattices. The location where elevated damage is concentrated is found to be directly associated with the presence of edge effects. By using the unit-cell approach, as introduced in Chapter 2, with stretch-dominated lattices, the lattice micro-architecture in the bulk of a specimen is shown to have only a minor influence on the estimated fatigue life; the small differences are explained by the cell wall stresses. The cells at the boundary layers are thus more influential on the estimated life. The differences in estimated fatigue life among the five lattices are thus attributed to the differences in the induced boundary layers in each of the lattices. Lastly, the role of specimen size is briefly investigated where larger lattices are found to give shorter fatigue life; further work is thus required to delineate why the specimen size affects the estimated fatigue response.

Chapter 5

Fracture

5.1 Introduction

In this chapter, the fracture behaviour of stochastic lattices, made up of elastic-brittle ligaments (or struts), will be studied and the results compared to their periodic counterparts. Previously, Fleck and Qiu (2007) and Romijn and Fleck (2007) had characterised the fracture behaviour of elastic-brittle periodic lattices – Triangular, Kagome, Hexagonal, Square and Diamond – in both their perfect and perturbed (by using the vertex perturbation technique described in Section 1.1.2) states. Here, a similar *'boundary-layer analyses'* (BLA) shall also be employed to quantify the bulk toughness of the non-periodic Voronoi lattices. The BLA approach assumes the existence of an idealised K-field around the crack-tip of these stochastic lattices and it will be used to investigate the effects of cell-regularity, relative density, mode mixity and T-stress, upon the predicted toughness, as well as the location of incipient cell wall fracture. Two commonly-used test specimen geometries will also be modelled using FE and the fracture toughness predicted by these will be compared to predictions by the BLA. The differences in predictions will be explained through a numerical-based 'displacement field analysis' (DFA) approach.

5.2 Methodology

Voronoi lattices – with a range of Λ – are generated following the procedure outlined in Section 1.1.3. They are modelled using finite elements; the procedures were described in Chapters 2 and 3 so they are not repeated here. It is worth emphasizing that the corresponding results for each Λ are based on an average of 20 independent tessellations: this is necessary because of the stochastic nature of the cell micro-architecture in Voronoi lattices. Two different methods are employed here to impose the remote

loading to these lattices. First, the BLA is used to study the idealised stress-field that would develop around the crack-tip, in a manner similar to existing literature (Choi and Sankar, 2005; Fleck and Qiu, 2007; Romijn and Fleck, 2007). In addition, two standard test-specimen geometries – the single-edge notched in three-point-bending (SEN-3PB) and the compact tension (CT) specimens – are also modelled using FE. The BLA approach tacitly assumes an *infinite-sized* lattice that is not influenced by edge-effects, i.e. the toughness estimated by the BLA is a bulk (intensive) value. However, with the standard test-specimen approach, the lattice may/may not be influenced by size and/or boundary effects; this is to be investigated in Section 5.4. One would expect similar toughness predictions by the BLA and the two standard specimen configurations, provided the latter are sufficiently large to minimise the impact of size effects. However, it will be shown later that this is not always the case and the reasons for this will be identified.

For both methods, a deterministic approach, similar to that employed in Choi and Sankar (2005); Fleck and Qiu (2007); Romijn and Fleck (2007), is employed to determine the fracture toughness of a lattice. The cell walls in a lattice are assumed to be elastic-brittle with no dependence on scale, i.e. failure always occurs at the same maximum stress, regardless of the cell wall dimensions. For such an idealised material, failure occurs when the local stress at the outermost fibre of any beam element in the lattice reaches the cell wall fracture strength of σ_f.

5.2.1 Boundary-layer analysis (BLA)

Figure 5.1 shows a schematic of a typical Voronoi lattice ($\Lambda = 1$) with $n \times n$ cells that has been implemented in ABAQUS/standard®. A long plane-strain crack of length $\alpha = nd_0/2$ is assumed to align along the negative x_1 axis, where $d_0 = l\sqrt{3}$ and l is the uniform cell wall length corresponding to a periodic Hexagonal lattice. The crack-tip is located at the nucleation point of the crack-tip cell. The displacement field associated with the in-plane stress field around a crack-tip, this is given in Eq.(1.14), is applied to the boundary nodes of the FE mesh. This approach was employed by Fleck and Qiu (2007) and Romijn and Fleck (2007). The predicted toughness corresponds to the value of applied stress intensity factor (SIF), K, such that the maximum local tensile stress

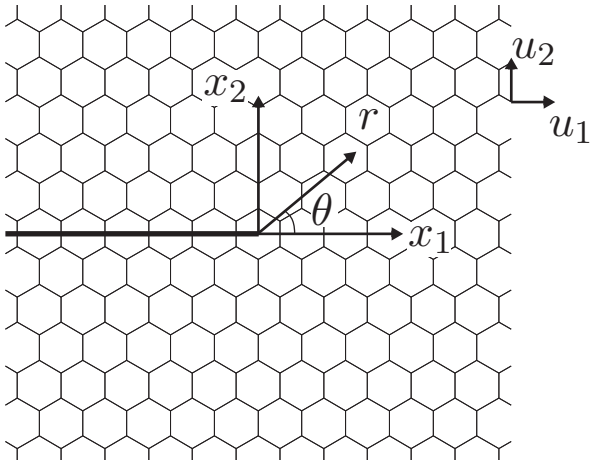

Figure 5.1: Schematic of the model used in a BLA that contains a long plane-strain crack aligned along the negative x_1 axis. The Cartesian coordinates (x_1, x_2) and polar coordinates (r, θ) are centred at the crack-tip.

in any ligament reaches σ_f.

The displacement field (u_1, u_2) associated with the asymptotic K-field – the leading term in Eq.(1.14) – around a plane-strain crack in an infinite elastic solid is given by (Kanninen and Popelar, 1985)

$$u_i = \frac{1}{2G^*_{\text{ps}}}\sqrt{\frac{r}{2\pi}}\left[K_{\text{I}}\hat{u}_i(\theta,\nu^*_{\text{ps}})^{\text{I}} + K_{\text{II}}\hat{u}_i(\theta,\nu^*_{\text{ps}})^{\text{II}}\right] \quad ; \quad i = 1,2 \tag{5.1}$$

where $\hat{u}_i(\theta,\nu^*_{\text{ps}})^{\text{I}}$ and $\hat{u}_i(\theta,\nu^*_{\text{ps}})^{\text{II}}$ are functions of θ; the plane-strain Poisson's ratio ν^*_{ps} of the lattices; and, G^*_{ps} is the macroscopic plane-strain shear modulus. For mixed-mode loading, the relative contributions of K_{I} and K_{II} are controlled by means of an elastic mode-mixity parameter M defined as (Shih, 1974)

$$M = \frac{2}{\pi}\tan^{-1}\left(\frac{K_{\text{II}}}{K_{\text{I}}}\right) \quad ; \quad 0 \leq M < 1 \tag{5.2}$$

where the limiting values of $M = 0$ and $M \to 1^-$ correspond to pure mode I and mode II SIF, respectively. The decoupling of modes in isotropic elasticity allows the total energy release rate $\mathcal{G}$ for mixed mode fracture to be written as

$$\mathcal{G} = \frac{K_{\text{I}}^2}{E^*_{\text{ps}}} + \frac{K_{\text{II}}^2}{E^*_{\text{ps}}} \tag{5.3}$$

from which an effective SIF may be defined as follows:

$$K_{\text{eff}} = \sqrt{K_{\text{I}}^2 + K_{\text{II}}^2} \quad . \tag{5.4}$$

To account for the second term of Eq.(1.14) – the T-stress – an additional term is added to the displacement field in Eq.(5.1), accordingly, as follows:

$$u_1 = \frac{(1-\nu^*_{\text{ps}})}{2G^*_{\text{ps}}} Tr\cos\theta \quad \text{and} \quad u_2 = -\frac{\nu^*_{\text{ps}}}{2G^*_{\text{ps}}} Tr\sin\theta \quad . \tag{5.5}$$

The magnitude of T-stress is typically normalised by the effective SIF to give the stress biaxiality ratio defined as

$$B = \frac{T}{K_{\text{eff}}\sqrt{\alpha}} \quad . \tag{5.6}$$

By imposing the K-displacement field on the lattice boundary, it is tacitly assumed that the lattices are isotropic and homogeneous with effective elastic properties that are known a priori. Recall that the macroscopic elastic properties of *infinite-sized* Voronoi lattices were previously presented in Chapter 2; see, specifically, Figs. 2.7 and 2.8. Since the elastic properties were obtained under plane-stress conditions, they need to be modified to their plane-strain equivalent before they can be used with Eq.(5.1). The elastic modulus of the lattices in the prismatic x_3 direction is $E_{33} = \overline{\rho}E_{\text{s}}$ and its Poisson's ratio is $\nu_{31} = \nu_{32} = \nu_{\text{s}}$ (Gibson and Ashby, 1997). Under plane-strain conditions, with $\epsilon_3 = 0$ and $\sigma_3 = \nu_{31}\sigma_1 + \nu_{32}\sigma_2$, the modified elastic moduli and Poisson's ratio become

$$E^*_{\text{ps}} = \frac{2E^*}{2-3\overline{\rho}^2\nu_{\text{s}}^2} \quad , \quad \nu^*_{\text{ps}} = \frac{2+3\overline{\rho}^2\nu_{\text{s}}^2}{2-3\overline{\rho}^2\nu_{\text{s}}^2} \quad , \quad G^*_{\text{ps}} = \frac{E^*_{\text{ps}}}{2(1+\nu^*_{\text{ps}})} \quad . \tag{5.7}$$

The finite element mesh used is similar to that described earlier in Section 2.5.2. A crack is generated along the negative x_1-axis by splitting the beams at $x_2 = 0$, so that a traction-free crack plane is created. Numerical checks have shown that it suffices to model each cell wall with four Timoshenko beams elements (B21) without any loss of

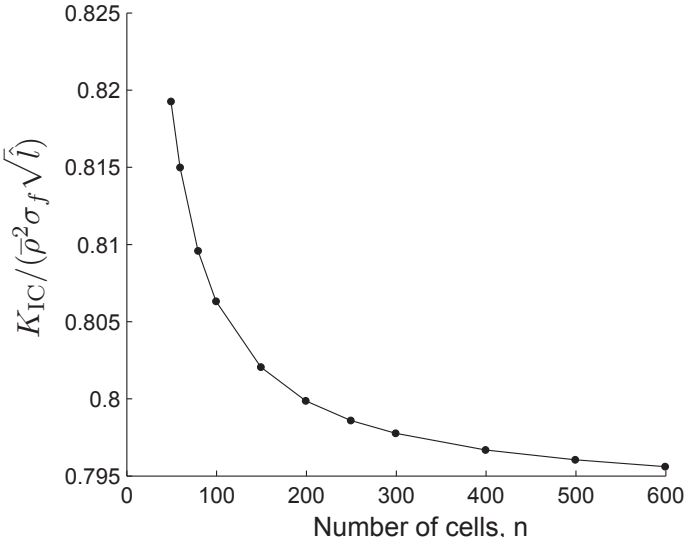

Figure 5.2: Typical variation of the mode I fracture toughness of a periodic Hexagonal lattice against overall lattice size of $n \times n$ cells predicted by a BLA.

accuracy. Even though a BLA is employed to estimate the fracture toughness of *infinite-sized* lattices, the actual lattice modelled in FE is *finite-sized*. By imposing Eq.(5.1) to the boundaries of the FE mesh, one tacitly assumes far-field loading conditions, i.e. the lattice is infinite. To this end, the lattice modelled would need to be sufficiently large so that its boundary does not affect the crack-tip stress state. The macroscopic fracture toughness of the Voronoi lattices was found to be sensitive to lattice size. Figure 5.2 shows how the mode I fracture toughness, K_{IC}, of a periodic lattice ($\Lambda = 1$) varies with the overall lattice size (of $n \times n$ cells). The same also applies to non-periodic Hexagonal lattices. As a compromise between computational time and numerical accuracy, all simulations were performed using lattices with 200×200 cells.

5.2.2 Standard test specimen configurations for toughness testing

Figure 5.3 shows the schematic of two *finite-sized* standard test-specimen geometries, viz. CT and SEN(B)-3PB, that are modelled using finite elements; hereinafter, they are simply referred to as standard specimens for brevity. The specimen size is dictated by its principal dimension W, whilst the rest of its dimensions scale proportionally with W according to ASTM E399-12e1 (2012), E1820-11e2 (2011) and D5045-99e1 (2007). The specimen size W will be normalised by their respective characteristic cell size to give W/d_0. Note that a K-based method, e.g. ASTM E399-12e1 (2012), recommends

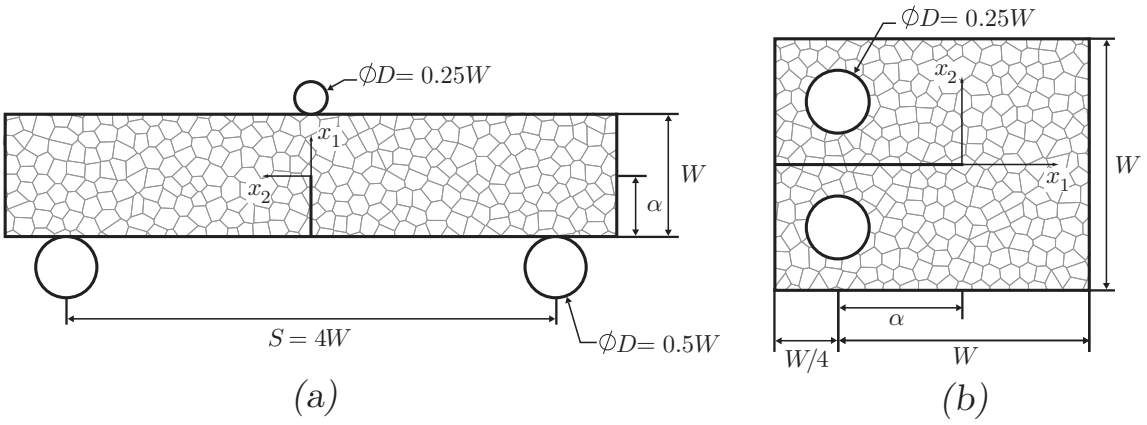

Figure 5.3: Schematics of the set-up for (a) SEN(B)-3PB and (b) CT specimen configurations

minimum test specimen size requirements to ensure that the plastic zone around the crack-tip is small compared to the specimen cross section so that fracture occurs under nominally linear-elastic conditions. However, this need not be considered here since the present work is concerned only with elastic-brittle ligaments where no plastic zone develops in the lattices. A macroscopic crack aligned in the x_1 direction – note the orientation of the axes in the SEN(B)-3PB specimen in Fig. 5.3a – of length $\alpha = 0.5W$ is used throughout the analysis.

One of the key objectives in this study is to compare the toughness prediction by the BLA for an *infinite-sized* lattice to those 'measured' by the two *finite-sized* standard specimen configurations. As it will be shown later, cell microstructural variations around the crack-tip can cause significant variations in the predicted toughness. Therefore, to make sensible comparisons, it is imperative that the topology of those cells surrounding the crack-tip is identical for both the standard specimens and that used in the BLA. To achieve this, each independent tessellation generates a master lattice which is 'trimmed' to give seven different specimen sizes, viz. $W/d_0 = 10, 15, 20, 25, 30, 50$ and 100, for each of the two configuration. The 'trimming' process, shown schematically in Fig. 5.4, generates lattices that contain identical set of cells surrounding the crack tip, regardless of W/d_0, for both standard specimens and that used in the BLA.

Frictionless surface interaction is used to model contact between the pins and specimen shown in Fig. 5.3, with the former as solid non-deformable bodies. For the standard

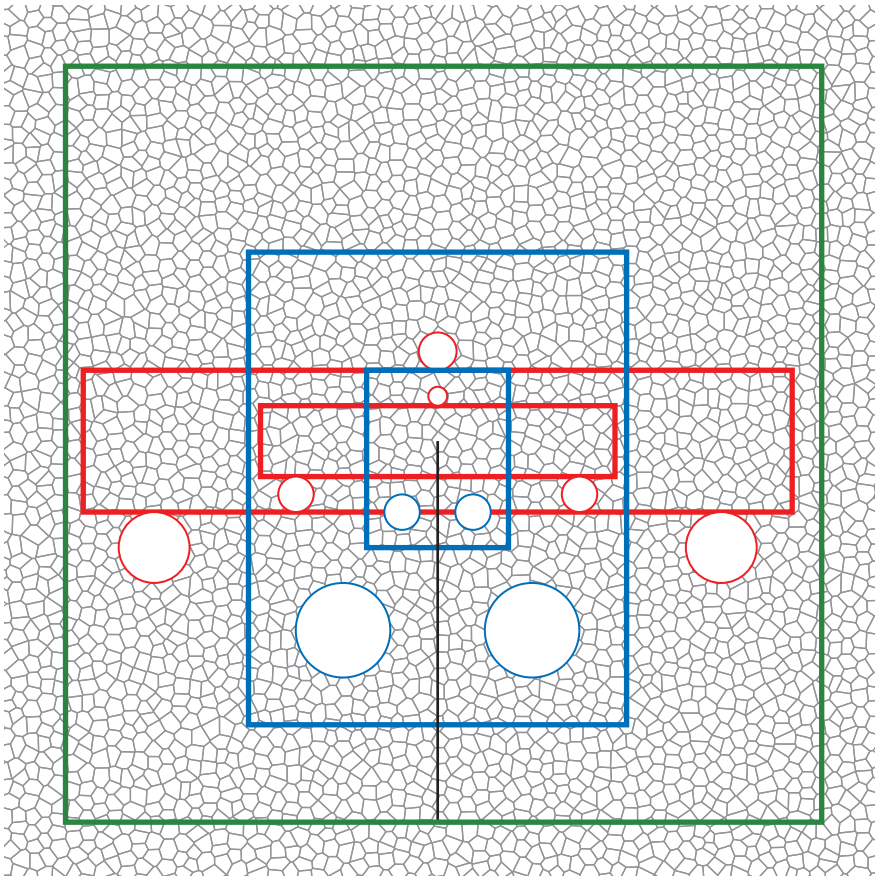

Figure 5.4: Schematic of the trimming process to generate CT (blue) and SEN(B)-3PB (red) specimens of various sizes (only two sizes are shown here). The actual dimension of the BLA lattice (green) used is much larger than the one shown here, which is for illustration purposes only.

SEN(B)-3PB configuration, a finite displacement is prescribed to the loading pin along the x_1 direction and all degrees of freedom of the other pins are constraint. For the standard CT configuration, a relative displacement is imposed on the two loading pins along the x_2 direction, whilst keeping their other degrees of freedom constraint. No other boundary conditions are imposed on the lattice itself. Just like in the BLA, the FE mesh is modelled with four Timoshenko beam (B21) elements per cell wall and plane strain conditions are enforced along the prismatic x_3 (out-of-plane) direction.

For the two different standard specimen configurations, fracture toughness is estimated by recording the pin load P_Q, corresponding to the onset of fracture in any ligament, and substituting this into (E399-12e1, 2012)

$$K_{\text{IC}} = 3\frac{P_Q}{\sqrt{W}}\frac{S}{W}\sqrt{\frac{\alpha}{W}} \frac{1.99 - \left(\frac{\alpha}{W}\right)\left(1-\frac{\alpha}{W}\right)\left[2.15 - 3.93\frac{\alpha}{W} + 2.7\left(\frac{\alpha}{W}\right)^2\right]}{2\left(1+2\frac{\alpha}{W}\right)\left(1-\frac{\alpha}{W}\right)^{3/2}} \tag{5.8}$$

to calculate the toughness predicted using a SEN(B)-3PB configuration and into

$$K_{\text{IC}} = \frac{P_Q}{\sqrt{W}}\left(2+\frac{\alpha}{W}\right) \frac{\left[0.886 + 4.64\frac{\alpha}{W} - 13.32\left(\frac{\alpha}{W}\right)^2 + 14.72\left(\frac{\alpha}{W}\right)^3 - 5.6\left(\frac{\alpha}{W}\right)^4\right]}{\left(1-\frac{\alpha}{W}\right)^{3/2}} \tag{5.9}$$

for the CT configuration.

5.3 Fracture toughness of *infinite-sized* Voronoi lattices

In this section, the 'boundary-layer'analysis (BLA) is employed to investigate the effects of cell-regularity Λ, relative density $\overline{\rho}$ and T-stress on the bulk mode I (K_{IC}) and mode II (K_{IIC}) toughness of Voronoi lattices. Mixed-mode loading - controlled by a mode-mixity parameter M - is introduced to construct the fracture loci of Voronoi lattices and how they are affected by Λ and T-stress. The sensitivity of the location of incipient cell wall fracture to mode-mixity M is also investigated.

5.3.1 Mode I and mode II fracture toughness

Figures 5.5a to 5.5f show the deformed FE mesh for Voronoi lattices, of identical relative density $\overline{\rho} = 0.1$, with different cell-regularity ($\Lambda \to 0^+, 0.7, 1$) subjected to pure mode I and II loadings. Only 50×50 cells are shown in each case; they were truncated from larger lattices of 200×200 cells.

The average fracture toughness of the lattices were fitted to the scaling law (Fleck and Qiu, 2007; Gibson and Ashby, 1997)

$$\frac{K_{\text{C}}}{\sigma_f\sqrt{\hat{l}}} = D\overline{\rho}^d \tag{5.10}$$

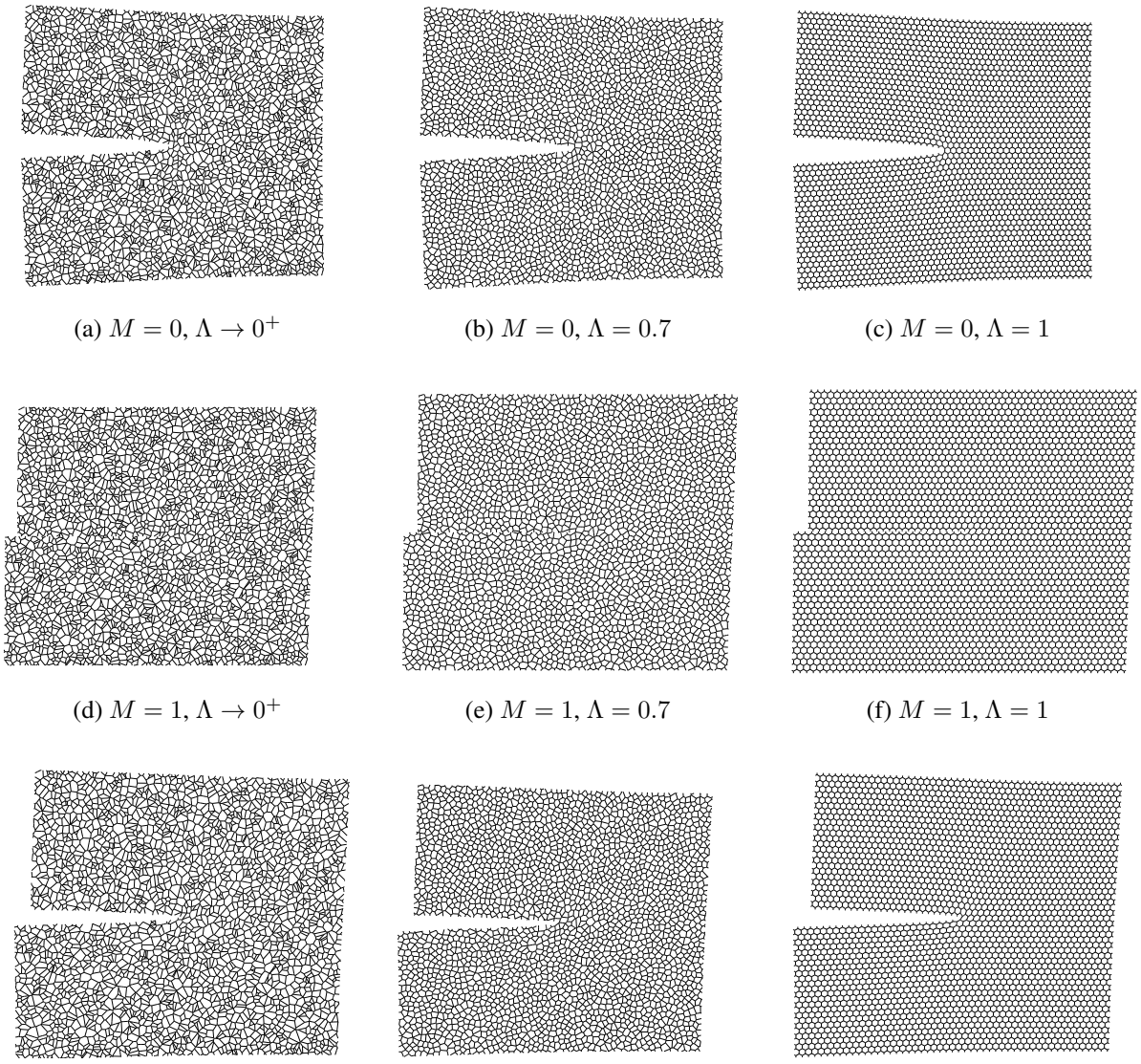

(a) $M = 0, \Lambda \to 0^+$ (b) $M = 0, \Lambda = 0.7$ (c) $M = 0, \Lambda = 1$

(d) $M = 1, \Lambda \to 0^+$ (e) $M = 1, \Lambda = 0.7$ (f) $M = 1, \Lambda = 1$

(g) $M = 0.5, \Lambda \to 0^+$ (h) $M = 0.5, \Lambda = 0.7$ (i) $M = 0.5, \Lambda = 1$

Figure 5.5: Typical lattice deformation under mode I, mixed-mode and mode II loadings. Lattices shown have cell-regularity $\Lambda \to 0^+, \Lambda = 0.7$ and $\Lambda = 1$, and identical relative density of $\overline{\rho} = 0.1$.

	Λ	0	0.25	0.5	0.6	0.7	0.8	1
Mode I	d	1.974	1.987	1.988	1.987	1.981	1.987	1.994
	D	0.691	0.790	0.825	0.795	0.836	0.887	0.927
Mode II	d	2.001	2.010	2.004	2.015	2.010	2.013	2.019
	D	0.420	0.442	0.461	0.479	0.480	0.480	0.486

Table 5.1: Fitted coefficients to the scaling law given in Eq.(5.10).

and plotted on a log-log scale in Fig. 5.6. Note that Eq.(5.10) uses the average cell wall length $\hat{l}$ from Table 2.2. Recall that for the non-periodic lattices, their toughness is an average of twenty tessellations but their respective error bars are not shown for the sake of clarity. Figure 5.6 shows that the predicted lattice toughness fits well the scaling law of Eq.(5.10) with the fitted coefficients tabulated in Table 5.1.

Regardless of cell-regularity or the loading mode, the fracture toughness K_{C} has a quadratic dependence on $\overline{\rho}$. This is to be expected since a Voronoi lattice, whether periodic or non-periodic, has an average nodal connectivity of 3 and, therefore, they deform primarily by cell wall bending with negligible contributions from axial stretch. The effects of cell-regularity upon the lattice toughness is determined by the pre-exponent D which is given in Table 5.1. It shows that the average mode I toughness is more sensitive to cell-regularity than its corresponding mode II counterpart.

Figure 5.7 plots $K_{\mathrm{C}}/(\sigma_f\overline{\rho}^2)$ against $\hat{l}$ for lattices with the same relative density $\overline{\rho} = 0.1$. The square root dependence of $K_{\mathrm{C}}/(\sigma_f\overline{\rho}^2)$ on the average cell wall length $\hat{l}$ (see Eq.(5.10)) is the same for both periodic and non-periodic lattices with identical $\overline{\rho}$. Therefore, adjusting either the cell wall thickness uniformly or the average cell wall length proportionally to obtain the required $\overline{\rho}$ has no effect upon the pre-exponent D in Eq.(5.10). This contradicts the findings of Choi and Sankar (2005) for cubic 3D lattices, where the authors reported a difference in response when $\overline{\rho}$ is adjusted by changing cell size rather than cell wall thickness; the validity of their results were similarly questioned by Romijn and Fleck (2007).

Figure 5.8 shows the variation of the average non-dimensional toughness $K_{\mathrm{C}}/(\sigma_f\overline{\rho}^2\sqrt{\hat{l}})$ with cell-regularity under pure mode I and II loadings. Again, each data point is the average of twenty tessellations and the error bar corresponds to their standard devi-

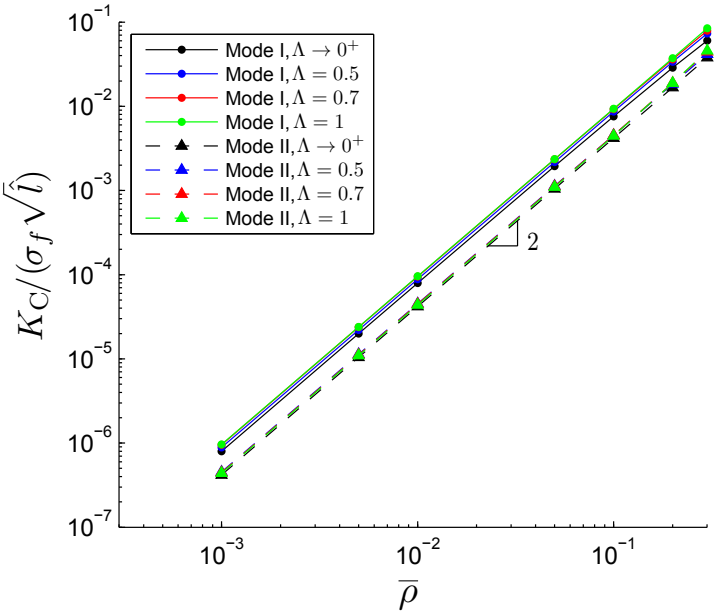

Figure 5.6: Fracture toughness of lattices with different cell-regularity against relative density.

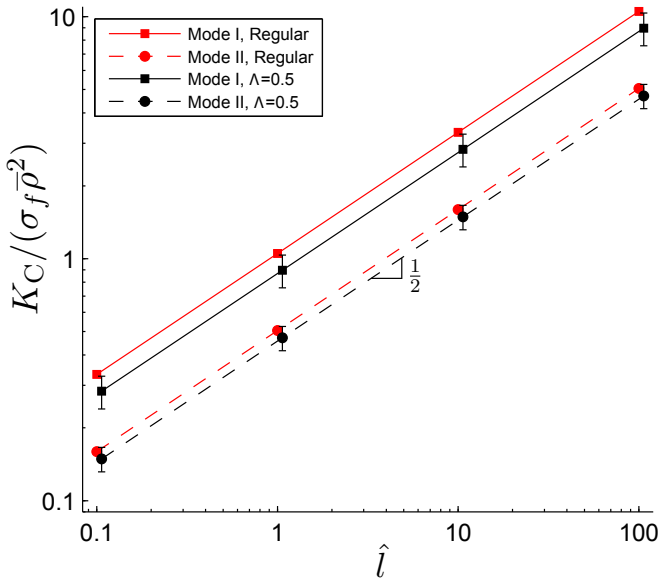

Figure 5.7: Variation of normalised fracture toughness $K_C/(\sigma_f\overline{\rho}^2)$ against average cell wall length $\hat{l}$ for stochastic Voronoi ($\Lambda = 0.5$) and Hexagonal ($\Lambda = 1$) lattices to mode I and mode II loadings. Each data point corresponding to a stochastic lattice is based on an average of twenty tessellations and the error bar indicates standard deviation. All lattices have identical relative density of $\overline{\rho} = 0.1$.

ation. The effect of $\overline{\rho}$ is eliminated by the non-dimensionalisation, so the two plots for $\overline{\rho} = 0.05$ and 0.1 nearly collapse on each other. One observes an almost linear reduction in the average mode I toughness with decreasing cell-regularity, by up to 25% between $\Lambda = 1$ and $\Lambda \to 0^+$. Note that a 15% reduction in $\overline{\rho}$ would be needed to achieve a corresponding reduction in the toughness of a periodic Hexagonal lattice ($\Lambda = 1$). This suggests that cell-regularity Λ has a significant effect upon the mode I toughness of the lattices, but is secondary compared to the effects of $\overline{\rho}$. No inference could be made for mode II loading since the fluctuations in toughness are nearly the same for all Λ. By contrast, as the cells become more irregular, the average in-plane elastic moduli of the lattices increases by up to 20% between $\Lambda = 1$ and $\Lambda \to 0^+$; this increase depends on $\overline{\rho}$ as seen in Fig. 2.7). Note that the standard deviation does not appear to be influenced by Λ. In general, the toughness can vary by up to $\pm 20\%$ from the mean value between tessellations. The main reason for the high variability is because cell wall fracture can initiate several cells away from the crack tip, depending on the local cell topology; this is to be addressed in Section 5.3.3.

Romijn and Fleck (2007) reported that for lattices with $\overline{\rho} = 0.01$, there is a 30% reduction in their average K_{IC} and a 20% increase in their average K_{IIC} value if vertex pertur-

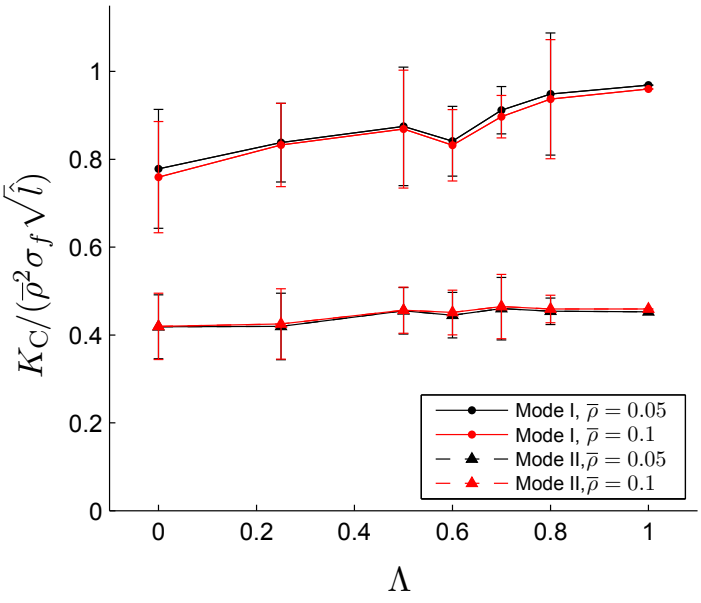

Figure 5.8: Variation of non-dimensional mode I and II fracture toughness $K_{\mathrm{C}}/(\sigma_f \overline{\rho}^2 \sqrt{l})$ against cell-regularity for lattices with $\overline{\rho} = 0.05, 0.1$. Each data point is an average of twenty tessellations and the error bar indicates standard deviation.

bation with $\kappa_v = 0.5$, see Eq.(1.3), is introduced into the lattice. As noted in Chapter 1, a non-periodic lattice generated using the vertex perturbation technique by Romijn and Fleck (2007) would still give a substantively less random cell microstructure (measured in terms of the distribution of cell area) than a Voronoi lattice of $\Lambda = 0.5$. Nevertheless, the difference in K_{IC} of the average $\Lambda = 0.5$ Voronoi lattice compared to the periodic Hexagonal is less than 10% whilst the difference in K_{IIC} is negligible. The reason for this discrepancy is unclear although one possibility is that the cells in a two-dimensional Voronoi lattice, regardless of its cell-regularity, are always convex unlike those generated by the random cell wall perturbation technique where the *local* Poisson's ratio may be negative - this is due to re-entrant cell walls - in some cases.

5.3.2 Mixed-mode fracture toughness

Figures 5.5g to 5.5i show the deformed FE mesh for Voronoi lattices, with different cell-regularity ($\Lambda \rightarrow 0^+, 0.7, 1$), under mixed mode loading of $M = 0.5$. At each mode-mixity M, the combinations of K_{I} and K_{II} needed for a cell wall to fracture are used to generate the fracture loci plotted in Fig. 5.9a. The loci are plotted for a constant $\overline{\rho} = 0.1$ and each data point is the average of 20 tessellations. It must be noted that the fracture loci are insensitive to $\overline{\rho}$.

The fracture locus of a periodic lattice comprises of two distinct straight line segments separated by a kink at $M \approx 0.15$; the same is reported by Fleck and Qiu (2007). This kink coincides with a jump in the location of wall fracture as mode-mixity changes, from A to B as shown in Fig. 5.9b. For the stochastic Voronoi lattices, the absence of a kink in Fig. 5.9a is a consequence of smoothing when averaging the results from twenty independent tessellations. In general, the smoothed loci appears as a quarter ellipse that are largely similar for different values of Λ.

Notwithstanding, the fracture locus of individual tessellations always shows straight line segments as shown in Fig. 5.10a for four different $\Lambda = 0.5$ tessellations. Without averaging, the loci remain inner convex envelopes, but unlike in Fig. 5.9a, are a series of straight segments separated at multiple kink(s), each corresponding to a jump in the cell wall fracture location at that mode-mixity. Figure 5.10b shows the lattice topology for tessellation 1. For this particular tessellation, fracture initiates at cell wall marked

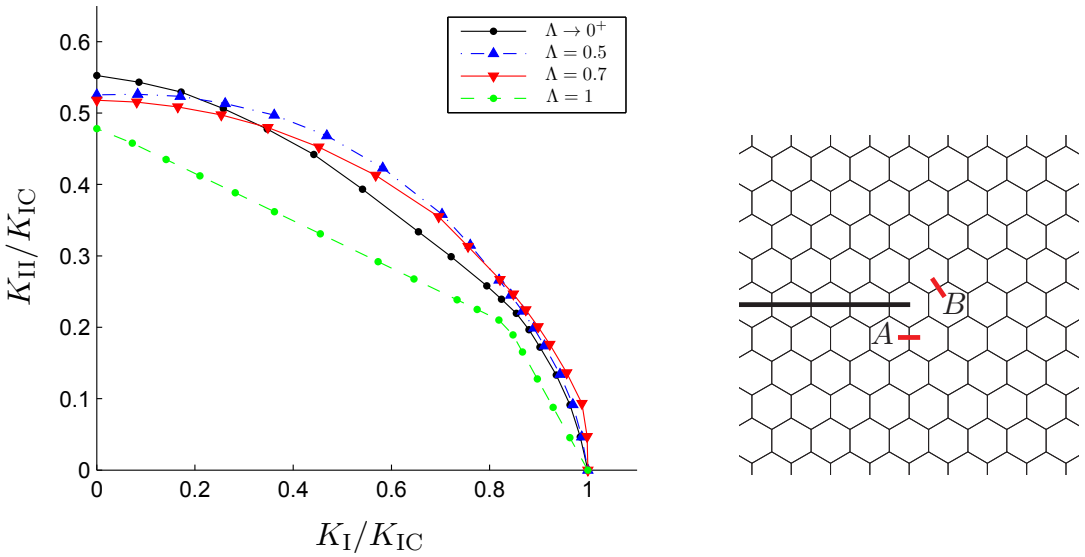

(a) (b)

Figure 5.9: (a) Normalised fracture loci for Hexagonal and stochastic Voronoi lattices. All lattices have identical relative density of $\overline{\rho} = 0.1$ and each data point corresponding to $\Lambda \neq 1$ is the average of twenty tessellations; (b) Location of cell wall fracture for a periodic Hexagonal lattice. Points A and B indicates the location of fractured cell wall under pure mode I and mode II loadings, respectively.

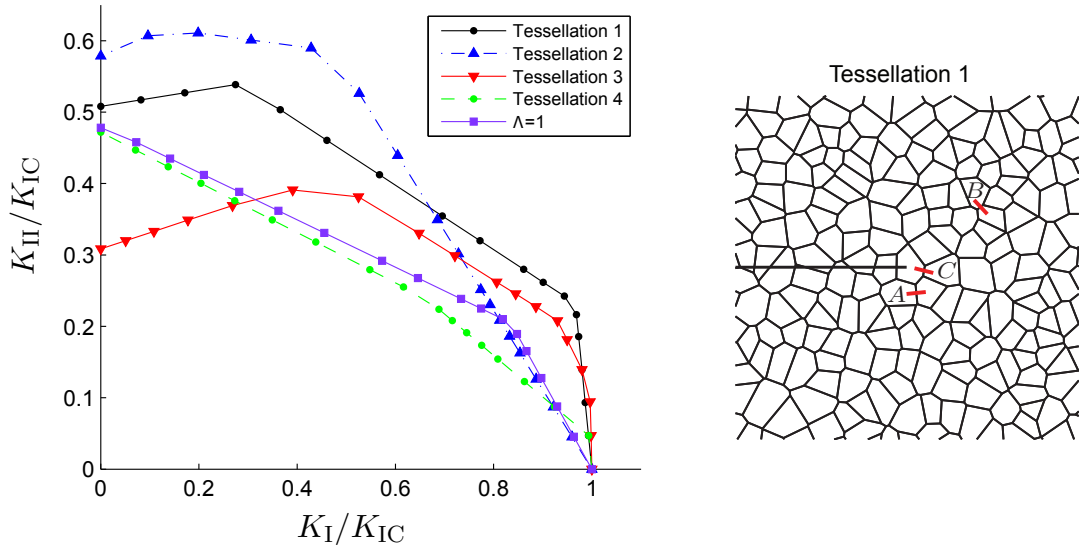

(a) (b)

Figure 5.10: (a) Normalised fracture locus of four typical Voronoi tessellations generated for $\Lambda = 0.5$ and $\Lambda = 1$; (b) Location of cell wall fracture for Tessellation 1 in (a) where A, B and C indicates the switch in fracture location with increasing mode-mixity M.

A if mode-mixity $M < 0.14$, at B if $0.14 \leq M \leq 0.6$ and at C if $M > 0.6$. Note that the number of kinks and at which mode-mixity it appears vary from one tessellation to another without a set pattern for non-periodic lattices: this contrasts with a periodic one.

5.3.3 Location of fracture initiation

Unlike solid materials, the crack path in lattices is, in general, discontiguous where the location of the incipient wall fracture can, in extreme cases, occur up to six cells away from the crack-tip cell (Motz and Pippan, 2002; Olurin et al., 2000; Saenz et al., 2011). For a Hexagonal lattice, fracture initiation always occurs at point A for pure mode I loading as shown in Fig. 5.9b. This contrasts with the assumption made by Gibson and Ashby (1997) and Maiti et al. (1984) where the cell wall immediately ahead of the crack-tip, part of the crack-tip cell, is assumed to fracture first. For mode-mixity $M \geq 0.15$, the fracture site switches to point B. All subsequent values of M, including for pure mode II fail at cell wall B. This switch coincides with a kink in the fracture locus in Fig. 5.9a. It is worth noting that $\overline{\rho}$ has no effect upon the location of fracture - this is consistent with that reported in Fleck and Qiu (2007).

For stochastic lattices, the number of kinks in the fracture loci - that correspond to a shift in fracture location - and at which mode-mixity they appear vary from one tessellation to another without a set pattern. It appears that local variations in the cell topology have a strong influence on the stress magnitude in individual cell walls and, consequently, the location of incipient wall fracture. The differences in the results between lattices of the same Λ are indicative of the sensitivity of the predicted toughness on the *local* cell topology surrounding the crack-tip. The cell-regularity parameter, Λ, is merely a global parameter that places a constraint on the minimum cell size and the distribution of cell sizes in a lattice, and it has no direct control over the cell topology surrounding the crack-tip.

Figure 5.11 shows the location of the fractured cell walls for Voronoi lattices of two different $\overline{\rho}$ (0.05 and 0.1) at three different mode-mixities - mode I, II and $M = 0.5$. Recall that the FE model, see Fig. 5.1, was set-up in such a way that the crack-tip coincides with the nucleus of the crack-tip cell. Each fracture location map plots the

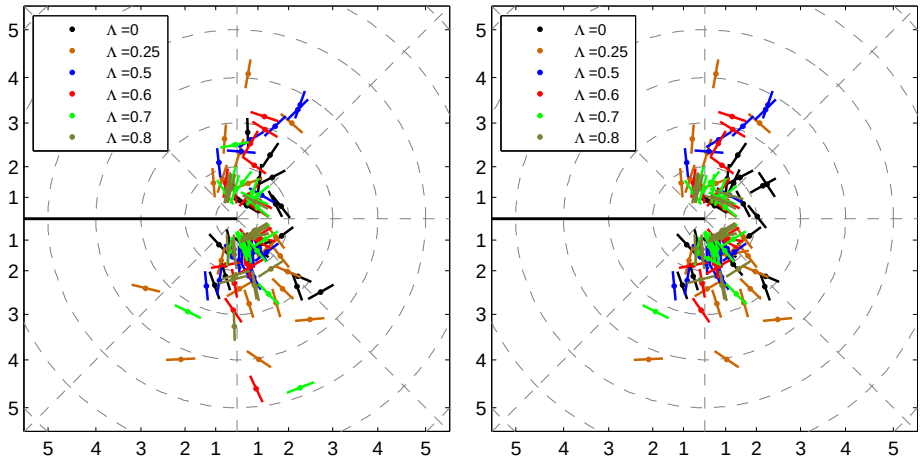

(a) $M = 0, \overline{\rho} = 0.05$ (b) $M = 0, \overline{\rho} = 0.1$

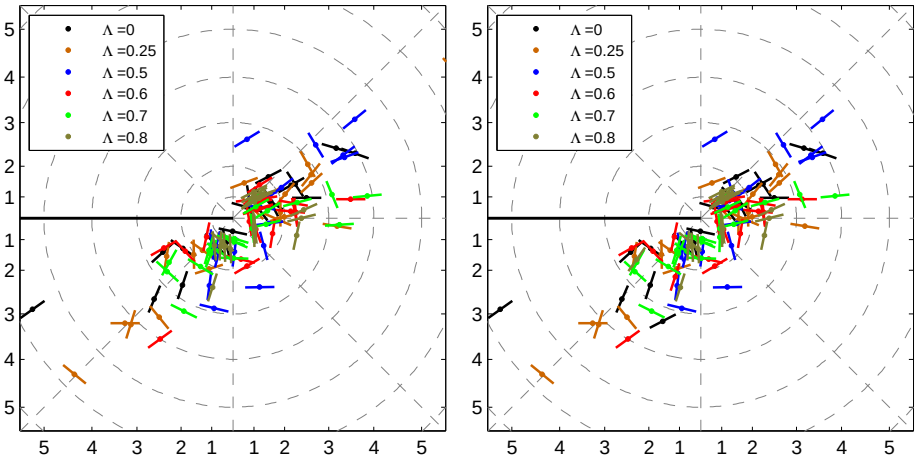

(c) $M = 0.5, \overline{\rho} = 0.05$ (d) $M = 0.5, \overline{\rho} = 0.1$

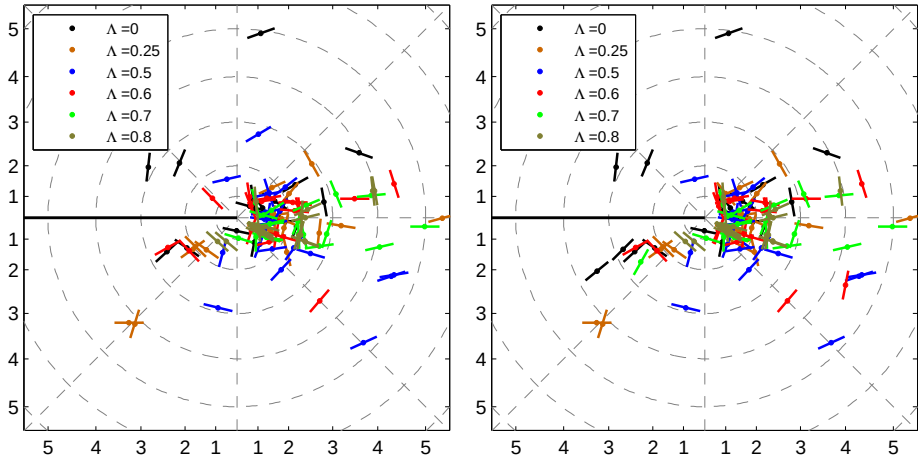

(e) $M = 1, \overline{\rho} = 0.05$ (f) $M = 1, \overline{\rho} = 0.1$

Figure 5.11: Location of incipient wall fracture in stochastic lattices. The mid-point of the fractured cell wall is shown as a dot and the orientation of the cell wall as a line. The circular contours indicate the average number of cells away from the crack-tip.

predicted fracture sites from all twenty tessellations carried out for every Λ investigated. The dot $\bullet$ in the failure map indicates the fracture site whilst the line indicates the orientation of the failed cell wall. The contours of constant radius give the average number of cells away from the crack-tip cell, calculated by taking the average distance of the cell vertices from the crack tip for one hundred tessellations. Unsurprisingly, there is a significant amount of scatter in the observed failure sites, indicating that the fracture process in stochastic Voronoi lattices is highly random. It is evident that the majority of the failures occur near the crack tip, in cells adjacent to the crack-tip cell. However, fractured cell walls were also observed up to six cells away from the crack-tip cell, which is consistent with experimental observations (Motz and Pippan, 2002; Olurin et al., 2000; Saenz et al., 2011). As Λ decreases, the observed fracture locations are increasingly dispersed which is consistent with the increased level of randomness in cell topology. Notice that $\overline{\rho}$ has almost no influence over the location of fracture, this is the same for Hexagonal lattices; compare (a,b), (c,d) and (e,f) in Fig. 5.11.

The loading mode appears to have a strong influence over how the failed cell walls are clustered around the vicinity of the crack-tip. Under mode I loading, most of the fractured cell walls are clustered between the sectors of $-120^\circ \lesssim \theta \lesssim -45^\circ$ and $45^\circ \lesssim \theta \lesssim 120^\circ$ - see Fig. 5.11a and b. In mode II, the majority of the fractured cell walls are clustered between $-30^\circ \lesssim \theta \lesssim 30^\circ$ ahead of the crack-tip, with significant notable exceptions behind the crack-tip. For mixed-mode loading (Fig. 5.11c and d shows the case for $M = 0.5$), the fractured cell walls are clustered between the sectors of $0^\circ \lesssim \theta \lesssim 45^\circ$ and $-135^\circ \lesssim \theta \lesssim -90^\circ$. As mode-mixity increases from 0 to 1, the clustering of the failed walls also shifts relative to the crack plane as depicted in Fig. 5.11. In general, it is observed that lattices of different Λ exhibit similar clustering patterns at the same mode-mixity. There appears to be no direct correlation between the location, orientation and length of fractured cell wall with variations in the macroscopic lattice toughness.

5.3.4 Effects of T-stress

By combining the displacement fields corresponding to the asymptotic K-field and T-stress, Eqs.(5.1) and (5.5) respectively, the effects of T-stress are investigated using the BLA method. Because no contact algorithm is incorporated into the FE model, the two sets of nodes that define the traction-free crack plane are not allowed to come into contact, thus limiting the range of B that can be investigated. In the present study, contact between the crack planes occurs at $B > 0.3$ (for mode I) and at $B > 0$ (for mode II). For mixed-mode loading, the mode-mixity directly influences when contact between the crack faces will occur; for example, at $M = 0.5$ crack closure occurs for $B \geq 0.2$ as shown in Fig. 5.12.

Figure 5.12 shows the effect of T-stress on the normalised effective toughness, $K_{\text{eff,C}}/K^0_{\text{eff,C}}$, where $K^0_{\text{eff,C}}$ is the corresponding critical SIF for $B = 0$. Again, the data points for $\Lambda \neq 1$ is the average of twenty tessellations. It would appear that the influence of T-stress on the normalised effective toughness is most pronounced for mode I loading with negative T-stresses. The normalised effective fracture toughness of a lattice decreases rapidly with increasing negative T-stresses: at $B = -1$, the reduction in effective toughness is, on average, nearly 75% for mode I and 50% for mode II loading.

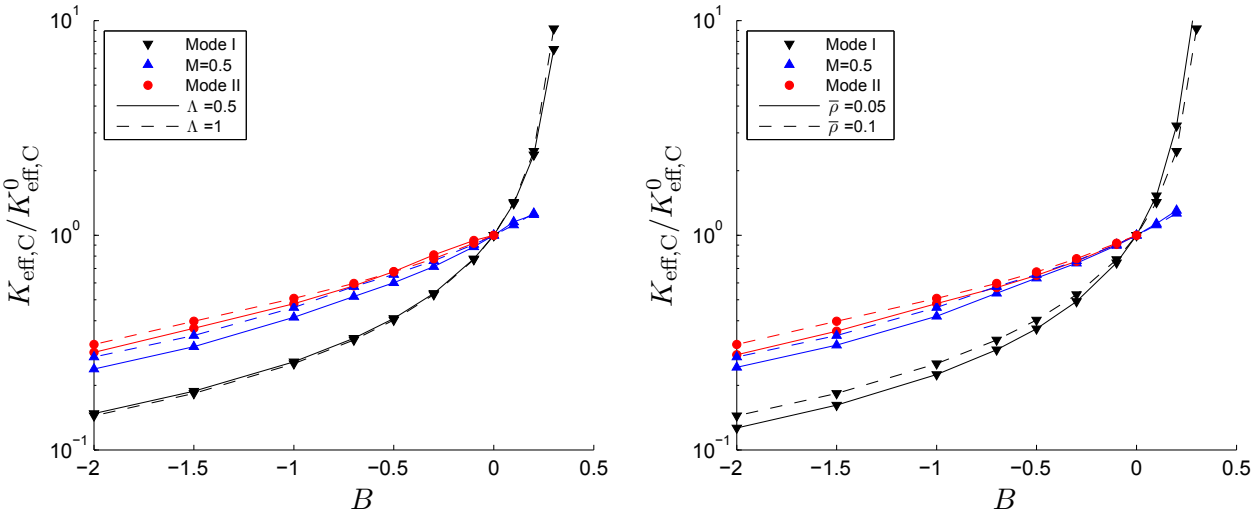

(a) Cell-regularity effect

(b) Density effect

Figure 5.12: Variation of the normalised toughness $K_{\text{eff,C}}/K^0_{\text{eff,C}}$ against T-stress for Voronoi lattices with different (a) cell-regularities and (b) relative densities

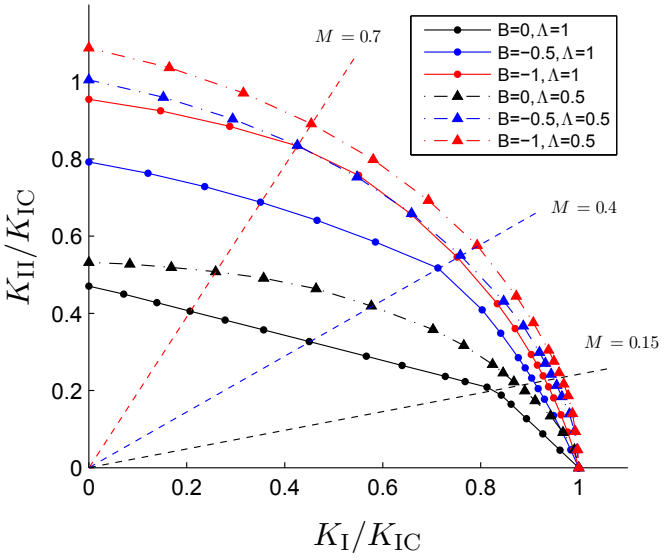

Figure 5.13: Fracture loci of Voronoi lattices at increasing negative T-stress. The two straight lines correspond to $M = 0.4$ and 0.7. All lattices have identical relative density of 0.1. Each data point corresponding to $\Lambda = 0.5$ is the average of twenty tessellations.

The opposite is true for positive T-stresses, since an additional negative displacement component in the x_2 direction reduces the cell deformation in the vicinity of the crack tip, leading to enhancement of the normalised effective toughness as seen in Fig. 5.12. Again, mode I loading is more sensitive to the presence of positive T-stresses than mode II.

Figure 5.12a shows that T-stress has the same effect on the normalised effective toughness $K_{\mathrm{eff,C}}/K^0_{\mathrm{eff,C}}$ for both the periodic Hexagonal and stochastic Voronoi ($\Lambda = 0.5$) lattices. At $M = 0.5$, the effective toughness of a stochastic Voronoi lattice is only marginally lower than a corresponding Hexagonal one for negative T-stresses. Figure 5.12b compares the same for lattices of different $\overline{\rho}$, at 0.05 and 0.1. In general, lattices of a higher $\overline{\rho}$ are less affected by a finite T-stress which agrees with Fleck and Qiu (2007). However, the reduction in effective toughness caused by a reduction in $\overline{\rho}$ is only marginal, and comparatively insignificant, compared to the overall reduction caused by the introduction of T-stresses. Regardless, the quadratic dependence of toughness $K^0_{\mathrm{eff,C}}$ on $\overline{\rho}$ still holds.

Figure 5.13 shows the effect of T-stress on the normalised fracture loci for lattices with $\Lambda = 0.5$ and 1. For negative T, the fracture locus expands as shown because mode I

toughness is more sensitive to the inclusion of T-stresses than mixed-mode or mode II. Unlike a Hexagonal lattice with zero T-stresses, the kink is now less prominent and the switch in the initial cell wall fracture location occurs at a higher mode mixity (at $M = 0.4$ and 0.7 for $B = -0.5$ and -1, respectively, indicated with dotted lines in Fig. 5.13). At $B = -1$, the $K_{\text{II}}/K_{\text{IC}}$ ratio becomes nearly doubled, from 0.47 to 0.95 and from 0.53 to 1.08, for a periodic lattice and a non-periodic lattice ($\Lambda = 0.5$), respectively.

In the presence of finite T-stress, the clustering of the incipient cell wall changes dramatically. Figure 5.14 shows the results for twenty lattices, with cell-regularity $\Lambda = 0.5$, subjected to mode I, mode II and mixed mode ($M = 0.5$) loading at different stress biaxiality ratio B. An increasing T-stress alters the clustering pattern and has the effect of shifting the fractured cell walls to locations more typical of mode I loading as described above. For high T-stress levels in Figs. 5.14j-l ($B = -2$ shown here), the fracture locations recorded were very similar irrespective of mode-mixity. Note also the observed locations for mode I remain unchanged at all values of B.

One likely reason for the significant dependence of T-stress to the effective macroscopic toughness of 2D Voronoi lattices is their near-unity Poisson's ratio ν^*_{ps}. Referring to Eq.(5.5), T-stress induces additional boundary displacement which is predominantly confined in the x_2 direction, with minimal contribution in the x_1 direction, if ν^*_{ps} is close to unity. Consequently, the effects of T-stress may not be as significant in lattices with Poisson's ratio between $0.3 - 0.5$ (e.g. other periodic lattices and foams (Gibson and Ashby, 1997)), and this would somewhat suppress the effect of T-stress upon toughness.

5.3.5 Comparison with periodic lattices

In this section, the bulk toughness of stochastic Voronoi lattices, estimated previously by the BLA, will be compared to existing results for periodic lattices obtained from the literature and were reviewed in Chapter 1.

Figure 5.15 compares the toughness of periodic lattices reported by Romijn and Fleck (2007) to the stochastic Voronoi lattices reported here. It is unsurprising that Voronoi lattices of any cell-regularity – only $\Lambda = 0.5$ is shown in Fig. 5.15 – have a quadratic

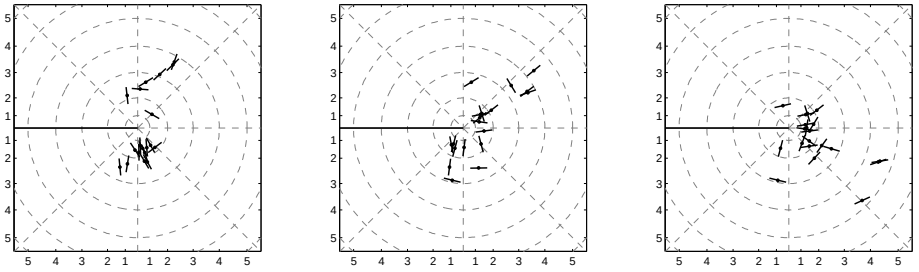

(a) $M = 0, B = 0$ (b) $M = 0.5, B = 0$ (c) $M = 1, B = 0$

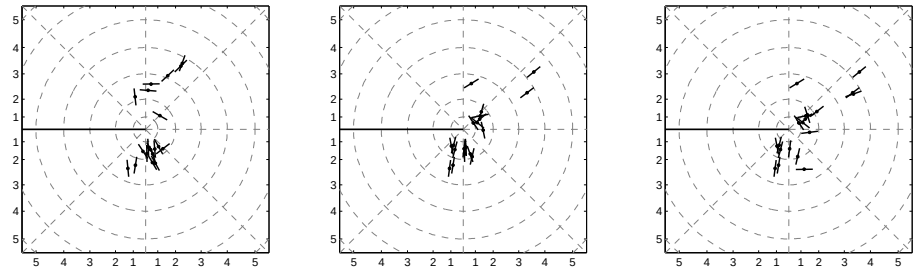

(d) $M = 0, B = -0.5$ (e) $M = 0.5, B = -0.5$ (f) $M = 1, B = -0.5$

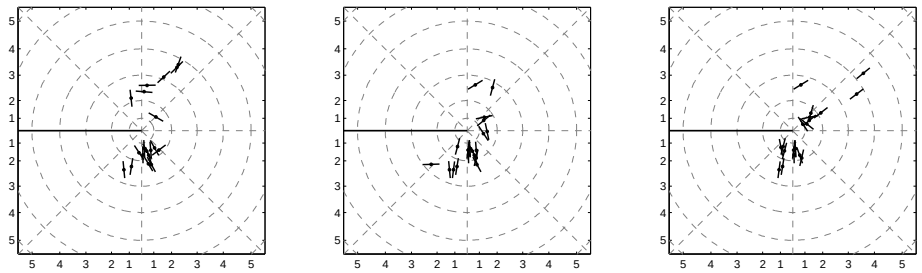

(g) $M = 0, B = -1$ (h) $M = 0.5, B = -1$ (i) $M = 1, B = -1$

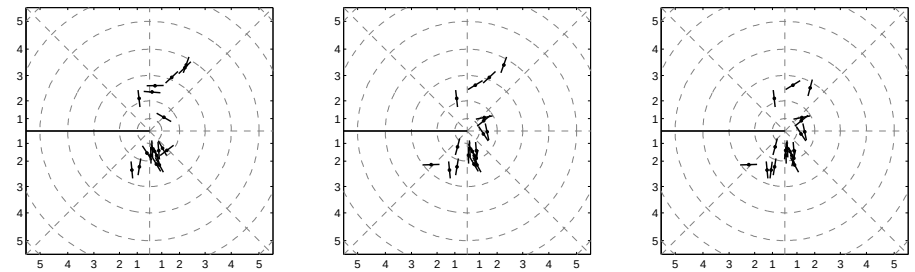

(j) $M = 0, B = -2$ (k) $M = 0.5, B = -2$ (l) $M = 1, B = -2$

Figure 5.14: Failure locations of twenty different Voronoi lattices with $\Lambda = 0.5$. The lattices are loaded under mode I, mode II and mixed mode ($M = 0.5$) with various values of negative T-stress.

dependence on relative density, much like the periodic Hexagonal lattices, since they also have average nodal connectivity of 3; this is exemplified by $d = 2$ in Eq.(5.10). Additionally, the pre-exponent D of both the Hexagonal and Voronoi lattices are also similar; hence, the two curves in Fig. 5.15 are close to one other, particular for mode II loading. The Triangular lattice, on the other hand, has an exponent of $d = 1$ whilst the Kagome has $d = 1/2$, both being stretch-dominated lattices. The Square and Diamond lattices, both are stretch-dominated architectures, also have an exponent $d = 1$ in mode I although their pre-exponent D is significantly lower than the Triangular lattice. Lattices that deform primarily by the same mechanism always have the same exponent d; however, a lower pre-exponent D leads to a lower bulk toughness; compare, for instance, the toughness of Diamond, Square and Triangular lattices in Fig. 5.15. Interestingly, the exponent d of a Square lattice, but not for Diamond, changes from 1 in mode I to 3/2 in mode II. This oddity is observed because a Square lattice deforms by stretch under uniaxial loading but by bending under shear. Overall, the Triangular lattice has superior toughness compared to all other lattice micro-architectures – only the Kagome lattice shows slightly higher toughness for $\overline{\rho} < 0.1$. Under mode I loading, the Hexagonal and Voronoi lattices, have the lowest toughness amongst all lattices. In

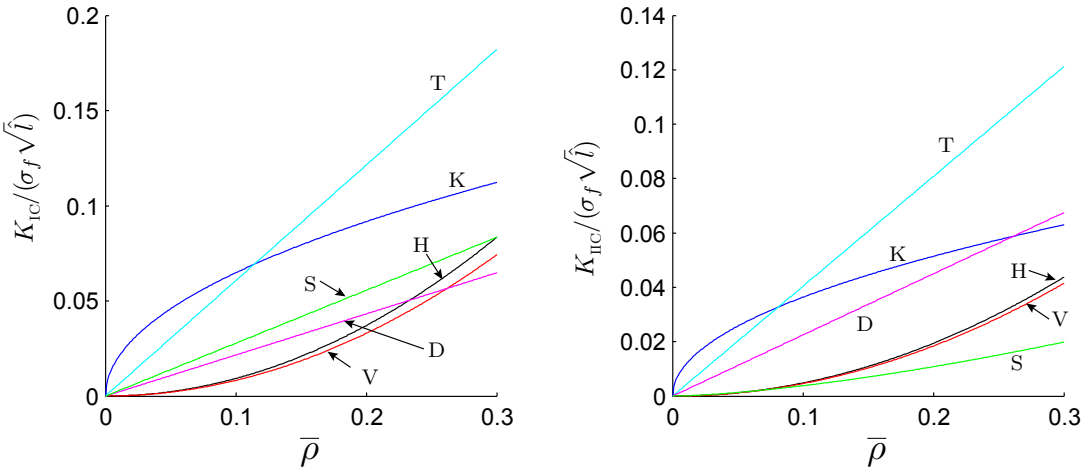

Figure 5.15: Comparison of fracture toughness between stochastic Voronoi ($\Lambda = 0.5$) and periodic lattices under (a) mode I and (b) mode II loadings. Each data point for Voronoi is based on an average of 20 tessellations. Curves plotted for periodic lattices are Eq.(1.17) with D and d as listed in Table 1.4.

mode II, the toughness of a Square lattice is even lower compared to the Hexagonal and stochastic Voronoi lattices.

Romijn and Fleck (2007) have previously reported that the toughness of some periodic lattices is highly sensitive to imperfections - see review in Section 1.1.2. However, the effects of $\overline{\rho}$ on toughness – this is reflected by the exponent d – have only been studied for a maximum possible value of $\kappa_v = 0.5$. All the periodic lattices, with the exception of Triangular, have an exponent of $d \approx 2$ following vertex perturbations: this suggests a shift in their dominant deformation from stretch to bending. The Triangular lattice, on the other hand, remains stretch-dominated even with the introduction of imperfections so that its exponent remains at $d = 1$. However, the aforementioned observations are based on results for $\kappa_v = 0.5$, which is unrealistically imperfect. At more reasonable values of κ_v, say $\kappa_v < 0.1$, the switch in the exponent d, from $d = 1$ to ≈ 2, is not expected to happen since the lattices are expected to deform by a combination of stretch and bending.

Romijn and Fleck (2007) reported the effects of κ_v on toughness – reduction or increase – for lattices of relative density $\overline{\rho} = 0.01$. The reduction in toughness, is greatest for the Kagome and Diamond lattices: a 90% and 80% reduction, respectively, at $\kappa_v = 0.5$. This huge reduction is primarily the result of a shift in the dominant deformation from $d = 1$ to $d \approx 2$. The Square lattice also exhibits a 80% reduction in toughness for mode II but only 20% in mode I at $\kappa_v = 0.5$. This is because a Square lattice, in its perfect (unperturbed) state, has $d = 1$ and $d = 1.5$ for mode I and II, respectively, but this switches to $d \approx 2$ for both modes (I and II) in its highly perturbed state. Consequently, the larger knock-down in mode I toughness. The bending-dominated Hexagonal lattice, on the other hand, shows a smaller reduction of 20% in mode I but an enhancement of 20% in mode II at $\kappa_v = 0.5$; the similar reduction/increase is because they have the same d for both its perfect and perturbed states. Even though the Triangular lattices remain stretch-dominated after vertex perturbation, their pre-exponent D is reduced significantly, by approximately 50% at $\kappa_v = 0.5$. However, as κ_v reduces, the reduction in toughness is found to reduce for all lattices. The reduction for $\kappa_v = 0.1$ is approximately 1/2 of the values indicated above for the extreme case of $\kappa_v = 0.5$; this applies to all the lattices. Even though, the disparity in toughness

between a Hexagonal lattice and the other four periodic micro-architectured lattices reduces in the presence of vertex perturbation, Romijn and Fleck (2007) found that the Hexagonal lattice always has the lowest toughness. Therefore, it is reasonable to conclude that the Square, Diamond, Triangular and Kagome lattices - even in their highly perturbed state - would have higher fracture toughness compared to stochastic Voronoi lattices of any cell-regularity Λ.

5.4 *Finite-sized* standard test specimens

Previously in Section 5.3, the 'bulk' toughness for Hexagonal and Voronoi lattices were predicted by using a BLA. Here, their fracture toughness will be predicted by modelling two types of standard test specimen geometries, viz. CT and SEN(B)-3PB, in FE. The objectives of this study are two fold. First, to establish how specimen size affects the predicted toughness by the two different specimen geometries. Recall that only elastic-brittle fracture is considered so the specimens are not bounded by any sizing requirements given by ASTM E399-12e1 (2012). Second, the effects of different test specimen geometries are to be investigated through comparing their predicted toughness to the corresponding bulk value obtained by BLA. If test specimen geometry is unimportant, and provided sufficiently large test specimens were modelled to eliminate size effects, then one would expect similar toughness predictions by the BLA and the two specimen geometries; however, it will be shown that this is not the case.

Recall that the lattice 'trimming' process, see Fig 5.4, ensures that identical cell topology exists around the crack-tip for both the standard test specimens and BLA; this eliminates variation in predicted toughness from cell microstructural variations around the crack-tip. To limit the number of dependent parameters that need to be considered, all FE simulations are restricted to Voronoi lattices of cell-regularity $\Lambda = 0.5$ and $\Lambda = 1$, with identical relative density of $\overline{\rho} = 0.1$. The effects of $\overline{\rho}$, average cell size $\hat{l}$ and material properties are accounted for by normalising the predicted toughness with $\overline{\rho}^2 \sigma_f \sqrt{\hat{l}}$. As in previous sections, each data point plotted are from an average of 20 tessellations and the error bar always refers to $\pm$ one standard deviation.

5.4.1 Effects of test specimen size

Figure 5.16a shows how the predicted toughness $K_{\mathrm{IC}}/(\overline{\rho}^2\sigma_f\sqrt{\hat{l}})$ varies with specimen size for a SEN(B)-3PB configuration. Notice that the specimen size is characterised here by the uncracked ligament length $(W-\alpha)/d_0$. A minimum of 10 cells are needed along the principal dimension W to 'measure' representative, i.e. size-independent, toughness values. The results show that reduced toughness can be expected if undersized specimens were used. For the smallest specimen $((W-\alpha)/d_0 = 5)$ simulated here, the toughness is $\approx$24% lower than its representative converged value.

A similar trend is also observed for perfect Hexagonal lattices in Fig. 5.16a. The slight variations around the converged toughness value originates from the pin-specimen contact geometry, which alternates between two configurations that correspond to specimen with odd and even number of Hexagonal cells along W (Christodoulou and Tan, 2013). The predicted toughness by a corresponding 'boundary-layer'analysis (BLA) is shown in the same figure as solid horizontal lines and their corresponding standard

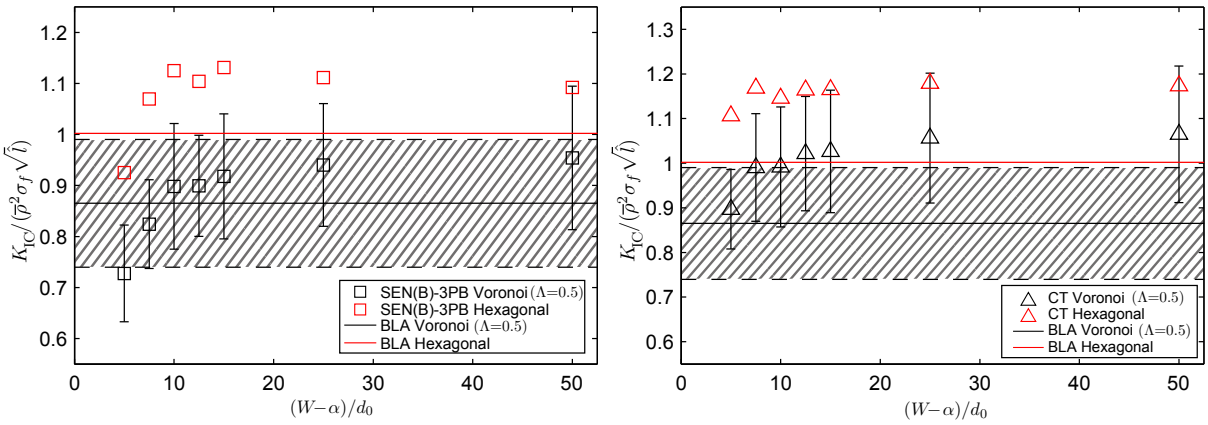

(a) (b)

Figure 5.16: Effects of uncracked ligament length $(W-\alpha)/d_0$ on the predicted toughness by a (a) SEN(B)-3PB and (b) CT standard specimen configuration. Data for Voronoi ($\Lambda = 0.5$) lattices are average of twenty tessellations and the error bars correspond to $\pm$ one standard deviation. Predictions by BLA are also plotted: solid horizontal line gives the mean value of twenty tessellations, while the hatched region corresponds to $\pm$ one standard deviation. Results from the corresponding Hexagonal lattices ($\Lambda = 1$) are also included.

deviation as a hatched region. Note that the BLA predicts normalised toughness close to unity with zero standard deviation for a Hexagonal lattice ($\Lambda = 1$). It is worth noting that the SEN(B)-3PB configuration consistently over-predicts the representative bulk toughness of a lattice, estimated from BLA, by approximately 10%. This is observed for both the $\Lambda = 0.5$ Voronoi and Hexagonal lattices. The cause of this anomaly will be identified later in Section 5.4.4.

Figure 5.16b plots the same for a CT configuration. Similar to the above, under-sized specimens also predict a reduced toughness value. A minimum specimen size of $(W-\alpha)/d_0 > 10$ is, also, needed to obtain a representative converged toughness value. However, the reduction in toughness for an under-sized specimen is less pronounced in the CT configuration – approximately 16% lower, compared to 24%, for the smallest specimen of $(W-\alpha)/d_0 = 5$. The discrepancy between the toughness predicted by a BLA and the CT configuration is even greater compared to the SEN(B)-3PB configuration. This difference is 23% for the Voronoi lattices and 17% for a Hexagonal lattice.

5.4.2 Strain maps

Continuous strain maps are generated – Appendix C describes the procedure – to elucidate the two different contributions to edge effects in a *finite-sized* specimen. The effects of overall specimen size on the strain field that develops in a specimen is first investigated. The strain field of a sufficiently large specimen, one which is unaffected by the aforesaid size-effect, will be compared to that predicted by a corresponding BLA: the objective is to identify the source of the discrepancies between the predicted toughness by the two test specimens and the BLA as shown in Fig. 5.16.

Figures 5.17 and 5.18 shows the strain maps for SEN(B)-3PB and CT specimens of various sizes. Also shown is the corresponding strain map – truncated to size for the purpose of comparison – predicted by a BLA. Each strain map plots the equivalent strain corresponding to the incipient cell wall fracture given by

$$\bar{\varepsilon}_{eq} = \frac{\overline{\rho} E_{\mathrm{s}}}{\sigma_f} \sqrt{\frac{2}{3} \varepsilon_{ij} \varepsilon_{ij}}. \tag{5.11}$$

Recall that all maps plotted are the average of twenty tessellations.

The incomplete cells at the boundary are more compliant compared to its bulk - so they are more likely to distort and rotate. Consequently, strain localisation bands – comprising of deformed cells of varying severity – are observed to emanate from the contact with the pin(s) into the bulk of the lattice; this is referred to as indentation-induced. The indentation-induced strain localisation bands develop within the un-cracked ligament of the SEN(B)-3PB configuration, whilst, they emanate at approximately $+45\,\mathrm{deg}\,/\,-45\,\mathrm{deg}$ from the top/bottom pin holes, respectively, into the bulk of the lattice in the CT configuration.

Two more strain localisation regions are observed, these are due to the presence of the crack; referred to as crack-induced. These two regions emanate at a direction of $\pm 120\,\mathrm{deg}$ from the x_1 axis. They are clearly evident in the strain maps from the BLA in Figs. 5.17 and 5.18 which corresponds to an idealised K-controlled fracture. A

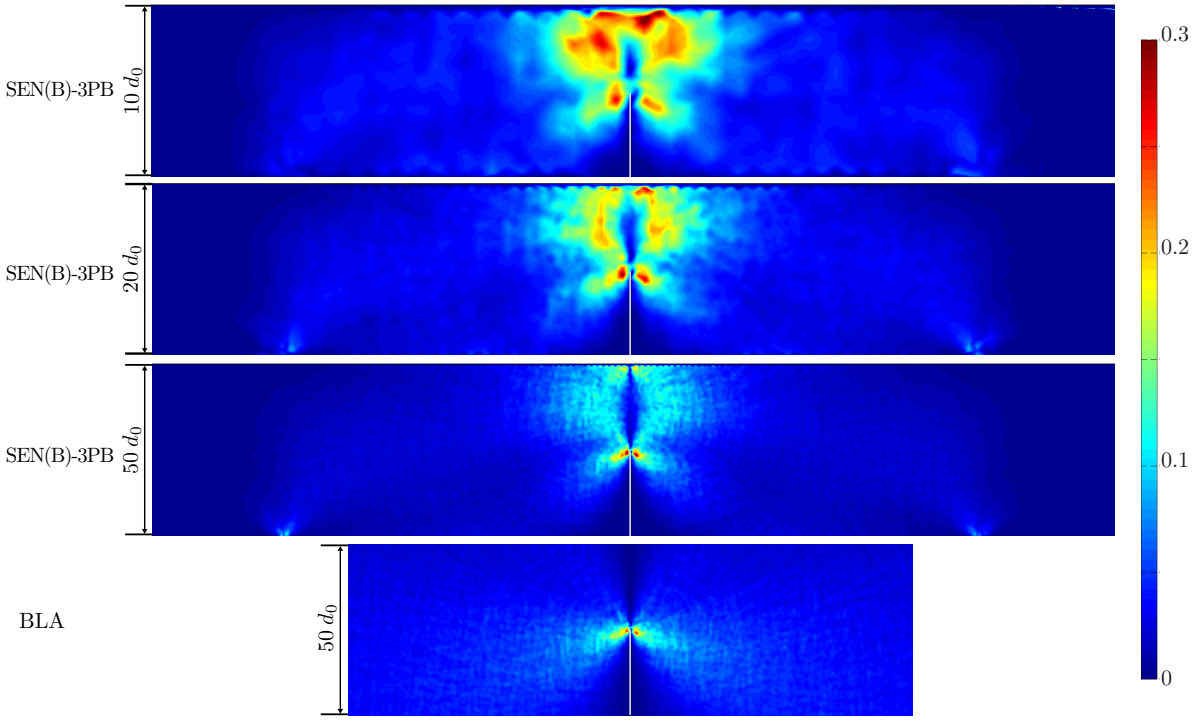

Figure 5.17: Equivalent strain ($\bar{\varepsilon}_{eq}$) maps for three specimen sizes, viz. $W/d_0 = 10, 20$ and 50, corresponding to the SEN(B)-3PB configuration. The corresponding strain map from a BLA is also shown. All maps plotted are the average of twenty Voronoi tessellations.

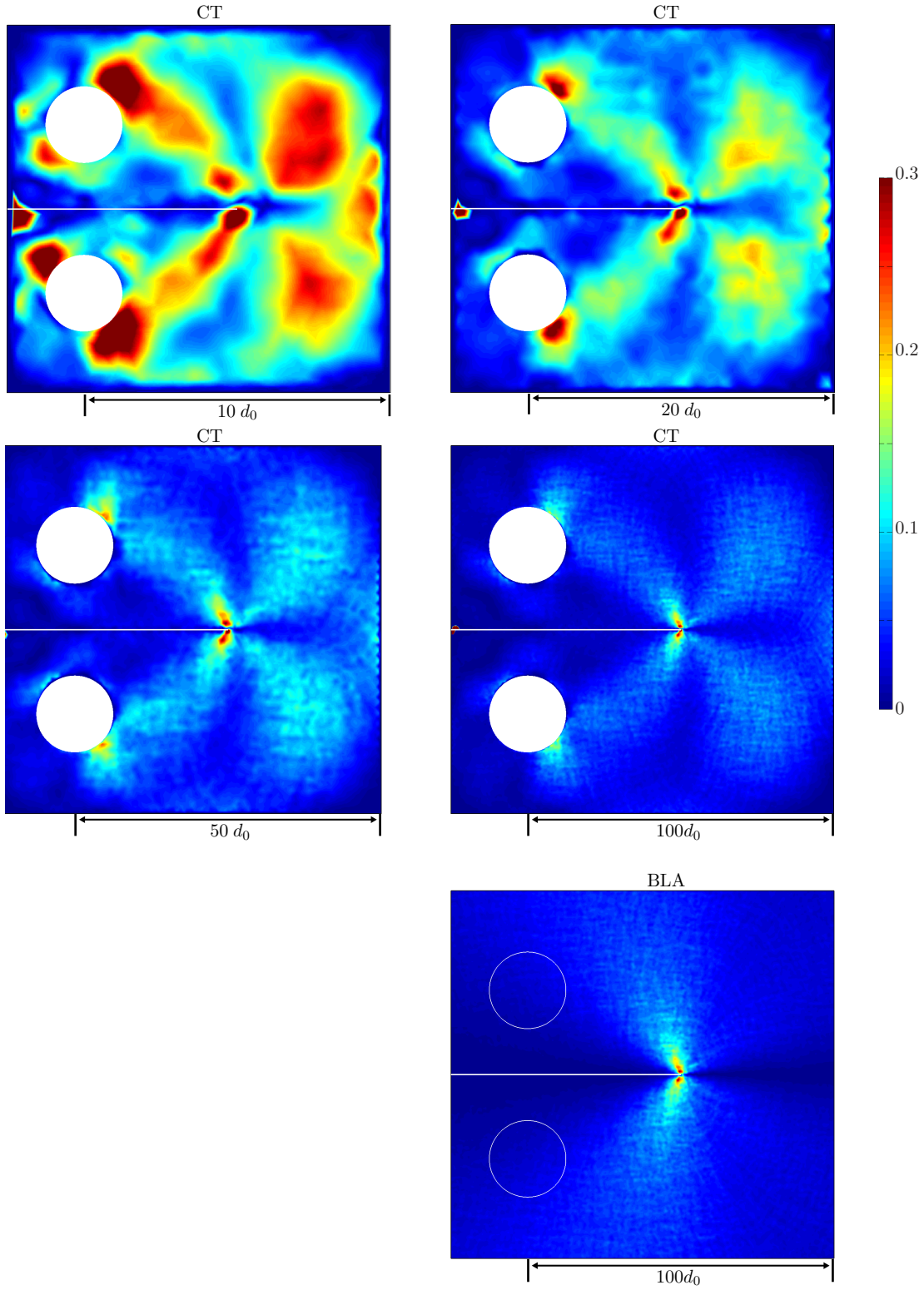

Figure 5.18: Equivalent strain ($\bar{\varepsilon}_{eq}$) maps for four specimens sizes, viz. $W/d_0 = 10, 20, 50$ and 100, corresponding to the CT configuration. The strain map predicted by a BLA is also shown with the corresponding location of the loading pins indicated for the purpose of comparison. All maps plotted are the average of twenty tessellations.

length of approximately $20d_0$ is required to diffuse the high strain concentration near the crack-tip to moderate levels, e.g. from $\bar{\varepsilon} > 0.3$ near the crack-tip to $\bar{\varepsilon} < 0.1$ in the far field.

Depending on the size of the specimen, the indentation-induced strain field(s) may interact with the crack-induced strain field; this is particularly obvious for the smaller specimens of $W = 10d_0$ and $20d_0$. In both configurations, the smallest specimen ($W/d_0 = 10$) shows considerable interactions between the indentation- and crack-induced fields. As W/d_0 increases, the interaction between the two fields reduces. Only when the specimens are sufficiently large ($W/d_0 = 50$ and 100), a crack-induced strain field reminiscent of the one predicted by a BLA is able to develop fully.

5.4.3 Discrepancies in predictions

For sufficiently-large test specimens, the interactions between the crack and indentation-induced strain field reduce considerably and, consequently, the toughness predicted by both the CT and SEN(B)-3PB specimens appear to reach a converge value. Even though specimen size does not affect the results, the predicted toughness by both standard specimens are still higher than that estimated by the BLA, see Fig. 5.16. Results from the SEN(B)-3PB specimen consistently over-predicts the toughness predicted by the BLA, by approximately 10%. This is observed for both the stochastic Voronoi and regular Hexagonal lattices. For the CT specimen, the difference is even greater, approximately 23% for Voronoi and 17% for Hexagonal. It is important to emphasise that the analyses are unaffected by cell microstructural variations around the crack-tip by virtue of how the lattices were generated (see Fig. 5.4 in Section 5.2.2), and any discrepancies in the predicted toughness must be due to the loading imposed at the boundary which is generic to the specific specimen geometry.

From the strain maps shown in Figs. 5.17 and 5.18, it is evident that the strain field for the larger specimens – $W/d_0 > 20$ – differs considerably compared to the corresponding idealised crack-induced strain field predicted by BLA. For the SEN(B)-3PB configuration, bands of strain localisation develop ahead of the crack-tip – a direct consequence of the compression induced by the loading pin. For the CT configuration, the strain localisation bands emanate from the crack-tip at approximately $\pm 135^\circ$

as opposed to $\pm 120^\circ$ predicted by an idealised BLA. Since the strain maps for the $W/d_0 > 20$ specimens reveal a more complex strain/stress state compared to the one predicted by the BLA, it is believed that the K-field may not uniquely characterise the crack-tip conditions in the two test specimens, even if they are unaffected by size-effects. As shown earlier in this Chapter, the inclusion of a +ve T-stress leads to an increase in the estimated toughness for Voronoi lattices. It is important to investigate whether higher order terms are present and if their presence can explain the discrepancies in the predicted toughness in Fig. 5.16.

5.4.4 Displacement field analysis (DFA)

A numerical-based displacement field analysis, or DFA for brevity, will be employed here to investigate the significance of the higher-order terms – see Eq.(1.14) – in relation to the crack-tip strain field that developed in the *finite-sized* test specimens of Figs 5.17 and 5.18. The method makes use of the nodal displacements predicted by the FE models, immediately before the incipient fracture of any cell wall. For simplicity, the analysis is performed using only Hexagonal lattices ($\Lambda = 1$) since their mechanical response is largely similar to the stochastic Voronoi lattices. Additionally, only the largest specimen of $W/d_0 = 100$ is used to prevent artefacts that might arise from the interaction between the crack- and indentation- induced strain fields.

5.4.4.a Formulations

The general form of the in-plane displacement field of a linear elastic cracked body, under pure mode I loading, can be expressed by a series expansion as follows (Liu et al., 2004; Williams, 1957):

$$
\begin{aligned}
u_1 &= \sum_{n=1}^{\infty} \left\{ A_n \frac{r^{n/2}}{2G^*} \left[\kappa^* \cos\frac{n}{2}\theta - \frac{n}{2}\cos\left(\frac{n}{2}-2\right)\theta + \left(\frac{n}{2}+(-1)^n\right)\cos\frac{n}{2}\theta \right] \right\} + u_1^T \\
u_2 &= \sum_{n=1}^{\infty} \left\{ A_n \frac{r^{n/2}}{2G^*} \left[\kappa^* \sin\frac{n}{2}\theta + \frac{n}{2}\sin\left(\frac{n}{2}-2\right)\theta - \left(\frac{n}{2}+(-1)^n\right)\sin\frac{n}{2}\theta \right] \right\} + u_2^T
\end{aligned}
\tag{5.12}
$$

where (r, θ) are polar coordinates centred at the crack tip as shown in Fig. 5.1, $\kappa^* = (3-\nu^*)/(1+\nu^*)$, G^* is the macroscopic lattice shear modulus and ν^* the macroscopic

lattice Poisson's ratio of Hexagonal lattices, given in Figs. 2.7 and 2.8. The first term in the series is proportional to the mode I SIF ($A_1 = K_{\mathrm{I}}/\sqrt{2\pi}$) and the second to the T-stress ($A_2 = T/4$). Equation (5.12) also includes contributions from rigid body translation (u_1^T, u_2^T).

The objective of DFA is to fit the displacement field predicted by FE to Eq.(5.12) for a pre-specified number of amplitude terms A_n, where $n = 1, \ldots, N$. The approach is similar to the ones employed in Sanford (1979), McNeill et al. (1987) and Yoneyama et al. (2007). The difference in this study is that the displacement field is predicted by FE rather than measured experimentally. Suppose that M points exist in a lattice with known in-plane displacements, then an over-determined set of simultaneous equations can be set-up by Eq.(5.12) which can be solved iteratively using the Newton-Raphson method. For points $k = 1, \ldots, M$, the error of the displacement prediction $(h_{1,k}, h_{2,k})$ at the i^{th} iteration is estimated as follows:

$$\begin{aligned} (h_{1,k})_i &= (u_{1,k})_i - U_{1,k} \\ (h_{2,k})_i &= (u_{2,k})_i - U_{2,k} \end{aligned} \tag{5.13}$$

where $(U_{1,k}, U_{2,k})$ is the known in-plane displacement from FE and $((u_{1,k})_i, (u_{2,k})_i)$ is the displacement estimated by Eq.(5.12). The corresponding unknown amplitude and translational terms at the i^{th} iteration are given by $(A_1)_i$, ... , $(A_N)_i$, $(u_1^T)_i$ and $(u_2^T)_i$. Equation (5.13) can be expanded using Taylor series to give

$$\begin{aligned} (h_{1,k})_{i+1} =& (h_{1,k})_i + \left(\frac{\partial h_{1,k}}{\partial A_1}\right)_i \Delta A_1 + \left(\frac{\partial h_{1,k}}{\partial A_2}\right)_i \Delta A_2 + \ldots \\ &+ \left(\frac{\partial h_{1,k}}{\partial A_N}\right)_i \Delta A_N + \left(\frac{\partial h_{1,k}}{\partial u_1^T}\right)_i \Delta u_1^T \\ (h_{2,k})_{i+1} =& (h_{2,k})_i + \left(\frac{\partial h_{2,k}}{\partial A_1}\right)_i \Delta A_1 + \left(\frac{\partial h_{2,k}}{\partial A_2}\right)_i \Delta A_2 + \ldots \\ &+ \left(\frac{\partial h_{2,k}}{\partial A_N}\right)_i \Delta A_N + \left(\frac{\partial h_{2,k}}{\partial u_2^T}\right)_i \Delta u_2^T \end{aligned} \tag{5.14}$$

Setting $(h_{1,k})_{i+1}$ and $(h_{2,k})_{i+1}$ to zero, the system of equations can be recast in a matrix format of

$$\mathbf{h} = \mathbf{b}\boldsymbol{\Delta} \tag{5.15}$$

where

$$\mathbf{h} = \begin{bmatrix} -h_{1,1} \\ \vdots \\ -h_{1,M} \\ -h_{2,1} \\ \vdots \\ -h_{2,M} \end{bmatrix} \quad , \quad \boldsymbol{\Delta} = \begin{bmatrix} \Delta A_1 \\ \Delta A_2 \\ \vdots \\ \Delta A_N \\ \Delta u_1^T \\ \Delta u_2^T \end{bmatrix}$$

and (5.16)

$$\mathbf{b} = \begin{bmatrix} \frac{\partial h_{1,1}}{\partial A_1} & \frac{\partial h_{1,1}}{\partial A_2} & \cdots & \frac{\partial h_{1,1}}{\partial A_N} & \frac{\partial h_{1,1}}{\partial u_1^T} & 0 \\ \vdots & \vdots & \ddots & \vdots & \vdots & \vdots \\ \frac{\partial h_{1,M}}{\partial A_1} & \frac{\partial h_{1,M}}{\partial A_2} & \cdots & \frac{\partial h_{1,M}}{\partial A_N} & \frac{\partial h_{1,M}}{\partial u_1^T} & 0 \\ \frac{\partial h_{2,1}}{\partial A_1} & \frac{\partial h_{2,1}}{\partial A_2} & \cdots & \frac{\partial h_{2,1}}{\partial A_N} & 0 & \frac{\partial h_{2,1}}{\partial u_2^T} \\ \vdots & \vdots & \ddots & \vdots & \vdots & \vdots \\ \frac{\partial h_{2,M}}{\partial A_1} & \frac{\partial h_{2,M}}{\partial A_2} & \cdots & \frac{\partial h_{2,M}}{\partial A_N} & 0 & \frac{\partial h_{2,1}}{\partial u_2^T} \end{bmatrix} .$$

The correction matrix $\boldsymbol{\Delta}$ is found by rearranging Eq.(5.15) to give $\boldsymbol{\Delta} = (\mathbf{b}^{\mathrm{T}}\mathbf{b})^{-1}\mathbf{b}^{\mathrm{T}}\mathbf{h}$. Since $\mathbf{b}^{\mathrm{T}}\mathbf{b}$ is positive-definite, the system of equations is readily solved using Cholesky decomposition. The entries in $\boldsymbol{\Delta}$ for the next iteration, viz. $(i+1)^{\text{th}}$, are updated accordingly as follows: $(A_1)_{i+1} = (A_1)_i + \Delta A_1$, ... , $(A_n)_{i+1} = (A_n)_i + \Delta A_n$, $(u_1^T)_{i+1} = (u_1^T)_i + \Delta u_1^T$ and $(u_2^T)_{i+1} = (u_2^T)_i + \Delta u_2^T$.

The predicted K_{IC} value by either Eq.(5.8) or (5.9) - depending on the configuration being investigated - is used as the initialisation value for $(A_1)_1$. All the higher-order and translational terms, viz. $(A_2)_1$, ... , $(A_M)_1$, $(u_1^T)_1$, $(u_2^T)_1$, are set to zero for iteration $i = 1$. The root mean square (RMS) error between the estimated displacement field and FE values for the i^{th} iteration is defined as

$$\text{RMS error}_i = \sqrt{\sum_{k=1}^{M} \frac{(h_{1,k})_i^2 + (h_{2,k})_i^2}{M}} \tag{5.17}$$

where M is the number of points with known displacement. A converged solution to Eq.(5.12) is deemed to be achieved if the RMS error between successive iterations is less than 1%. In all cases, it was found that the iterative procedure converges within 4 iterations. It is worth noting that the starting point of the iterative procedure, viz. $(A_n)_1$, $(u_1^T)_1$ and $(u_2^T)_1$, has no influence on the final converged results.

Two prerequisites must, however, be met if the DFA is to return meaningful and accurate results. First, the converged solution for all unknown amplitudes A_n must be independent of the number of terms N in the series expansion. Second, the set of points with known displacement $k = 1, \ldots, M$, must be selected so that they give a converged set of amplitude terms A_n. Ayatollahi and Nejati (2010) recommend that points too close to the crack tip and/or specimen boundaries should be avoided as they have a significant influence on the amplitude terms. The choice of the M points used in the present study is investigated next.

5.4.4.b Selection of M known 'displacement' points

An annulus of inner radius r_{DFA}, centred at the crack-tip, and two cells in width is introduced. All nodes in the FE mesh that lie within this annulus are included in the set of M known points used to fit Eq.(5.12). Figure 5.19 shows the variation of estimated A_1 and A_2 values with annulus radius r_{DFA}/d_0 for $N = 4, 8, 10$ and 15 terms. The radius R corresponding to the best converged A_1 and A_2 terms is chosen for the final DFA. Further analyses reveal that changing the width of the annulus, to include more/less known points, does not affect the results shown in Fig. 5.19. For the 'boundary-layer'problem, convergence of both A_1 and A_2 is reached between $50 \leq r_{\text{DFA}}/d_0 \leq 80$. In the case of the SEN(B)-3PB configuration, A_1 and A_2 convergence is reached for an annulus radius of $30 \leq r_{\text{DFA}}/d_0 \leq 40$. If a larger radius is chosen, the converged results begin to diverge, albeit only slightly, as the outer annulus is closer to the boundaries. The CT configuration shows converged results for $r_{\text{DFA}}/d_0 > 20$.

5.4.4.c Number of terms

Figure 5.19 appears to show a significant difference in the results when using low or high number of terms, N. Therefore, the minimum number of terms N needed

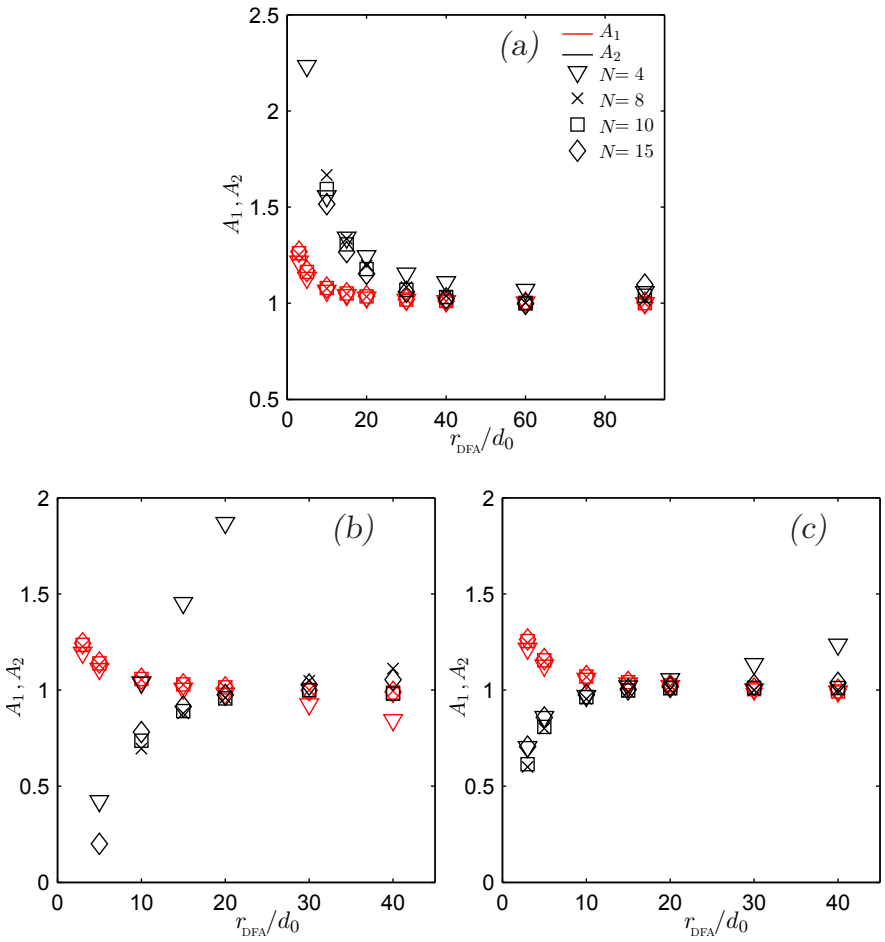

Figure 5.19: Variation of the amplitude terms A_1 and A_2 with annulus radius R/d_0 in the (a) 'boundary-layer'problem, (b) SEN(B)-3PB and (c) CT configurations.

to achieve converged A_n coefficients must be determined. Figure 5.20 plots the normalised SIF at the instant of fracture - estimated by A_1 - against the number of terms N considered in Eq.(5.12). For comparison, the toughness predicted by Eqs.(5.8), (5.9) and the corresponding BLA are also shown as horizontal lines. It is of interest to examine whether the converged results for the SIF at the instant of fracture, K_{IC}, is identical for both specimen configurations and BLA, and how these estimates compare to the K_{IC} predicted by Eqs.(5.8) and (5.9).

It is hardly surprising that the K_{IC} estimated by a DFA of the boundary-layer problem is identical to the applied SIF at fracture in Eq.(5.1), since the conditions are of ideal K-controlled fracture. The slight increase in A_1 for $N > 2$ is due to the numerical nature of the analysis. In a CT configuration, the K_{IC} estimated by DFA converges to the corresponding K-controlled BLA value for $N \geq 7$. This suggests that for a sufficiently

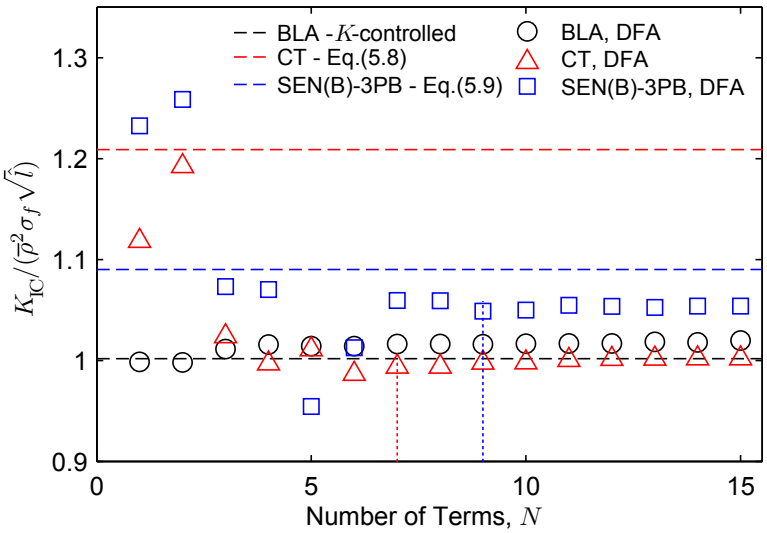

Figure 5.20: Variation of K_{IC} estimate with increased number of terms, N. The symbols denote displacement field analysis (DFA) and the straight lines corresponds to predictions from Eqs.(5.8) and (5.9).

'large' CT specimen configuration - where the crack-tip stress concentration is not influenced by any boundary effects - the stress singularity at the onset of fracture is the same as for the idealised K-controlled fracture given by the BLA. However, Eq. (5.9) seems to over estimate its magnitude by approximately 20%.

Displacement field analysis of the SEN(B)-3PB configuration shows that at least nine terms are needed to obtain a converged K_{IC} value, which is lower than what is predicted by Eq.(5.8). Although the converged toughness estimated by the DFA is still approximately 5% higher than the corresponding from BLA and the one predicted by DFA of the CT configuration. This suggests that the specific geometry of a SEN(B)-3PB specimen influences the magnitude of SIF that is needed to initiate fracture, resulting to higher toughness estimates. This is believed to be related to crack-deflection and crack-bridging. Unlike in solid materials, fracture in lattice materials typically occurs within a sector between $\pm 45^\circ - 90^\circ$ from the crack-plane and between 1-6 cells away from the crack-tip. The maximum bending stress in a SEN(B)-3PB configuration occurs at the mid-span of the specimen, i.e. directly ahead of the crack-tip. Hence the opening stress, σ_{22}, varies substantially along the x_2 direction, something which is less pronounced in the CT configuration and the BLA model. Since the fractured ligaments is few cells away from the point of maximum opening stress, a higher stress singularity

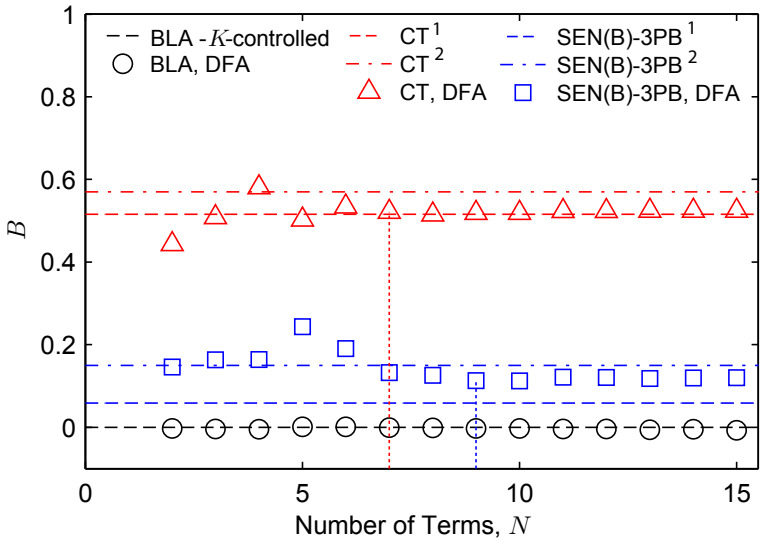

Figure 5.21: Estimates of stress biaxiality ratio, B, with increased number of higher-order amplitude terms, N. Results from existing literature are also plotted: [1] Leevers and Radon (1982) and [2] Larsson and Carlsson (1973).

at the crack-tip is required to obtain the same stress conditions at the fracture location in a SEN(B)-3PB geometry compared to the CT specimen.

Figure 5.21 plots the value of T-stress estimated by the DFA, through parameter A_2. Note that the T-stress has been normalised to give the stress biaxiality ratio $B = T\sqrt{\pi\alpha}/K_{\mathrm{IC}}$, where K_{IC} is the critical SIF estimated by A_1. For the BLA, the converged value of B is zero, which is to be expected since it corresponds to K-controlled fracture. Although, significant T-stress is induced in both specimen configurations. Convergence of the stress biaxiality ratio B in the CT and SEN(B)-3PB configurations is again obtained with seven and nine terms, respectively. Theoretical estimates for B are given by Larsson and Carlsson (1973) and Leevers and Radon (1982), which are plotted in the same Figure as horizontal lines; notice that the two theoretical estimates vary slightly from one another. The B value estimated by a DFA of the CT configuration is in excellent agreement with the theoretical predictions reported in Larsson and Carlsson (1973). For the SEN(B)-3PB configuration, however, the estimated B by DFA is closer to the theoretical estimate in Leevers and Radon (1982) - the reason behind this inconsistency remains unclear. Notwithstanding, the good agreement with the theoretical predictions from literature in Fig. 5.21 provide further validation for the results given by DFA.

5.5 Summary

The fracture toughness and the location of fracture initiation were studied with the boundary-layer analysis method for stochastic Voronoi lattices of varying degree of cell-regularity, Λ. The pure mode I toughness of a Voronoi lattice decreases as it becomes more irregular with an overall reduction of up to 25% for completely random lattices. There is no indication that pure mode II fracture toughness is affected significantly by cell irregularities. The macroscopic toughness of the lattices was found to have a quadratic dependence upon $\overline{\rho}$ for all values of Λ because of their bending dominated response. The Voronoi lattices, whether periodic Hexagonal or non-periodic, have a greater resistance to mode I than mode II loading. The mode I toughness of the lattices are more sensitive to cell topological variations in the vicinity of the crack tip than mode II. Fracture loci for the lattices are obtained in combined mode I and mode II stress intensity factor space. Although there are considerable variations between the fracture locus of different tessellations with the same Λ, this study shows there is a 70% chance the critical effective SIF of a stochastic Voronoi lattice will be greater than a corresponding Hexagonal one of the same relative density for all mode mixities $M > 0$. The effects of including T-stress was also investigated where a significant decrease/increase in fracture toughness is observed: for example, at $B = -1$, the reduction in the effective toughness of the lattice is nearly 75% for mode I and 50% for mode II loadings. This trend reverses with positive T-stresses. The present study found that the reduction/increase in toughness caused by changes in relative density or cell-regularity is insignificant when compared to the overall reduction/increase due to the inclusion of a T-stress.

Significant scatter in the initial cell wall fracture location is observed: the majority of failed cell walls occur near the crack tip, although they are also observed at up to five cells away from the crack-tip cell, suggesting a highly discontinuous cracking path that is bridged by many un-cracked ligaments. As mode-mixity changes from mode I to mode II, the clustering of the fractured cell walls shifts relative to the crack plane and is reminiscent of the evolution of the plastic zone shape in fully dense solids from LEFM. The introduction of a T-stress changes considerably the clustering of the fractured cell walls: mode I remains, in general, unaffected, whilst for mode II and mixed mode

loadings at high T-stresses, the clustering is reminiscent of that seen in mode I loading. There is no correlation between the calculated fracture toughness for different lattice realisations, with the same Λ and $\overline{\rho}$, and the location where cell wall cracking first initiates.

The effects of specimen size and configurations on the estimated toughness were investigated for stochastic Voronoi lattices, by studying two standard specimen geometries, the CT and SEN(B)-3PB. It was shown that at least 10 cells are needed along the uncracked ligament length $(W-\alpha)/d_0$ for both the CT and SEN(B)-3PB configurations to estimate a converged value for toughness, unaffected by specimen size. The origin of this size effect was found to be the result of interactions between the indentation- and crack- induced strain concentrations. Furthermore, it was shown that the fracture toughness obtained by using standardised procedures developed for solid materials and polymers, viz. ASTM E399, E1820 and D5045, are approximately 20% and 10% higher than a corresponding idealised boundary-layer analysis for the CT and SEN(B)-3PB configurations, respectively. Displacement field analysis revealed that the actual SIF at the onset of fracture are indeed close to that predicted by the boundary-layer analysis which suggest that the ASTM test procedures overestimate the toughness of stochastic Voronoi lattices considerable. The numerical results are further validated by comparing the stress biaxiality ratio B, estimated by a displacement field analysis, to theoretical predictions obtained from the literature.

Chapter 6

Conclusions and further research

6.1 Conclusions

This thesis addressed some important aspects of the mechanical response of lattice materials by investigating: (1) their monotonic uniaxial and shear mechanical properties, and how they are affected by edge effects and specimen size; (2) their fatigue performance in compression and shear; and, (3) their brittle fracture response. Five periodic lattice micro-architectures – viz. the Hexagonal, Triangular, Square, Diamond and Kagome – and the stochastic Voronoi were studied in order to highlight the differences in their macroscopic response.

The findings from these analyses, presented previously in Chapters 2-5, are summarised below.

6.1.1 Edge effects

In Chapter 2, the bulk uniaxial and shear moduli, and yield strength, of *infinite-sized* periodic lattices were estimated, through judicious choice of unit-cells; it was demonstrated that their predictions are in excellent agreement with the scaling laws from existing literature. The moduli and strength of stretch-dominated micro-architectures - Triangular, Diamond, Kagome and Square (uniaxial loading only) - scale linearly with $\overline{\rho}$. As for the bending-dominated micro-architectures - Hexagonal and Square (shear loading only) - their moduli scale with $\overline{\rho}^3$, and their yield strength with $\overline{\rho}^2$. Additionally, the average bulk properties of stochastic Voronoi lattices were found to be broadly similar to periodic Hexagonal lattices; however, varying degree of knock-down/enhancement in their mechanical properties was noted depending on Λ and $\overline{\rho}$; again, an excellent agreement with results in the literature is demonstrated.

In Chapter 3, *finite-sized* Square, Kagome and Triangular lattices were investigated

to elucidate the mechanism(s) responsible for their respective edge effects; results for Hexagonal, Diamond and Voronoi lattices are available in the literature. For all lattices, horizontal and/or vertical boundary layers are found to emanate from the horizontal stressed and lateral stress-free surfaces, respectively; their range of influence is found to depend on lattice micro-architecture and the imposed loading.

Under uniaxial loading, the modulus and strength of a Square lattice depends on $\overline{W}$ if $\lambda \neq 0.5$; $\overline{H}$ and $\overline{\rho}$ were found to be insignificant. It was shown that this size-dependent effect, unlike the rests, is a direct consequence of its open-cells on the stress-free L and R boundaries and there is no mechanism involved. In shear, however, a Square lattice develops a weak vertical boundary layer that extends by one cell in width from each end of the specimen and if $\overline{W}$ is small, this leads to a considerable reduction in its effective properties. Additionally, a horizontal stiff boundary layer also develops that extends by more than one cell in height into its bulk region. For lattices with $\overline{H} = 1$ and very large $\overline{W}$, a significant enhancement of it effective modulus is observed $G^*/(G^*)_{\text{UC}} = 1.8$; however this is not observed for $\tau_y^*/(\tau_y^*)_{\text{UC}}$.

A Kagome lattice, under uniaxial loading, develops two weak vertical bending boundary layers (BBLs); its range of influence increases with decreasing relative density $\overline{\rho}$. The cells outside these BBLs – in the bulk-region – were found to have the same 'local' modulus as its *infinite-sized* counterpart. If the lattices is sufficiently wide and the relative density is high enough, $\overline{W} > 100$ and $\overline{\rho} > 0.1$, then their effective properties approach its *infinite-sized* counterpart. On the other hand, if a lattice has a small width $\overline{W}$ and of sufficiently low $\overline{\rho}$, it deforms primarily by bending, rather than stretch; this leads to a substantial reduction in their effective modulus and strength since they scale with $\overline{\rho}^3$ and $\overline{\rho}^2$, respectively. Under shear, the Kagome lattice develops two angular-shaped BBLs – one from each end of the stress-free lateral boundaries L and R – where their range of influence depends on $\overline{H}$; as a result, the effective shear properties depend on aspect ratio $\overline{W}/\overline{H}$. The 'local' modulus of the BBLs is found to be $G = 0.5(G^*)_{\text{UC}}$ whereas for the 'bulk' region $(G^*)_{\text{UC}}$. For the critical aspect ratio $\overline{W}/\overline{H} = 1$, the entire lattice is covered by the BBLs and the effective stiffness is only $G^*/(G^*)_{\text{UC}} = 0.5$; as $\overline{W}/\overline{H}$ increases, the effective properties approach those for an infinite-sized lattice. For $\overline{W}/\overline{H} < 1$, the relative density $\overline{\rho}$ becomes a dominant parameter; at sufficiently low $\overline{\rho}$,

the Kagome lattices deforms primarily by bending rather than stretch, and a significant reduction in its effective properties is noted.

The Triangular lattice in uniaxial loading develops strong horizontal - one cell in height - and weak vertical - of half cell in width - boundary layers. A dependence of effective properties on both $\overline{W}$ and $\overline{H}$ is obtained, although in any case the estimated properties are within 5% of the bulk properties. Under shear, two weak vertical boundary layers develop, whose extend depends on $\overline{H}$; for $\overline{W}/\overline{H} >> 1$, the effective properties approach those for an infinite-sized lattice. A $\overline{H} = 2$ lattice does not develop a boundary layer regardless of $\overline{W}$ and its effective properties are those for an infinite-sized lattice; $G^*/(G^*)_{\text{UC}} = \tau_y^*/(\tau_y^*)_{\text{UC}} = 1$. If $\overline{W}/\overline{H} << 1$, the effective shear properties reduce significantly without a lower bound. Unlike the Kagome lattice, the Triangular lattice is always a stretch-dominated micro-architecture regardless of $\overline{W}/\overline{H}$ and $\overline{\rho}$ and its mechanical properties scale linearly with $\overline{\rho}$.

6.1.2 Fatigue

In Chapter 4, the fatigue performance of periodic lattices (Diamond, Triangular, Kagome, Square and Hexagonal) in shear and C-C cyclic loading were studied by implementing a fatigue damage model – modified to consider nonlocal damage effects – into the FE models. The effects of imperfections upon their fatigue response were also studied.

The fatigue life (N_f) and endurance strength of stretch-dominated lattices are found to be significantly affected by imperfections; the extent of the reduction depends on their micro-architecture. The Diamond lattice was found to be the least sensitive of all the stretch-dominated micro-architectures whilst the Kagome and Triangular lattices presents significantly reduced fatigue life if imperfections are introduced; this is for both shear and C-C loading. A perfect Square lattice under C-C fatigue gives unrealistically high N_f; it reduces to values similar to the Diamond lattice when imperfections are introduced. On the other hand, the fatigue performance of bending dominated lattices - Hexagonal and Square under shear - were found to be insensitive to imperfections. The fatigue life of the perfect lattices, without imperfections, depends on their micro-architecture; however, there is no indication that stretch-dominated micro-

architectures has any significant advantage over their bending-dominated counterparts.

Damage accumulation in stretch-dominated lattices were found to occur in only a few cell walls. The consequence of this is that macroscopic modulus damage accumulation rate, up until the point of first cell wall failure, is nearly zero. By contrast, the bending-dominated lattices accumulate damage over a significantly large area of the lattice; this leads to a more progressive macroscopic modulus damage accumulation rate. For both stretch and bending-dominated lattices, the locations where damage accumulates were found to be determined by the presence of boundary layers. The differences in fatigue performance among the five micro-architectures is attributed to differences in the stress distribution within the boundary layers of each lattice.

6.1.3 Fracture

In Chapter 5, the brittle fracture response of stochastic lattices was investigated by utilising the Voronoi construction.

Voronoi lattices, regardless of their cell-regularity Λ, always have a greater resistance to fracture in mode I compared to mode II. As Λ reduces, the mode I toughness reduces by up to 25%, whilst its mode II toughness is relatively unaffected. The toughness of the lattices have a quadratic dependence on $\overline{\rho}$ at all Λ - a result of their bending-dominated deformation. Under mixed mode loading, the fracture locus differs significantly between tessellations even for lattices with identical cell regularity Λ. For negative/positive T-stress, a significant decrease/increase in effective fracture toughness is observed, respectively.

The crack propagation in stochastic Voronoi lattice is found to be highly discontiguous, with fractured cell wall fractures observed at up to six cells away from the crack-tip. With increasing mode-mixity from mode I to mode II, the location of cell wall fracture shifts relative to the crack plane. With high negative T-stress, the location of cell wall fracture changes drastically; for mode II and mixed mode loadings at high T-stresses, the location is reminiscent of that seen in mode I loading, whilst mode I remains in general unaffected.

It was shown that the CT and SEN(B)-3PB test specimens require at least 10 cells

in their uncracked ligament to 'measure' a converged toughness that is unaffected by specimen size. The origin of this size effect has been traced to interactions between the indentation- and crack-induced strain fields. Additionally, it was shown that the 'measured' toughness by the CT and SEN(B)-3PB specimens is 20% and 10% higher than the ones estimated by an idealised K-controlled fracture; the source behind this discrepancy is found to be the equations for K_{IC} as given by the ASTM testing standards.

6.2 Further research

The results reported in this thesis have addressed several hitherto unexplored aspects of the mechanical response of micro-architectured lattice materials. Several aspects of this work would benefit from a more thorough, in-depth, investigation, whilst the rests lay the foundation for further work as follows:

1. The current investigation into edge effects, and their impact on the effective macroscopic properties, was confined to strictly periodic lattices. However, all real micro-architectured lattices have some inherent imperfections; it is unclear to what extent the conclusions of Chapter 3 are affected for imperfect lattices. This needs to be addressed in the future so that a better understanding is obtained for the response of real lattice material. Both imperfections in the form of vertex perturbation, controlled using parameter κ_v, and buckling eigenmodes will be interesting to be investigated.

2. The presence of edge effects was investigated for lattices subjected to simple loading; uniaxial and simple shear. Currently, it is unknown whether - and how - the edge effect mechanisms reported in Chapter 3 change under more complex loadings, such as biaxial and combined axial-shear loading. An extension of the current work is thus necessary to address this.

3. In Chapter 4, some preliminary results show that the fatigue performance of lattice material is affected by specimen size. A detailed work is required to quantify this dependence on specimen size and to reveal the mechanism responsible for this.

4. The dependence of toughness on specimen size was highlighted for stochastic Voronoi and periodic Hexagonal lattice. This work is proposed to be extended to include the other four periodic lattice micro-architectures which is currently missing from literature.

5. The study on fracture was restricted to elastic-brittle lattices, whilst the majority of lattices, in real-life, are constructed using metals or polymers. A proposed extension of this work is to relax the elastic-brittle material assumption and to include the effects of cell wall plasticity. This is potentially useful to advise the sizing of test specimens for the toughness testing of lattice materials.

Appendix A

Square lattice - Shear

Here, each matrix is presented in its entirety for each of the three cases studied for an infinite wide lattice, and $\overline{H} = 1, 3, 5$. The equations that need to be solved are the following

$$\mathbf{Mm} = \mathbf{F} \quad . \tag{A.1}$$

The number of unknowns for each case are 8, 14 and 20 respectively. The slope-deflection equations are written in the following form

$$\boldsymbol{\theta} = \frac{l}{E_s I}\boldsymbol{\Theta}\mathbf{m} \tag{A.2}$$

and are used to determine the deformation strain for a given applied external force.

A.1 Square lattice $\overline{H} = 1$, 8 unknowns

$$\mathbf{m} = \begin{pmatrix} M_{T1} \\ M_{1T} \\ M_{B2} \\ M_{2B} \\ M_{12} \\ M_{21} \\ M_{11} \\ M_{22} \end{pmatrix} \quad , \quad \mathbf{F} = \begin{pmatrix} 0 \\ 0 \\ F\lambda l \\ F\lambda l \\ Fl \\ 0 \\ 0 \\ 0 \end{pmatrix} \tag{A.3}$$

$$\mathbf{M} = \begin{pmatrix} -3\lambda & 3\lambda & 0 & 0 & 0 & 0 & 1 & 0 \\ 0 & 0 & -3\lambda & 3\lambda & 0 & 0 & 0 & 1 \\ 1 & 1 & 0 & 0 & 0 & 0 & 0 & 0 \\ 0 & 0 & 1 & 1 & 0 & 0 & 0 & 0 \\ 0 & 0 & 0 & 0 & 1 & 1 & 0 & 0 \\ 0 & 1 & 0 & 0 & 1 & 0 & -2 & 0 \\ 0 & 0 & 0 & 1 & 0 & 1 & 0 & -2 \\ 0 & 0 & 0 & 0 & 3 & -3 & 1 & -1 \end{pmatrix} \tag{A.4}$$

$$\boldsymbol{\theta} = \begin{pmatrix} \theta_{T1} \\ \theta_{1T} \\ \theta_{B2} \\ \theta_{2B} \\ \theta_{12} \\ \theta_{21} \\ \theta_{11} \\ \theta_{22} \end{pmatrix} \quad , \quad \boldsymbol{\Theta} = \begin{pmatrix} \frac{\lambda}{3} & -\frac{\lambda}{6} & 0 & 0 & 0 & 0 & 0 & 0 \\ -\frac{\lambda}{6} & \frac{\lambda}{3} & 0 & 0 & 0 & 0 & 0 & 0 \\ 0 & 0 & \frac{\lambda}{3} & -\frac{\lambda}{6} & 0 & 0 & 0 & 0 \\ 0 & 0 & -\frac{\lambda}{6} & \frac{\lambda}{3} & 0 & 0 & 0 & 0 \\ 0 & 0 & 0 & 0 & \frac{1}{3} & -\frac{1}{6} & 0 & 0 \\ 0 & 0 & 0 & 0 & -\frac{1}{6} & \frac{1}{3} & 0 & 0 \\ 0 & 0 & 0 & 0 & 0 & 0 & \frac{1}{6} & 0 \\ 0 & 0 & 0 & 0 & 0 & 0 & 0 & \frac{1}{6} \end{pmatrix} \tag{A.5}$$

A.2 Square lattice $\overline{H} = 3$, 14 unknowns

$$\mathbf{m} = \begin{pmatrix} M_{T1} \\ M_{1T} \\ M_{B2} \\ M_{2B} \\ M_{12} \\ M_{21} \\ M_{23} \\ M_{32} \\ M_{34} \\ M_{43} \\ M_{11} \\ M_{22} \\ M_{33} \\ M_{44} \end{pmatrix}, \quad \mathbf{F} = \begin{pmatrix} 0 \\ 0 \\ F\lambda l \\ F\lambda l \\ Fl \\ Fl \\ Fl \\ 0 \\ 0 \\ 0 \\ 0 \\ 0 \\ 0 \\ 0 \end{pmatrix} \tag{A.6}$$

$$\mathbf{M} = \begin{pmatrix} \frac{\lambda}{2} & -\frac{\lambda}{2} & 0 & 0 & 0 & 0 & 0 & 0 & 0 & 0 & -\frac{1}{6} & 0 & 0 & 0 \\ 0 & 0 & \frac{\lambda}{2} & -\frac{\lambda}{2} & 0 & 0 & 0 & 0 & 0 & 0 & 0 & 0 & 0 & -\frac{1}{6} \\ 1 & 1 & 0 & 0 & 0 & 0 & 0 & 0 & 0 & 0 & 0 & 0 & 0 & 0 \\ 0 & 0 & 1 & 1 & 0 & 0 & 0 & 0 & 0 & 0 & 0 & 0 & 0 & 0 \\ 0 & 0 & 0 & 0 & 1 & 1 & 0 & 0 & 0 & 0 & 0 & 0 & 0 & 0 \\ 0 & 0 & 0 & 0 & 0 & 0 & 1 & 1 & 0 & 0 & 0 & 0 & 0 & 0 \\ 0 & 0 & 0 & 0 & 0 & 0 & 0 & 0 & 1 & 1 & 0 & 0 & 0 & 0 \\ 0 & 1 & 0 & 0 & 1 & 0 & 0 & 0 & 0 & 0 & -2 & 0 & 0 & 0 \\ 0 & 0 & 0 & 0 & 0 & 1 & 1 & 0 & 0 & 0 & 0 & -2 & 0 & 0 \\ 0 & 0 & 0 & 0 & 0 & 0 & 0 & 1 & 1 & 0 & 0 & 0 & -2 & 0 \\ 0 & 0 & 0 & 1 & 0 & 0 & 0 & 0 & 0 & 1 & 0 & 0 & 0 & -2 \\ 0 & 0 & 0 & 0 & \frac{1}{2} & -\frac{1}{2} & 0 & 0 & 0 & 0 & \frac{1}{6} & -\frac{1}{6} & 0 & 0 \\ 0 & 0 & 0 & 0 & 0 & 0 & \frac{1}{2} & -\frac{1}{2} & 0 & 0 & 0 & \frac{1}{6} & -\frac{1}{6} & 0 \\ 0 & 0 & 0 & 0 & 0 & 0 & 0 & 0 & \frac{1}{2} & -\frac{1}{2} & 0 & 0 & \frac{1}{6} & -\frac{1}{6} \end{pmatrix} \tag{A.7}$$

$$\boldsymbol{\theta} = \begin{pmatrix} \theta_{T1} \\ \theta_{1T} \\ \theta_{B2} \\ \theta_{2B} \\ \theta_{12} \\ \theta_{21} \\ \theta_{23} \\ \theta_{32} \\ \theta_{34} \\ \theta_{43} \\ \theta_{11} \\ \theta_{22} \\ \theta_{33} \\ \theta_{44} \end{pmatrix}, \quad \boldsymbol{\Theta} = \begin{pmatrix} \frac{\lambda}{3} & -\frac{\lambda}{6} & 0 & 0 & 0 & 0 & 0 & 0 & 0 & 0 & 0 & 0 & 0 & 0 \\ -\frac{\lambda}{6} & \frac{\lambda}{3} & 0 & 0 & 0 & 0 & 0 & 0 & 0 & 0 & 0 & 0 & 0 & 0 \\ 0 & 0 & \frac{\lambda}{3} & -\frac{\lambda}{6} & 0 & 0 & 0 & 0 & 0 & 0 & 0 & 0 & 0 & 0 \\ 0 & 0 & -\frac{\lambda}{6} & \frac{\lambda}{3} & 0 & 0 & 0 & 0 & 0 & 0 & 0 & 0 & 0 & 0 \\ 0 & 0 & 0 & 0 & \frac{1}{3} & -\frac{1}{6} & 0 & 0 & 0 & 0 & 0 & 0 & 0 & 0 \\ 0 & 0 & 0 & 0 & -\frac{1}{6} & \frac{1}{3} & 0 & 0 & 0 & 0 & 0 & 0 & 0 & 0 \\ 0 & 0 & 0 & 0 & 0 & 0 & \frac{1}{3} & -\frac{1}{6} & 0 & 0 & 0 & 0 & 0 & 0 \\ 0 & 0 & 0 & 0 & 0 & 0 & -\frac{1}{6} & \frac{1}{3} & 0 & 0 & 0 & 0 & 0 & 0 \\ 0 & 0 & 0 & 0 & 0 & 0 & 0 & 0 & \frac{1}{3} & -\frac{1}{6} & 0 & 0 & 0 & 0 \\ 0 & 0 & 0 & 0 & 0 & 0 & 0 & 0 & -\frac{1}{6} & \frac{1}{3} & 0 & 0 & 0 & 0 \\ 0 & 0 & 0 & 0 & 0 & 0 & 0 & 0 & 0 & 0 & \frac{1}{6} & 0 & 0 & 0 \\ 0 & 0 & 0 & 0 & 0 & 0 & 0 & 0 & 0 & 0 & 0 & \frac{1}{6} & 0 & 0 \\ 0 & 0 & 0 & 0 & 0 & 0 & 0 & 0 & 0 & 0 & 0 & 0 & \frac{1}{6} & 0 \\ 0 & 0 & 0 & 0 & 0 & 0 & 0 & 0 & 0 & 0 & 0 & 0 & 0 & \frac{1}{6} \end{pmatrix} \tag{A.8}$$

The following are the equivalent of Eq. (3.17) for the $\overline{H} = 3$ lattice:

$$M_{T1} = M_{B4} = \frac{6\lambda^2 + c_1\lambda + 0.5c_2}{c} Fl \tag{A.9}$$

$$M_{1T} = M_{4B} = \frac{6\lambda^2 - 0.5c_2}{c} Fl \tag{A.10}$$

$$M_{11} = M_{44} = \frac{3c_1\lambda^2 + 3c_2\lambda}{c} Fl \tag{A.11}$$

$$M_{23} = M_{32} = \frac{Fl}{2} \tag{A.12}$$

$$M_{12} = M_{43} = \frac{-0.5c_3\lambda^2 + 6c_2\lambda + 0.5c_2}{c} Fl \tag{A.13}$$

$$M_{21} = M_{34} = \frac{0.4c_2\lambda^2 + 6c_1\lambda + 0.5c_3}{c} Fl \tag{A.14}$$

$$M_{22} = M_{33} = \frac{0.2c_2\lambda^2 + 5.4c_2\lambda + 0.4c_2}{c} Fl \tag{A.15}$$

where $c = 12\lambda + c_1$ and $c_1 = \frac{13}{14}, c_2 = \frac{15}{14}, c_3 = \frac{11}{14}$. The shear strain, γ_{12} is obtained as follows

$$\begin{aligned} \gamma_{12} &= \frac{u_T + u_B + u_{12} + u_{23} + u_{34}}{3l + 2\lambda l} \\ &= \frac{\lambda\left(\theta_{T1} + \theta_{B2}\right) + \theta_{12} + \theta_{11} + \theta_{23} + \theta_{22} + \theta_{34} + \theta_{33}}{3 + 2\lambda} \end{aligned} \tag{A.16}$$

A.3 Square lattice $\overline{H} = 5$, 20 unknowns

$$\mathbf{m} = \begin{pmatrix} M_{T1} \\ M_{1T} \\ M_{B2} \\ M_{2B} \\ M_{12} \\ M_{21} \\ M_{23} \\ M_{32} \\ M_{34} \\ M_{43} \\ M_{45} \\ M_{54} \\ M_{56} \\ M_{65} \\ M_{11} \\ M_{22} \\ M_{33} \\ M_{44} \\ M_{55} \\ M_{66} \end{pmatrix}, \quad \mathbf{F} = \begin{pmatrix} 0 \\ 0 \\ F\lambda l \\ F\lambda l \\ Fl \\ Fl \\ Fl \\ Fl \\ Fl \\ 0 \\ 0 \\ 0 \\ 0 \\ 0 \\ 0 \\ 0 \\ 0 \\ 0 \\ 0 \\ 0 \end{pmatrix} \tag{A.17}$$

$$\mathbf{M} = \begin{pmatrix}
\frac{\lambda}{2} & -\frac{\lambda}{2} & 0 & 0 & 0 & 0 & 0 & 0 & 0 & 0 & 0 & 0 & 0 & 0 & -\frac{1}{6} & 0 & 0 & 0 & 0 & 0 \\
0 & 0 & \frac{\lambda}{2} & -\frac{\lambda}{2} & 0 & 0 & 0 & 0 & 0 & 0 & 0 & 0 & 0 & 0 & 0 & 0 & 0 & 0 & 0 & -\frac{1}{6} \\
1 & 1 & 0 & 0 & 0 & 0 & 0 & 0 & 0 & 0 & 0 & 0 & 0 & 0 & 0 & 0 & 0 & 0 & 0 & 0 \\
0 & 0 & 1 & 1 & 0 & 0 & 0 & 0 & 0 & 0 & 0 & 0 & 0 & 0 & 0 & 0 & 0 & 0 & 0 & 0 \\
0 & 0 & 0 & 0 & 1 & 1 & 0 & 0 & 0 & 0 & 0 & 0 & 0 & 0 & 0 & 0 & 0 & 0 & 0 & 0 \\
0 & 0 & 0 & 0 & 0 & 0 & 1 & 1 & 0 & 0 & 0 & 0 & 0 & 0 & 0 & 0 & 0 & 0 & 0 & 0 \\
0 & 0 & 0 & 0 & 0 & 0 & 0 & 0 & 1 & 1 & 0 & 0 & 0 & 0 & 0 & 0 & 0 & 0 & 0 & 0 \\
0 & 0 & 0 & 0 & 0 & 0 & 0 & 0 & 0 & 0 & 1 & 1 & 0 & 0 & 0 & 0 & 0 & 0 & 0 & 0 \\
0 & 0 & 0 & 0 & 0 & 0 & 0 & 0 & 0 & 0 & 0 & 0 & 1 & 1 & 0 & 0 & 0 & 0 & 0 & 0 \\
0 & 1 & 0 & 0 & 1 & 0 & 0 & 0 & 0 & 0 & 0 & 0 & 0 & 0 & -2 & 0 & 0 & 0 & 0 & 0 \\
0 & 0 & 0 & 0 & 0 & 1 & 1 & 0 & 0 & 0 & 0 & 0 & 0 & 0 & 0 & -2 & 0 & 0 & 0 & 0 \\
0 & 0 & 0 & 0 & 0 & 0 & 0 & 1 & 1 & 0 & 0 & 0 & 0 & 0 & 0 & 0 & -2 & 0 & 0 & 0 \\
0 & 0 & 0 & 0 & 0 & 0 & 0 & 0 & 0 & 1 & 1 & 0 & 0 & 0 & 0 & 0 & 0 & -2 & 0 & 0 \\
0 & 0 & 0 & 0 & 0 & 0 & 0 & 0 & 0 & 0 & 0 & 1 & 1 & 0 & 0 & 0 & 0 & 0 & -2 & 0 \\
0 & 0 & 0 & 1 & 0 & 0 & 0 & 0 & 0 & 0 & 0 & 0 & 0 & 1 & 0 & 0 & 0 & 0 & 0 & -2 \\
0 & 0 & 0 & 0 & \frac{1}{2} & -\frac{1}{2} & 0 & 0 & 0 & 0 & 0 & 0 & 0 & 0 & \frac{1}{6} & -\frac{1}{6} & 0 & 0 & 0 & 0 \\
0 & 0 & 0 & 0 & 0 & 0 & \frac{1}{2} & -\frac{1}{2} & 0 & 0 & 0 & 0 & 0 & 0 & 0 & \frac{1}{6} & -\frac{1}{6} & 0 & 0 & 0 \\
0 & 0 & 0 & 0 & 0 & 0 & 0 & 0 & \frac{1}{2} & -\frac{1}{2} & 0 & 0 & 0 & 0 & 0 & 0 & \frac{1}{6} & -\frac{1}{6} & 0 & 0 \\
0 & 0 & 0 & 0 & 0 & 0 & 0 & 0 & 0 & 0 & \frac{1}{2} & -\frac{1}{2} & 0 & 0 & 0 & 0 & 0 & \frac{1}{6} & -\frac{1}{6} & 0 \\
0 & 0 & 0 & 0 & 0 & 0 & 0 & 0 & 0 & 0 & 0 & 0 & \frac{1}{2} & -\frac{1}{2} & 0 & 0 & 0 & 0 & \frac{1}{6} & -\frac{1}{6}
\end{pmatrix} \tag{A.18}$$

$$\boldsymbol{\theta} = \begin{pmatrix} \theta_{T1} \\ \theta_{1T} \\ \theta_{B2} \\ \theta_{2B} \\ \theta_{12} \\ \theta_{21} \\ \theta_{23} \\ \theta_{32} \\ \theta_{34} \\ \theta_{43} \\ \theta_{45} \\ \theta_{54} \\ \theta_{56} \\ \theta_{65} \\ \theta_{11} \\ \theta_{22} \\ \theta_{33} \\ \theta_{44} \\ \theta_{55} \\ \theta_{66} \end{pmatrix}$$

$$\boldsymbol{\Theta} = \begin{pmatrix}
\frac{\lambda}{3} & -\frac{\lambda}{6} & 0 & 0 & 0 & 0 & 0 & 0 & 0 & 0 & 0 & 0 & 0 & 0 & 0 & 0 & 0 & 0 & 0 & 0 \\
-\frac{\lambda}{6} & \frac{\lambda}{3} & 0 & 0 & 0 & 0 & 0 & 0 & 0 & 0 & 0 & 0 & 0 & 0 & 0 & 0 & 0 & 0 & 0 & 0 \\
0 & 0 & \frac{\lambda}{3} & -\frac{\lambda}{6} & 0 & 0 & 0 & 0 & 0 & 0 & 0 & 0 & 0 & 0 & 0 & 0 & 0 & 0 & 0 & 0 \\
0 & 0 & -\frac{\lambda}{6} & \frac{\lambda}{3} & 0 & 0 & 0 & 0 & 0 & 0 & 0 & 0 & 0 & 0 & 0 & 0 & 0 & 0 & 0 & 0 \\
0 & 0 & 0 & 0 & \frac{1}{3} & -\frac{1}{6} & 0 & 0 & 0 & 0 & 0 & 0 & 0 & 0 & 0 & 0 & 0 & 0 & 0 & 0 \\
0 & 0 & 0 & 0 & -\frac{1}{6} & \frac{1}{3} & 0 & 0 & 0 & 0 & 0 & 0 & 0 & 0 & 0 & 0 & 0 & 0 & 0 & 0 \\
0 & 0 & 0 & 0 & 0 & 0 & \frac{1}{3} & -\frac{1}{6} & 0 & 0 & 0 & 0 & 0 & 0 & 0 & 0 & 0 & 0 & 0 & 0 \\
0 & 0 & 0 & 0 & 0 & 0 & -\frac{1}{6} & \frac{1}{3} & 0 & 0 & 0 & 0 & 0 & 0 & 0 & 0 & 0 & 0 & 0 & 0 \\
0 & 0 & 0 & 0 & 0 & 0 & 0 & 0 & \frac{1}{3} & -\frac{1}{6} & 0 & 0 & 0 & 0 & 0 & 0 & 0 & 0 & 0 & 0 \\
0 & 0 & 0 & 0 & 0 & 0 & 0 & 0 & -\frac{1}{6} & \frac{1}{3} & 0 & 0 & 0 & 0 & 0 & 0 & 0 & 0 & 0 & 0 \\
0 & 0 & 0 & 0 & 0 & 0 & 0 & 0 & 0 & 0 & \frac{1}{3} & -\frac{1}{6} & 0 & 0 & 0 & 0 & 0 & 0 & 0 & 0 \\
0 & 0 & 0 & 0 & 0 & 0 & 0 & 0 & 0 & 0 & -\frac{1}{6} & \frac{1}{3} & 0 & 0 & 0 & 0 & 0 & 0 & 0 & 0 \\
0 & 0 & 0 & 0 & 0 & 0 & 0 & 0 & 0 & 0 & 0 & 0 & \frac{1}{3} & -\frac{1}{6} & 0 & 0 & 0 & 0 & 0 & 0 \\
0 & 0 & 0 & 0 & 0 & 0 & 0 & 0 & 0 & 0 & 0 & 0 & -\frac{1}{6} & \frac{1}{3} & 0 & 0 & 0 & 0 & 0 & 0 \\
0 & 0 & 0 & 0 & 0 & 0 & 0 & 0 & 0 & 0 & 0 & 0 & 0 & 0 & \frac{1}{6} & 0 & 0 & 0 & 0 & 0 \\
0 & 0 & 0 & 0 & 0 & 0 & 0 & 0 & 0 & 0 & 0 & 0 & 0 & 0 & 0 & \frac{1}{6} & 0 & 0 & 0 & 0 \\
0 & 0 & 0 & 0 & 0 & 0 & 0 & 0 & 0 & 0 & 0 & 0 & 0 & 0 & 0 & 0 & \frac{1}{6} & 0 & 0 & 0 \\
0 & 0 & 0 & 0 & 0 & 0 & 0 & 0 & 0 & 0 & 0 & 0 & 0 & 0 & 0 & 0 & 0 & \frac{1}{6} & 0 & 0 \\
0 & 0 & 0 & 0 & 0 & 0 & 0 & 0 & 0 & 0 & 0 & 0 & 0 & 0 & 0 & 0 & 0 & 0 & \frac{1}{6} & 0 \\
0 & 0 & 0 & 0 & 0 & 0 & 0 & 0 & 0 & 0 & 0 & 0 & 0 & 0 & 0 & 0 & 0 & 0 & 0 & \frac{1}{6}
\end{pmatrix} \tag{A.19}$$

The following are the equivalent of Eq. (3.17) for the $\overline{H} = 5$ lattice:

$$M_{T1} = M_{B6} = \frac{6\lambda^2 + d_1\lambda + 0.5d_2}{d} Fl \tag{A.20}$$

$$M_{1T} = M_{6B} = \frac{6\lambda^2 - 0.5d_2}{d} Fl \tag{A.21}$$

$$M_{11} = M_{66} = \frac{3d_1\lambda^2 + 3d_2\lambda}{d} Fl \tag{A.22}$$

$$M_{34} = M_{43} = \frac{Fl}{2} \tag{A.23}$$

$$M_{12} = M_{65} = \frac{-0.5d_3\lambda^2 + 6d_2\lambda + 0.5d_2}{d} Fl \tag{A.24}$$

$$M_{21} = M_{56} = \frac{0.5d_3\lambda^2 + 6d_1\lambda + 0.5d_4}{d} Fl \tag{A.25}$$

$$M_{22} = M_{55} = \frac{0.2\lambda^2 + 5.8\lambda + 0.5d_3}{d} Fl \tag{A.26}$$

$$M_{23} = M_{54} = \frac{-2d_5\lambda^2 + (6 + 2d_5)\,\lambda + 0.5\,(2d_6 + d_5)}{d} Fl \tag{A.27}$$

$$M_{32} = M_{45} = \frac{2d_5\lambda^2 + (6 - 2d_5)\,\lambda + (d_6 - d_7)}{d} Fl \tag{A.28}$$

$$M_{33} = M_{44} = \frac{d_5\lambda^2 + (6 - d_5)\,\lambda + d_6}{d} Fl \tag{A.29}$$

where $d = 12\lambda + d_1$ and $d_1 = \frac{181}{195}, d_2 = \frac{209}{195}, d_3 = \frac{168}{195}, d_4 = \frac{153}{195}, d_5 = \frac{1}{65}, d_6 = \frac{30}{65}, d_7 = \frac{1}{390}$. The shear strain, γ_{12} is obtained as follows

$$\begin{aligned} \gamma_{12} &= \frac{u_T + u_B + u_{12} + u_{23} + u_{34} + u_{45} + u_{56}}{5l + 2\lambda l} \\ &= \frac{\lambda\,(\theta_{T1} + \theta_{B2}) + \theta_{12} + \theta_{11} + \theta_{23} + \theta_{22} + \theta_{34} + \theta_{33} + \theta_{45} + \theta_{44} + \theta_{56} + \theta_{55}}{5 + 2\lambda} \end{aligned} \tag{A.30}$$

Appendix B

Estimation of $\hat{r_G}$

The average value of $r_G(\lambda)$ of Eqs. (3.39) and (3.40), is estimated so that the area bounded between the curve below $r_G(\lambda)$ and above line $r_G = \hat{r}_G$ equates the area bounded above $r_G(\lambda)$ and below $r_G = \hat{r}_G$. As an example consider the curve of Figure B.1.

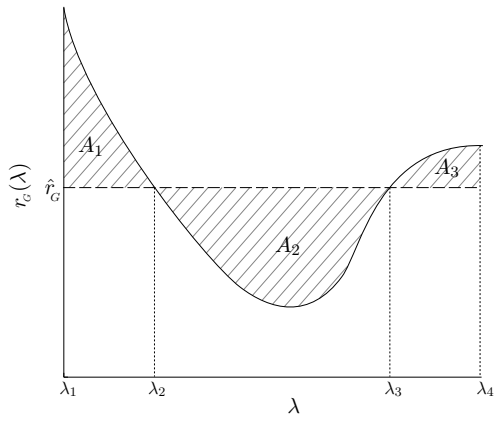

Figure B.1: Estimating $\hat{r}_G$.

In total, three areas are bounded by the line and curve, A_1, A_2, A_3 are given by

$$
\begin{aligned}
A_1 &= \int_{\lambda_1}^{\lambda_2} r_G(\lambda)\,\mathrm{d}\lambda - (\lambda_2 - \lambda_1)\hat{r}_G \\
A_2 &= -\int_{\lambda_2}^{\lambda_3} r_G(\lambda)\,\mathrm{d}\lambda + (\lambda_3 - \lambda_2)\hat{r}_G \\
A_3 &= \int_{\lambda_3}^{\lambda_4} r_G(\lambda)\,\mathrm{d}\lambda - (\lambda_4 - \lambda_3)\hat{r}_G
\end{aligned}
\tag{B.1}
$$

By equating the total area above to the total area below the line, i.e. $A_1 + A_3 = A_2$, gives

$$(\lambda_4 - \lambda_1)\hat{r}_G = \int_{\lambda_1}^{\lambda_4} r_G(\lambda)\,\mathrm{d}\lambda \quad . \tag{B.2}$$

This result is the same as the mean value of n data points, if the $r_G(\lambda)$ is discritised at n equally spaced points in the range $\lambda_1 - \lambda_4$.

Appendix C

Macroscopic strain maps

Macroscopic strain maps are generated to assist with the visualisation of the deformation field at the cell-scale. The approach follows the one used by Tekoglu and Onck (2008). Each cell in a lattice is first triangulated, using Delaunay triangulation. For illustration, a Voronoi lattice is used, which presents the most complicate geometry; as shown in Figure C.1. The total number of triangles n, after triangulation, depends on the number of vertices of a given cell.

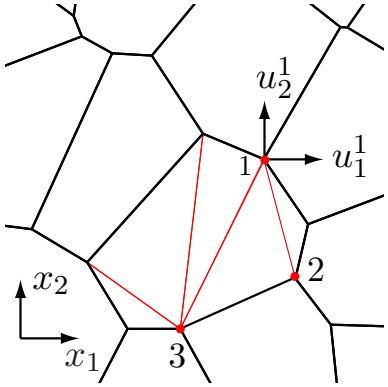

Figure C.1: Delaunay triangulation of a single cell with 7 vertices which gives 5 triangles, shown in red, following triangulation.

When the technique is used for the triangular lattice, no triangulation is required prior to any further analysis.

By assuming that each triangulated region j has a constant strain, i.e. forming a constant strain triangle in standard FE terminology, the vertex displacements u_i ($i = 1, 2$) from the FE analysis can be used to estimate its strain by

$$\boldsymbol{\varepsilon}_j = \begin{bmatrix} \varepsilon_{11} \\ \varepsilon_{22} \\ \varepsilon_{12} \end{bmatrix} = \frac{1}{2A_j} \begin{bmatrix} x_2^{23} & 0 & x_2^{31} & 0 & x_2^{12} & 0 \\ 0 & x_1^{32} & 0 & x_1^{13} & 0 & x_1^{21} \\ x_1^{32} & x_2^{23} & x_1^{13} & x_2^{31} & x_1^{21} & x_2^{12} \end{bmatrix} \begin{bmatrix} u_1^1 \\ u_2^1 \\ u_1^2 \\ u_2^2 \\ u_1^3 \\ u_2^3 \end{bmatrix} \tag{C.1}$$

where A_j is the area of triangle, $x_i^{pq} = x_i^p - x_i^q$ where $p, q = 1, 2, 3$ and u_i^p is the displacement of node p in the direction i. The overall or 'apparent' strain of a cell, $\varepsilon^{\text{cell}}$, is based on the weighted area-average strain of the n triangulated regions in that cell.

$$\boldsymbol{\varepsilon}^{\text{cell}} = \frac{\sum_{j=1}^{n} \boldsymbol{\varepsilon}_j A_j}{\sum_{j=1}^{n} A_j} \tag{C.2}$$

where $\boldsymbol{\varepsilon}_j$ is the strain tensor for triangle j, A_j is the area of triangle j for a cell with n triangles.

Appendix D

Abaqus/Standard numerical methods

This Appendix describes the numerical methodologies adopted by the commercial finite element package Abaqus/Standard, with particular emphasis on those required in this work.

Abaqus/Standard constructs the stiffness matrix which is solved either through the stiffness method for linear problems, or Newton's method for nonlinear problems. For nonlinear problems, the solution cannot be calculated by solving a system of linear equations given by the stiffness matrix. Abaqus/Standard estimates the solution by specifying the loading as a function of time and incrementing time to compute the nonlinear response of the system. Sources of nonlinearity can be due to material, element geometry and boundaries. In this thesis, only material nonlinearity was considered; all finite element models were performed within a small-strain context.

Abaqus/Standard divides the simulation into a number of time increments and finds the approximate equilibrium solution at the end of each time increment. Using the Newton's method, it often takes Abaqus/Standard several iterations to determine an acceptable solution to each time increment. An iteration is an attempt to find an acceptable approximate equilibrium solution in an increment. If the solution is deemed not acceptable, Abaqus/Standard tries another iteration; with each iteration the solution should converge closer to equilibrium. If not, Abaqus/Standard tries to find a solution with smaller time increment. In this thesis, automatic time incrementation was used with initial time increment set to 0.01s for 1s step duration.

D.1 Determining convergence

To better understand the process used by Abaqus/Standard to estimate an equilibrium configuration, consider a body with external forces, P, and the internal forces, I. For the

body to be in equilibrium, $P - I = 0$. To estimate the response of a nonlinear body to a small load increment δP_0 - at displacement u_0 and load P_0 - Abaqus/Standard uses the tangent modulus K_0 to calculate a displacement correction δu_0. Abaqus/Standard then calculates the structures internal forces I_1 for displacement $u_1 = u_0 + \delta u_0^1$ and calculates

$$R_1 = P_1 - I_1$$

where $P_1 = P_0 + \delta P_0$ and R_1 is the force residual for the iteration with δu_0. If $R_1 = 0$ for all degrees of freedom in the model, then the structure is in equilibrium and the solution is adopted as a point of the load-deflection curve. However this is never the case for a nonlinear problem. A tolerance value is used by Abaqus/Standard for R_1 in order to adopt a solution as an equilibrium state; a value of 0.5% of the average force (time and space averaged) in the structure is used.

If the iteration is not deemed to have converged, Abaqus/Standard uses the tangent modulus at u_1, K_1, together with R_1 to determine another displacement correction δu_1 that brings the structure closer to equilibrium. A new force residual is calculated, R_2, and if it still does not fulfil the convergence criteria, the process is repeated. Each iteration requires Abaqus/Standard to construct the model's stiffness matrix and solve the system of equations; thus the computational cost of each increment is the same as for a single linear analysis. As a consequence the computational cost of a nonlinear analysis, is many times that of its linear counterpart.

D.2 Viscous damping

Solving nonlinear problems is usually unstable and Abaqus/Standard provides an automatic mechanism for stabilizing unstable quasi-static problem by adding a damping to the model. Viscous forces of the form

$$F_v = cM\frac{\delta u}{\delta t}$$

are added to the global equilibrium equations

$$P - I - F_v = 0$$

where M is an artificial mass matrix, c the viscous damping factor, $\frac{\delta u}{\delta t}$ are the nodal velocities and δt is the time increment.

In most problems the first increment of the analysis is stable, hence there is no need to apply damping. The damping factor is then determined such that the viscous dissipation energy is a small percentage of the extrapolated strain energy for the next time increment; a value between 1×10^{-4} to 1×10^{-3} was used in this work depending on the problem at hand. However, in order to ensure that the inclusion of viscous dissipation does not interfere with the accuracy of the finite element solution, the viscous damping energy is compared with the total strain energy of the structure.; the ratio of the two has to be small and not exceed the tolerance specified in the solver.

Bibliography

Abad EMK, Khanoki SA, Pasini D. Fatigue design of lattice materials via computational mechanics: Application to lattices with smooth transitions in cell geometry. International Journal of Fatigue 2013;47:126–36.

Ahad FR, Enakoutsa K, Solanki KN, Bammann DJ. Nonlocal modeling in high-velocity impact failure of 6061-t6 aluminum. International Journal of Plasticity 2014;55:108–32.

Andrews EW, Gioux G, Onck PR, Gibson LJ. Size effects in ductile cellular solids. Part II: Experimental results. International Journal of Mechanical Sciences 2001;43:701–13.

Ashby MF. Materials Selection in Mechanical Design. Elsevier: Butterworth-Heinemann, 2005.

Ashby MF, Evans AG, Fleck NA, Gibson LJ, Hutchinson JW, Wadley HNG. Metal foams: a design guide. Boston: Butterworth Heinemann, 2000.

Ayatollahi MR, Nejati M. An over-deterministic method for calculation of coefficients of crack tip asymptotic field from finite element analysis. Fat Fract Eng Mater Struct 2010;34:159–76.

Banhart J, Brinkers W. Fatigue behavior of aluminium foams. Journal of Materials Science Letters 1999;18:617–9.

Bannantine JA, Comer JJ, Handrock JL. Fundamentals of Metal Fatigue Analysis. Prentice Hall, 1989.

Bastawros A F, Bart-Smith H, Evans AG. Experimental analysis of deformation mechanisms in a closed-cell aluminum alloy foam. Journal of the Mechanics and Physics of Solids 2000;48:301–22.

Bazant ZP. Instability ductility and size effect in strainsoftening concrete. Journal of the Engineering Mechanics Division 1976;102:331–44.

Bazant ZP, Cedolin L. Finite element modeling of crack band propagation. Journal of Structural Engineering 1976;108:331–44.

de Berg M, van Kreveld M, Overmars M, Schwarzkopf O. Computational Geometry: algorithms and applications. 2nd ed. Springer-Verlag Berlin Heidelberg, 2000.

Brezny R, Green DJ. Characterization of edge effects in cellular materials. Journal of Materials Science 1990;25:4571–8.

Calladine CR. Buckminster fuller's "tensegrity" structures and clerk maxwell's rules for the construction of stiff frames. International Journal of Solids and Structures 1978;14:161–72.

Chaboche JL. Continuous damage mechanics. a tool to describe phenomena before crack initiation. Nucl Engng Design 1981;:233–47.

Chaboche JL, Lesne PM. A non-linear continuous fatigue damage model. Fatigue Fract Engng Mater Struct 1988;11:1–17.

Chen C, Fleck NA. Size effects in the constrained deformation of metallic foams. Journal of the Mechanics and Physics of Solids 2002;50:955–77.

Chen C, Lu TJ, Fleck NA. Effect of imperfections on the yielding of two-dimensional foams. Journal of the Mechanics and Physics of Solids 1999;47:2235–72.

Choi S, Sankar BV. A micromechanical method to predict the fracture toughness of cellular materials. International Journal of Solids and Structures 2005;42:1797–817.

Christodoulou I, Tan PJ. Role of specimen size upon the measured toughness of cellular solids. Journal of Physics: Conference Series 2013;451:012004.

Cote F, Deshpande VS, Fleck NA. Shear fatigue strength of a prismatic diamond sandwich core. Scripta Materialia 2007a;56:585–8.

Cote F, Deshpande VS, Fleck NA, Evans AG. The compressive and shear responses of corrugated and diamond lattice materials. International Journal of Solids and Structures 2006;43:6220–42.

Cote F, Fleck NA, Deshpande VS. Fatigue performance of sandwich beams with a pyramidal core. International Journal of Fatigue 2007b;29:1402–12.

D5045-99e1 . Standard Test Methods for Plane-Strain Fracture Toughness and Strain Energy Release Rate of Plastic Materials. American Society for Testing and Materials, 2007.

Dattoma V, Giancane S, Nobile R, Panella FW. Fatigue life prediction under variable loading based on a new non-linear continuum damage mechanics model. International Journal of Fatigue 2006;28:89 – 95.

Deshpande VS, Ashby MF, Fleck NA. Effective properties of the octet-truss lattice material. Journal of the Mechanics and Physics of Solids 2001a;49:1747–69.

Deshpande VS, Ashby MF, Fleck NA. Foam topology bending versus stretching dominated architectures. Acta Materialia 2001b;49:1035–40.

Diebels S, Steeb H. The size effect in foams and its theoretical and numerical investigation. Proceedings of the Royal Society A 2002;458:2869–83.

E1820-11e2 . Standard Test Method for Plane-Strain Fracture Toughness K_{IC} of Metallic Materials. American Society for Testing and Materials, 2011.

E399-12e1 . Standard Test Method for Measurement of Fracture Toughness. American Society for Testing and Materials, 2012.

E8/E8M-13a . Standard Test Methods for Tension Testing of Metallic Materials. American Society for Testing and Materials, 2013.

Fatemi A, Yang L. Cumulative fatigue damage and life prediction theories: a survey of the state of the art for homogeneous materials. International Journal of Fatigue 1998;20:9–34.

Fleck NA, Deshpande VS. The resistance of clamped sandwich beams to shock loading. Journal of Applied Mechanics 2004;71:386–401.

Fleck NA, Deshpande VS, Ashby MF. Micro-architectured materials: past, present and future. Proceedings of the Royal Society A 2010;466:2495–516.

Fleck NA, Qiu X. The damage tolerance of elastic-brittle, two-dimensional isotropic lattices. Journal of the Mechanics and Physics of Solids 2007;55:562–88.

Gibson LJ. Biomechanics of cellular solids. Journal of Biomechanics 2005;38:377–99.

Gibson LJ, Ashby MF. Cellular Solids: Structure and Properties. UK:Cambridge University Press, 1997.

Giry C, Dufour F, Mazars J. Stress-based nonlocal damage model. International Journal of Solids and Structures 2011;48:3431–43.

Grenestedt JL. Effective elastic behavior of some models for 'perfect' cellular solids. International Journal of Solids and Structures 1999;36:1471–501.

Guo XDE, McMahon TA, Keaveny TM, Hayes WC, Gibson LJ. Finite element modeling of damage accumulation in trabecular bone under cyclic loading. Journal of Biomechanics 1994;27:145–55.

Harte AM, Fleck NA, Ashby MF. Fatigue failure of an open cell and a closed cell aluminium alloy foam. Acta Materialia 1999;47:2511–24.

Harte AM, Fleck NA, Ashby MF. The fatigue strength of sandwich beams with an aluminium alloy foam core. International Journal of Fatigue 2001;23:499–507.

Hutchinson RG, Fleck NA. Micro-architectured cellular solids-the hunt for statically determinate periodic trusses. ZAMM - Journal of Applied Mathematics and Mechanics 2005;85:607–17.

Hyun S, Torquato S. Optimal and manufacturable two-dimensional, kagome-like cellular solids. Journal of Materials Research 2002;17:137–44.

Jones RM. Mechanics of composite materials. Taylor & Francis, 1999.

Kachanov LM. Introduction to continuum damage mechanics. Martinus Nijhoff Publishers, 1986.

Kanninen MF, Popelar CH. Advanced fracture mechanics. OUP, New York, 1985.

Lakes RS. Size effects and micromechanics of a porous solid. Journal of Materials Science 1983;18(9):2572–80.

Lakes RS. Experimental microelasticity of two porous solids. International Journal of Solids and Structures 1986;22:55–63.

Larsson SG, Carlsson AJ. Influence of non-singular stress terms and specimen geom-

etry on small-scale yielding at crack tips in elastic-plastic materials. Journal of the Mechanics and Physics of Solids 1973;21:263–77.

Leevers PS, Radon JC. Inherent stress biaxiality in various fracture specimen geometries. International Journal of Fracture 1982;19:311–25.

Lemaitre J. A Course on Damage Mechanics. Springer-Verlag Berlin Heidelberg GmbH, 1992.

Li K, Gao XL, Subhash G. Effects of cell shape and cell wall thickness variations on the elastic properties of two-dimensional cellular solids. International Journal of Solids and Structures 2005;42:1777–95.

Li S. On the unit cell for micromechanical analyses of fibre-reinforced composites. Proceedings of the Royal Society: A 1999;455:815–38.

Li S. General unit cells for micromechanical analyses of unidirectional composites. Composites Part A: Applied Science and Manufacturing 2000;32:815–26.

Li S. Boundary conditions for unit cells from periodic microstructures and their implications. Composites Science and Technology 2008;68:1962–74.

Liu XY, Xiao QZ, Karihaloo BL. Xfem for direct evaluation of mixed mode sifs in homogeneous and bi-materials. Int J Numer Meth Eng 2004;59(8):1103–18.

Maiti SK, Ashby MF, Gibson LJ. Fracture toughness of brittle cellular solids. Scripta Metallurgica 1984;18:213–7.

Maxwell JC. On the calculation of the equilibrium and stiffness of frames. Philosophical Magazine Series 4 1864;27:294–9.

McCullough KYG, Fleck NA, Ashby MF. The stress-life fatigue behaviour of aluminium alloy foams. Fatigue and Fracture of Engineering Materials and Structures 2000;23:199–208.

McNeill SR, Peters WH, Sutton MA. Estimation of stress intensity factor by digital image correlation. Eng Fract Mech 1987;28:101–12.

MIL-HDBK-5H . Military Handbook - MIL-HDBK-5H: Metallic Materials and Elements for Aerospace Vehicle Structures. U.S. Department of Defense, 1998.

Motz C, Friedl O, Pippan R. Fatigue crack propagation in cellular metals. International Journal of Fatigue 2005;27:1571–81.

Motz C, Pippan R. Fracture behaviour and fracture toughness of ductile closed-cell metallic foams. Acta Materialia 2002;50:2013–33.

Olurin O, Fleck N, Ashby M. Deformation and fracture of aluminium foams. Materials Science and Engineering 2000;A291:136–46.

Olurin OB, McCullough KYG, Fleck NA, Ashby MF. Fatigue crack propagation in aluminium alloy foams. International Journal of Fatigue 2001;23:375–82.

Onck P, Andrews EW, Gibson LJ. Size effects in ductile cellular solids. Part I: Modeling. International Journal of Mechanical Sciences 2001;43:681–99.

Pijaudier-Cabot G, Bazant ZP. Nonlocal damage theory. Journal of Engineering Mechanics 1987;113:1512–33.

Queheillalt DT, Deshpande VS, Wadley HNG. Truss waviness effects in cellular lattice structures. Journal of Mechanics of Materials and Structures 2007;2:1657–75.

Rakow JF, Waas AM. Size effects in metal foam cores for sandwich structures. AIAA Journal 2004;42:1331–7.

Rakow JF, Waas AM. Size effects and the shear response of aluminum foam. Mechanics of Materials 2005;37:69–82.

Rice J. Limitations to the small scale yielding approximation for crack tip plasticity. Journal of the Mechanics and Physics of Solids 1974;22:17–26.

Richard B, Ragueneau F. Continuum damage mechanics based model for quasi brittle materials subjected to cyclic loadings: Formulation, numerical implementation and applications. Engineering Fracture Mechanics 2013;97:383 – 406.

Romijn NER, Fleck NA. The fracture toughness of planar lattices: Imperfection sensitivity. Journal of the Mechanics and Physics of Solids 2007;55:2538–64.

Saenz EE, Carlsson LA, Karlsson AM. In situ analysis of crack propagation in polymer foams. Journal of Materials Science 2011;46:5487–94.

Samal MK, Seidenfuss M, Roos E. A new mesh-independent rousseliers damage model: Finite element implementation and experimental verification. International Journal of Mechanical Sciences 2009;51:619–30.

Sanford RJ. A general method for determining mixed-mode stress intensity factors from isochromatic fringe patterns. Eng Fract Mech 1979;11:621–33.

Schaffner G, Guo XDE, Silva MJ, Gibson LJ. Modelling fatigue damage accumulation in two-dimensional voronoi honeycombs. International Journal of Mechanical Sciences 2000;42:645–56.

Shih CF. Small-scale yielding analysis of mixed mode plane-strain crack problems. ASTM STP 1974;560:187 – 210.

Silva MJ, Hayes WC, Gibson LJ. The effects of non-periodic microstructure on the elastic properties of two-dimensional cellular solids. International Journal of Mechanical Sciences 1995;37:1161–77.

Smith DJ, Ayatollahi MR, Pavier MJ. On the consequences of T-stress in elastic brittle fracture. Proceedings of the Royal Society A 2006;462:2415–37.

Sugimura Y, Rabiei A, Evans AG, Harte AM, Fleck NA. Compression fatigue of a cellular AL alloy. Materials Science and Engineering 1999;A269:38–48.

Symons D, Fleck N. The imperfection sensitivity of isotropic two-dimensional elastic lattices. Journal of Applied Mechanics 2008;75:051011–1–8.

Tan PJ, Reid SR, Harrigan JJ, Zou Z, Li S. Dynamic compressive strength properties of aluminium foams. Part I–experimental data and observations. Journal of the Mechanics and Physics of Solids 2005;53:2174 –205.

Tekoglu C, Gibson LJ, Pardoen T, Onck P. Size effects in foams: Experiments and modeling. Progress in Materials Science 2011;56:109–38.

Tekoglu C, Onck PR. Size effects in two-dimensional voronoi foams: A comparison between generalized continua and discrete models. Journal of the Mechanics and Physics of Solids 2008;56:3541–64.

Timoshenko SP, Gere JM. Mechanics of materials. Van Nostrand Reinhold Co, 1972.

Timoshenko SP, Goodier JN. Theory of elasticity. McGraw-Hill, 1970.

Wadley HNG, Fleck NA, Evans AG. Fabrication and structural performance of periodic cellular metal sandwich structures. Composites Science and Technology 2003;63:2331–43.

Wallach JC, Gibson LJ. Mechanical behavior of a three-dimensional truss material. International Journal of Solids and Structures 2001;38:7181–96.

Wang AJ, McDowell DL. In-plane stiffness and yield strength of periodic metal honeycombs. Journal of Engineering Materials and Technology 2004;126:137–56.

Warhadpande A, Jalalahmadi B, Farshid Sadeghi TS. A new finite element fatigue modeling approach for life scatter in tensile steel specimens. International Journal of Fatigue 2010;32:685 –97.

Weinzapfel N, Sadeghi F. Numerical modeling of sub-surface initiated spalling in rolling contacts. Tribology International 2013;59:210 –21.

Wicks N, Guest SD. Single member actuation in large repetitive truss structures. International Journal of Solids and Structures 2004;41:965–78.

Williams ML. On the stress distribution at the base of a stationary crack. Journal of Applied Mechanics 1957;24:109–14.

Yoneyama S, Ogawa T, Kobayashi Y. Evaluating mixed-mode stress intensity factors from full-field displacement fields obtained by optical methods. Eng Fract Mech 2007;74:1399–412.

Zhu HX, Hobdell JR, Windle AH. Effects of cell irregularity on the elastic properties of 2D Voronoi honeycombs. Journal of the Mechanics and Physics of Solids 2001;49:857 –70.

Zupan M, Deshpande VS, Fleck NA. The out-of-plane compressive behaviour of woven-core sandwich plates. European Journal of Mechanics - A/Solids 2004;23:411–21.